INSTITUT POLYTECHNIQUE DE PARIS

NNT : 20XXIPPAXXXX

Thèse de doctorat

ÉCOLE POLYTECHNIQUE

IP PARIS

Electronic properties of silver chloride: influence of excitons on the charge dynamics

Thèse de doctorat de l'Institut Polytechnique de Paris
préparée à École Polytechnique

École doctorale n°626 École Doctorale de l'Institut Polytechnique de Paris (ED IP Paris)
Spécialité de doctorat: Physics

Thèse présentée et soutenue à Palaiseau, le xx December 2020, par

ARNAUD LORIN

Composition du Jury :

Maurizia Palummo Professor at the University of Rome *Tor Vergata*, Italy (Departement of Physics)	Rapporteure
Giovanni Onida Professor at the University of Milan Statale, Italy (Departement of Physics)	Rapporteur
Silvana Botti Professor at the Friedrich Schiller Universität in Jena, Germany (Abbe Center of Photonics)	Examinatrice
Jean-François Guillemoles CNRS Research Director at the Institut du Photovoltaïque (UMR 9006)	Examinateur
Lucia Reining CNRS Research Director at the École Polytechnique (UMR 7642)	Directrice de thèse
Francesco Sottile Research Engineer at the École Polytechnique (UMR 7642)	Co-directeur de thèse
Matteo Gatti CNRS Researcher at the École Polytechnique (UMR 7642)	Invité

Contents

Table of notation and conventions

Abbreviations and acronyms	
DFT	Density Functional Theory
KS	Kohn-Sham
LDA	Local Density Approximation
TDDFT	Time Dependent Density Functional Theory
ALDA	Adiabatic Local Density Approximation
RPA	Random Phase Approximation
MBPT	Many-Body Perturbation Theory
PPM	Plasmon Pole Model
BSE	Bethe-Salpeter Equation
IPA	Independent Particle Approximation
EMT	Effective Medium Theory
MP	Monkhorst-Pack
BZ	first Brillouin zone
wf	wave-function
+ c.c.	adding the complex conjugate of the previous quantity
$f(1)$	function of one space and time variable $f(\mathbf{r}_1, t_1)$

Notation for crystals	
$\mathbf{G}$	reciprocal lattice vector
$\mathbf{k}$	vector in the BZ
$\mathbf{q}$	momentum transfer in the BZ
$\mathbf{Q}$	full momentum transfer ($\mathbf{Q} = \mathbf{q} + \mathbf{G}$)
$\mathbf{r}$	real space vector
Ω	volume of unit cell

Eigenvalues and eigenfunctions	
$\psi_{n\mathbf{k}}(\mathbf{r})$	one-particle wavefunction (e.g. Kohn-Sham), for state $(n, \mathbf{k})$
$\varepsilon_{n\mathbf{k}}$	energy of the Kohn-Sham state $(n, \mathbf{k})$
$\phi_{n\mathbf{k}}$	quasi-particle wavefunction, for state $(n, \mathbf{k})$
$E_{n\mathbf{k}}$	quasi-particle energy of state $(n, \mathbf{k})$
E_λ	exciton energy (eigenvalue of the excitonic Hamiltonian)
A_λ	excitonic eigenvector (of the excitonic Hamiltonian)
φ	many-body wave-function

Polarizability and dielectric matrices	
$\chi^0_{\mathbf{GG'}}(\mathbf{q}, \omega)$	independent-particle polarizability matrix
$\chi_{\mathbf{GG'}}(\mathbf{q}, \omega)$	full polarizability matrix
$\chi(1, 2)$	full polarizability (in real space, real time)
$\epsilon_M(\omega)$	macroscopic dielectric function
$\epsilon^{-1}_{\mathbf{GG'}}$	inverse dielectric matrix
$L(1, 2, 3, 4)$	Two-particle (4-point) correlation function
$P(1, 2)$	irreducible time-ordered polarizability
$\Gamma(1, 2, 3)$	3-point vertex function

Green's functions	
$G(\mathbf{r}, \mathbf{r}', \omega)$	one particle Green's function (in frequency domain)
$G(1, 2)$	one particle Green's function $G(\mathbf{r}_1, t_1, \mathbf{r}_2, t_2)$ in real space-time
$G_0(1, 2)$	independent-particle Green's function
$G^{(2)}(1, 2, 3, 4)$	two particle Green's function

density and potentials	
$n(\mathbf{r}, t)$	density of electrons
$\delta n(\mathbf{r}, t)$	induced density
$V^{\text{ext}}(\mathbf{r}, t)$	external perturbation
$v_{\text{xc}}(\mathbf{r})$	exchange-correlation potential
$v_{\text{c}}(\mathbf{r}, \mathbf{r}')$	Coulomb potential $v_{\text{c}}(\mathbf{r}, \mathbf{r}') = \frac{1}{\lvert\mathbf{r}-\mathbf{r}'\rvert}$
$W(1, 2)$	screened Coulomb interaction

Fourier transforms

$$f(t) = \int_{-\infty}^{\infty} f(\omega) e^{-i\omega t} d\omega$$

$$f(\omega) = \frac{1}{2\pi} \int_{-\infty}^{\infty} f(t) e^{i\omega t} dt$$

$$f(\mathbf{r}) = \sum_{\mathbf{G}} \int_{-\infty}^{\infty} f(\mathbf{q}) e^{i(\mathbf{q}+\mathbf{G})\cdot\mathbf{r}} d\mathbf{q}$$

$$f(\mathbf{q}+\mathbf{G}) = \frac{1}{8\pi^3} \int_{-\infty}^{\infty} f(\mathbf{r}) e^{-i(\mathbf{q}+\mathbf{G})\cdot\mathbf{r}} d\mathbf{r}$$

List of Figures

List of Tables

Part I

Introduction

Chapter 1

Historical motivation

The initial motivation for the present thesis was the theoretical study of the color formation phenomenon observed by Edmond Becquerel on silver chloride (AgCl) plates when exposed to monochromatic light. This phenomenon allowed him to propose the first color photography technique and to produce the first color pictures in 1848 [1]. This process did not lead to a concrete use due to its technical problems. It was nevertheless a first step towards color photography. The interest for Becquerel's technique was renewed in the years 2000s, following the discovery of pictures at the Museum of Natural History in Paris. A research study then began at the CRC (Centre de recherche pour la Conservation des Collections), a laboratory affiliated to the Museum of Natural History, in order to understand the mechanisms allowing the coloring of the material. This was an experimental investigation, but because of the sensitivity of the material to light irradiation, a project to study its optical properties by theoretical means was also designed: this project lead to the present thesis. The initial objective was to understand, using the tools of theoretical spectroscopy, the microscopic mechanisms allowing the phenomenon of coloring to take place.

In this Introduction, after a short report of the history of photography, we will address some details of Becquerel's process.

1.1 A brief history of photography

Photography, as most inventions, did not appear one day, out of nowhere to be ready to use. Its genesis is a long process of maturation, involving many participants, and the result of the combination of many different concepts. Even though a comprehensive view of the history of photography is beyond the aims of this thesis (the reader is oriented to either a classic book [2], a more recent point of view [3], or directly to a research quaterly [4]), it is still useful to highlight the major advances in order to draw the context in which the first photography was developed. A quick overview of the most important achievements will be given in the following.

The origin of photography is related to the question of light and its interaction with matter. One of the pioneers was Nicéphore Niépce. His interest in photography lead him to the invention of a process to fix an image on a support, i.e. to the creation of photography. The earliest photographic image that still survives today, the *Point de vue du Gras*, taken from the windows of the inventor in 1826, shown in Fig 1.1. His technique required a very long exposition time (from several hours to some days) and the resulting photographs were still lacking precision and clarity, but Niépce kept improving and testing new methods. Later, he collaborated with Louis Daguerre, another inventor interested in photography. Nicéphore Niépce died in 1833, leaving to Daguerre the task to improve the photographic process. In 1839, François Arago presented the works of Louis Daguerre to the French Academy of Sciences. This year marks the begin of photography outside the inventors' circle. Indeed, the novel photographic technique, known as Daguerrotype, was acclaimed by people and spread throughout the general public at great speed.

Figure 1.1: *Point de vue du Gras* photographic image, taken in 1826 by Nicéphore Niépce. Today conserved at the University of Texas, Austin, USA.

1.2 Becquerel's first color photography

Still, the Daguerrotype was a black and white photography, so the activity among inventors and researchers was still intense in order to achieve the fixation of colors on a support. Materials able to change color with exposition to light had been known for a long time, but it is only in the 18th and 19th centuries that these properties began to attract the attention of scientists. Edmond Becquerel was a physicist investigating the effects of light on materials. In his research activities, he discovered the photovoltaic effect and studied phosphorescence and luminescence properties. Following the works of Seebeck, Hunt and Herschel on silver chloride [5, 6], in 1848 Becquerel developed the first color photographic process. He managed to fix the colors of the solar spectrum in a photochromatic image (as he called it), which is represented in Fig. 1.2. He discussed this achievement in a report presented to the French Academy of Sciences [1]. The technique developed by Becquerel was later rarely used, since it required long duration of exposure and, more importantly, since the image could not be stabilized. The original photochromatic image is still preserved in complete darkness. So the rise of color photography as a popular technique will have to wait the beginning of the 20th century with the photocromy procedure patented by the Lumière brothers [7]. Nevertheless, the work of Becquerel raises fundamental questions on how silver chloride is able to absorb and retain the color of the light.

Before ending this section, we would like to mention two alternative methods that also emerged in the XIX century:

- Ducos du Hauron's color photography, the pioneer of the three-color photography (which later inspired the color substractive technique), patented in 1868. This technique was recently rediscovered and studied at the ESRF synchrotron [8].

- Lippmann interference photochrome, a two-step technique to fix colors on a plate, which awarded his inventor the Nobel prize in Physics in 1908 (at present the only Nobel prize granted to a photography-related technique [1]) [9, 10].
  Though this method was also abandoned, in favor of the three-color photochromes, it has been recently rediscovered, due to its high resolution and the impossibility to copy the obtained image. The optically varied device that is used today to issue security documents (passports, driving licences, badges, etc.) is based on Lippmann's technique [11, 12].

[1] If we exclude the Nobel prize awarded to Dennis Gabor for the invention of holography.

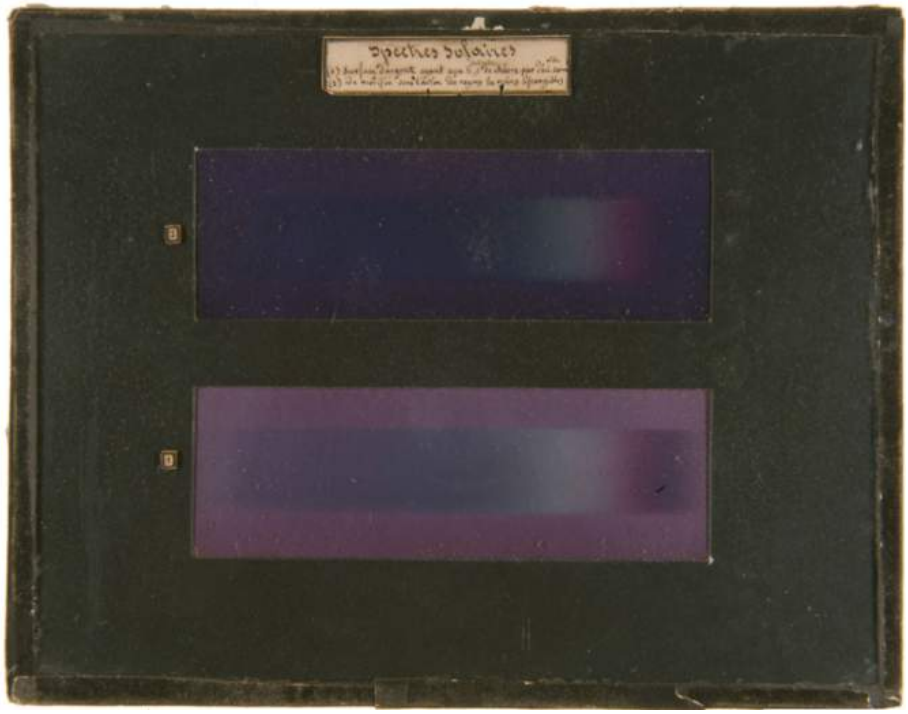

Figure 1.2: *Solar spectrum*, Edmond Becquerel 1848, Musée Nicéphore Niépce, Chalon-sur-Saône (France)

1.3 What is the origin of the colors?

Becquerel explained in his report [1] the protocol to produce his photograph. A quick summary of the process is given here: the base material is a silver plate which is combined with chlorine, by immersion in a copper chlorine solution or by electrolysis using a hydrochloric acid solution, in order to form a layer of silver chloride. The sensitized layer is colored by the exposition to light: the resulting image reminds the colors of the incident light, to form directly the picture on the photo-plate.

The physical mechanisms leading to the formation of the colors in the photochromatic picture have been the source of many debates throughout the 19th century, but no definitive answer could be delivered [13–16]. Two different explanations were put forward. The first one is the pigmentary hypothesis, implying the presence of colored elements, for example impurities due to the process used for the preparation of the material. The second one is the interference hypothesis, relying on interference between structures at the microscopic scale, in a similar fashion as for the Lippman photography mentioned above. This debate went on for more than 50 years and was not settled until the beginning of the present thesis.

Recently, a research project started at the Centre de Recherche sur la Conservation (CRC) in the National Museum of Natural History in Paris, using the experimental tools of the 21th century to answer the question of the origin of the colors of Becquerel's photography. This project was carried out in the PhD thesis of Victor de Seauve [17] (started in 2015 and defended in 2018). His study ruled out the two hypotheses mentioned before, and put forward a new explanation based on a plasmonic origin and a photoadaptive mechanism.

The research team at CRC was able to replicate in the laboratory the procedure described by Becquerel [1]. They could hence examine the sensitized plates in great detail, during and after exposure to monochromatic light of various wavelengths. They found that the optical properties of the samples evolve differently according to the exposition wavelength, see the left panel of Fig 1.3 for an example.

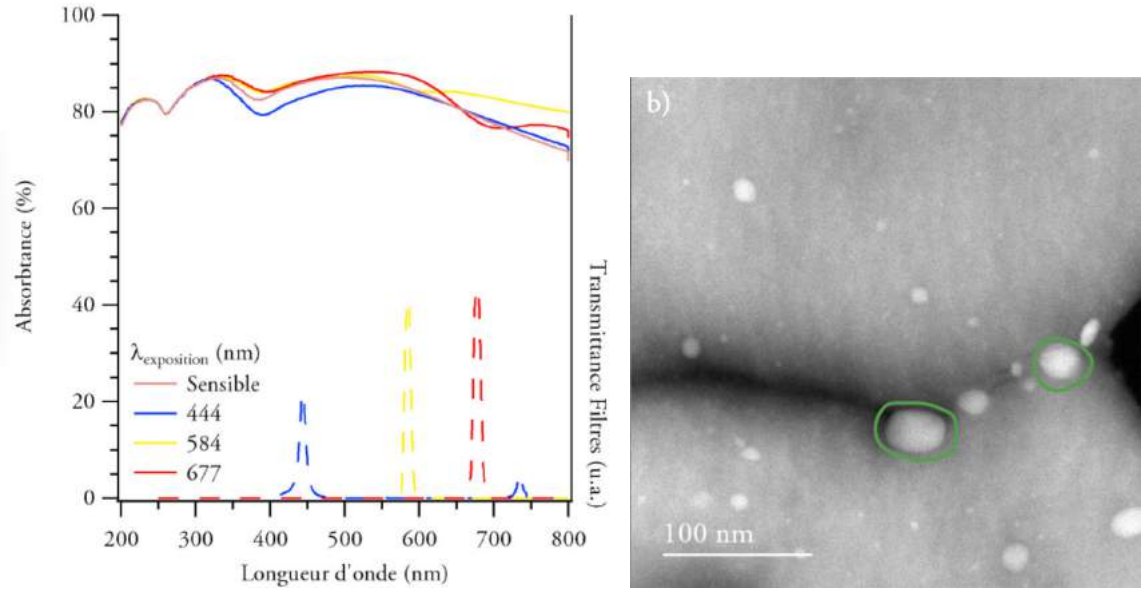

Figure 1.3: Left: Absorbance of silver chloride plates reproducing Becquerel's process, prepared by Victor de Seauve. The plates are exposed to light of different wavelengths, shown by the dashed lines, corresponding to different colors. The resulting absorbances are shown by the continuous lines. The absorbance for a non-exposed (called "sensible") sample is also presented, shown in light pink. Right: Dark field image of silver nanoparticles embedded in silver chloride. Both images are taken from [18].

The study has confirmed the key role of silver chloride as the active element, excluding other chemical components. By means of photoemission and X-ray absorption spectroscopies the team demonstrated that the sensitized layer does not undergo chemical change. Moreover, using scanning electron microscopy they did not find the presence of periodic structures, refuting the interference hypothesis. Finally they could relate the changes of absorbance spectra (left panel of Fig. 1.3) to the presence and modification of silver nanoparticles in the sample (right panel of Fig. 1.3). This finding makes the sensitized layers similar to Ag-AgCl compounds that have been studied as plasmonic photocatalyst [19–21]. Similar behavior of photo-adaptation has been reported also for silver nanoparticles at the surface of TiO_2 films [22–24].

It has been shown that nanoparticles are already present in the sensitized sample, at different locations: inside the AgCl grains or at their edge boundaries. The particles have plasmon resonances at different energies because of the different environment and because of their size distribution, which varies between 15 and 150 nm. When light is shined on the material, the nanoparticles with resonance at the wavelength of the light get excited. The disexcitation of the nanoparticle can happen through the transfer of electrons from the nanoparticle to the silver chloride environment. This leads to the positive electric charging of the nanoparticle, which in turn induces the emission of positively charges silver ions into the silver chloride. The great mobility of Ag^+ ions in the AgCl matrix allows them to recombine with the electrons, forming new nanoparticles. By repeating this process many times, the nanoparticles change their size, and their resonance energy moves away from the energy of the light until they can no longer absorb. The displacement of all the transition energies away from the light frequency creates, at the macroscopic level, a depletion in the absorption spectrum at the energy of the light. The sample thus appears with the color of the light because the absorption rate has decreased.

At the beginning of the thesis, the plasmonic hypothesis was not yet finalized and other hypotheses were considered, including the possible role of defects or the involvement of self trapped exciton in silver chloride [25, 26]. Moreover, spectroscopy experiments on AgCl are challenging for its great sensitivity to light or X-Ray irradiation. In order to get theoretical understanding of silver

chloride in a controlled manner, a collaboration was started between the Theoretical Spectroscopy group at the Laboratoire des Solides Irradiés and the CRC at the Museum of Natural History. With the new plasmonic hypothesis, the aim of the work has been shifted to the study of the key process, the charge dynamics as response to an external perturbation, with the long-term goal to understand the charge transfer at the interface between silver nanoparticles and silver chloride.

Chapter 2

Silver Chloride

Besides being the key component in the first color photography in history realized by E. Becquerel in 1848 [27], silver chloride is a versatile material, long known for a large variety of applications. For instance, it is a reference electrode for electrochemical measurements [28], and in its nanostructured phase it has remarkable antimicrobial properties [29–31]. Moreover, it has been recently shown that silver clusters at AgCl surfaces form an efficient photocatalytic system [20, 32–35]. The largest range of applications of AgCl is related to its optical properties: it is responsible for several shades in stained glass [36], and it is widely used as photochromic material in photosensitive glasses [37]. In particular, AgCl is a crucial ingredient in photographic paper to produce the latent image[38–40].

In this chapter we will provide a short summary of experimental results and calculations on the electronic and optical properties of AgCl. Refs [41, 42] give an extended review of the investigations on AgCl.

2.1 Experimental optical spectra

The photochromic properties of AgCl that make it appealing for applications are at the same time problematic for spectroscopy experiments: its electronic and optical properties can be changed significantly by irradiation with light [43–46], thus affecting the reliability of the measured spectra. The main effect of X-ray or electron beams is radiolysis: the chemical decomposition by the ionizing radiation [47–49] and partial reduction of AgCl to metallic Ag have been observed.

Information about the band gap has been extracted from optical measurements that were performed four to five decades prior to the present work. In particular, Ref. [50] reported measurements of the absorption edges of silver halides and their fine structure in 1961. From these results, the indirect band gaps of AgCl and AgBr at different temperatures were extracted. Excitonic effects were invoked to explain the observations. Later, Carrera and Brown [51] measured the absorption coefficient of silver chloride and silver bromide in the near and extreme ultra-violet, in two frequency ranges: between 3.5 to 6.7 eV and between 30 and 240 eV. Additional optical absorption data are available in Ref.[52].

The spectra show a strong dependence on temperature T. Measurements of the absorption edge as a function of temperature have been carried out in [53]. The work reports absorption, fluorescence and photocurrent measurements on silver chloride. Results can be extrapolated to zero temperature by fitting the measured absorption coefficient with $\alpha = \alpha_0 e^{-\epsilon/T}$ between 387 nm and 400 nm. The indirect gap is so estimated at 3.25 eV (382 nm).

The strong temperature dependence can be seen on Fig. 2.1 for the reflectivity [54] in the left panels, and for the extinction coefficient and index of refraction, in the right panels. Both results show a sharpening of structures and a shift to higher energy with lower temperature. Similar trends were observed in earlier absorption measurements [55]. The authors also point out the influence of sample preparation, which is confirmed by results in [56].

Unfortunately, not much details can be extracted from these results. Instead, the left panel of Fig. 2.2 shows the room temperature reflectivity results of [52], with their interpretation in terms

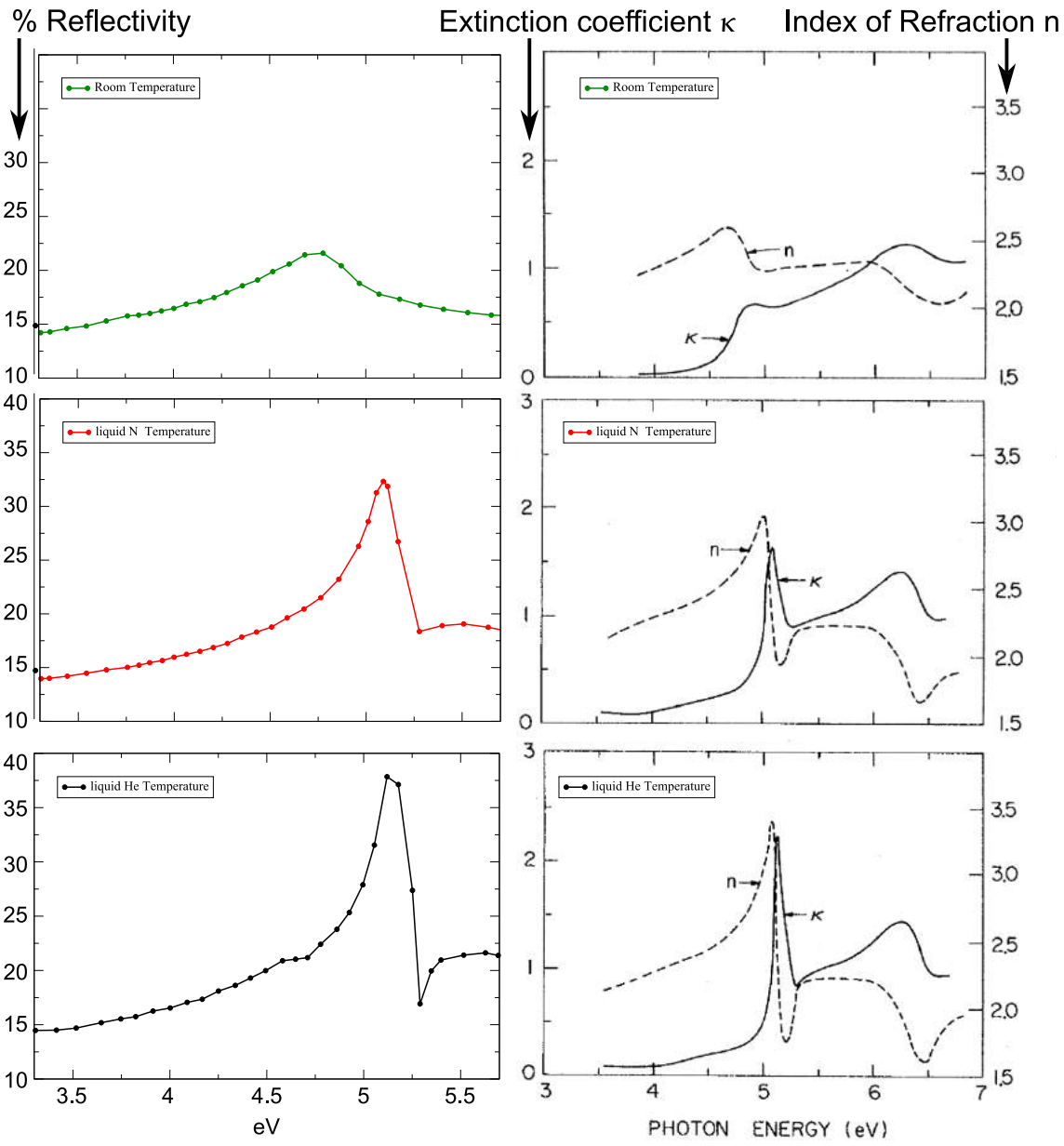

Figure 2.1: Reflectivity data of AgCl at different temperatures are displayed on the left panel. From top to bottom: room temperature (dark green), liquid nitrogen (red) and liquid helium (black) temperature data taken from Ref. [54]. Right panels show the refraction index n and the extinction coefficient κ for AgCl, again for different temperatures. Refraction index and extinction coefficient figures are taken from Ref. [51].

of interband and excitonic transitions. From these measurements, the real and imaginary parts of the dielectric function have been extracted, as given in the right panel. These results must, however, be supposed to carry a significant error bar, both because of the room temperature and because of the Kramers-Kronig relation applied over a limited range of frequency.

Altogether, these experimental results give precious indications concerning the optical properties of AgCl, but they do not allow one to infer precise information concerning the electron addition and removal band gaps, nor concerning the intrinsic optical spectra of AgCl in absence of impurities, phonons or other external influence. Therefore, predictive first principles calculations

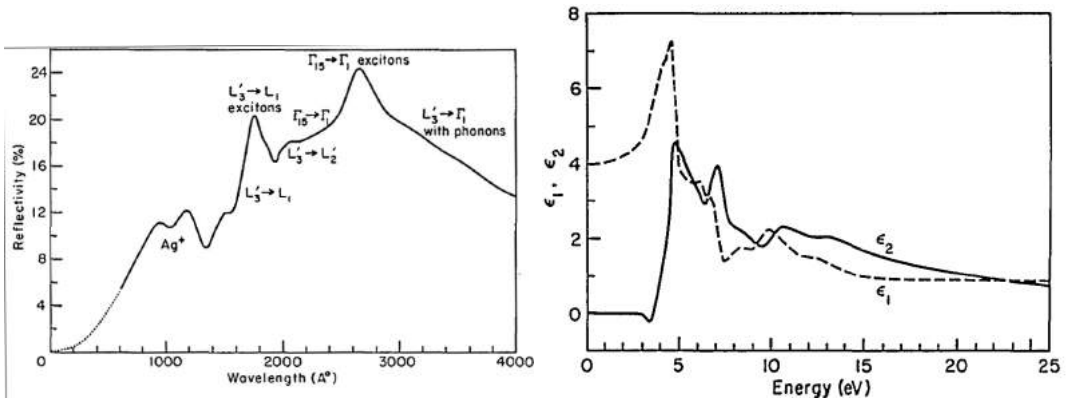

Figure 2.2: Reflectivity spectrum of AgCl at room temperature, taken from Ref. [52]. Right panel: real and imaginary parts of the dielectric function, obtained via Kramers-Kronig transformation of the reflectivity data [52].

have an important role to play.

2.2 Review of previous calculations

Theoretical simulations are a valuable tool to provide a solid benchmark and remove possible ambiguities from experimental results. Early work was done on the basis of tight-binding models or empirical pseudopotentials [57, 58]. Several first-principles studies [59–65] within density functional theory [66, 67] (DFT) have focused on ground-state properties and the Kohn-Sham electronic structure. However, these methods cannot access the band gap, a fundamental ingredient for the optical properties. Only recently, band structure calculations using the GW approximation [68] (GWA) within many-body perturbation theory [69] (MBPT) have yielded more reliable numbers for the photoemission gaps [70–72]. The different results for the band gaps are summarized in Table 2.1. They cover a broad range of values. Moreover, and most importantly, to the best of our knowledge, MBPT studies for the optical properties of silver chloride were missing before the work of this thesis.

	Direct gap	Indirect gap
LDA	3.348[a], 3.34[b], 2.91[c], 3.10[d], 2.909[e], 2.8[g]	0.636[a], 0.65[b], 0.59[c], 0.96[d] 0.6[g] 0.633[e], 0.56[f]
PBE	3.094[a], 3.221[e]	0.94[a], 0.940[h], 0.94[i], 0.87[j], 0.935[e]
GWA	5.05[c]	2.16[i],2.97[c], 2.62[j], 2.99[k]

a Reference [60]
b Reference [59]
c Reference [71]
d Reference [62]
e Reference [63]
f Reference [64]
g Reference [65]
h Reference [61]
i Reference [70]
j Reference [72], G^0W^0
k Reference [72], GW^0

Table 2.1: Calculated direct and indirect band gap of silver chloride. LDA stands for the local density approximation to DFT (see Ch. 4). PBE stands for the Perdew-Burke-Ernzerhof functional. G^0W^0 and GW^0 are flavors of the GW approximation explained in Ch. 6.

Chapter 3

Theoretical challenges

Describing, understanding and predicting the properties of a material from a theoretical perspective has been a long lasting challenge. Since the introduction by Erwin Schrödinger of the equation that carries his name, it has become possible in principle to describe the dynamics of electrons and ions in a material: through the many-body wavefunctions of a material, one can in principle calculate any observable and therefore, any of its properties. However, the Schrödinger equation turns out to be impossible to solve, even numerically, when the number of electrons increases beyond just a few, let alone when it comes to macroscopic numbers as it is the case in a typical piece of material: even in a tiny sample used in experiments the number of electrons and ions is at least of the order of 10^{23}. Nevertheless, the Schrödinger equation gives a framework for elucidating the properties of a material, including the essential ingredient, the quantum nature of electrons. Researchers over many decades have developed theories involving simplified equations, which opens the possibility to make predictions and comparison with experiments. These theories can be approximations to the Schrödinger equation, or they can also be an in principle exact reformulation of the expressions that yield a given observable, avoiding the explicit appearance of the many-body wavefunctions. A prominent example is Density Functional Theory (DFT) introduced in Ch. 4, where ground-state observables such as the total energy are expressed in terms of the density instead of the ground state wavefunction. Another example is many-body perturbation theory (see Ch. 6), where observables are expressed in terms of a one-body Green's function or Green's functions of higher order, and then approximated by a perturbation expansion in the Coulomb interaction. According to the property of interest and the material that is studied, these approaches can be more or less convenient. In all cases however, approximations have to be made at some point to make calculations on real materials feasible.

Here we are interested in a specific class of properties, linked to the interaction of matter with radiation. As we have seen in the two previous chapters, we wish to understand the spectroscopic properties of a material - here in particular, silver chloride - and of different materials put together, such as silver nanoparticles in AgCl. The focus lies on the absorption of light. Moreover, we are interested in the consequences, namely, on the dynamics of the charges in a material that is excited by an external source.

The first question to be answered is the level of theory that is needed to respond to our questions in a satisfactory way. A vast choice of approaches is available, ranging from simple models such as effective medium theory, to advanced first principles calculations in the framework of many-body perturbation theory. As it turns out, the calculation of absorption spectra of silver chloride alone already constitutes a challenge for various reasons: in particular, the localized d silver states are not well described by simple functionals used in density functional theory and time-dependent density functional theory, the material exhibits bound excitonic states in the band gap that are pure many-body effects, and its band structure does not fall into any class of typical band structures that give rise to models such as the Wannier model for bound excitons. Therefore, a part of the present work is devoted to determine the theoretical ingredients that are mandatory for a reliable description.

Most experiments focus on the macroscopic properties, such as light absorption. However, it

is worthwhile to elucidate what happens in the material on an atomic scale, not least because these processes determine much of the performance of applications using the material, and this knowledge can be crucial: for example, in solar cell applications the dynamics of charges at an interface between semiconductors is responsible to a large extent for the quality of the device. In the present thesis we are interested in the density changes induced by the response to an external perturbation. This is a microscopic information that is at the origin of light absorption, but that cannot be inferred by simply looking at absorption spectra. Theory can play a crucial role here. However, whereas many-body effects in electronic spectra have been studied extensively, still little is known about their impact on the microscopic charge response. It is therefore most interesting to investigate the effect of various material characteristics and many-body contributions on this phenomenon.

At the same time, as explained in the Ch. 1, Becquerel's photochromatic process involves silver nanoparticles. The dynamics of the charges at the interface between AgCl and the nanoparticles is of critical importance for the explanation of the origin of the colors in Becquerel's invention. However, even within a well understood theoretical framework it will remain challenging to describe this dynamics, as the size of the nanoparticles is beyond what is accessible with *ab initio* methods. This requires an additional analysis of what is important at the interface and what can be discarded: for example, an analysis of the importance of excitons close to the interface.

This discussion leads up to the following goals that constitute a guideline for the present thesis:

- to understand electronic excitations in AgCl in detail,
- to develop a tool to predict the dynamics of excited charges in a realistic interacting material,
- to apply this tool to AgCl, and to distinguish many-body effects from specific material properties,
- to describe the charge dynamics at a model interface between AgCl and silver, as a first step to the understanding of excited silver nanoparticles in an AgCl matrix.

In the following part, a summary of the theoretical and methodological approaches used in this thesis is given. In the third part, the *ab initio* study of silver chloride is presented. The successes and problems of the different approaches are highlighted and a model is presented that allows us to overcome some of the numerical difficulties. Subsequently, we introduce our approach to study the induced density, and we show and analyze results for silver chloride, comparing different levels of theory. In a last chapter, an exploratory study of the interface, the problems to face, and possible solutions are exposed. Finally, conclusions are drawn in a last part and outlooks are proposed.

Part II

Methodology

Chapter 4

Density Functional Theory

Density Functional Theory (DFT) is today the most used method [73] for tackling ground-state properties of materials. It is an exact theory that permits one to write and calculate observables as functionals of the electron density, instead of requiring the knowledge of the many-body wavefunction. DFT is based on the theorems demonstrated in the 60's by Pierre Hohenberg and Walter Kohn [66].

Let us consider a system of interacting electrons in an external potential. The Schrödinger equation reads:

$$\left(\sum_i \hat{T}_i + \sum_{i<j} v_{\mathrm{c}}(|\mathbf{r}_i - \mathbf{r}_j|) + \sum_i V^{\mathrm{ext}}(\mathbf{r}_i)\right) \varphi(\mathbf{r}_1, \mathbf{r}_2, \ldots, \mathbf{r}_N) = E\varphi(\mathbf{r}_1, \mathbf{r}_2, \ldots, \mathbf{r}_N), \tag{4.1}$$

with v_{c} the Coulomb interaction between two electrons and $\hat{T}_i$ and $\hat{V}^{\mathrm{ext}}$ the kinetic term and the external potential acting on each electron. The external potential uniquely defines the system (the kinetic operator and Coulomb interaction are the same for every system of electrons). And since every system in the ground state is described by a wavefunction,[1] we can say that every observable is a functional of the wavefunction of the system $O = O[\varphi] = \langle\varphi|\hat{O}|\varphi\rangle$. What makes this equation hard to solve for a real system is the Coulomb interaction between the electrons.

4.1 The Hohenberg-Kohn theorem

Hohenberg and Kohn instead proposed [66] (HK) and demonstrated that any observable of a system, in its ground state, can be formally expressed as a functional of the ground state electron density. The demonstration shows the one-to-one correspondence between the ground state density of a system and the external potential. We do not report here the demonstration, that can be found in the original paper [66], as well as in many books [74–76] and recent reviews [77–79].

We would like to remark the huge simplification, in principle, that the HK theorem implies. In the Schrödinger equation approach, we have to solve the many-body equation (that scales exponentially with the number of electrons) to find the 3N variables wavefunction $\varphi(\mathbf{r}_1, \mathbf{r}_2, \ldots, \mathbf{r}_N)$. Once we have the wavefunction,[2] we can evaluate any observable via the expectation value of the corresponding operator, with the wavefunction. This corresponds to a $3N$-dimensional integral. However, in the density functional formalism, every observable is a unique functional of the density $O = O[n]$, the electron density being a simple function of 3 variables. Let us take the example of the total energy of a system, that can be written as

$$E = T[n] + E_{ee}[n] + \int d\mathbf{r}\, V_{ext}(\mathbf{r})n(\mathbf{r}) = F[n] + \int d\mathbf{r}\, V^{ext}(\mathbf{r})n(\mathbf{r}), \tag{4.2}$$

[1] Degenerate ground states require a generalization of this concept.

[2] We should also consider to problem to store such a wavefunction: already in a system with 10 electrons, this is a function of a huge number of arguments, m^{30}, where m is the number of mesh points of space discretization. Assuming a very rough modeling of space as a cube of 100x100x100 mesh points, the wavefunction would require 8×10^{30} bytes, or 8×10^{18} terabytes. That is a lot of terabytes.

where $T[n]$ is the kinetic energy term, and $E_{ee}[n]$ is the electron-electron interaction term, both written as a functional of the density. The sum of these two terms, which are independent of the system, is sometimes called the universal functional $F[n]$. The simplification is undoubtful, at least in principle. We do not know however how the kinetic energy and the electron-electron interaction energy depend on the density. The parallel with the Schrödinger equation approach is striking. In the latter, the Schrödinger equation contains very well-known terms. It is in practice impossible to solve, but if we did, we would have the many-body wavefunction. If we have the many-body wavefunction, we can evaluate every observable, via the expectation value (again very difficultly, for it is a 3N integral). In the density functional formalism, we know that we can write in principle each observable as a functional of the density, that seems to be a much simpler integral, but, first, we do not know the functional dependence on the density and second, we do not know the density.

If, by chance, we knew the expression of $T[n]$ and $E_{ee}[n]$ as a functional of the density, we could use the variational theorem and compute both the ground-state density and the ground-state total energy, by minimizing the total energy functional of the density of Eq 4.2. We do not know the universal functional $F[n] = T[n] + E_{ee}[n]$, but it turns out that this minimization strategy, permits one to devise a very powerful procedure to tackle the many-body problem in the density functional formalism, as demonstrated by Walter Kohn and Lu Sham in 1965 [67].

4.2 The Kohn-Sham approach

The idea of Kohn and Sham [67] (KS) was to use an auxiliary system of non-interacting electrons that has the same density as the interacting system. As before, we refer to the literature for the demonstration of the existence of such auxiliary system [74–76]. The introduction of this independent particle system is obtained via minimization of the total energy functional of the density, with the density supposed to be equal to that of a non interacting system. The obvious advantage is that we know how to write the density of a non-interacting system: $n(\mathbf{r}) = \sum_i |\psi_i(\mathbf{r})|^2$. The wavefunctions ψ_i are the solution of a set of equations (called the KS equations) for non-interacting electrons:

$$\left[-\frac{1}{2}\nabla^2 + v_{\mathrm{KS}}([n], \mathbf{r})\right] \psi_i(\mathbf{r}) = \varepsilon_i \psi_i(\mathbf{r}). \tag{4.3}$$

The eigenvalues ϵ_i mathematically are Lagrange multipliers and cannot be formally interpreted as addition or removal energies measured in photoemission. The KS equations constitute an enormous advantage with respect to the many-body Schrödinger equation. They are easy to solve, similarly to the Hartree equations, even though they require a self-consistent procedure. However, the KS potential

$$v_{\mathrm{KS}}([n], \mathbf{r}) = V^{\mathrm{ext}}(\mathbf{r}) + v_H([n], \mathbf{r}) + v_{\mathrm{xc}}([n], \mathbf{r}) \tag{4.4}$$

contains, beside the external and the Hartree potential, an unknown term, the exchange-correlation potential $v_{\mathrm{xc}}(\mathbf{r}) = \frac{\delta E_{\mathrm{xc}}([n])}{\delta n(\mathbf{r})}$ defined as the functional derivative of the exchange-correlation energy with respect to the density. This latter term enters the definition of the total energy

$$E = T_0[n] + E_H[n] + \int V^{\mathrm{ext}}(\mathbf{r}) n(\mathbf{r}) d\mathbf{r} + E_{xc}[n], \tag{4.5}$$

and again it is the only unknown term, since we know how to write the kinetic energy of non-interacting electrons T_0 in terms of the one-particle KS wavefunctions[3] and we also know the Hartree energy. The exchange-correlation energy constitutes then the unknown of the KS approach, just as the universal functional $F[n] = T[n] + E_{ee}[n]$ is unknown in the Hohenberg and Kohn theorem. Writing down this term will permit us to have an idea of how difficult it is to evaluate the exchange-correlation energy

$$E_{\mathrm{xc}}([n]) = F[n] - T_0[n] - E_H[n] = T[n] - T_0[n] + E_{ee}[n] - E_H[n]. \tag{4.6}$$

[3] Strictly speaking $T_0[n]$ is only an implicit functional of the density. We write, in fact, $T_0 = -\sum_i \int \psi_i^*(\mathbf{r}) \frac{\nabla^2}{2m} \psi_i(\mathbf{r}) d\mathbf{r}$ and, since $\psi_i = \psi_i([n])$ are unique functionals of the density, so is T_0.

$E_{\rm xc}$ is defined as the sum of two differences: i) the difference between the kinetic energy of the system and the kinetic energy of the auxiliary independent particle system; ii) the difference between the electron-electron interaction and its value in the Hartree approximation. The exchange correlation energy is then defined as everything we do not know: we strip out the independent particle kinetic energy, because we know how to write it, from the unknown kinetic energy, and we strip out an estimate of the electron-electron interaction, in the Hartree approximation (i.e. from classical electrostatics), from the exact electron-electron interaction. What do we have left? The difficult part, the extra mile to go from $T_0[n]$ to $T[n]$, and to go from $E_H[n]$ to $E_{ee}[n]$. It turns out that to find approximations for $E_{\rm xc}$ is indeed very difficult, even more difficult if we search an for explicit functional of the density (like the Hartree energy). In spite of this intrinsic difficulty, DFT is today widely applicable to a vast range of systems (not only in electronic structure calculations). There are many reasons for that:

- the set of one-particle equations is a massive advantage with respect to any (many-body) wavefunction based approach, in terms of scaling, cpu workload, memory requirements, and, in general, in all numerical implementation aspects; this comes also from the fact that the one particle equations are local equations, in the sense that all potentials act as multiplicative operators[4] to the one-particle wavefunctions, unlike, for instance, Hartree-Fock equations, instrinsically non-local.

- the $E_{\rm xc}$ is unknown, but it is also a *small* quantity, being defined (see Eq. (4.6)) as energy differences. It is reasonable to prefer to approximate small quantities, rather than the full universal functional $F[n]$.

- very simple approximations (see below) are able to give qualitatively and, often, quantitatively very good results.

- the KS scheme, which in principle gives only the correct density, can be used as starting point to describe even spectroscopy features, like optical absorption (via time-dependent extension to DFT) or photoemission spectra (when coupled with Green's functions approaches).

It is therefore not astonishing to see the funding papers of Walter Kohn among the most cited in the overall physics literature and, in general, DFT as *the method* to tackle electronic structure problem [80].

Approximations

The simplest approximation, proposed by Kohn and Sham [67], is the Local Density Approximation (LDA). If we write the exchange correlation energy in terms of the exchange-correlation energy density (or exchange-correlation energy per particle)

$$E_{\rm xc} = \int n(\mathbf{r})\epsilon_{\rm xc}([n],\mathbf{r})d\mathbf{r}$$

we can define the LDA as

$$E_{\rm xc}^{\rm LDA} = \int n(\mathbf{r})\epsilon_{\rm xc}^{\rm LDA}(n(\mathbf{r}))d\mathbf{r}, \tag{4.7}$$

where $\epsilon_{\rm xc}^{\rm LDA}(n(\mathbf{r}))$, evaluated at $\mathbf{r}$, is the exchange and correlation energy density of the homogeneous electron gas with density $n(\mathbf{r})$. This procedure is possible because the exchange correlation energy density for the homogeneous electron gas, though unknown as well, can be numerically evaluated (for many densities) using Quantum Monte Carlo techniques [81]. Though extremely simple, this approximation turns out to be very good, in particular for describing the molecules' bond lengths [82], or lattice constants [83], both situations in which LDA results are within $2 \div 3\%$ with respect to experiments.

[4] While this is true in KS theory, we have to consider that: i) some approximations for $v_{\rm xc}$ might be non local (see hybrid functional below); ii) the use of non-local pseudopotentials makes the external potential non-local.

Better approximations are required, however, to describe other quantities, like bulk modulus or cohesive energies of solids. The next generation of approximations for the exchange-correlation density functional is represented by the generalized gradient approximation (GGA) [84], in which the exchange correlation energy depends locally on the density and its gradient, as in $E_{\text{xc}} = \int f(n(\mathbf{r}), \nabla n(\mathbf{r}))d\mathbf{r}$. GGA's do not automatically improve all situations in which LDA results are poor (for example, GGA lattice constants are in general not better than LDA results, often worse), but they improve LDA results in many situations, like in the description of bulk moduli [85] or cohesive energies [86].

Though not used in this thesis, we would like to mention another class of approximations, the hybrid functionals [87], originally introduced by Axel Becke in 1993. The main idea is to create a non-local exchange correlation potential by mixing ingredients from pure functionals of the density with orbital dependent non-local ingredients, like the Fock exchange term. Again, the use of a more complicated functional (much more complicated in this case) does not guarantee an automatic improvement of the description of all quantities (lattice constants of solids are often worse using hybrids than LDA or GGA), but some observables greatly benefit from the non-local treatment of the exchange and correlation term: typical examples are bond dissociation energies [88] or dipole moments [89] of molecules.

Also the band gap is an observable of the system. It is defined as a difference of ground state total energies, and as such it is in principle given exactly by DFT. However, the functional is unknown. A first approximation is to use Kohn-Sham DFT, and to interpret the band gap of the KS system as the true band gap of the system. This is a strong approximation, as the Kohn-Sham system is designed to give exactly the density, but not others observables. Therefore, even with the exact exchange correlation potential, the band gap of the KS system will be different from the band gap of the real system. The difference is called the derivative discontinuity [90, 91]. Again, the density functional for this quantity is unknown, although some promising attempts for approximations exist; see, e.g. [92–94]. Therefore, others techniques have to be used to access the band gap. However, the Kohn-Sham energies and wavefunctions can be used as starting point for other approaches, and in particular, for calculations using the GW approximation, which will be introduced in Ch. 7.

Chapter 5

Time-dependent density functional theory

The aim of this chapter is to show how to use the density functional formalism to describe spectroscopy quantities, like optical absorption, reflectivity, refraction indeces, etc. To this end, we will introduce time-dependent density functional theory (TDDFT) and the linear response theory.

5.1 Time-dependent Kohn-Sham equations

In the previous chapter we have discussed DFT. The one-to-one correspondence between external potential and electron density permits us to describe, in principle, every observable exclusively in terms of the density. The Hohenberg-Kohn theorem however concerns only static external potentials. While this is convenient for ground-state calculations for a system of electrons in the static ionic potential, it is not appropriate for the description of the interaction of the same system with external potentials that are time dependent. However, the DFT formalism has been extended to time-dependent external potentials in the article by Runge and Gross [95] in 1984 that formalises earlier works [96, 97] in which DFT had been already used in the time-dependent case. The literature covering the TDDFT foundations, including the demonstrations of theorems, problems, caveats, tricks, is very ample. We cite here a series of books [98–100] that cover however only a small part of the vast TDDFT world. Similarly to the Hohenberg-Kohn theorem, the Runge-Gross theorem establishes a one-to-one correspondence between a time-dependent external potential and the time-dependent density, for a given initial state and up to a purely time-dependent function. Similarly to the static case, a set of time-dependent Kohn-Sham equations can be derived[1]. In such a way the time-dependent density can be calculated from $n(\mathbf{r},t) = \sum_i |\psi_i(\mathbf{r},t)|^2$, where the one-particle wavefunctions ψ_i are the solutions of:

$$\left[-\frac{1}{2}\nabla^2 + V^{\text{ext}}(\mathbf{r},t) + v_H([n],\mathbf{r},t) + v_{\text{xc}}([n],\mathbf{r},t)\right]\psi_i(\mathbf{r},t) = i\frac{\partial\psi_i(\mathbf{r},t)}{\partial t}. \tag{5.1}$$

Here $V^{\text{ext}}(\mathbf{r},t)$ is the time-dependent external potential (e.g. a time-dependent perturbation plus the static ionic potential), $v_H([n],\mathbf{r},t)$ is the time-dependent Hartree potential, and $v_{\text{xc}}([n],\mathbf{r},t)$ is the unknown time-dependent exchange-correlation potential. From the solution of the time-dependent KS equations one can evaluate time-dependent observables, like the dipole operator or an optical spectrum. In this thesis we focus on specific spectroscopic quantities that are related to linear response functions (optical absorption, extinction coefficient, etc). It is then very useful to analyse the TDDFT formalism from the point of view of the linear response theory that will be introduced in the next section.

[1] In this case the equations are not found by minimizing an energy functional, but by searching extrema of a time dependent action functional [96].

5.2 Linear response theory

In order to study optical properties, the density-density response function χ, also called polarizability, is particularly useful. At zero temperature, it is defined as:

$$\chi(\mathbf{r},\mathbf{r}',t-t') = -i\theta(t-t')\,\langle N|\,[\hat{n}(\mathbf{r},t),\hat{n}(\mathbf{r}',t')]\,|N\rangle\,. \tag{5.2}$$

Here the expectation value of the commutator of the density operator at different times is taken with respect to the ground-state many-body wavefunction $|N\rangle$. Adopting the Lehmann representation in the frequency domain we can write χ as:

$$\chi(\mathbf{r},\mathbf{r}',\omega) = \sum_{\lambda}\left[\frac{\rho^*_\lambda(\mathbf{r})\rho_\lambda(\mathbf{r}')}{\omega - E_\lambda + i\eta} - \frac{\rho^*_\lambda(\mathbf{r}')\rho_\lambda(\mathbf{r})}{\omega + E_\lambda + i\eta}\right], \tag{5.3}$$

where $\rho_\lambda(\mathbf{r}) = \langle\lambda|\,\hat{n}(\mathbf{r})\,|N\rangle$ is the expectation value of the density operator taken between the many-body ground state and an excited state $|\lambda\rangle$. The full polarizability has poles at the excitation energies of the many-body system $\pm E_\lambda$ corresponding to transitions between $|N\rangle$ and $|\lambda\rangle$. The positive infinitesimal $\eta \to 0^+$ ensures causality.

The polarizability χ is the linear response function that relates an external potential to the induced density, following the formula

$$\delta n(\mathbf{r},t) = \int dt' \int d\mathbf{r}'\chi(\mathbf{r},\mathbf{r}',t-t')\delta V^{\text{ext}}(\mathbf{r}',t'). \tag{5.4}$$

χ is a crucial quantity: its macroscopic component is related to the loss function and to other spectroscopic quantities. Due to the integral in the previous equation, one instead needs the entire function χ to obtain the first-order change of the electron density δn when the electron system is subjected to a time-dependent external perturbation. The full structure of χ will be extensively used in Ch. 11.

We also introduce the inverse dielectric function ϵ^{-1}, defined as

$$\delta V^{tot}(\mathbf{r},t) = \int dt' \int d\mathbf{r}'\epsilon^{-1}(\mathbf{r},\mathbf{r}',t-t')\delta V^{\text{ext}}(\mathbf{r}',t'), \tag{5.5}$$

where the total potential (sum of the external plus induced potential $\delta V^{\text{tot}} = \delta V^{\text{ind}} + \delta V^{\text{ext}}$) has a linear dependence with the external potential. Combining Eq. (5.5) and Eq. (5.4), we obtain schematically

$$\begin{aligned}\epsilon^{-1} &= \frac{\delta V^{\text{tot}}}{\delta V^{\text{ext}}} = \frac{\delta V^{\text{ext}} + \delta V^{\text{ind}}}{\delta V^{\text{ext}}} = 1 + \frac{\delta V^{\text{ind}}}{\delta V^{\text{ext}}} \\ &= 1 + v_{\text{c}}\frac{\delta n}{\delta V^{\text{ext}}} = 1 + v_c\chi,\end{aligned}$$

where we have used the Poisson equation for the induced potential $\delta V^{\text{ind}}(\mathbf{r},t) = \int \frac{\delta n(\mathbf{r}',t)}{|\mathbf{r}-\mathbf{r}'|}d\mathbf{r}'$. We can write this relation in real space and frequency domain:

$$\epsilon^{-1}(\mathbf{r},\mathbf{r}',\omega) = \delta(\mathbf{r}-\mathbf{r}') + \int d\mathbf{r}''\, v_{\text{c}}(\mathbf{r},\mathbf{r}'')\chi(\mathbf{r}'',\mathbf{r}',\omega) \tag{5.6}$$

or, for periodic systems, in reciprocal space:

$$\epsilon^{-1}_{\mathbf{G}\mathbf{G}'}(\mathbf{q},\omega) = \delta_{\mathbf{G}\mathbf{G}'} + \sum_{\mathbf{G}''}\frac{4\pi}{|\mathbf{q}+\mathbf{G}''|^2}\chi_{\mathbf{G}'',\mathbf{G}'}(\mathbf{q},\omega). \tag{5.7}$$

This equation implies that from the polarizability χ we can directly obtain the inverse dielectric function. The Appendix C summarizes the relations between the dielectric function and the measurable quantitities connected to specific experiments such as optical absorption, reflectivity, extinction coefficient, loss function, etc.

We then need a practical tool to evaluate the full polarizability avoiding the use of the full many-body ground state wavefunction that enter the definition of Eq. (5.2).

5.3 The Dyson equation for the polarizability

The density-functional formalism provides a convenient way to evaluate the full polarizability χ. In the definition (5.2) of the full polarizability for an interacting electron system one needs to know the complicate many-body wavefunctions. However, the same expression for an independent-particle system is much simpler. In this case, the many-body wavefunction $|N\rangle$ becomes a single Slater determinant and Eq. (5.3) simplifies into:

$$\chi^0(\mathbf{r},\mathbf{r}',\omega) = \sum_{ij}(f_i - f_j)\frac{\rho_{ij}^*(\mathbf{r})\rho_{ij}(\mathbf{r}')}{\omega - (\varepsilon_j - \varepsilon_i) + i\eta} \tag{5.8}$$

where $\rho_{ij}(\mathbf{r}) = \psi_i^*(\mathbf{r})\psi_j(\mathbf{r})$ and $\varepsilon_i, \psi_i, f_i$ are the eigenvalues, eigenfunctions and occupation numbers of the independent particle system, in which the electrons are subjected to an effective potential, such as the mean-field potential of the Hartree or Hartree-Fock equation.

The Kohn-Sham scheme also yields a system of independent particles. The specific property of this auxiliary system is that it has the same density as the real interacting system. The induced density $\delta n(\mathbf{r},t)$ can be then calculated in two equivalent manners:

$$\begin{aligned}
\delta n(\mathbf{r},t) &= \int dt' \int d\mathbf{r}'\, \chi(\mathbf{r},\mathbf{r}',t,t')\delta V^{\text{ext}}(\mathbf{r}',t') \quad \text{interacting system} \\
\delta n(\mathbf{r},t) &= \int dt' \int d\mathbf{r}'\, \chi^{\text{KS}}(\mathbf{r},\mathbf{r}',t,t')\delta V^{\text{tot}}(\mathbf{r}',t') \quad \text{non-interacting system.}
\end{aligned}$$

Since the left hand sides are the same, we have

$$\int dt' \int d\mathbf{r}'\chi(\mathbf{r},\mathbf{r}',t,t')\delta V^{\text{ext}}(\mathbf{r}',t') = \int dt' \int d\mathbf{r}'\chi^{\text{KS}}(\mathbf{r},\mathbf{r}',t,t')\delta V^{\text{tot}}(\mathbf{r}',t')$$

which relates the full polarizability χ to the Kohn-Sham independent-particle polarizability χ^{KS}. In the Kohn-Sham picture, the total potential is the KS potential of Eq. (4.4). We can rewrite, schematically, the previous equation as

$$\begin{aligned}
\chi &= \chi^{\text{KS}}\frac{\delta V^{\text{ext}} + \delta v_H + \delta v_{\text{xc}}}{\delta V^{\text{ext}}} = \chi^{\text{KS}}\left(1 + \frac{\delta v_H}{\delta V^{\text{ext}}} + \frac{\delta v_{\text{xc}}}{\delta V^{\text{ext}}}\right) \\
&= \chi^{\text{KS}} + \chi^{\text{KS}}\left(\frac{\delta v_H}{\delta n}\frac{\delta n}{\delta V^{\text{ext}}} + \frac{\delta v_{\text{xc}}}{\delta n}\frac{\delta n}{\delta V^{\text{ext}}}\right) \\
&= \chi^{\text{KS}} + \chi^{\text{KS}}\left(v_{\text{c}} + f_{\text{xc}}\right)\chi.
\end{aligned}$$

The last line has the form of a Dyson equation that can be solved for the polarizability χ. Here we have introduced the exchange-correlation kernel as the functional derivative of the exchange-correlation potential with respect to the density:

$$f_{\text{xc}}(\mathbf{r},\mathbf{r}',t,t') = \frac{\delta v_{\text{xc}}(\mathbf{r},t)}{\delta n(\mathbf{r}',t')} \quad . \tag{5.9}$$

With all indices the Dyson equation in the frequency domain reads:

$$\chi(\mathbf{r},\mathbf{r}',\omega) = \chi^{\text{KS}}(\mathbf{r},\mathbf{r}',\omega) + \int d\mathbf{r}''d\mathbf{r}'''\,\chi^{\text{KS}}(\mathbf{r},\mathbf{r}'',\omega)\Big[v_{\text{c}}(\mathbf{r}'',\mathbf{r}''') + f_{\text{xc}}(\mathbf{r}'',\mathbf{r}''',\omega)\Big]\chi(\mathbf{r}''',\mathbf{r}',\omega). \tag{5.10}$$

Here the independent-particle polarizability χ^{KS} has the form of Eq. (5.8), built with Kohn-Sham ingredients. In the following, χ^0 will stand for an independent particle polarizability built with Kohn-Sham eigenvalues and wavefunctions.

Many approximations have been proposed for the exchange-correlation kernel. We mention here some of the most common approximations in literature, which are also used in this thesis:

- the random phase approximation (RPA) where the kernel is zero $f_{xc} \approx 0$;

- the adiabatic local density approximation (ALDA), which is space-time local and is obtained as the derivative of the LDA $v_{\rm xc}$: $f_{\rm xc}^{\rm ALDA}(\mathbf{r},\mathbf{r}',t,t') = \delta(\mathbf{r}-\mathbf{r}')\delta(t-t') \left.\frac{dv_{\rm xc}^{\rm LDA}}{dn}\right|_{n=n(\mathbf{r})}$.

Both RPA and ALDA give good results for the loss function of many materials. However, for the optical properties of solids both RPA and ALDA turn out to be poor approximations. The problem with the ALDA kernel is related to the lack of the $1/q^2$ behavior that should be present in the optical limit $q \to 0$ of the kernel for gapped materials [101]. Indeed, this long-range component of the kernel has been shown to be crucial in order to simulate excitonic effects [102]. The correct $1/q^2$ behavior has been proposed in different forms in the literature [102–105]. Two of those long-range corrected kernels will be tested on AgCl:

- the simple static and scalar kernel with a long-range contribution of the form $f_{\rm xc} = \alpha/q^2$, where α is a real negative number, following the recipe described in Refs. [102, 103].
- the recent bootstrap kernel [106, 107], which relates the parameter α to response functions that can be calculated from first principles.

From the solution of the Dyson equation (5.10) for the polarizability χ, and thanks to Eq. (5.6) or Eq. (5.7), one obtains the microscopic dielectric function, which can be used to evaluate many macroscopic observables via appropriate average operations described in Appendix C.

Chapter 6

Many body perturbation theory

The problems of density functional theory and its time dependent counterpart give a strong motivation for the search of other methods to access spectroscopic properties of materials. One prominent approach is many body perturbation theory (MBPT). It relies on approximations for the one-body Green's function G, and for observables expressed as functionals of G. This method has the advantage that explicit expressions for many observables as functional of the Green's function are known. However, as it will be exposed, this comes at the expense of larger calculations, as the Green's function is a function of two space, spin and time arguments, whereas the density is a local function of space and time.

As explained in Ch. (4), Kohn-Sham eigenvalues cannot be interpreted as a band structure. However, they often give a good overview and constitute a convenient starting point for further calculations. In the present chapter, we will present an approach in the framework of MBPT that allows us to obtain a more meaningful band structure, by adding quasi-particle corrections obtained in the Green's function formalism. A more complete description of Green's functions and of the fundamental ingredients of MBPT can be found, e.g., in [68, 108–110].

The one-body Green's function

The time-ordered one particle Green's function of a system in equilibrium at zero temperature and fixed particle number is defined as

$$iG(1,2) = \langle N| \mathcal{T}\hat{\Psi}(1)\hat{\Psi}^\dagger(2) |N\rangle \tag{6.1}$$

where $\hat{\Psi}$ are field operators, the time ordering operator $\mathcal{T}$ is defined as:

$$\mathcal{T}\hat{\Psi}(1)\hat{\Psi}^\dagger(2) = \begin{cases} \hat{\Psi}(1)\hat{\Psi}^\dagger(2) \text{ if } t_2 < t_1 \\ -\hat{\Psi}^\dagger(2)\hat{\Psi}(1) \text{ if } t_1 < t_2 \end{cases} \tag{6.2}$$

and $|N\rangle$ is the N-particle ground state of the system. Here, we use the compact notation $1 \equiv (\mathbf{r}_1, \sigma_1, t_1)$ for a space, spin, time argument. The Green's function can be viewed as the probability amplitude for propagation of an additional hole or electron in the system. Insertion of a complete set of $N+1$ and $N-1$-particle states between the field operators and fourier transform from time to frequency yields G in the Lehmann representation as a sum over many-body states s:

$$G(\mathbf{r}, \mathbf{r}', \omega) = \lim_{\eta \to 0} \sum_s \frac{F_s(\mathbf{r}) F_s^*(\mathbf{r}')}{\omega - \Delta E_s + i\eta sgn\,(E_s - \mu)}. \tag{6.3}$$

Here, E_s are electron addition or removal energies,

$$\begin{aligned} \Delta E_s &\equiv E_{N+1,s} - E_N \qquad \text{for electron addition} \\ \Delta E_s &\equiv E_N - E_{N-1,s} \qquad \text{for electron removal,} \end{aligned} \tag{6.4}$$

where E_N is the N-particle ground state total energy and $E_{N\pm1,s}$ are $N \pm 1$-particle total energies of the system in some ground - or excited many-body state s. The Dyson amplitudes F_s are defined as

$$\begin{aligned} F_s &\equiv \langle N|\hat{\Psi}(\mathbf{r})|N+1,s\rangle \qquad \text{for electron adition} \\ F_s &\equiv \langle N|\hat{\Psi}(\mathbf{r})|N-1,s\rangle \qquad \text{for electron removal,} \end{aligned} \tag{6.5}$$

and the sign of the small imaginary part depends on the energies relative to the chemical potential μ. Spin is not shown explicitly here and in the following.

As we can see, the poles of the one-body Green's function are the electron addition and removal energies. These are the energies measured in inverse and direct photoemission, respectively. An experimental photoemission spectrum can therefore be approximately described by the spectral function, which is proportional to the imaginary part of G.

For non-interacting electrons, the Green's function reduces to

$$G^0(\mathbf{r},\mathbf{r}',\omega) = \sum_i \frac{\psi_i(\mathbf{r})\psi_i^*(\mathbf{r}')}{\omega - \varepsilon_i + i\eta \mathrm{sgn}(\varepsilon_i - \mu)}, \tag{6.6}$$

where ψ_i and ε_i are the single -paricle orbitals and energies, respectively. In the single-particle basis where G^0 is diagonal, the matrix elements of the spectral function are δ-peaks, at the energies of the single particles. In interacting systems this is no longer true, but unless the interaction is too strong, one can still find dominant peaks in the spectral function that are remnants of the δ-peaks of the non-interacting particles. These dominant peaks are therefore called quasi-particle peaks. In periodic solids, the quasi-particle peaks give the band structure. Therefore, contrary to the KS energies the one-body Green's function gives direct access to the band structure, and we will see in the following how it can be approximated.

Hedin's equations

The time evolution of G is given by its equation of motion:

$$\int d3\, [(i\partial_{t_1} - h_0(1))\, \delta(1,3) - \Sigma_{\mathrm{xc}}(1,3)]\, G(3,2) = \delta(1,2). \tag{6.7}$$

Here, h_0 is the Hartree hamiltonian. The self-energy Σ_{xc} plays the role of an exchange-correlation potential that is non-local in space, spin and time. It represents an effective interaction between the propagating particle and the medium. The self-energy can be written as

$$\Sigma_{\mathrm{xc}}(1,2) = \lim_{V\to 0} i \int d3d4\, v_c(1,3) \frac{\delta G(1,4)}{\delta V(3)} G^{-1}(4,2), \tag{6.8}$$

where V is a fictitious external potential applied to the system and set to zero at the end of the calculation.

Based on this approach of functional derivatives, in 1965 Hedin [68] proposed a set of equations allowing the calculation of the Green's function:

$$G(1,2) = G^0(1,2) + \int d3d4\, G^0(1,3)\Sigma_{\mathrm{xc}}(3,4)G(4,2), \tag{6.9}$$

$$\Sigma(1,2) = i \int d3d4\, G(1,4)W(3,1^+)\Gamma(4,2,3), \tag{6.10}$$

$$\Gamma(1,2,3) = \delta(1,2)\delta(1,3) + \int d4d5d6d7\, \frac{\delta\Sigma_{\mathrm{xc}}(1,2)}{\delta G(4,5)} G(4,6)G(7,5)\Gamma(6,7,3), \tag{6.11}$$

$$W(1,2) = v_c(1,2) + \int d3d4\, v_c(1,3)P(3,4)W(4,2), \tag{6.12}$$

$$P(1,2) = -i \int d3d4\, G(2,3)G(4,2)\Gamma(3,4,1), \tag{6.13}$$

where G^0 is here the Hartree Green's function, which can be computed from Eq. (6.7) by setting $\Sigma_{\text{xc}} = 0$, and which has the form of (6.6). These equations link various quantities. Besides the self-energy, they contain the screened Coulomb interaction W, the irreducible polarizability P, and the vertex function Γ. The screened Coulomb interaction can also be written as $W = v_c + v_c\chi v_c$, with $\chi = P + Pv_c\chi$, which makes a direct link to Ch. (5) and shows how the dielectric function can be obtained from Hedin's equations. Note, however, that one has to take care of the fact that here we work with time-ordered quantities.

In principle Hedin's equations should be solved self-consistently, but this is clearly out of reach. Indeed, the main purpose of the equations is to design approximations for the one-body Green's function. Hedin proposed one of the most prominent approximations, the so called GW approximation [68], presented in the next section.

6.1 The GW approximation

The GW approximation reduces Γ to the first term $\delta(1,2)\delta(1,3)$, which means that variations of Σ_{xc} are neglected. With this, the equation for the self energy writes

$$\Sigma_{\text{xc}}(1,2) = iG(1,2)W(2,1^+), \tag{6.14}$$

and the irreducible polarizability is

$$P(1,2) = -iG(2,1)G(1,2). \tag{6.15}$$

This greatly simplifies the equations as the polarizability P is given as the product of two independently propagating particles. Since the self-energy is built with the screened Coulomb interaction, the GW approximation contains the physics of the polarization of the system when a charge is added or removed from the system.

In principle, even the one-body G are still governed by the fully interacting system, and it has a complicated spectral function. An additional approximation is therefore usually made to simplify the calculations, namely, the quasi-particle approximation. In this approximation G has the structure of the independent-particle Green's function G^0 (Eq. (6.16)). However, now the wavefunctions ψ_i are quasi-particle wavefunctions ϕ and the ε_i quasi-particle energies E_i, which should in principle be obtained self-consistently as approximation to the GW result.

In a periodic solid, this approximation reads then

$$G(\mathbf{r},\mathbf{r}',\omega) \approx G^0(\mathbf{r},\mathbf{r}',\omega) = \sum_{n\mathbf{k}} \frac{\phi_{n\mathbf{k}}(\mathbf{r})\phi^*_{n\mathbf{k}}(\mathbf{r}')}{\omega - E_{n\mathbf{k}} \pm i\eta}. \tag{6.16}$$

In this approximation, it is possible to rewrite Eq (6.7) to get an equation similar to the Schrödinger equation for the quasi-particle wavefunctions $\phi_{n\mathbf{k}}(\mathbf{r})$ and energies $E_{n\mathbf{k}}$ [68, 111],

$$\left[-\frac{1}{2}\nabla^2 + V^{\text{ext}}(\mathbf{r}) + v_H([n],\mathbf{r})\right]\phi_{n\mathbf{k}}(\mathbf{r}) + \int d\mathbf{r}'\Sigma_{\text{xc}}(\mathbf{r},\mathbf{r}',E_{n\mathbf{k}})\phi_{n\mathbf{k}}(\mathbf{r}') = E_{n\mathbf{k}}\phi_{n\mathbf{k}}(\mathbf{r}), \tag{6.17}$$

where the self-energy Σ_{xc} plays the role of an effective non-local and energy-dependent potential. As pointed out above, the generalized eigenvalues of Eq. (6.17) can be interpreted as addition and removal energies, and are used to build the theoretical band structure.

The resolution of this equation requires the knowledge of Σ_{xc}, and the evaluation of Σ_{xc} requires, in principle, the solution of Eq. (6.17), which makes the problem self-consistent. Many calculations replace the quasi-particle wavefunctions and eigenvalues by Kohn-Sham ones. Moreover, they evaluate the screened Coulomb interaction W using the RPA for ϵ^{-1} following Eqs. (5.8) and (5.10). From these they compute the self energy and solve Eq. (6.17) to get the quasi-particle energies and wavefunctions. These two approximations define the G^0W^0 approach [112–115]. This approach is not self consistent as the self energy is not updated with the new energies and wavefunctions.

A further simplification is obtained by evaluating the quasi-particle eigenvalues perturbatively with respect to the KS ones, and by making use of the fact that the self-energy is approximately linear around the quasi-particle energy. Using Eq. (6.17) and Eq. (4.3), this yields

$$E_{n\mathbf{k}} = \varepsilon_{n\mathbf{k}} + Z_{n\mathbf{k}}\big[\,\langle\Sigma_{\rm xc}(\varepsilon_{n\mathbf{k}})\rangle - \langle v_{\rm xc}\rangle\,\big], \tag{6.18}$$

with the quasi-particle renormalization factor $Z_{n\mathbf{k}} = \left[1 - \left\langle \frac{\partial\Sigma_{\rm xc}(\omega)}{\partial\omega}\Big|_{\varepsilon_{n\mathbf{k}}} \right\rangle\right]^{-1}$. Here, expectation values are taken with the KS wavefunctions $\psi_{n\mathbf{k}}$.

The G^0W^0 approach based on KS calculations with approximate functionals such as the LDA or GGA has met broad success for many materials[111, 114–116], but it encounters problems when it comes to materials with localized electrons [111, 116–120]. These are often transition metal oxides and other correlated materials where d or f electrons are important, but as we will see, the problem also concerns AgCl, because of the hybridisation between Ag $4d$ and Cl $3p$ electrons. These materials require better starting eigenvalues and wavefunctions, or self-consistency. A prominent self-consistent approach is quasi-particle self-consistent GW [117, 118] (QSGW).

In this approach, Eq. (6.17) is approximated by an effective Schrödinger equation with a static Hamiltonian, and the resulting eigenvalues and eigenfunctions are used to build a new quasi-particle Green's function and screened Coulomb interaction. The procedure can be iterated to self-consistency and often improves over G^0W^0 results [111, 116–120].

Intermediate calculations can also be realized, where one keeps the screening computed from the Kohn-Sham calculation but recomputes the Green function and self energy at each iteration: this is the GW^0 approximation.

One delicate point in the evaluation of the GW self-energy is frequency integration. Since $\Sigma_{\rm xc}$ is a product of G and W in real space and time, it becomes a convolution in frequency space,

$$\Sigma_{\rm xc}(\mathbf{r},\mathbf{r}',\omega) = \frac{i}{2\pi}\int d\omega'\, e^{i\eta\omega'} G(\mathbf{r},\mathbf{r}',\omega+\omega')W(\mathbf{r},\mathbf{r}',\omega'). \tag{6.19}$$

We have performed the frequency integration using the Godby-Needs plasmon-pole model (PPM) [121] for the frequency dependence of the inverse dielectric function. In reciprocal space, the model reads

$$\epsilon^{-1}_{\mathbf{G}\mathbf{G}'}(\mathbf{q},\omega) = \delta_{\mathbf{G}\mathbf{G}'} + \frac{\Omega^2_{\mathbf{G}\mathbf{G}'}(\mathbf{q})}{\omega^2 - (\omega^p_{\mathbf{G}\mathbf{G}'}(\mathbf{q}) - i\eta)^2}, \tag{6.20}$$

where Ω and ω^p are parameters that are fitted to two RPA calculations of ϵ^{-1}, one for $\omega = 0$ and one for a frequency on the imaginary axis, of the order of the plasmon frequency. This fit is done for every $(\mathbf{q},\mathbf{G},\mathbf{G}')$ element of ϵ^{-1}. In this way, the frequency integration in Eq. (6.19) is done analytically.

A alternative to the PPM is the numerical calculation of the integration. These calculations are more expensive, and we have performed them to verify that the plasmon pole model results are correct for AgCl. The technique to realize the integral that we have used is the contour deformation technique [122], where one chooses a contour in the complex plane that yields the result of the frequency integral (6.19) in form of a sum over residues plus an integration on the imaginary frequency axis.

6.2 Bethe-Salpeter equation

The many body perturbation theory allows one to compute the polarizability of a material. This represents an alternative to the TDDFT, when the available approximations to the $f_{\rm xc}$ kernel turn out to be too crude to describe some relevant features of the material. This is the case for bound excitons, for which none of the exchange and correlation kernels is sufficient. Bound excitons are bound pairs of an electron and a hole, that are observed when the system is excited by an external perturbation, such as as light.

When we consider light absorption, we are interested in neutral excitations: excitations that do not change the total charge of the system. In an independent-particle picture, the system gets

excited by moving an electron from the valence band to the conduction band. In the presence of interaction, it can be seen as generating a hole and an electron interacting with the rest of the system and with each other. Their propagation is given by the two particles Green's function $G^{(2)}$. Therefore it is crucial for the absorption to study the two particles Green's function. More precisely, we will look at the two-particles correlation function defined by

$$L(1,2,3,4) = -G^{(2)}(1,2,3,4) + G(1,2)G(3,4), \tag{6.21}$$

which is minus the two-particles Green's function plus an uncorrelated part.

From this quantity the density-density response function χ can be obtained as

$$\chi(\mathbf{r}_1, \mathbf{r}_2; t_1 - t_2) = -iL(\mathbf{r}_1, t_1, \mathbf{r}_1, t_1, \mathbf{r}_2, t_2, \mathbf{r}_2, t_2). \tag{6.22}$$

As described in Appendix C, the absorption coefficients of a material can be obtained from χ. Therefore, knowledge of the correlation function L will enable us to compute the absorption spectrum of a material.

Similar to the one-body Green's function G, the two-body correlation function L obeys a Dyson equation, called the Bethe-Salpeter Equation (BSE) [123, 124]. This equation can be derived starting from the fact that, right as $\chi = \delta n/\delta V$ with n the density and V a local perturbation, $L = \delta G/\delta V^{\mathrm{nl}}$ with V^{nl} a generalized non-local perturbation. Schematically, the BSE is derived by using

$$\begin{aligned} L &= \delta G/\delta V^{\mathrm{nl}} = -G(\delta G^{-1}/\delta V^{\mathrm{nl}})G = GG + G(\delta(V_H + \Sigma)/\delta V^{\mathrm{nl}})G \\ &= GG + G(-iv_c + \delta\Sigma/\delta G)(\delta G/\delta V^{\mathrm{nl}})G, \end{aligned} \tag{6.23}$$

where V_H is the Hartree potential and the last expression has been obtained using the chain rule for functional derivatives. The term $\delta G/\delta V^{\mathrm{nl}}$ on the right side is again L. The functional derivative of Σ has to be approximated. In the GWA and neglecting variations of the screening upon perturbation of the system, this yields

$$\begin{aligned} L(1,2,3,4) = L^0(1,2,3,4) + L^0(1,2,\bar{5},\bar{6})\,[&-iv(\bar{5},\bar{7})\delta(\bar{5},\bar{6})\delta(\bar{7},\bar{8}) \\ &+iW(\bar{5},\bar{6})\delta(\bar{5},\bar{7})\delta(\bar{6},\bar{8})]\,L(\bar{7},\bar{8},3,4). \end{aligned} \tag{6.24}$$

Here, barred indices are integrated over. $L^0(1,2,3,4) = G(1,3)G(4,2)$ is the two-particle correlation function in absence of interaction between the two particles, and W is the screened Coulomb interaction, which is usually calculated in the RPA. As before, we will not consider spin in the following.

As a further approximation, usually the quasiparticle approximation (6.16) is made for G in L_0 and the frequency dependence of W is neglected in the kernel of the BSE. In this case, one can immediately set $t_1 = t_2$ and $t_4 = t_3$ in Eq. (6.24). In equilibrium, L depends then only on one time difference, or one frequency after fourier transformation. Instead of solving the BSE for every frequency, the resulting equation can be reformulated as an eigenvalue problem with an effective electron-hole hamiltonian H_{exc}, where v_c and W show up as effective electron-hole interactions [125–128]. This hamiltonian is usually expressed in a basis of pairs of orbitals. In systems with a gap at zero temperature, only pairs of an occupied and an unoccupied orbital contribute to the absorption spectrum, so the pair corresponds to a transition $|t\rangle$. In this basis the hamiltonian reads

$$\langle t|\, H_{\mathrm{exc}}\, |t'\rangle = E_t\delta_{t,t'} + \langle t|\, v_c - W\, |t'\rangle\,, \tag{6.25}$$

where the energy E_t is the difference between an unoccupied and an occupied quasiparticle state, calculated in the GWA, and

$$\begin{aligned} \langle t|\, v_c\, |t'\rangle = \langle n_1\mathbf{k}_1 n_2\mathbf{k}_2|\, v_c\, |n_1'\mathbf{k}_1' n_2'\mathbf{k}_2'\rangle = 2\int d\mathbf{r}d\mathbf{r}'\phi^*_{n_2\mathbf{k}_2}(\mathbf{r})\phi_{n_1\mathbf{k}_1}(\mathbf{r})v_c(\mathbf{r},\mathbf{r}') \\ \phi_{n_2'\mathbf{k}_2'}(\mathbf{r}')\phi^*_{n_1'\mathbf{k}_1'}(\mathbf{r}'), \end{aligned} \tag{6.26}$$

$$\langle t|\, W\, |t'\rangle = \langle n_1\mathbf{k}_1 n_2\mathbf{k}_2|\, W\, |n_1'\mathbf{k}_1' n_2'\mathbf{k}_2'\rangle = \int d\mathbf{r}d\mathbf{r}'\phi^*_{n_2\mathbf{k}_2}(\mathbf{r})\phi_{n_2'\mathbf{k}_2'}(\mathbf{r})W(\mathbf{r},\mathbf{r}') \\ \phi_{n_1\mathbf{k}_1}(\mathbf{r}')\phi^*_{n_1'\mathbf{k}_1'}(\mathbf{r}') \quad (6.27)$$

are, respectively, matrix elements of the repulsive electron-hole (e-h) exchange interaction and of the direct e-h interaction, which is usually attractive. Here, we have defined the transitions t : $(n_1\mathbf{k}_1) \to (n_2\mathbf{k}_2)$. Most of the time the calculations are realized with the Kohn-Sham wavefunctions and eigenvalues. For a given $\mathbf{q}$, only wavevectors $\mathbf{k}_1$ and $\mathbf{k}_2$ that differ by $\mathbf{q}$ contribute to $\chi(\mathbf{q})$. Therefore, the basis is made of resonant transitions $(v, \mathbf{k}-\mathbf{q}) \to (c, \mathbf{k})$ and antiresonant transitions $(c, \mathbf{k}) \to (v, \mathbf{k}+\mathbf{q})$, and H_{exc} takes a block matrix form:

$$H_{\text{exc}} = \begin{pmatrix} R & K^{R,A} \\ K^{A,R} & A \end{pmatrix}, \quad (6.28)$$

with the resonant matrix R, the anti-resonant A, and the coupling elements K. In the optical limit $\mathbf{q} \to 0$, $A = -R^*$ and $K^{A,R} = -[K^{R,A}]^*$. The diagonal blocks A and R are hermitian and the coupling blocks K symmetric. Therefore, neglecting the coupling terms is a significant simplification; this is the Tamm-Dancoff approximation [129, 130] (TDA). It is usually a good approximation for absorption spectra of solids.

In the transition basis the correlation function is given by

$$\langle t|\, L(\omega)\, |t'\rangle = \langle t|\left[\frac{1}{\omega - H_{exc} + i\eta}\right]|t'\rangle \left(f_{n_1'\mathbf{k}_1} - f_{n_2'\mathbf{k}_2}\right) \quad (6.29)$$

where t' correspond to the transition $(n_1'\mathbf{k}_1) \to (n_2'\mathbf{k}_2)$, and f are occupation numbers.

The solution of the eigenvalue problem $H_{\text{exc}}A_\lambda = E_\lambda A_\lambda$ yields the elements of L needed to derive χ, and from this ϵ_M^{-1}. In the TDA the result reads:

$$\epsilon_M^{-1}(\omega) = 1 + \lim_{\mathbf{q}\to 0} \frac{8\pi}{N_k\Omega_0 q^2} \sum_\lambda \frac{\left|\sum_t A_\lambda^t \tilde{\rho}_t(\mathbf{q})\right|^2}{\omega - E_\lambda + i\eta}, \quad (6.30)$$

where $\tilde{\rho}_t(\mathbf{q})$ are the oscillator strengths defined in Eq.(5.8).

The macroscopic dielectric function can also be calculated directly in the TDA as

$$\epsilon_M(\omega) = 1 - \lim_{\mathbf{q}\to 0} \frac{8\pi}{N_k\Omega_0 q^2} \sum_\lambda \frac{\left|\sum_t \bar{A}_\lambda^t \tilde{\rho}_t(\mathbf{q})\right|^2}{\omega - \bar{E}_\lambda + i\eta}, \quad (6.31)$$

where $\bar{A}_\lambda$ and $\bar{E}_\lambda$ are solutions of a modified H_{exc}, where the bare Coulomb interaction v_c of the electron-hole exchange does not have its long-range component $v_c(\mathbf{G} = 0)$. Note that the sets of E_λ and $\bar{E}_\lambda$ contain both positive and negative energies. They are typically different from the independent-particle transition energies E_t. If the smallest excitation energy $\bar{E}_\lambda$ is smaller than the direct gap (i.e. the smallest E_t), then the corresponding excited state of the many-body system is called a bound exciton state, and the difference $E_t - \bar{E}_\lambda$ is its binding energy. The spectrum changes also above the independent-particle gap, mostly because the coefficients $\bar{A}_\lambda$ mix the previously independent transitions contained in $\tilde{\rho}$, which can be seen from comparison with Eq. (5.8). These changes are also called exitonic effects.

The comparison between Eq. (6.31) and the independent-particle approximation suggests to analyze spectra in terms of the independent transitions that contribute to a given many-body transition λ. The strength of the eigenvectors of the excitonic hamiltonian, $|\bar{A}_\lambda^t|^2$ as a function of t or E_t indicates how much each transition between an occupied and an empty state is mixed into the excitonic eigenstate λ. The electron-hole correlation in real space can be examined by investigating the e-h wavefunction,

$$\Psi_\lambda(\mathbf{r}_h, \mathbf{r}_e) = \sum_t \bar{A}_\lambda^t \phi^*_{v\mathbf{k}}(\mathbf{r}_h)\phi_{c\mathbf{k}}(\mathbf{r}_e). \quad (6.32)$$

In particular, one can fix the position $\mathbf{r}_h = \mathbf{r}_h^0$ of the hole and visualize the corresponding density distribution of the electron, $n(\mathbf{r}_e) = |\Psi_\lambda(\mathbf{r}_h^0, \mathbf{r}_e)|^2$.

Finally, the partial sum over a transition range, called cumulant, and defined as

$$\mathcal{I}(t_{\max}) \equiv \left| \sum_{t=1}^{t_{\max}} \bar{A}_\lambda^t \tilde{\rho}_t \right|^2 \tag{6.33}$$

takes the phase of the coefficients and matrix elements into account. As a result of positive or negative interference effects, the exciton λ contributes more or less to the absorption spectrum. If the value of Eq. (6.33) for $t_{\max} \to \infty$ is negligibly small, the exciton is said to be dark. Otherwise, if it has a significant contribution to the absorption spectrum the exciton is called bright. Examining the cumulant as a function of $t_{\max}$ gives insight into the origin of dark or bright excitons.

It is also possible to do the calculations without the Tamm-Dancoff approximation. This is particularly important when one is interested in the full response function χ, and not just in absorption spectra. The Hamiltonian is then non Hermitian and the expression for L is different than in the Tamm-Dancoff approximation. Moreover, since our aim is to use χ in order to calculate induced densities, we need all the elements of the matrix in reciprocal space, and not just the head of the matrix to which BSE calculations are usually limited. Once the diagonalization $H_{\text{exc}} A_\lambda = E_\lambda A_\lambda$ has been performed as usual, the full matrix χ takes the following expression [109, 131]:

$$\chi_{\mathbf{G}\mathbf{G}'}(\mathbf{q}, \omega) = \sum_{\lambda\lambda'} \frac{\sum_t \bar{A}_\lambda^t \tilde{\rho}_t(\mathbf{q}+\mathbf{G}) S^{-1}_{\lambda\lambda'} \sum_{t'} \bar{A}_{\lambda'}^{t'} \tilde{\rho}_{t'}(\mathbf{q}+\mathbf{G}')}{\omega - E^\lambda + i\eta}, \tag{6.34}$$

where the overlap matrix S is defined as

$$S_{\lambda\lambda'} = \sum_t A_\lambda^{t*} A_{\lambda'}^t. \tag{6.35}$$

The result for $\mathbf{G} = \mathbf{G}' = 0$ and $\mathbf{q} \to 0$ brings us back to the absorption spectrum, where we look at the macroscopic response to an external macroscopic perturbation. The remaining elements yield information about the microscopic density response to a macroscopic or microscopic perturbation, and about the macroscopic density response to a microscopic perturbation. We will use Eq. (6.34) for the calculations of the induced density including excitonic effects.

Chapter 7

Effective medium theory

The goal of the Effective Medium Theory (EMT) (see e.g. [132–135] for an introduction to the general framework and some applications) is to obtain the macroscopic response function of a composite system (such as a layered material or spheres embedded in a matrix) starting from the knowledge of the response properties of its constituents and their geometric arrangement. The resulting expressions are enforced by the boundary conditions of the fields at the interface between the constituents.

Here we consider the specific case of a layered system made of slabs of two different materials that are repeated infinitely in the stacking direction z, as shown in Fig. 7.1. The two slabs have thicknesses l_1 and l_2, and their macroscopic dielectric functions are ϵ_1 and ϵ_2, respectively. The aim is to obtain the macroscopic dielectric function of the whole system: $\bar{\mathbf{D}} = \epsilon\bar{\mathbf{E}}$, where $\bar{\mathbf{D}}$ is the macroscopic displacement field and $\bar{\mathbf{E}}$ is the macroscopic electric field; both fields are averaged over the entire system. In the following we will omit for simplicity the frequency dependence of the fields: all the relations will be understood to hold for each ω.

We first consider a plane-wave electric field $\mathbf{E}_\perp$ whose polarization direction is perpendicular to the stacking direction, i.e. in the plane parallel to the interface between the two slabs. In the unit cell at the origin (and analogously in all the other unit cells), the displacement field is given

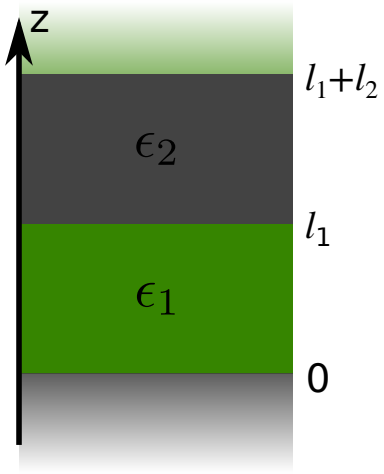

Figure 7.1: Multilayer system with two differents materials.

by:

$$\mathbf{D}_\perp(\boldsymbol{x}) = \epsilon_1\theta(l_1 - z)\mathbf{E}^1_\perp(\boldsymbol{x}) + \epsilon_2\theta(z - l_1)\mathbf{E}^2_\perp(\boldsymbol{x}), \tag{7.1}$$

with z the vertical component of the position $\boldsymbol{x}$, $\mathbf{E}^1$ and $\mathbf{D}^1$ the electric and displacement fields, respectively, in the first material and $\mathbf{E}^2$ and $\mathbf{D}^2$ the electric and displacement fields, respectively, in the second material. The average of a field over a periodic system is the average in the unit cell. The macroscopic displacement field is hence given by

$$\bar{\mathbf{D}}_\perp = \frac{1}{l_1 + l_2}\int_0^{l_1+l_2} \mathbf{D}_\perp(\boldsymbol{x})d\boldsymbol{x}. \tag{7.2}$$

$\mathbf{E}_\perp$ is continuous through the interface $\mathbf{E}^1_\perp(z = l_1^-) = \mathbf{E}^2_\perp(z = l_1^+)$. For simplicity, we assume that the wavelength of the field λ is large compared to the thicknesses l_1, l_2 of the slabs. So we can consider the field to be constant $\mathbf{E}(\boldsymbol{x}) = \bar{\mathbf{E}}_\perp$. The macroscopic displacement field is:

$$\bar{D}_\perp = \frac{1}{l_1 + l_2}(l_1\epsilon_1 + l_2\epsilon_2)\bar{E}_\perp. \tag{7.3}$$

We thus obtain the searched relation between the macroscopic dielectric function of the whole system $\epsilon_\perp$ and those of its constituents, ϵ_1 and ϵ_2:

$$\epsilon_\perp = \frac{l_1\epsilon_1 + l_2\epsilon_2}{l_1 + l_2}. \tag{7.4}$$

If $l_1 = l_2$, the macroscopic dielectric function $\epsilon_\perp = (1/2)(\epsilon_1 + \epsilon_2)$ is the average of the dielectric functions of the two constituents.

We now consider a plane-wave electric field $\mathbf{E}_\parallel$ polarized along the stacking direction z, i.e. perpendicular to the interface. In the first unit cell, we have the following relation between the electric field and the displacement field:

$$\mathbf{E}_\parallel(\boldsymbol{x}) = \theta(l_1 - z)\epsilon_1^{-1}\mathbf{D}^1_\parallel(\boldsymbol{x}) + \theta(z - l_1)\epsilon_2^{-1}\mathbf{D}^2_\parallel(\boldsymbol{x}). \tag{7.5}$$

The macroscopic electric field is:

$$\bar{\mathbf{E}}_\parallel = \frac{1}{l_1 + l_2}\int_0^{l_1+l_2} \mathbf{E}_\parallel(\boldsymbol{x})d\boldsymbol{x}. \tag{7.6}$$

In this case the displacement field is continuous at the interface, $\mathbf{D}^1_\parallel(z = l_1^-) = \mathbf{D}^2_\parallel(z = l_1^+)$. With the same hypothesis as before regarding the wavelength of the fields, we find the following relation

$$\epsilon_\parallel^{-1} = \frac{l_1\epsilon_1^{-1} + l_2\epsilon_2^{-1}}{l_1 + l_2}. \tag{7.7}$$

If $l_1 = l_2$, the inverse macroscopic dielectric function $\epsilon_\parallel^{-1} = (1/2)(\epsilon_1^{-1} + \epsilon_2^{-1})$ is the average of the inverse dielectric functions of the two constituents.

The EMT approach is based on the assumption that the separation between the slabs is abrupt and that the constituent materials conserve their bulk dielectric function. There is no microscopic effect of the presence of the interface between the two slabs. We therefore expect EMT to be better for large slabs.

Part III

Results

Chapter 8

Silver Chloride : state-of-the-art calculations

Silver chloride is the fundamental ingredient for Becquerel's photography [136]. It hence deserves a full *ab initio* study. This is not trivial: in particular, the presence of silver necessitates particular care for its pseudopotential, and a detailed study of this topic will be presented in the first section of this chapter[1]. The band structure of silver chloride is then presented using different levels of theory. This is followed by a study of the optical properties, with time dependent density functional theory in the third section and by solving the Bethe-Salpeter equation in the fourth section.

The aim of this chapter is to gain extensive understanding of electronic excitations in silver chloride. Particular emphasise will be put on exitonic effects in the absorption spectrum which, as we will see, are important to understand the observations. The calculations are a computational challenge, and new methodology had to be developed to face this challenge.

8.1 Pseudopotentials

Core electrons make the density and wavefunctions quickly vary close to the center of the atoms. With the codes that will be used the wavefunctions are decomposed in a plane wave basis: the description of these wavefunctions would require an unaffordably large plane-wave cutoff $\mathbf{G}_{max}$. We thus explicitly take into account only the valence electrons and use pseudopotentials to represent the cores. The pseudopotentials used are of Troullier-Martins [138] type for both species, silver and chlorine. We have generated the pseudopotential using the FHI98PP package [139]. We used LDA functional in the Perdew-Wang parametrization [140] with scalar relativistic corrections.

The ground-state configuration of Ag is

$$1s^2 2s^2 2p^6 3s^2 3p^6 4s^2 3d^{10} 4p^6 5s^1 4d^{10} \text{ or } [Kr]5s^1 4d^{10}.$$

However, pseudopotentials are usually created in a slightly ionized state of the atom [141]. Moreover, it is generally established that spectroscopy calculations require valence shells to be complete, because of the strong spatial overlap between electrons in the same shell and the consequent strong exchange effects [142–144]. Here we use the atomic configuration

$$1s^2 2s^2 2p^6 3s^2 3p^6 4s^2 3d^{10} 4p^6 4d^{10}$$

to create the pseudopotential of silver, with the $4spd$-shell $4s^2 4p^6 4d^{10}$ in the valence, which corresponds to a singly ionized atom.

Different cutoff radii, where the true wavefunction in the atom matches the pseudo-wavefunction, were tested for the different orbitals. For a smaller cutoff radius, the pseudopotential is more accurate but also more expensive, i.e. "harder". To illustrate this, a soft pseudopotential and a

[1] This chapter as well as chapters 9 and 10 are summarized in a submitted paper *First-principles study of excitons in the optical spectra of silver chloride*, Arnaud Lorin, Matteo Gatti, Lucia Reining, Francesco Sottile (preprint [137])

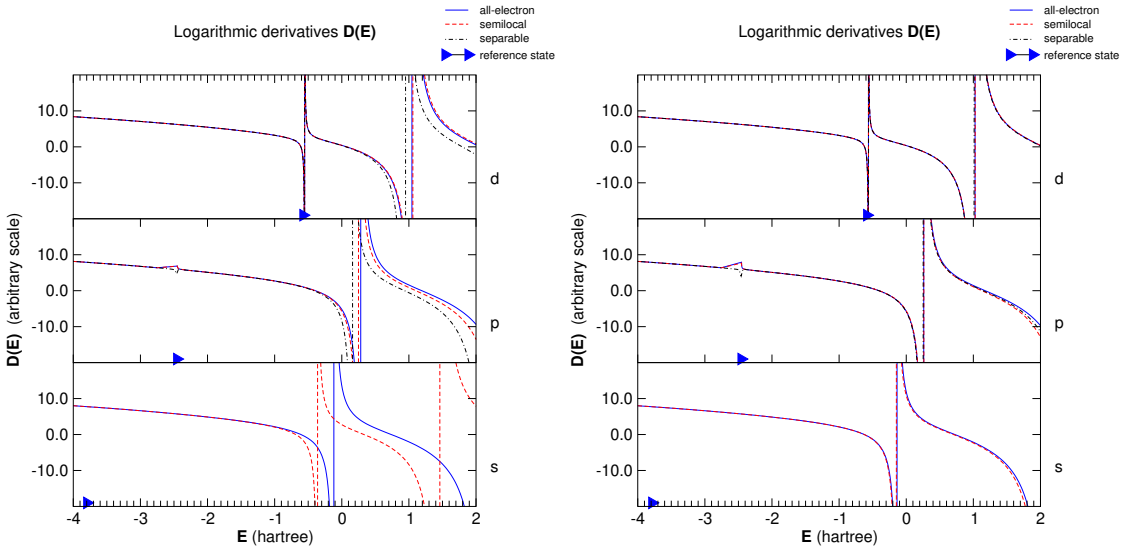

Figure 8.1: Logarithmic derivatives for a soft (left) and a hard (right) pseudopotential for silver, evaluated at $r = 3.4$ Bohr.

hard pseudopotential are compared. In Fig. 8.1, the logarithmic derivative for the wavefunctions corresponding to the two pseudopotentials is shown. In the left panel the logarithmic derivative of the soft pseudopotential is plotted, while in the right panel the logarithmic derivative of the hard pseudopotential is shown. The soft pseudopotential is defined with cutoff radii of 1.6 a.u. for the s, 2.1 a.u. for the p and 1.8 a.u. for the d component. For the hard pseudopotential the cutoff radii were set to 0.9 a.u. for the s, 2.3 a.u. for the p, and 1.5 a.u. for the d component, obtaining satisfactory logarithmic derivatives and excitation energies. The red and black curves represent the pseudopotential in a semi-local and separable form, respectively [139]. The blue curves are the all-electron reference. The separable form is the one used in the following. The soft pseudopotential reproduces badly the all-electron calculation, particularly for the s states around 0 Hartree, where the divergence of the dashed red and dashed black curves are not aligned with the blue curve. The s state is the local reference component, used to represent higher momentum states. This bad description of the states close to 0 Hartree is problematic because they are the states that will form the conduction bands together with the silver p states and chlorine s states. The hard potential solves this problem as can be seen from the right panel of the figure: the divergences are well described by the pseudopotential. Moreover preliminary calculations with the soft pseudopotential predicted AgCl to be a metal, which is not correct. The hard pseudopotential does not have this problem. It gives a good description of silver at the expense of smaller cutoff radii and thus an increase of the cutoff energy needed to describe it.

Chlorine does not present the same difficulty, and we have created the pseudopotential using an atomic configuration of $1s^2 2s^2 2p^6$ for the core and $3s^2 3p^{4.5} 3d^{0.5}$ for the valence electrons. Cutoff radii were 1.6 a.u. for s and p components and 1.8 a.u. for the d component.

8.2 Ground-state properties

With these pseudopotentials it is now possible to carry out ground state calculations for silver chloride with DFT-LDA. First, the convergence with respect to the cutoff energy is studied, followed by the evaluation of the theoretical lattice parameter. All ground state and band structure calculations are carried out using the Abinit package [145].

Silver chloride has a face centered cubic crystal structure with one variety of atom in the octahedral sites of the other, similarly to sodium chloride. The lattice parameter used for the

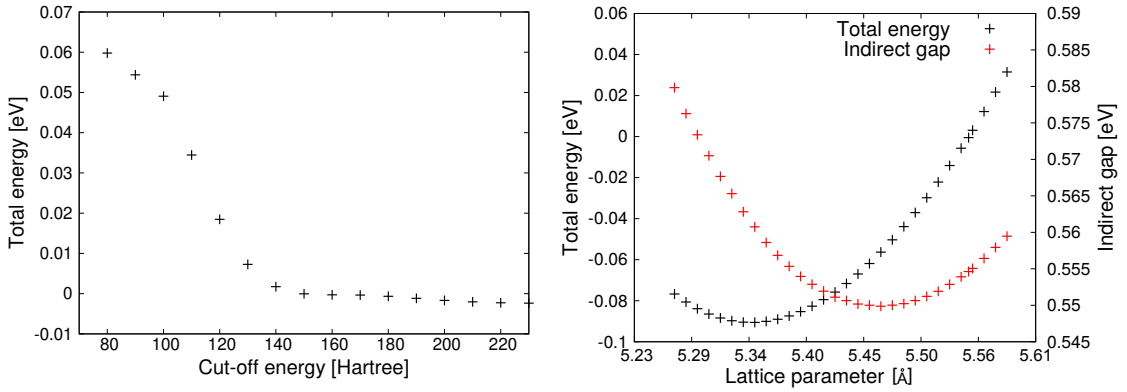

Figure 8.2: Left: convergence of the total energy with respect to the energy cutoff. For the total energy the difference to the total energy with a cutoff of 150 Hartree is shown, in order to ease the reading. The total energy at this cutoff is 4394.9875 eV. Right: total energy and indirect band gap calculated in KS-LDA as function of the lattice parameter.

convergence study and in the rest of this thesis is the experimental one [146, 147], $a_{\text{exp}} = 5.55$ Å. Concerning the convergence with respect to the **k**-point grid we find that the total energy is converged within 1 meV for a 8×8×8 Monkhorst-Pack **k**-point grid [148]. On the left hand side of Fig. 8.2 is shown the convergence of the total energy with respect to the cutoff energy. We see that below a cutoff of 150 Hartree the total energy changes rapidly while above 150 Hartree the behavior of the total energy changes and evolves slower than previously. A cutoff of 150 Hartree yields then results that are converged up to 2.5 meV. Achieving an even better convergence would require a much larger cutoff since the curve evolves very slowly above 150 Hartree. In the following the cutoff energy is set to 150 Hartree. This high cutoff is needed because of the strongly localized semi-core $4s$ and $4p$ states of silver.

The total energy calculation as a function of the lattice parameter a, shown in the right panel of Fig. 8.2, yields the equilibrium value of $a = 5.35$ Å. The LDA underestimates hence the lattice parameter with respect to the experimental value [146, 147] $a_{\text{exp}} = 5.55$ Å at room temperature [2], in agreement with earlier calculations [59, 60, 63, 65]. For our discussions, we accept an error bar for transition energies of 0.1-0.2 eV. The uncertainty induced on transition energies by the error in the lattice constant lies well within this limit. This is illustrated in Fig. 8.2, where the total energy and indirect band gap as a function of the lattice parameter are shown. In the following the experimental lattice parameter will be used.

The charge density is plotted in Fig. 8.3. The intensity is dominated by the electrons around silver with its 10 $4d$ electrons and the semi-core electrons.

8.3 Kohn-Sham band structure

The converged results for AgCl are used to compute the band structure of the material. Since we are dealing with a non-magnetic material, here and in the following we omit spin, which will only lead to prefactors.

The band structure of silver chloride computed along different high symmetry lines is shown in Fig. 8.4. Two approximations to the exchange-correlation potential are used: the Local Density Approximation (LDA) and the Generalized Gradient Approximation (GGA) of Perdew-Burke-Ernzerhof [84]. The two band structures are quite similar. The main effect of the GGA is an opening of the gap by about 0.35 eV with an almost rigid shift of the conduction bands with respect to the valence bands, which compares well with others results in the literature [60, 63]. For this reason, only the LDA results will be described in more detail.

[2] The lattice parameter decreases at lower temperature: Lawn [149] finds a value of 5.51Å at 83K

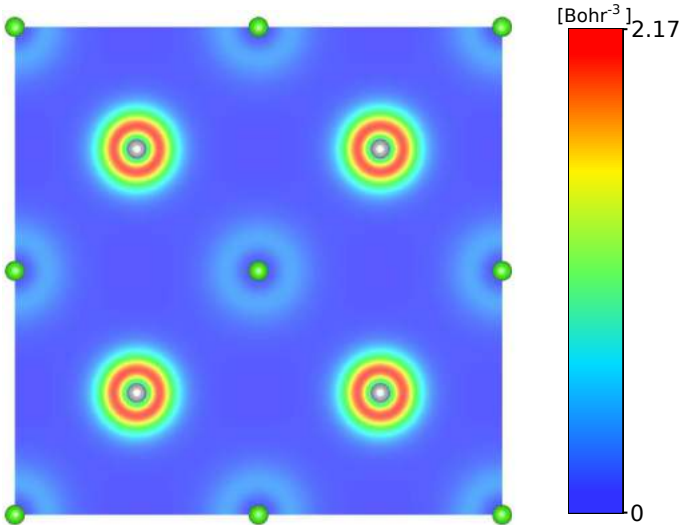

Figure 8.3: Charge density of silver chloride in the [100] plane passing through the atoms. The chlorine atoms are represented by the green dots while the silver atoms are represented by the grey dots.

The top valence is located at L and the bottom conduction at Γ. The minimum gap of 0.56 eV is indirect between these two points. The minimal direct gap, with the $8 \times 8 \times 8$ **k**-point grid, is located in the ΓK direction, at around 2/9 of the distance from Γ, its value is 2.78 eV. The direct gap at Γ is 2.86 eV. These different values compare well with other LDA results reported in Tab. 2.1.

No inverse photoemission experiments are available for silver chloride. Therefore it is not possible to have a direct estimation of the experimental quasi particle gap. The values of the gaps have to be extracted from optical experiments [42] and Raman spectroscopy [41, 150]. The direct gap can be estimated from the onset of the absorption spectrum. In optical experiments, the indirect gap is not accessible directly as the photon does not carry enough momentum to allow such a transition. However the transition can take place with the help of phonons, in the so-call phonon assisted absorption [41, 42]. This process gives rise to a tail decaying toward low energy in the spectra and presents a specific behavior with the temperature. However, optical experiments do not give direct access to the quasi-particle band gap as one should also take into account the binding energy of the excitons, that may be formed in the absorption process. This issue is addressed in Sec. 8.7 and Chap. 10. However, independently of this problem, the LDA and the GGA gaps are drastically smaller than the experimental values. The experimental direct optical gap is [51] 5.1 eV, while the experimental indirect gap is 3.25 eV [50, 150].

Earlier theoretical studies [41, 42, 57, 151, 152] have found that Ag^+ 4d and Cl^- 3p ionic states have similar energy in the crystal, leading to strong hybridization in the valence band. While their mixing is zero at Γ, it is strong elsewhere, notably at L. This **k**-dependent hybridization and the strong $p-d$ repulsion cause the upward curvature of the top-valence bands at Γ (i.e. a negative hole effective mass) and make AgCl an indirect semiconductor. On the contrary, in the alkali halides, which share the same rocksalt crystal structure, the ionic energy levels are well separated, leading to a much larger ionic character of the compounds and a direct band gap.

Our calculations, as shown by the band structure in Fig. 8.4 and the projected density of states (PDOS) in Fig. 8.5, confirm this picture. While Cl 3s states are located at ∼ -15 eV (not shown), the valence band region includes 8 bands. They are very close to each other at the Γ point, where from the bottom to the top we count 3 degenerate Ag t_{2g} states[3], 2 degenerate Ag e_g states, and 3 degenerate Cl 3p states. The hybridization between Ag 4d and Cl 3p increases moving away from the Γ point towards the top and the bottom of the valence bands at the L point, where Ag 4d and

[3]The crystal field at Ag site has a cubic point symmetry (O_h).

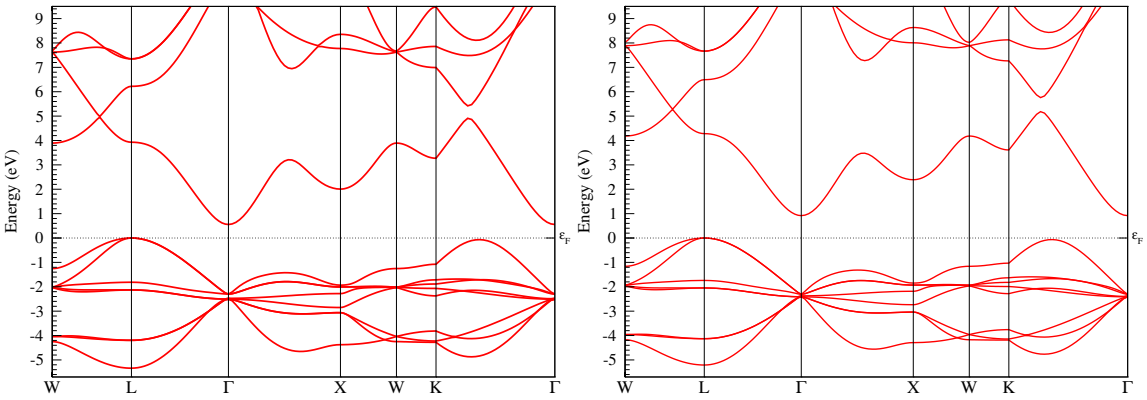

Figure 8.4: Kohn-Sham band structure of silver chloride. Left: LDA calculation, right: GGA calculation. The main difference is a rigid increase of the gap by 0.35 eV in the GGA.

Cl $3p$ are strongly mixed. Their interaction gives rise to dispersive bands. Instead, three Ag $4d$ bands, which are not dispersive between Γ and L, remain at the center of the valence manifold, giving rise to a pronounced sharp peak in the PDOS. Finally, the lowest conduction band has a delocalized Ag $5s$ and Cl $4s$ character at the Γ point [64] and mixed Ag $5s$ - Cl $3p$ elsewhere.

Fig. 8.5 compares the calculated PDOS with the photoemision spectra measured by Tejeda *et* al. [151] and Mason [153]. The two experimental spectra were taken at the same photon energy but their shape shows a quite strong difference, notably around -4 eV. Mason's experiment is realized at 83 K, while Tejeda *et* al.'s experiment is done at room temperature. Mason mentions the formation of photolytic silver at room temperature, but not at the surface, region probed by the XPS. This illustrates the experimental problems encountered with AgCl. The top valence energy is set to 0 for all curves. The width of the valence band is 6 eV for both experimental spectra, close to the LDA width of 5.3 eV. Both spectra also show a main peak at -3.1 eV and a shoulder just below the top valence as well as a shoulder (peak for Mason) at -4.5 eV. These photoemission spectra mainly probe Ag $4d$ state as can be understood from the photoionization cross-sections [154] for photons with $h\nu = 1486.6$ eV. The photoemission spectrum is thus mostly given by the PDOS of silver d states. We find that the shoulder just below the top valence band is correctly described by the LDA calculation, the shoulder at -4.5 eV (peak for Mason) is also reproduced by the LDA calculation, but not at the correct energy. The main peak can be attributed to the non dispersive band at the center of the band structure. These states are poorly described by the LDA, as there is a difference of 1 eV between the LDA peak in the d state PDOS and the main peak in the photoemission spectra. The difficulty to describe localized states such as d states as well as giving correct gaps, is known a problem of the KS-LDA approach. The results can be improved by using many body perturbation theory, for example in the GW approximation, as we will discuss next.

8.4 Many-body perturbation theory: G_0W_0 and QSGW band structures

Kohn-Sham eigenvalues should not be interpreted as electron addition or removal energies. A correct description of such quasi-particle energies can be obtained from the poles of the one-body Green's function, for which good estimates are often obtained using the GW approximation for the self-energy introduced in ch. 6. Different flavors of this approximation exist. As we will discuss in the following, their choice is important in the case of AgCl. All GW calculations have been realized with the Abinit package [155]. In the next subsection the G^0W^0 approximation is considered.

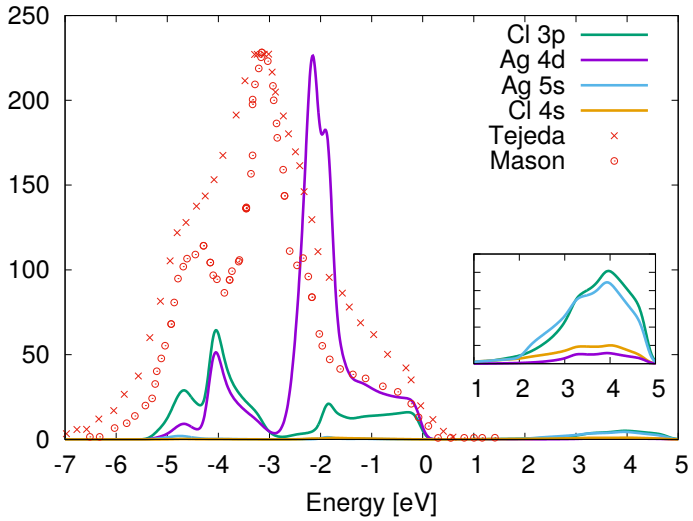

Figure 8.5: Projected density of states computed in LDA compared with experimental photoemission spectra from Mason[153] and Tejeda *et* al.[151] at a photon energy $h\nu = 1486.6$ eV. The top valence is aligned with the origin of the abscissa axis. The insert shows a zoom of the calculated conduction bands.

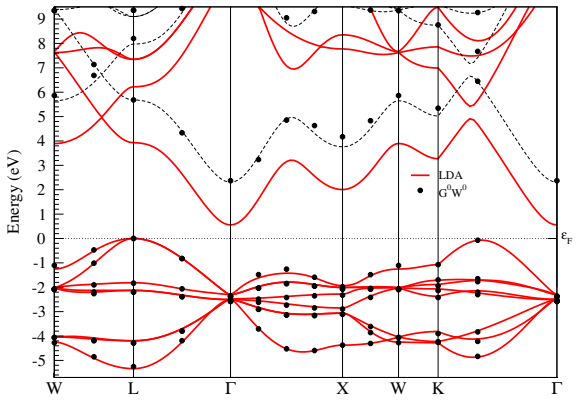

Figure 8.6: Band structure of silver chloride computed with LDA (continuous line) and G^0W^0. The G^0W^0 results are represented by the dots. The dashed lines represent a rigid shift of the conduction band by 1.9 eV.

G^0W^0

The G^0W^0 calculation has been realized using a 4 (4×4×4) MP **k**-point grid. The screening was computed with 5000 planewaves to describe the wavefunctions; 550 bands were included in the calculation and the size of the dielectric matrix was set to 1500 **G** vectors. The self-energy was computed with a cutoff of 4000 planewaves for the wavefunctions and 820 bands were included in the calculation. The band structure of silver chloride evaluated in G^0W^0 is shown in Fig. 8.6. The top of the valence band is aligned to zero.

The G^0W^0 band structure looks similar to the KS-LDA one, up to an almost rigid shift of 1.8-1.9 eV of the conduction bands. For illustration, the dashed curve shows this rigid shift of 1.9 eV of the lowest conduction bands in KS-LDA.

This size of the band-gap opening is in agreement with the value of 1.75 eV recently obtained by Zhang and Jiang [72] in a G^0W^0 full-potential linearized augmented plane wave calculation starting from a KS-GGA band structure. Instead, van Setten *et* al [70] reported a much smaller G^0W^0 correction to the KS-GGA gap: 1.25 eV. The reason for this large discrepancy should not be

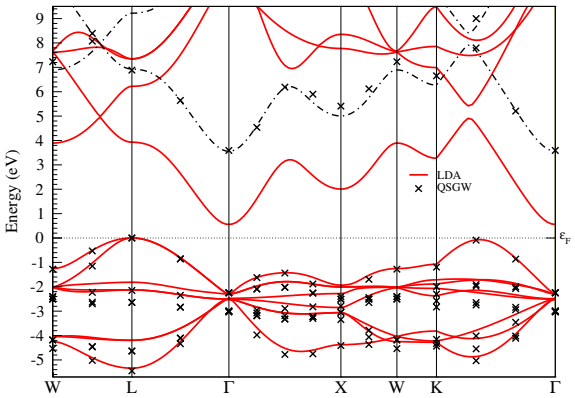

Figure 8.7: Band structure of silver chloride computed with LDA and QSGW. The QSGW are represented by the crosses. The dot-dashed lines represent a rigid shift of the conduction band by 3 eV.

ascribed to inaccuracies in the pseudopotentials [72], but rather to an underconvergence problem: their automatized algorithm employed only 155 bands (compared to 820 in the present work). On the contrary, Gao *et* al.[71] found a much larger G^0W^0 correction starting from KS-LDA, i.e. 2.38 eV, and had to include up to 2500 empty bands in the G^0W^0 calculation. A similar situation was previously encountered in other materials like ZnO [156–158] and TiO_2 [159], where semicore electrons have to be explicitly included in the GW calculation. The origin of the problem in those calculations was identified [158, 159] with the use of the f-sum rule in the Hybertsen-Louie [112] plasmon pole model (PPM), which was adopted also by Ref. [71] for AgCl. Indeed, also in the present case our results obtained with the Godby-Needs PPM agree (within 0.2 eV at most) with the accurate contour-deformation (CD) calculation that avoids any PPM (see Tab. 8.1). As a final validation, we have also employed the effective energy technique [160] (EET) that accounts approximately for all empty states and allows reaching convergence much more easily than the traditional sum-over-states scheme. Using the EET (here used within the PPM) the values for the band gaps are once again in agreement within 0.1 eV (see Tab. 8.1). This suggest that our careful pseudopotential calculations are of similar quality as the all-electron calculations of Ref. [72].

The G^0W^0 indirect band gap is now 2.4 eV and the direct gap at Γ is 4.6-4.8 eV. Both are still smaller than the experimental optical gaps (see Tab. 8.1). However, in situations with large *pd* hybridization as for AgCl, the LDA starting point may not be reliable [118]. At the same time, also the large corrections obtained within the G^0W^0 scheme question the first-order perturbative approach itself.

QSGW

In order to overcome the problem of the KS-LDA starting point and assess the G^0W^0 perturbative scheme, we have performed QSGW calculations which are based on a quasi-particle self-consistent scheme as explained in Ch. 6. The new band structure is shown in Fig. 8.7; again, top-valence bands are aligned. At first sight, there is no drastic change in the dispersion of the valence and conduction bands. However, a closer look shows that, whereas the G^0W^0 valence bands were essentially on top of the KS-LDA ones, QSGW results slightly increase – by 0.1 eV – the valence bandwidth and push the narrow Ag 4*d* bands down by 0.5 eV, leading to a better agreement with photoemission results [151, 153]. The most obvious change is the almost rigid shift of the conduction bands with respect to KS-LDA, which has passed from 1.9 eV in G^0W^0 to 3.0 eV, as indicated by the dot-dashed line in Fig. 8.7.

With this shift, the indirect gap becomes 3.7 eV while the direct band gap is 5.9 eV. The fact that band gaps now seem to be overestimated with respect to experiment (see Tab. 8.1) may have two reasons. First, the self-consistent RPA screening in QSGW is too weak, which brings results

	Indirect	Direct
LDA	0.56	2.78
G^0W^0 (PPM)	2.4	4.8
G^0W^0 (CD)	2.4	4.6
G^0W^0 (EET)	2.4	4.7
QSGW	3.7	5.9
evQSGW	3.2	5.7
GW^0	2.7	4.8
Absorption onset (Exp.)	3.25	5.13

Table 8.1: Direct and indirect photoemission gaps of AgCl calculated in different approximations compared to experimental (Exp.) absorption onsets from optical measurements (Refs. [50, 51]) which provide a lower bound due to excitonic effects (see Sec. 8.7 and Ch. 10).

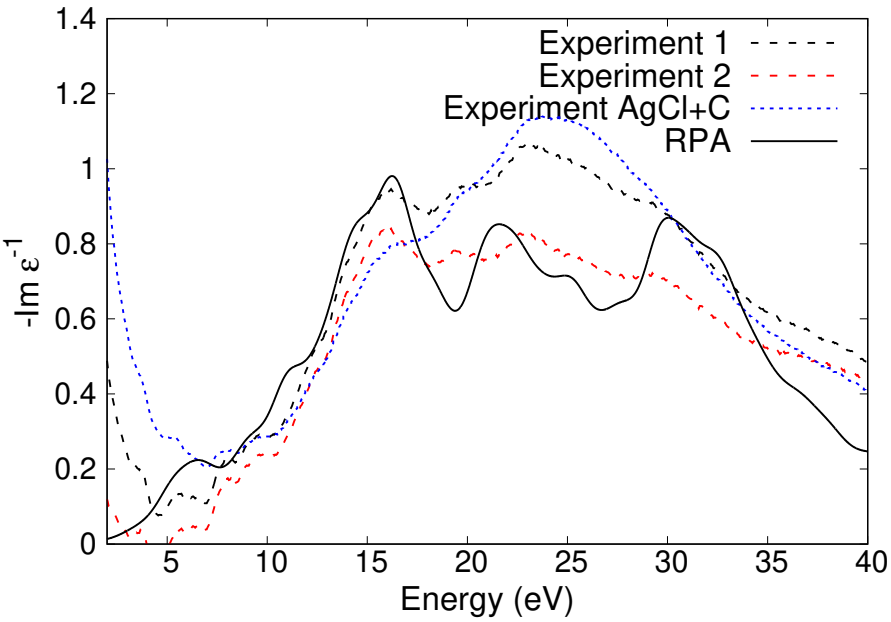

Figure 8.8: Electron energy loss spectra of silver chloride. Dashed lines are the experimental results normalized in two different ways. The loss function, -Im ϵ^{-1} computed within RPA is shown by the black solid line. The dotted blue curve shows the data as measured, including a carbon capping.

too close to Hartree-Fock [111, 118, 120, 161]. Second, the experimental optical gaps are affected by excitonic effects (see Sec. 8.7 and Ch. 10).

We have also performed a QSGW calculation where only the QP eigenvalues are calculated self-consistently, while the QP wavefunctions are constrained to remain the KS-LDA orbitals. This further calculation is named 'evQSGW' in Tab. 8.1. It gives band gaps that are intermediate between the G^0W^0 and the full QSGW results, illustrating the impact of the change of the wave-functions on the band structure. Finally, we have tested the effect of the update of the screened Coulomb interaction W: a QSGW calculation, in which we keep the W fixed at the level of the RPA-LDA, named 'GW^0' in Tab. 8.1. The resulting gap (direct 4.8 eV and indirect 2.7 eV) is closer to the G^0W^0 value than to the QSGW one. In the QSGW calculation in AgCl the modification of the screened interaction W is hence a critical effect.

8.5 Electron Energy Loss Spectra: experiment and simulation

Since W seems to play a key role, it is interesting to examine it directly. This can be done by studying the loss function, which is the imaginary part of the inverse dielectric function. It can be measured directly using Electron Energy Loss Spectroscopy (EELS).

No data were available at the beginning of this thesis, but an opportunity to acquire EELS data on pure silver chloride appeared during a Scanning tunneling electron microscopy experiment at the Laboratoire de Physique des Solides (LPS) in Orsay [162]. Our collaborators from the CRC were investigating the surface plasmons of silver nanoparticles embedded in, or on top of, silver chloride. This opportunity was used to realize an experiment of electron energy loss spectroscopy on silver chloride which I attended. A location of the sample was selected for its absence of silver nanoparticles and the measurement was realized also on a second position to verify the resulting spectra. A further complication was the sample capping by a carbon layer, used to protect the sample from radiation damage. Therefore, for the presence of this carbon layer the measured data could not be used directly. To get rid of the carbon contribution a spectrum of the carbon deposit alone was also measured.Since the effective medium theory (Ch. 7) tells us that the inverse dielectric functions of each material add up, it is possible to subtract the carbon contribution if the relative normalization of the two spectra is separately known. Fig. 8.8 shows the results of the experiment as well as the RPA calculation of the Loss function -Im $\epsilon^{-1}(\mathbf{q} \to 0, \omega)$ with LDA energies and wavefunctions. Two ways of normalization have been used: a normalization aligning the maximum of the elastic peaks at $\omega = 0$, named "Experiment 1" in the figure, and a normalization by the total intensity of each spectrum, named "Experiment 2" in the figure. The experimental curves are then scaled by an arbitrary factor. The spectra are cut at the low energy part is characterized by the elastic peak, which is not usable. The measured data (dotted blue curve) are also represented with an arbitrary normalization.

The two experimental curves are quite similar in their shape for energies higher than 5 eV, showing that the method of normalization might not be important. Theory gives good results at low energy: the peak at 16 eV is correctly described and the shoulders at lower energy in the experimental spectra are also present in the RPA spectrum. At higher energy, the RPA spectrum has a peak at 21 eV, which is at 19 eV in the experimental spectra. However, the RPA spectrum lacks intensity in this energy range, and above 33 eV it does not agree with experiment.

It should be noted that the calculation of the dielectric function has been realized with vanishing momentum, but in this kind of experiment the flux of electrons is localized in a fraction of space. Therefore, the experimental EELS spectrum is the result of an integration over many momenta. The dielectric function for larger momentum transfer is known to be shifted toward higher energy. This might explain the different behavior at high energy.

Overall, the RPA based on Kohn-Sham ingredients compares quite well with experiment, although this comparison remains rather qualitative, in particular in view of issues with the normalization of the experimental spectra, and because the experiment is not momentum resolved. Moreover, the presence of the elastic peak and the lack of resolution does not allow us to discuss in detail the lower energy part of the spectrum. Therefore, we move in the following to optical spectra.

8.6 Absorption spectrum within time-dependent density functional theory

As explained in Ch. 5, absorption spectra can in principle be obtained using time dependent density functional theory in the linear response regime or solving the Bethe-Salpeter equation. Since the time dependent density functional approach is computationally much cheaper, we will first examine to which extent it could be used to describe optical spectra of AgCl.

The linear response TDDFT calculations were carried out using the DP code [163]. Convergence for both absorption and the extinction coefficient over a frequency range of 0 to 10 eV was reached using 2048 shifted $\mathbf{k}$ points [164], 965 plane waves for the wavefunctions, 59 $\mathbf{G}$ vectors for the

polarizability matrix including crystal local field effects (see Appendix C), 13 occupied bands, and 20 unoccupied bands.

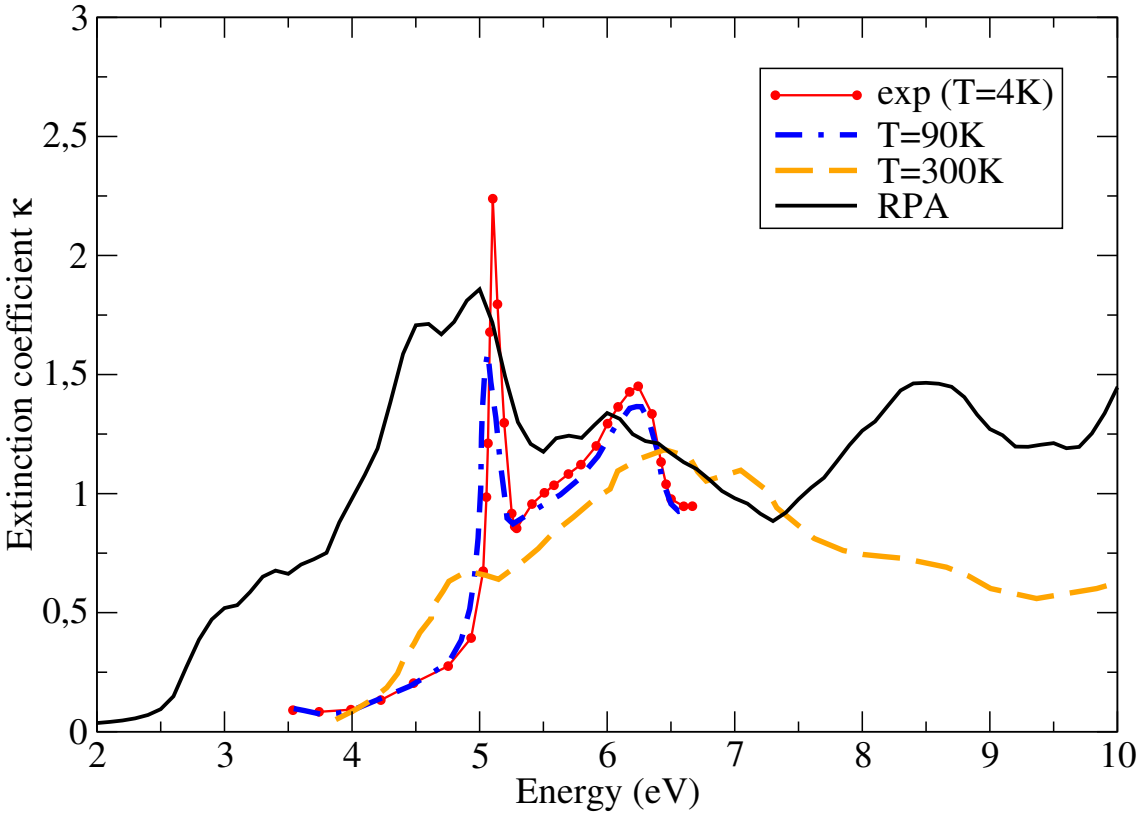

Figure 8.9: Extinction coefficient of AgCl as a function of energy. The RPA calculation based on the KS-LDA band structure (black solid curve) is compared to experimental data from Ref. [51] measured at 4 K (red curve), at 90 K (blue curve) and at room temperature (orange curve).

Fig. 8.9 shows the extinction coefficient $\kappa(\omega) = \mathrm{Im}\sqrt{\varepsilon_M(\omega)}$ where ϵ_M is the macroscopic dielectric function (see Appendix C). We compare the RPA result (black curve) with three experiments at different temperatures: 4 K (red curve), 90 K (blue curve), 300 K (orange curve). The spectra have been measured up to 6.7 eV in Ref. [51]. The wider range at room temperature has been obtained by combining results from different sources. The shape of the measured spectra is strongly affected by temperature: the very sharp peak at the onset of the spectrum around 5.1 eV is clearly visible only at low temperatures, while the room-temperature spectrum is much broader. Since our calculations do not include the effect of temperature, comparison to the low-temperature experiment should be more meaningful. Still, keeping this fact in mind, also the room temperature experiment gives important indications. Overall, the RPA and experimental spectrum at 300 K are similar. However, the absorption onset is underestimated in the RPA, by more than 1 eV. Moreover, the RPA entirely misses the sharp feature at the onset of the low-temperature experimental result. The underestimate of the onset is a common problem in KS-RPA spectra [128]. Since in the RPA the exchange-correlation kernel $f_{\mathrm{xc}} = 0$ and since, as explained in Ch. 5, only short-range components of v_c contribute to optical spectra, the onset is determined by the interband transitions in χ_0, as can be seen from Eq. (5.8) and Eq. (5.10). It suffers therefore both from the use of the LDA, and from the fact that even the exact KS band gap would be smaller than the measured band gap. The results do not change when f_{xc} is taken into account within the adiabatic local density approximation (ALDA): in Fig. 8.10 the ALDA (dashed green curve) is hardly distinguishable from the RPA (black curve). The ALDA can neither lead to a significant opening of the optical gap, nor to a significant change in the spectral shape.

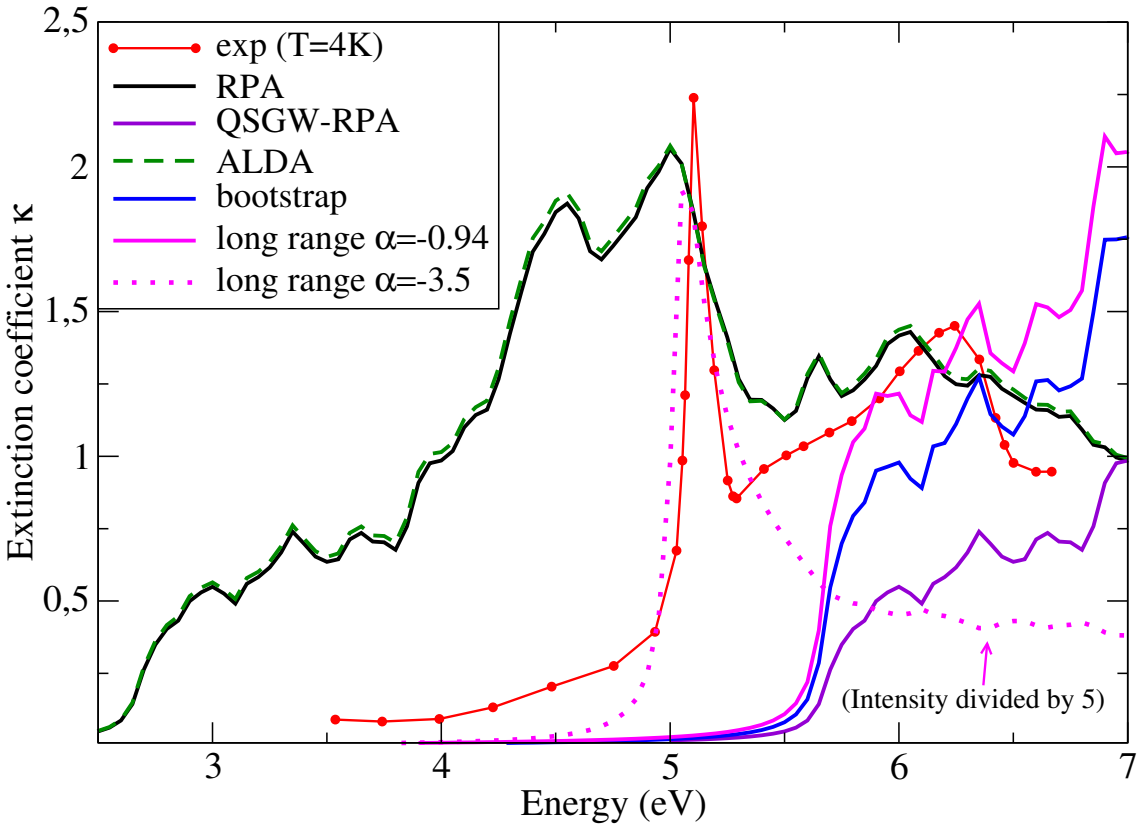

Figure 8.10: Comparison between the extinction coefficient of AgCl measured at 4 K with several TDDFT approximations. Since the energy range is limited to 3-7 eV, these spectra have been calculated with only 4 conduction bands.

It is well established [101, 102] that the ALDA suffers from the absence of a long-range contribution that in nonzero-band-gap materials would diverge as $1/q^2$ in the long wavelength limit, $q \to 0$. The exact xc kernel should contain such a contribution. Several suggestions exist in literature how to include a long-range component in $f_{\rm xc}$ [102–105] (see Ch 5). All kernels of this family start from a χ_0 built with a quasiparticle band structure from GW or similar approaches, instead than from a KS one. A simple static and scalar $f_{\rm xc}$ with a long-range contribution can then simulate the effects of the electron-hole interaction by shifting spectral weight to lower energies.

In order to simulate these missing excitonic effects, we have examined the long-range kernel [102] of type α/q^2, where the band-gap opening at the QSGW level is accounted for by a scissor corection of 3.0 eV. The result is given by the pink curve in Fig. 8.10. The value of $\alpha = -0.94$ has been obtained from Eq. (4) of Ref. [103] using an experimental dielectric constant of AgCl [165] $\epsilon_\infty = 4$. In contrast to the ALDA, the long-range kernel does shift the spectral weight to lower energies with respect to the QSGW-RPA result (violet curve), where $f_{\rm xc} = 0$. However, the spectral onset remains the same, overestimating the experimental result, and the sharp peak is still missing. A larger value of $|\alpha|$ in the long-range kernel α/q^2 would enhance the excitonic effects. However, in order to reproduce the sharp experimental peak, we should increase the strength $|\alpha|$ to very large values, which would completely destroy the spectrum. For example, the dotted curve in Fig. 8.10 is obtained with $\alpha = -3.5$. Note that its overall intensity is divided by a factor 5 in the plot, while all spectral features at higher energies have collapsed. This failure of static long-range kernels is confirmed also by similar approaches, such as the recent bootstrap kernel [106, 107] (see the blue curve in Fig. 8.10, obtained with the implementation of Eq. (5) of Ref.[107]).

Therefore, we can conclude that TDDFT with the presently available simple approximations does not give a good description of the optical properties of AgCl, and in particular, of the strong

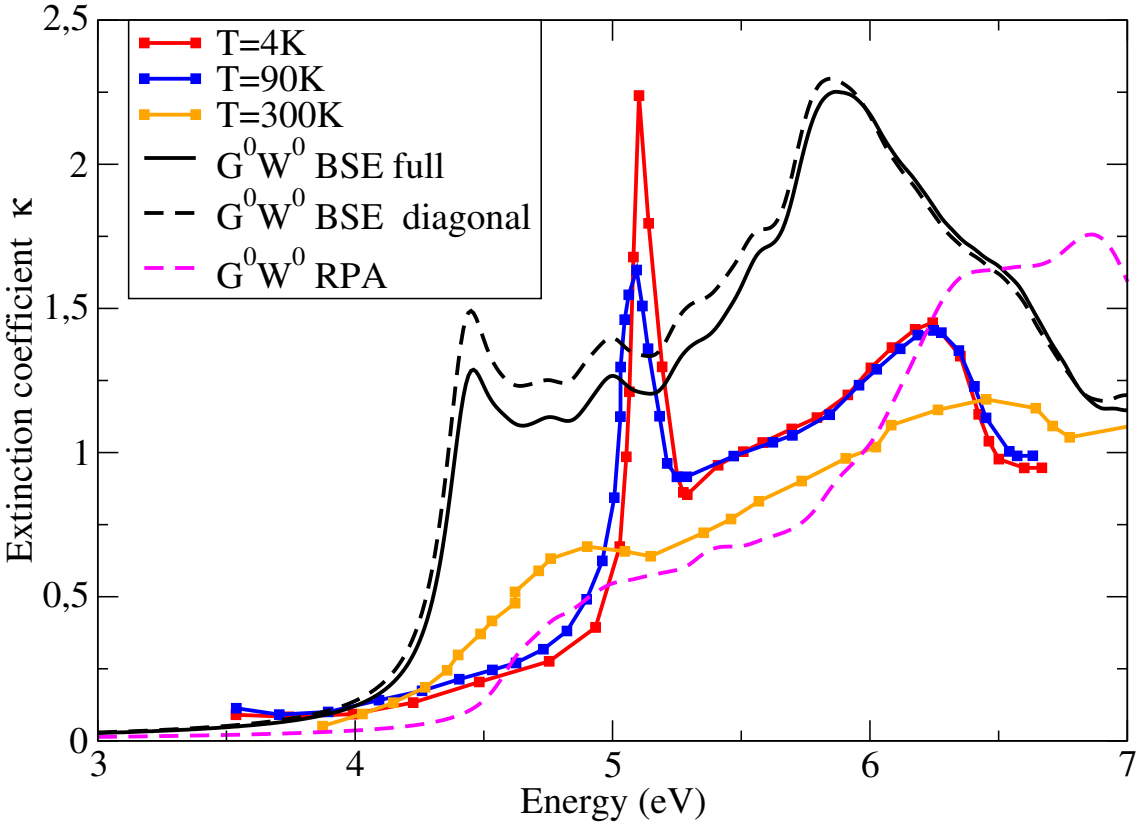

Figure 8.11: Comparison between the experimental extinction coefficient of AgCl from Ref. [51] at different temperatures and MBPT calculations (with 2084 **k** points): G^0W^0-RPA obtained with 1.9 eV scissor correction (pink dashed line), G^0W^0+BSE obtained with the full RPA screening matrix $W_{\mathbf{GG'}}(\mathbf{q})$ (black solid line) or using only its diagonal contribution (black dashed line).

excitonic effects that should explain the remaining discrepancy between theory and experiment. For this reason, we have to move on to a full description in the framework of MBPT, by solving the Bethe-Salpeter equation as explained in Ch. 6.

8.7 Absorption spectrum within the Bethe-Salpeter equation

All BSE calculations have been performed using the EXC code [166]. As input, we use the KS band structure corrected by a scissor shift taken from our GW calculation. We have verified that this reproduces well the effect of the true GW corrections. In the following we will refer to G^0W^0+BSE for BSE calculations that use a scissor correction of 1.9 eV, determined from the G^0W^0 band structure[4]. In a similar way, a scissor correction determined from the QSGW band structure will be used with a BSE calculation and will be referred to as QSGW+BSE.

The results presented in this section are based on a full G^0W^0+BSE calculation with 2084 shifted [164] **k**-points, 8 occupied and 6 unoccupied bands. To obtain the spectra $\varepsilon_M(\omega)$, we have used the Haydock iterative scheme [167, 168], instead of generating eigenvalues and eigenvectors of the electron-hole hamiltonian. The LDA-RPA screened Coulomb interaction W is used to account for the electron-hole attraction.

Fig. 8.11 shows the extinction coefficient for G_0W_0+RPA and G_0W_0+BSE. The G_0W_0+RPA designates an RPA calculation that employs a scissor correction to reproduce the G^0W^0 band structure. The onset of the spectrum (pink dashed line in Fig. 8.11) underestimates the experimental

[4]The effect of using the full G^0W^0 has been tested and does not change the result at low energy.

threshold and does not show a pronounced peak at low energy: it merely shifts the LDA-RPA spectrum to higher energy. The electron-hole interaction in the BSE shifts oscillator strength to lower energies, and a peak forms (black solid line in Fig. 8.11). However, the G_0W_0+BSE spectrum is now at an even lower energy and the excitonic peak is much too weak with respect to experiment.

BSE calculations in solids are often done by neglecting the off-diagonal elements of the screening matrix [126, 128] $W_{\mathbf{GG'}}(\mathbf{q})$ that represents the direct electron-hole interaction. This is not an issue when the electron-hole pair is delocalized enough to justify a space-averaged screening. The first excitonic peak in AgCl is influenced by this approximation: taking into account the full spatial details of screening (solid black line in Fig. 8.11) reduces the peak intensity by about 10% with respect to the approximation of diagonal screening (dashed black line in Fig. 8.11). Still, the difference is small compared to the discrepancy to experiment.

The G_0W_0+BSE calculation remains qualitative for several reasons. First, as pointed out above, the G_0W_0 band structure from an LDA starting point is not reliable for AgCl. Second, the spectrum is also strongly dependent on the Brillouin zone sampling, and a $\mathbf{k}$-point convergence test performed with a reduced number of conduction bands shows that a set of 6912 $\mathbf{k}$ points is needed instead of 2084 employed here. While the first issue could be solved by using the QSGW band structure as a starting point for the BSE calculation, the main computational problem would still remain the setting up of the full screening matrix $W_{\mathbf{GG'}}(\mathbf{q})$ that should be calculated self-consistently for too many $\mathbf{q}$ points.

In order to overcome this problem, we will complement the first principles calculations with a model screening, where the parameters of the model are fitted to the *ab initio* results. The next chapter will be devoted to the exploration of the model, which turns out to be a powerful tool to get reliable results.

Chapter 9

Model screening

The BSE calculation of the absorption spectra using fine **k**-point grids can become prohibitive, because the screening has to be computed for all $\mathbf{q} = \mathbf{k} - \mathbf{k}'$, the differences between **k**-points. However, as it will be shown below, the convergence of the screening can mostly be achieved on a coarse grid. It should therefore be possible to use a model for the dielectric function using the information on a rough **q**-point grid to interpolate the dielectric function on a finer **q**-point grid.

9.1 Model dielectric function

Many models have been proposed for the dielectric function [169–180]. In particular, for bulk semiconductors a successful model was suggested in Ref. [181]. It represents the static dielectric function as

$$\epsilon(q) = 1 + \frac{1}{\frac{1}{\epsilon(q\to 0)-1} + \alpha\left(\frac{q}{q_{TF}}\right)^2 + \frac{q^4}{4\omega_p}}, \tag{9.1}$$

where $q_{TF} = 2(3\bar{n}/\pi)^{1/6}$ and $\omega_p = \sqrt{4\pi\bar{n}}$, with $\bar{n}$ the average density. α is a parameter set to 1.563, following Ref. [181]. This model dielectric function only gives the diagonal in reciprocal space, but, as we will see, it is sufficient for the present purpose.

Although the model is very simple, its use requires care. First, the "average density" should not be the average density of all electrons, but only of those valence electrons that participate to the screening. This difference is well defined in a simple semiconductor such as silicon, but less obvious in materials like AgCl with electrons of different character in the valence bands. Since the model screening depends strongly on the density, comparison of the model results with various choices for the valence density to an, even not fully converged, *ab initio* calculation in a few **q** points is sufficient to see that the screening is determined by the electrons in the 8 upper valence states, i.e. the Ag 4*d* and Cl 3*p* electrons. To include some of the remaining, more tightly bound, electrons in the average density would clearly lead to overscreening. We therefore use the model with an average density $\bar{n} = 0.056$ Bohr^{-3}. A second issue is the dielectric constant at $\mathbf{q} \to 0$, which is an important ingredient in the model, as we will explain in the following. In a fully non-empirical scheme, its value has to be obtained from the *ab initio* calculations.

9.2 Analysis of the model with silicon and silver chloride

Let us first examine some general properties of the static dielectric function. For this purpose, KS-LDA calculations were performed for a prototype semiconductor, bulk silicon. The finer the grid, the more wavevectors **q** are available at which the dielectric function can be computed since we require $\mathbf{q} = \mathbf{k} - \mathbf{k}'$. The calculations are done both including and excluding the commutator of the position operator $\hat{r}$ with the non-local part of the Hamiltonian [182]. This commutator affects only the calculation at $\mathbf{q} \to 0$ as it only appears in the calculation of the dipole matrix elements at $\mathbf{q} \to 0$. The origin of non-local part of the Hamiltonian can be the non-local part

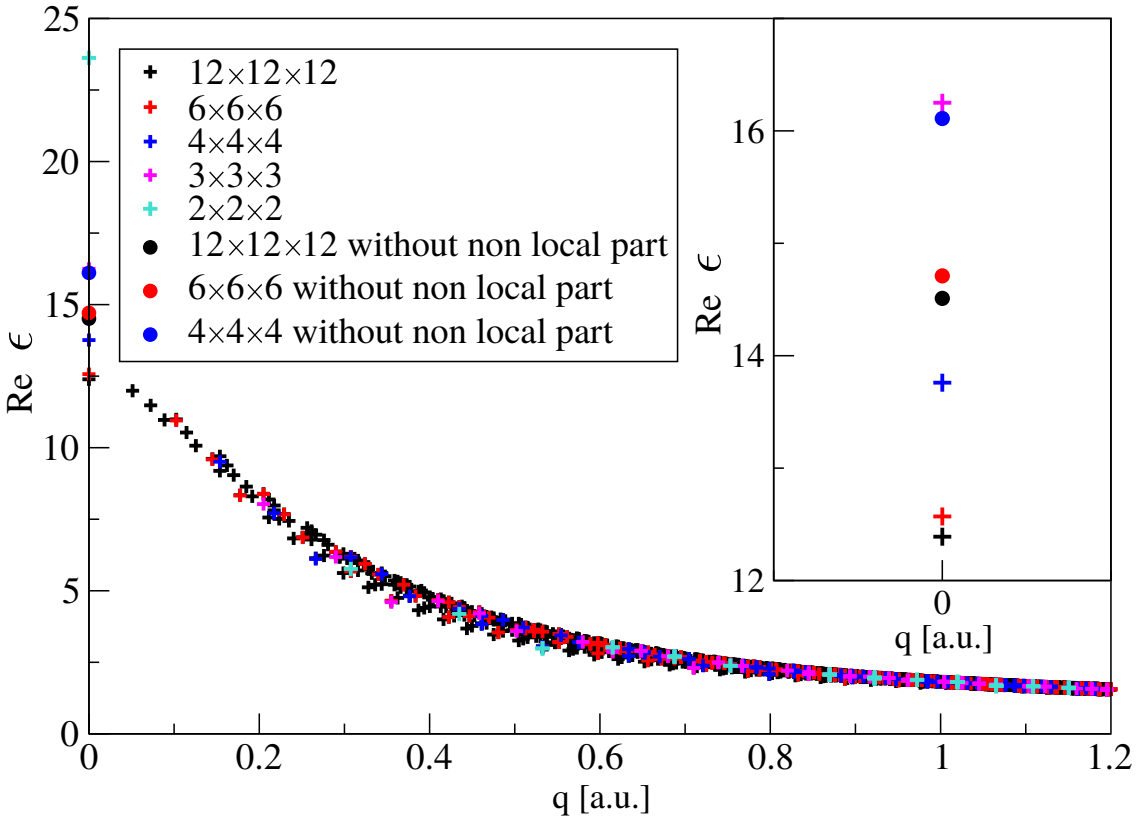

Figure 9.1: Bulk silicon: Static dielectric function as a function of wavevector $\mathbf{q}$, for different $\mathbf{k}$-point grid sizes. Plus (circle) symbols are results from calculations including (excluding) the commutator with the non-local pseudopotential. In the insert: zoom on $\mathbf{q} = 0$.

of the pseudopotential (this is the case here) or a non-local self-energy. Fig. 9.1 shows the static dielectric function of silicon as a function of $\mathbf{q}$.

At non-vanishing momentum one can see the anisotropy of the material, as the points are not aligned along a line, but several points coexist for the same momentum size. One can also see that the anisotropy is not large as the points are still distributed around the same curve with small deviation. The points for the coarse $\mathbf{k}$-point grids are already well converged. The situation is different for $\mathbf{q} \to 0$. First, even when the commutator is taken into account, the convergence is more difficult than at non-vanishing momentum. Moreover, when considering the calculations without commutator the dielectric function moves further away from the converged value and, as expected, the dielectric constant does not converge toward the correct value.

This difficulty of convergence at $q \to 0$ is explained by the fact that at $q \to 0$ the denominator of the dielectric function has a factor $(\Delta\varepsilon)^3$ whereas for $q \neq 0$ it has a factor $\Delta\varepsilon$, where $\Delta\varepsilon$ is the energy difference between the empty and occupied Kohn-Sham states. This enhances the dependence on the dispersion, thus a finer sampling of the Brillouin zone is required.

At $\mathbf{q} \to 0$, inclusion or exclusion of the commutator as well as the convergence of the dielectric constant are often not problematic in fully *ab initio* GW or BSE calculations. In these situations, the dielectric function enters integrals over the first Brillouin zone. In the limit of infinite number of k points (in practice, at convergence), the contribution from $\mathbf{q} \to 0$ is vanishing small. However, when the dielectric model is used with a wrong input for the dielectric constant at $\mathbf{q} \to 0$, the whole model dielectric function is wrong. This can be seen in Fig. 9.2. The left panel of Fig. 9.2 shows the static dielectric function for silver chloride computed *ab initio* (shown by black and red crosses) and the associated dielectric model (shown by black and red line, respectively). We see

that with a wrong dielectric constant (red crosses), the model dielectric function (shown by the red line) is not correct over a large range of wavevectors.

From these results it appears that the dielectric constant at $\mathbf{q} \to 0$, which is a crucial ingredient of the model, can be problematic. I have therefore searched for a way to avoid this complication. The idea is to rewrite the model using another wavevector $\mathbf{q}_0$ as input:

$$\epsilon(q) = 1 + \frac{1}{\frac{1}{\epsilon(q_0)-1} + \alpha\frac{(q^2-q_0^2)}{q_{TF}^2} + \frac{q^4-(q_0)^4}{4\omega_p}}, \tag{9.2}$$

where $\epsilon(q_0)$ is the dielectric function at the wavevector q_0. The choice of the q_0 where the model parameter should be determined is constrained: for larger q, and taking into account crystal local field effects, the local anisotropy of the crystal induces a scattering around the function $\epsilon(q)$ and therefore some arbitrariness. One therefore has to choose a value q_0 that is small enough to yield a well defined $\epsilon(q_0)$, and large enough to converge fast with the **k**-point grid. In any case, for any $q_0 \neq 0$, the problem of the commutator is avoided.

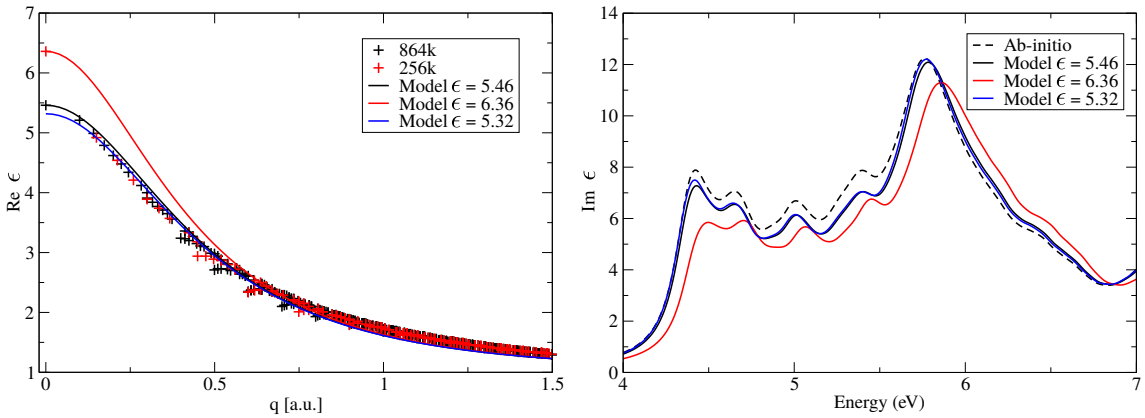

Figure 9.2: Silver chloride, effects of the model electron-hole screening on BSE results. Left panel: *ab initio* LDA-RPA (crosses) and model (solid lines) dielectric constants $\epsilon(\mathbf{q}, \omega = 0)$ as a function of $\mathbf{q}$. The *ab initio* results are obtained using 4-shifted $4\times4\times4$ (red) or $6\times6\times6$ (black) Monkhorst-Pack grids of $\mathbf{k}$ points, corresponding to 256 or 864 $\mathbf{k}$ points in the full Brillouin zone, respectively. The black cross at $q \to 0$ also contains the correction for the non-local pseudopotential, while the red cross does not. Model results are fitted to the *ab initio* results at $q = 0$ (respective color code) or at $q = 0.15$ a.u. (blue), where results on the smaller grid are already converged. Right panel: BSE spectra obtained with 864 shifted **k**-points, 8 valence and 6 conduction bands. The screening of the electron-hole interaction is taken from the results shown in the left panel: either the diagonal of the *ab initio* screened Coulomb interaction (dashed black), or the model screening fitted to the 864 **k**-points result at $q = 0$ (solid black), or to the 256 **k**-points result at $q = 0$ (red) or at $q = 0.15$ a.u. (blue).

This approach, as we will show subsequently, is very powerful to converge optical spectra calculated from the BSE. As a byproduct, once the model parameters are determined this allows one also to extrapolate the dielectric constant at $q \to 0$. This is demonstrated in the left panel of Fig. 9.2: the model dielectric function obtained from the fit to the *coarse* first-principles calculation at $q_0 = 0.15$ a.u. (blue curve) compares very well to the one fitted to the best first-principles calculation at $q = 0$ (black curve); from the fit at $q_0 = 0.15$ a.u. to the *unconverged* calculation, one can read an RPA dielectric constant $\epsilon(q \to 0) = 5.32$, which compares well with the converged *ab initio* result $\epsilon(q \to 0) = 5.46$, and which is much better than the result $\epsilon(q \to 0) = 6.36$ of the unconverged *ab initio* calculation itself.

The right panel of Fig. 9.2 shows the absorption spectra computed within G_0W_0+BSE using as screening the different models obtained in the left panel of the figure as well as the converged full *ab initio* screening. The calculation is done on a 864 shifted **k**-point grid. We can see that the

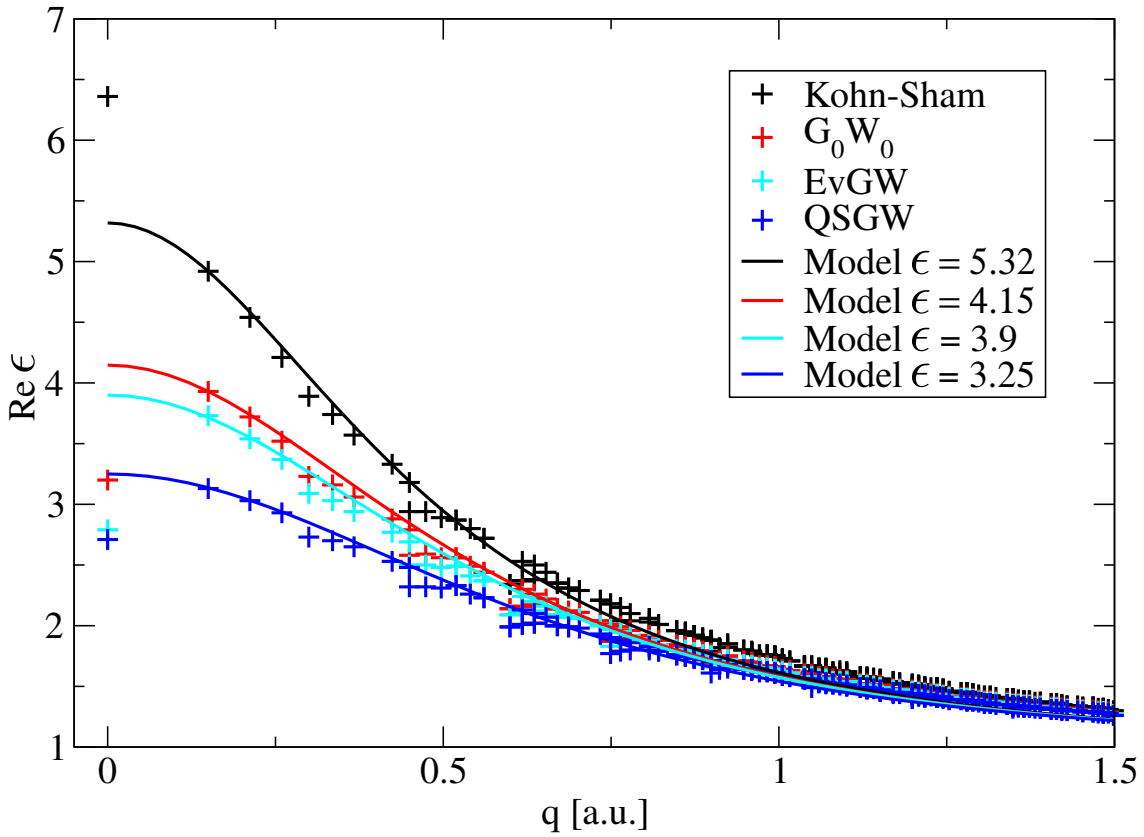

Figure 9.3: Silver chloride: static dielectric constant as function of momentum transfer calculated using different levels of theory: Kohn-Sham LDA, G^0W^0, evQSGW and QSGW. All calculations are done using a 4-times shifted $4 \times 4 \times 4$ Monkhorst-Pack **k**-point grid and 340 bands. The commutator with the non-local potentials (pseudopotential and self-energy, when applicable) is neglected. The fit of the model results at $\mathbf{q}_0$=(-0.125,-0.125,0) in units of the reciprocal lattice (q_0 =0.15 a.u.) yields the dielectric constants.

model fitted to the dielectric constant of the unconverged dielectric function (red line) performs poorly with respect to the *ab initio* screening (dashed line), giving incorrect intensity and position for the different peaks, whereas the model from the converged dielectric function (black line) is close to the results using the *ab initio* screening. The modified model fitted at $q_0 = 0.15$ a.u. gives an absorption close to the model from the correct dielectric function.

This shows that the model fitted at $q_0 \neq 0$ can be used to extrapolated the correct dielectric constant at $q \to 0$ with significantly reduced computational effort, and it confirms the efficiency of the model fitted at $q_0 \neq 0$ in the context of BSE calculations.

9.3 The dielectric function in the different approximation

In this study the converged RPA dielectric constant is found to be 5.46, larger than the experimental value, which is found to lie between 3.7 [183] and 3.97 [184]. Other calculations based on KS-LDA [71] also find too large dielectric constants, similar to ours. This may be traced back to the Kohn-Sham band gap, whose influence on the dielectric constant is in the RPA not compensated by f_{xc}. However, for consistency we use the RPA value in order to simulate the RPA screening. Since over-screening leads to underestimation of the excitonic effects, we have calculated the dielectric function also using G^0W^0, evQSGW and QSGW results as input for the RPA. Results are shown in Fig. 9.3. As expected, the strongest screening is obtained in the KS-RPA, the same result as

presented in Fig. 9.2. Self-energy corrections to the eigenvalues calculated in G_0W_0 open the gap and lower the screening, with an effect that is particularly visible at smaller wavevectors. Self-consistency on the eigenvalues further opens the gap and lowers the screening, again with a stronger effect at smaller wavevectors. Self-consistency in the wavefunctions in QSGW enhances the trend, with an effect that is significant at small q, but almost negligible above $q \approx 1$ a.u. These *ab initio* results have been obtained using a 4-times shifted $4\times4\times4$ grid, neglecting the commutator with the non-local pseudopotential and, in the case of the GW calculations, neglecting the commutator with the non-local self-energy. As a result, while the differences between the various approximations are significant but reasonable and smooth for $q \neq 0$, the same does not hold for $q \to 0$. In particular, the results are visibly discontinuous as a function of q and the dielectric constant at $\mathbf{q} \to 0$ is clearly too small when GW ingredients are used. The error due to the neglect of the commutator with the non-local self-energy is sizeable, and of opposite sign with respect to the pseudopotential contribution. We therefore determine the screening at $q_0 = 0.15$ a.u., and then use Eq. (9.2) to obtain the full $\epsilon(q)$. This allows us to extrapolate the dielectric constants at vanishing wavevector. As stated previously, we obtain $\epsilon(q \to 0) = 5.32$ in Kohn-Sham, and we find 4.15 in G_0W_0-RPA, 3.9 in evQSGW-RPA, and 3.25 in QSGW-RPA, respectively. The GW results are therefore closer to the experimental range of 3.7-3.97 than the Kohn-Sham ones, and the help of the model in avoiding the calculation of the commutators is particularly welcome.

The results for the dielectric constant, together with the EELS results in the previous chapter, illustrate the limits of comparisons to experiment and of choosing the more appropriate level of theory: besides the experimental uncertainties due to the limited resolution, temperature, etc, different aspects of the dielectric function are highlighted by different experiments. Each comparison on its own is often rather qualitative, and more insight can be gained by combining the different approaches. In particular, whereas the EELS spectra clearly show the positions of the dominant collective excitations, the normalization issues prevent us from getting clear information about intensities. The dielectric constant, on the other hand, should be a quite reliable way to quantify whether a given theoretical approach tend to under- or overscreen.

In conclusion, by using a previously proposed model for the wavevector-dependent dielectric constant in a modified way, we have obtained a very efficient approach to simulate the fully *ab initio* screening. This allows us to perform reliable BSE calculations in an affordable way, which we will use in the following chapter to analyze excitons in AgCl.

Chapter 10

Excitons in silver chloride

With the model approach developed in Ch. 9, we have now the necessary tools to perform a BSE calculation at the required level, including self-consistency in QSGW. The calculations use 6912 shifted **k**-points, 8 valence bands and 6 conduction bands. A G^0W^0-based calculation with the same parameters is also realized for comparison.

The aim of this chapter is to present reliable BSE calculations of silver chloride, in order to establish the importance of the electron-hole interaction, to elucidate the nature of the excitons and to discuss the correlation between electron and hole.

10.1 Excitonic effects: role of the screening and comparison to experiment

Calculations with different flavors of GW are realized within RPA and BSE. All spectra are calculated with LDA wavefunctions. Fig. 10.1 shows the obtained absorption spectra. G_0W_0+BSE and QSGW+BSE spectra differ for two reasons. First, they contain a different scissor correction: 1.9 eV or 3.0 eV to simulate the G_0W_0 or QSGW band gap opening, respectively. Second, the model screening Eq. (9.1) is evaluated with the values extrapoleted to $\mathbf{q} \to 0$ with the help of the model, namely, $\epsilon(\mathbf{q} \to 0) = 5.32$ or $\epsilon(\mathbf{q} \to 0) = 3.25$ for the G_0W_0+BSE and QSGW+BSE spectra, respectively. The energy of the first exciton peak (solid lines) moves from 4.4 eV in G_0W_0+BSE to 5.25 eV in QSGW+BSE. By comparing the BSE spectra with the corresponding RPA results (dashed lines), we find that the reduced screening in QSGW+BSE crucially enhances excitonic effects with respect to G_0W_0+BSE. The exciton binding energy for the first peak is 0.21 eV within G_0W_0+BSE and becomes 0.43 eV within QSGW+BSE. The larger redshift of the QSGW+BSE spectra partially compensates the larger scissor correction in the QSGW-RPA result with respect to G_0W_0-RPA. Most importantly, the oscillator strength of the excitonic peak is greatly increased.

Our final results for the extinction coefficient are shown in Fig. 10.2. The combined use of the converged **k**-point grid and QSGW ingredients, which was made possible thanks to the model screening, improves remarkably the comparison with experiment (red line) with respect to the G_0W_0+BSE spectra (black line) in Fig. 8.11. The QSGW+BSE results (blue line) reproduce the first sharp excitonic peak and place it at 5.3 eV, very close to the experimental peak at 5.1 eV.

Also the second prominent structure that is visible in the experiment around 6.3 eV is found in the calculations, at 6.6 eV and 5.95 eV for QSGW+BSE and G^0W^0+BSE, respectively. The intensity of the calculated spectrum is higher than the measured one. This could be due, at least partially, to experimental uncertainties. Also the fact that here we use the LDA wavefunctions to build the spectrum may lead to an overestimation of intensities, as has been shown in [185]. Another cause may be the scissor used, which is correct at low energy but is not as good at higher energies.

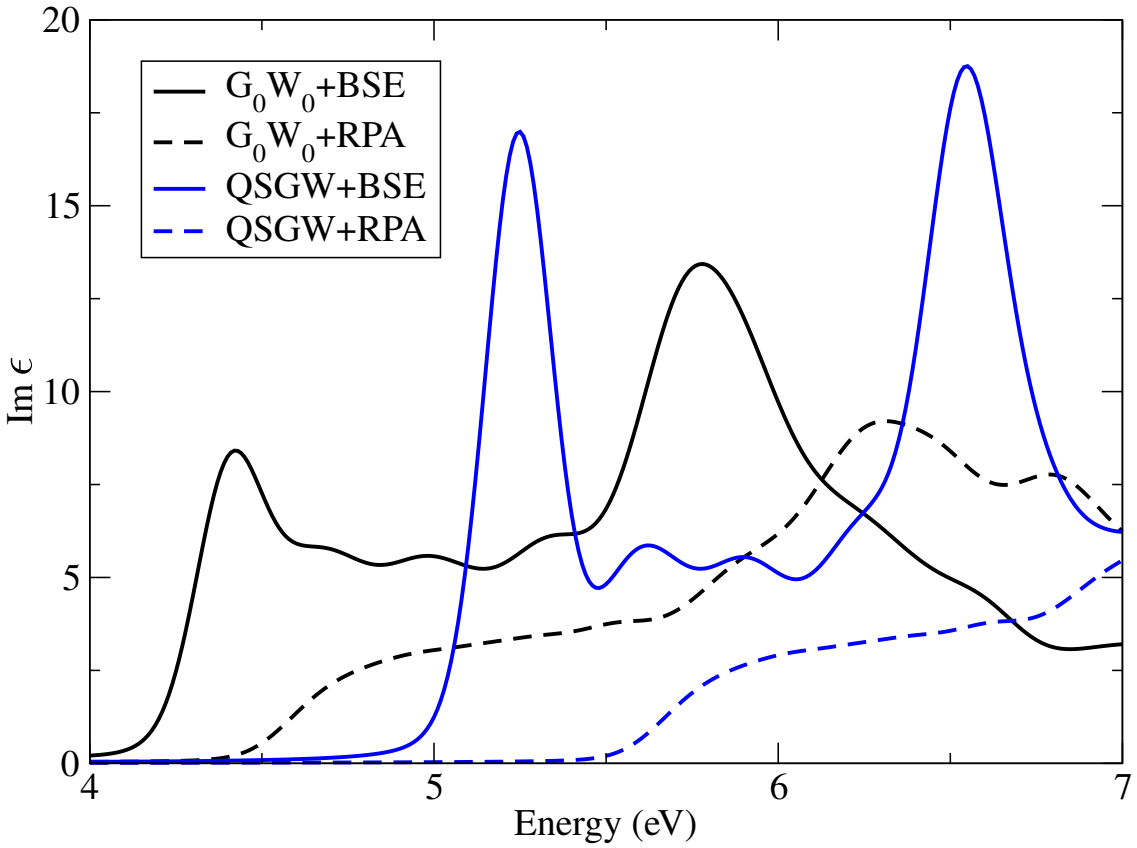

Figure 10.1: Absorption spectra of AgCl calculated in the RPA (dashed lines) and from the BSE (solid lines), using scissor corrections and model screenings obtained from G_0W_0 (black lines) or QSGW (blue lines).

10.2 Analysis of the exciton

In order to go beyond the information given by the absorption spectra alone and analyze the exciton character in more detail, the diagonalization of the excitonic hamiltonian (see Eq. (6.25)) is required. This is a much heavier task than to use the Haydock algorithm to get the absorption spectra. The parameters of the calculation have to be lowered in order for it to be achievable. Moreover, it is not reasonable to use a non symmetric **k**-point grid as this would break the symmetry of the Hamiltonian. This is not a problem for the macroscopic dielectric function calculation, where it instead allows for a better convergence. By the way of contrast, for the analysis of the exciton, spacial properties of the exciton are examined and it is important to maintain the symmetry of the Hamiltonian. The calculation is realized with a four-times shifted $6 \times 6 \times 6$ Monkhorst-Pack **k**-point grid, 8 occupied bands and 6 unoccupied bands.

First, thanks to the eigenvalues obtained by the diagonalization, the origin of the exciton peaks in the spectra can be identified. The sharp peak at the onset of the spectrum is due to a three-fold degenerate exciton state, hereafter referred to as bright exciton. However, this is not the lowest eigenvalue of the Hamiltonian. A two-fold degenerate exciton state is present roughly 50 meV below the bright exciton. This exciton is not visible in the spectrum and is thus a dark exciton.

It is then possible to analyse the composition of these excitons in terms of coefficients A^t_λ (see Ch. 6)that mix the vertical transition t between valence and conduction bands. In the following we refer to the G^0W^0 +BSE calculation, but similar conclusions are obtained from QSGW+BSE.

We find that the transitions contributing the most for all excitons take place between the top most valence band and bottom conduction bands. The independent-particle transition (at

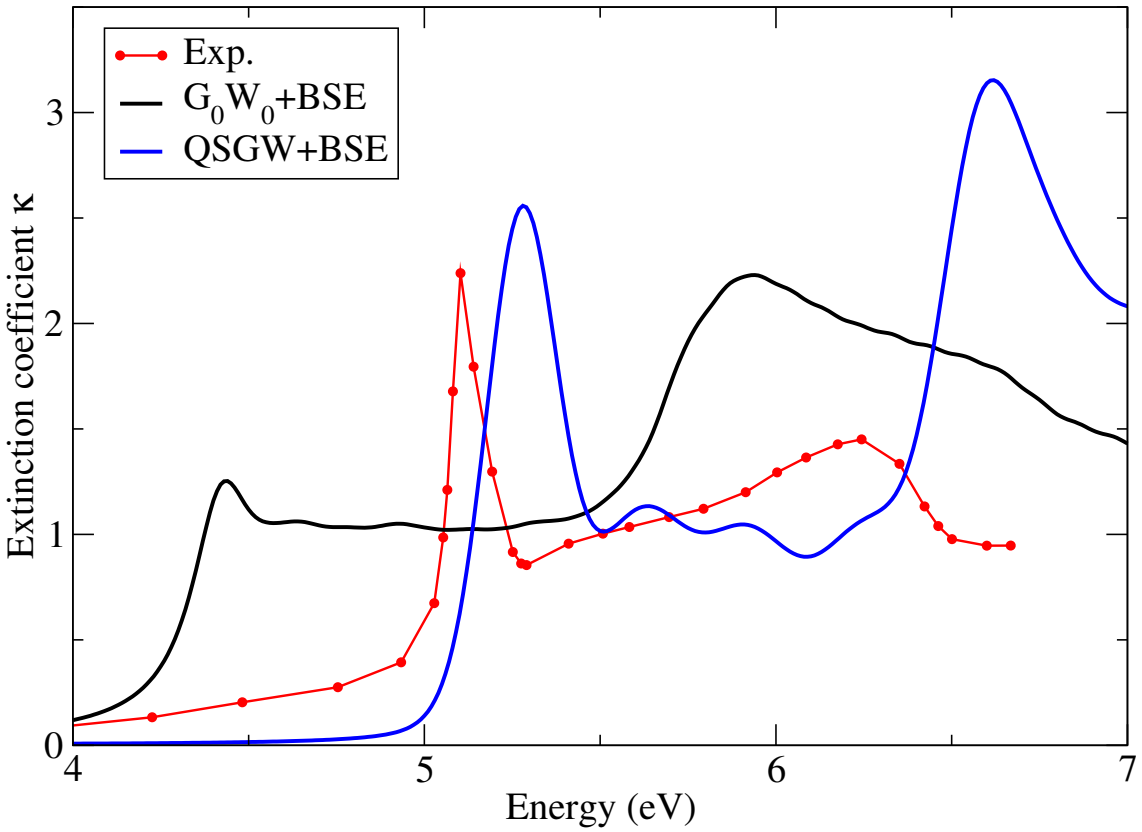

Figure 10.2: Extinction coefficient of AgCl: comparison between experimental results[51], and G_0W_0+BSE and QSGW+BSE calculations.

E=4.68 eV) with the strongest weight is at the $\mathbf{k}$ point in the line ΓK at 2/9 of the distance from Γ. The transition (with E=4.75) is between at the $\mathbf{k}$ points at 1/6 of the line ΓX. At a slightly larger energy is the transition at Γ. A first difference between the bright and dark exciton appears here: the bright excitons have contributions from the Γ point while the dark excitons do not. All the $\mathbf{k}$ points that contribute the most lie close to the minimum direct gaps in the band structure. In this region, around the Γ point, the valence and conduction bands are almost parallel, which means that many transitions of similar energy can mix and favour strong excitonic effects [186, 187].

The red curves in Fig 10.3 show the cumulant sums $\mathcal{I}(t_{\max})$ (see Eq. (6.33)) for the first excitons. The vertical bars, called weights, are the $\left|\bar{A}^{\lambda}\tilde{\rho}^{t}\right|$ plotted as a function of the transition energies E_t. Due to the absolute values, the weights do not distinguish bright and dark excitons. The intensity in the spectrum is instead the result of interference effects between the different transitions, which is expressed by the fact that both $\bar{A}^{t}_{\lambda}$ and $\tilde{\rho}_t$ are complex numbers. This effect can be analyzed studying the cumulant sums. Indeed, when $t_{\max} \to \infty$ the cumulant gives the total intensity of the oscillator strength of the exciton. For the two dark excitons, the order of magnitude of the cumulant is 10^{-9},i.e. numerically zero, whereas for the bright excitons it is 0.01. For the dark excitons the cumulant is always numerically zero. For the bright excitons all transitions give a positive contribution to the sum, as a result of constructive interference. The first transition contributes a fraction of the total oscillator strength, but transitions up to high energy contribute to the oscillator strength.

The detailed investigation of the $\bar{A}_{\lambda}$ shows that, for the dark excitons, the coefficients at $\mathbf{k} \neq 0$ are even functions of $\mathbf{k}$: $\bar{A}_{\lambda}(\mathbf{k}) = \bar{A}_{\lambda}(-\mathbf{k})$, while for the bright excitons they are odd: $\bar{A}_{\lambda}(\mathbf{k}) = -\bar{A}_{\lambda}(-\mathbf{k})$. Since for the same transitions the oscillator strengths are also odd: $\tilde{\rho}(\mathbf{k}) = -\tilde{\rho}(-\mathbf{k})$, the products $\bar{A}_{\lambda}(\mathbf{k})\tilde{\rho}(\mathbf{k})$ interfere constructively for the bright excitons and destructively for the

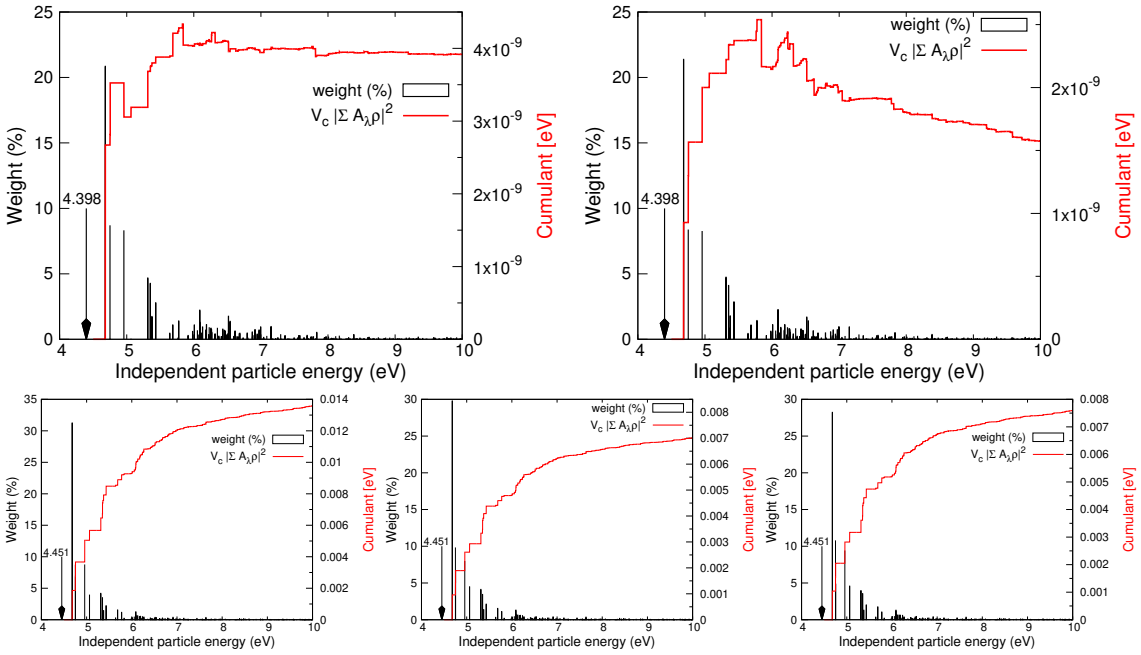

Figure 10.3: Weight (black bars) and cumulant sum (red line) of the intensity of the two dark (top line) and three bright excitons (bottom line). The energy of the exciton is indicated by an arrow.

dark excitons. This different mixing of formerly independent transitions is a typical manifestation of the many-body excitonic effects.

We can further contrast the character of the dark and bright excitons by examining their electron-hole correlation function $\Psi_\lambda(\mathbf{r}_h, \mathbf{r}_e)$. Fixing the hole at position $\mathbf{r}_h$, its square modulus gives the electron probability distribution in the electron-hole pair (in each case we take the sum over the degenerate states λ). The electron-hole interaction correlates the position of the hole and the electron, it is thus necessary to compare different positions for the hole. Since the top-valence band has a mixed Ag $4d$ - Cl $3p$ character, two different locations for the hole are considered: close to the Ag or close to the Cl sites. In order to avoid the nodes of the valence wavefunctions, the hole position is slightly shifted away from the atomic sites. Therefore the electron density plots do not have the cubic symmetry of the crystal. The corresponding electron distributions are displayed in Figs. 10.4 and 10.5 in the color contour plots that represent a cut in the [101] plane of AgCl passing through the atoms: the upper panels are for the hole located close to Ag atoms and the bottom panels for the hole close to the Cl atoms; the left panels correspond to calculation using W in the RPA (W-RPA), while the right panels to the calculation using W in the QSGW approach (W-QSGW). The first figure shows the sum of the electron distribution for the two degenerate dark excitons and the second one the sum of the three degenerate bright excitons. The saturation intensity is the same in each column but it is 1.8 time larger for the dark than for the bright exciton.

The spatial distributions obtained from W-RPA and W-QSGW are qualitatively similar. However, the W-QSGW calculation significantly increases the electron density close to the hole, consistently with the fact that the self-consistent screening leads to a stronger electron-hole interaction.

The analysis of these plots reveals several aspects of the excitons. In both the dark and bright excitons, the intensity is stronger when the hole is placed close to silver than when it is placed close to chlorine. This difference is more evident for the dark exciton than for the bright one. More importantly, the bright exciton is more delocalized than the dark exciton, whose envelop has a spatial extension that is smaller than 2 unit cells. In the bright exciton, when the hole is placed close to a Ag site, there is some intensity around silver atoms, but the electron density is mainly localized around chlorine atoms; when the hole is instead placed close to a Cl site, the

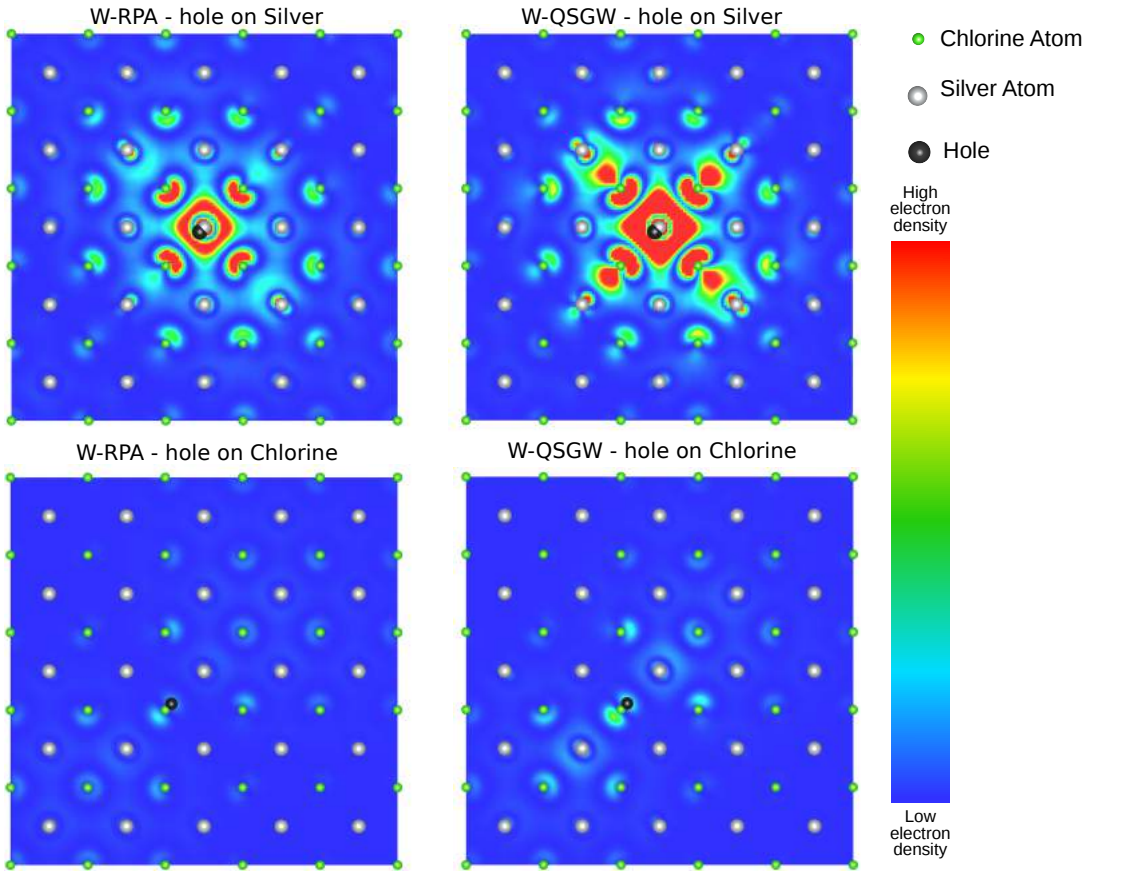

Figure 10.4: Electron density distribution for the two degenerate lowest-energy dark excitons. Cuts along the [101] plane of for W RPA (left panels) and W QSGW (right panels). The hole has been placed close to the Ag atom (top panels) and close to the Cl atom (bottom panels). Cl (Ag) atoms are represented by green (grey) balls, while the hole position is black.

electron density is again mostly localized around chlorine atoms. It is interesting here to make a comparison with LiF, which has the same crystal structure as AgCl. Since LiF is a wide-gap insulator, one would expect a tightly bound electron-hole pair with the hole located at F sites and the electron at neighboring Li sites. BSE calculations [127, 188, 189] instead have shown that the electron charge is always localized on F atoms (and only weakly on Li atoms). In other words, the role of Cl in the exciton of AgCl is analogous to F in LiF.

As can be seen in Fig.10.4 and Fig.10.5, the bright exciton with a hole close to chlorine and the dark exciton with hole close to silver have a spherical shape, whereas the other two cases present an elongated shape. An explanation for the difference between these pictures can be drawn from the dominant single-particle transitions that give rise to each exciton. We distinguish the two possible hole locations: When the hole is situated at a silver atom, the dark exciton is formed by the dipole-forbidden transition Ag $3d \rightarrow 4s$, yielding a spherical shape to the electron distribution; instead, the bright exciton, thanks to the Cl-Ag hybridization of the valence band, has the character of a dipole-allowed transition Ag $d \rightarrow$ Cl p, giving rise to an axial electron distribution. When the hole is located at a chlorine atom, the dark exciton has the character of the dipole-forbidden transition Cl $3p \rightarrow$ Cl $3p$ and the corresponding electron distribution has an axial distribution; instead, the character of the bright exciton is the dipole-allowed Cl $3p \rightarrow$ Cl $4s$, which is possible thanks to the fact that the Cl $4s$ contribute to the conduction band (see Fig. 8.5) around the Γ point where the exciton is formed. This results again in a spherical shape of the electron distribution.

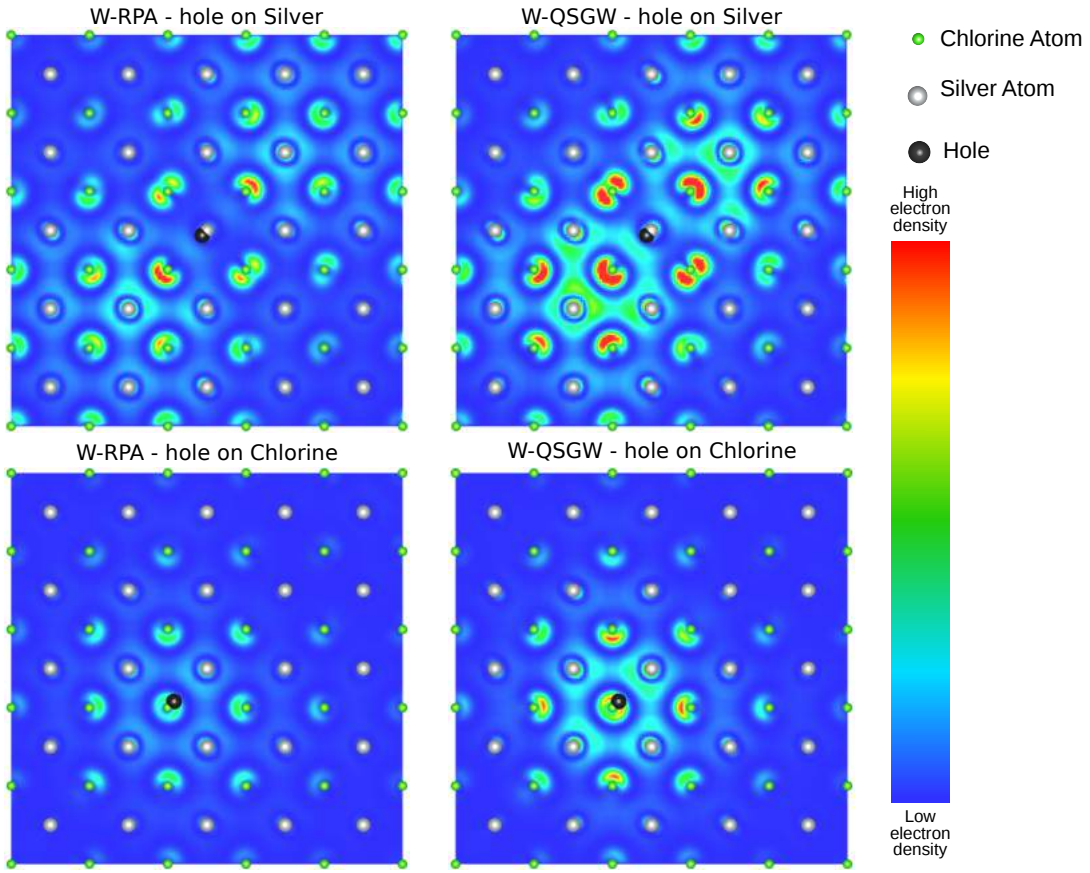

Figure 10.5: Same as the previous figure for the three degenerate bright excitons.

10.3 Summary

Our Bethe-Salpeter calculations have shown the existence of bound excitons in AgCl with significant binding energy. When these calculations are performed on top of a QSGW band structure and screening calculation, the onset of optical absorption is found close to the experimental results.

The analysis of the excitons reveals the presence of a two-fold degenerate dark exciton at lower energy than the bright exciton, which is itself three-fold degenerate. A more detailed analysis shows that the bright and dark excitons are composed of similar transitions, close to the gap. However for the bright exciton, non negligible contributions come from high energy transitions. The dark and bright excitons differ one from another, by the behavior of their mixing coefficients under inversion: these coefficients are odd for the bright exciton and even for the dark exciton. The correlation function gives precious insight into the nature of the exciton showing in particular the preference of the electron to localize on chlorine in the bright exciton, independently of the position of the hole. However, it is not obvious to deduce from the information to what extent, and how, the exciton will influence the response of the material to an external perturbation. This is a question that has not been addressed in an *ab initio* framework in the literature so far, and it will be the topic of the next chapter.

Chapter 11

Linear density response

The linear density-density response function of materials has been a topic of intense studies for decades. In particular, the calculation from first principles of optical absorption spectra including the effects of the electron-hole interaction, the excitonic effects, has seen much progress over the last 30 years. However, much less studies are devoted to the consequences of the response of a material to a perturbation, namely, the charge dynamics induced by a perturbation. An important reason lies in the fact that such a study requires a description of the response on a microscopic level, which was up to recently not possible when excitonic effects were to be included. One of the main aims of the present thesis is to fill this gap.

This chapter is then dedicated to the study of charge dynamics in linear response. On the methodological side, we will discuss how various ingredients combine to give the final results. Since little is known, we will also dedicate some space to the convergence requirements of the calculations, and elucidate what is important. We will use the results to shine new light on the physics of the induced charge dynamics and in particular, on the effects of the electron-hole interaction. Of major interest will be the question of how to design a perturbation in order to be able to observe an exciton in real space and time. Beside excitonic effects, other important questions concern the role of the long-range Coulomb interaction.

11.1 Formalism

When an external perturbation is applied to a system, the latter will be excited, going from its original ground state to an excited state. In a one particle picture this means that electrons will make a transition from their valence state to a conduction state, but of course, here we will work in a many-body framework, and transitions will take place between many-body states. In any case, on the level of the electrons the transitions are characterized by a rearrangement of the charge: this change the charge density of the system: this is called the induced density. If the perturbation is periodic the system will start to oscillate between the ground and excited states, while for a sudden perturbation the system will eventually decay back to equilibrium.

We will study the induced density with different perturbations, considering silver chloride as main target. At first, we present the equations necessary to define and compute the induced density. In the second section, the effect of the perturbation is discussed. In the remaining sections the induced density computed with different polarizabilities is studied.

In linear response, the induced density δn is given by

$$\delta n(\mathbf{r},t) = \iint \chi(\mathbf{r},\mathbf{r}',t-t')V^{\text{ext}}(\mathbf{r}',t')d\mathbf{r}'dt', \tag{11.1}$$

where χ is the polarizability of the system and V^{ext} is the external potential applied to the system. We work in the linear response framework throughout this thesis.

For a periodic system, Eq. (11.1) can be written in reciprocal space

$$\delta n_{\mathbf{G}}(\mathbf{q},\omega) = \sum_{G'} \chi_{\mathbf{G}\mathbf{G}'}(\mathbf{q},\omega)V^{\text{ext}}_{\mathbf{G}'}(\mathbf{q},\omega). \tag{11.2}$$

Fourier transforming back to real space, we get the induced density (in real space-time) as a function of the polarizability in reciprocal space (and frequency domain):

$$\delta n(\mathbf{r},t) = \int d\mathbf{q} \int_{-\infty}^{+\infty} d\omega \sum_{\mathbf{G},\mathbf{G}'} e^{i((\mathbf{q}+\mathbf{G})\cdot\mathbf{r}-\omega t)} \chi_{\mathbf{G}\mathbf{G}'}(\mathbf{q},\omega) V^{\text{ext}}_{\mathbf{G}'}(\mathbf{q},\omega). \tag{11.3}$$

Eq 11.1 is real in real space and time whereas $\chi_{\mathbf{G}\mathbf{G}'}(\mathbf{q},\omega)$ is complex (see later). The sums run over all reciprocal lattice vectors.

In real space and time, the external potential is also real and, by using these two properties, the integration on the reciprocal space-frequency hyperspace can be simplified in two different ways (see appendix B):

$$\delta n(\mathbf{r},t) = 2\text{Re}\left(\int_{-\infty}^{+\infty} d\omega \int_{\mathbf{q}_+} d\mathbf{q} \sum_{\mathbf{G},\mathbf{G}'} e^{i((\mathbf{q}+\mathbf{G})\cdot\mathbf{r}-\omega t)} \chi_{\mathbf{G}\mathbf{G}'}(\mathbf{q},\omega) V^{\text{ext}}_{\mathbf{G}'}(\mathbf{q},\omega) \right) \tag{11.4}$$

$$= 2\text{Re}\left(\int d\mathbf{q} \int_{0}^{+\infty} d\omega \sum_{\mathbf{G},\mathbf{G}'} e^{i((\mathbf{q}+\mathbf{G})\cdot\mathbf{r}-\omega t)} \chi_{\mathbf{G}\mathbf{G}'}(\mathbf{q},\omega) V^{\text{ext}}_{\mathbf{G}'}(\mathbf{q},\omega) \right). \tag{11.5}$$

Expression 11.5 is the one that have been coded in this thesis (see Appenix B), ant that is used in the calculations. In order to better understand the underlying physics, it is also useful to see how the ingredients of the polarizability enter in the construction of the induced density. This will be particularly convenient to study the role of the transitions, of the broadening and of the level of approximation we choose for the polarizability. Starting from the exact expression for χ (Eq 5.3), a general expression for χ is

$$\chi_{\mathbf{G}\mathbf{G}'}(\mathbf{q},\omega) = \sum_{\lambda} \frac{A_{\mathbf{G},\lambda}(\mathbf{q}) B^{*}_{\mathbf{G}',\lambda}(\mathbf{q})}{\omega - E^{\lambda} + i\eta}. \tag{11.6}$$

For example in the case of the independent-particle polarizability $A_{G,\lambda} = B_{G,\lambda} = \tilde{\rho}_G = \langle \phi_c | \, e^{-i(\boldsymbol{q}+\boldsymbol{G})\cdot\boldsymbol{r}} \, | \phi_v \rangle$, where λ stands for a transition $v\mathbf{k}-\mathbf{q} \rightarrow c\mathbf{k}$. We define the partial Fourier transform of $A_{\mathbf{G},\lambda}(\mathbf{q})$ as $A_\lambda(\mathbf{r},\mathbf{q}) \equiv \sum_G e^{i(\mathbf{q}+\mathbf{G})\mathbf{r}} A_{\mathbf{G},\lambda}(\mathbf{q})$ and similarly for B. This definition is convenient as in the independent-particle polarizability $A_\lambda(\mathbf{r},\mathbf{q}) = \phi^{*}_{ck}(r)\phi_{vk-q}(\mathbf{r})$. With this general expression, a formula for the induced density can be derived. Let us consider a real perturbation, periodic in time, with only one frequency ω_0: $V^{\text{ext}}_{\mathbf{G}'}(\omega,\mathbf{q}) = \delta(\omega-\omega_0) V^{\text{ext}}_{\mathbf{G}'}(q)$. Inserting this expression for the external potential[1]

$$\delta n(\mathbf{r},t) = 2\sum_{\lambda} Re\left(\int d\mathbf{q} \int_{0}^{+\infty} d\omega \sum_{\mathbf{G}} e^{i((\mathbf{q}+\mathbf{G})\cdot\mathbf{r}-\omega t)} \frac{A_{\mathbf{G},\lambda}(\mathbf{q})\delta(\omega-\omega_0)}{\omega - E^{\lambda} + i\eta} \sum_{\mathbf{G}'} B^{*}_{\mathbf{G}',\lambda}(\mathbf{q}) V^{\text{ext}}_{\mathbf{G}'}(\mathbf{q}) \right) \tag{11.7}$$

$$= 2\sum_{\lambda} Re\left(\int \sum_{\mathbf{G}} e^{i((\mathbf{q}+\mathbf{G})\cdot\mathbf{r}-\omega_0 t)} \frac{A_{\mathbf{G},\lambda}(\mathbf{q})}{\omega_0 - E^{\lambda} + i\eta} R^{*}_{\lambda}(\mathbf{q}) d\mathbf{q} \right) \tag{11.8}$$

$$= 2\sum_{\lambda} Re\left(\int \; e^{-i\omega_0 t} \frac{A_{\lambda}(\mathbf{r},\mathbf{q})}{\omega_0 - E^{\lambda} + i\eta} R^{*}_{\lambda}(\mathbf{q}) d\mathbf{q} \right), \tag{11.9}$$

with $R^{*}_{\lambda}(\mathbf{q}) \equiv \sum_{\mathbf{G}'} B^{*}_{\mathbf{G}',\lambda}(\mathbf{q}) V^{\text{ext}}_{\mathbf{G}'}(\mathbf{q})$, or, in real space:

$$R^{*}_{\lambda}(\mathbf{q}) = \int_{\Omega} d\mathbf{r} B^{*}_{\lambda}(\mathbf{r},\mathbf{q}) V^{\text{ext}}(\mathbf{r},\mathbf{q}). \tag{11.10}$$

[1] To be precise the full formula for the external potential would be $V^{\text{ext}}_{\mathbf{G}'}(\omega,\mathbf{q}) = \delta(\omega-\omega_0)V^{\text{ext}}_{\mathbf{G}'}(\mathbf{q}) + \delta(\omega+\omega_0){V^{\text{ext}}_{-\mathbf{G}'}}^{*}(-\mathbf{q})$ in order to keep the potential as a real quantitiy in real space. However, since the Fourier transform of the simplified formula 11.5 spans only over positive energies, we will use only the resonant part of the perturbation.

Finally taking the real part:

$$\delta n(\mathbf{r},t) = 2\int \sum_{\lambda} \left| \frac{A_\lambda(\mathbf{r},\mathbf{q})R^*_\lambda(\mathbf{q})}{\omega_0 - E^\lambda + i\eta} \right| \cos\left(\mathbf{q}.\mathbf{r} - \omega_0 t + \phi^\lambda_E(\omega_0) + \phi^\lambda_A(\mathbf{r}) + \phi^\lambda_R\right) d\mathbf{q}, \tag{11.11}$$

where ϕ^λ_E is the phase of $1/(\omega_0 - E_\lambda + i\eta)$. The phase of $A_\lambda(\mathbf{r},\mathbf{q})$ is $\mathbf{q}\cdot\mathbf{r} + \phi^\lambda_A(\mathbf{r})$, it has been split because by definition $A_\lambda(\mathbf{r},\mathbf{q})$ includes a phase $\mathbf{q}\cdot\mathbf{r}$. ϕ^λ_R is the phase of R^λ.

If the external potential has only one momentum $\mathbf{q}_0$, we have a plane-wave perturbation:

$$\delta n(\mathbf{r},t) = 2\sum_{\lambda} \left| \frac{A_\lambda(\mathbf{r},\mathbf{q}_0)B^*_\lambda(\mathbf{q}_0)}{\omega_0 - E^\lambda + i\eta} \right| \cos\left(\mathbf{q}_0.\mathbf{r} - \omega_0 t + \phi^\lambda_E(\omega_0) + \phi^\lambda_A(\mathbf{r}) + \phi^\lambda_R\right). \tag{11.12}$$

Instead, if the external potential is $\delta(\mathbf{r}-\mathbf{r}_0)$, we will have a perturbation localized in a specific place:

$$\delta n(\mathbf{r},t) = 2\int \sum_{\lambda} \left| \frac{A_\lambda(\mathbf{r},\mathbf{q})B^*_\lambda(\mathbf{r}_0,\mathbf{q})}{\omega_0 - E^\lambda + i\eta} \right| \cos\left(\mathbf{q}.\mathbf{r} - \omega_0 t + \phi^\lambda_E(\omega_0) + \phi^\lambda_A(\mathbf{r}) + \phi^\lambda_B(\mathbf{r}_0)\right) d\mathbf{q}. \tag{11.13}$$

In the following, these two perturbations (plane-wave or localized) will be used to study the density response of AgCl.

11.2 Discussion

Equation 11.11 is quite complex, but helpful to discuss the physics of the induced density.

To first get a sense of the physical process in this equation, let us start by discussing the terms inside the sum. Let us assume, at first, that there is only one transition in the sum and one $\mathbf{q} = \mathbf{q}_0$ in the integral. This simple case of one transition in the sum can be seen as an approximation in which we perturb the system with an energy close to one specific transition of the system that has no other transitions with close energy. All illustrations will be done using silver chloride. For simplification, we use the independent particle approximation (IPA), so $\chi \to \chi^0$. The discussion represents however also the interacting case, where the transitions are of more complex nature.

One transition

In Eq 11.11 each transition acts like an oscillator that is excited by the perturbation. The intensity of this oscillator is controlled by two terms: the first is the energy attenuation factor at the denominator $1/\sqrt{(\omega - E_\lambda)^2 + \eta^2}$: the more the energy of the perturbation is close to the energy of the transition, the easiest it is to excite the transition. In the extreme case where the perturbation energy tends to the energy of a transition $\omega \to E_\lambda$ this intensity seems to go to infinity, as η is supposed to be infinitesimal. Indeed for vanishing broadening, the intensity increases as $1/(|\omega - E_\lambda|)$ close to a transition. But we know that the lifetime of a perturbation is not infinite and thus the energy of the transition has a small imaginary part that prevents the factor from diverging. The second term is the spatial overlap term R_λ, i.e. the overlap between the wavefunction of the transition and the perturbation as one can see from Eq 11.10: the more the perturbation overlaps with a transition wavefunction, the more it can excite this transition. The spatial shape of the density induced by this oscillator is controlled by the $A_\lambda(r, q_0)$ term. In the IPA case, this is the product between the conduction state and the valence state of the transition at the position $\mathbf{r}$ in space. Finally the cosinus term controls the evolution in time of the oscillator: we see the typical factor of a plane wave meaning that the system oscillates with the frequency of the perturbation. An additional phase factor is present, causing the reaction of the material to be shifted in time with respect to the perturbation (in the case of a plane wave propagating between t=$-\infty$ and t=$+\infty$ the notion of retarded or advanced is not pertinent).

The perturbation fixes some parameters in the equation: namely ω_0 and indirectly, R_λ. It is interesting to understand the effect of these parameters on the induced density. R_λ is controlled

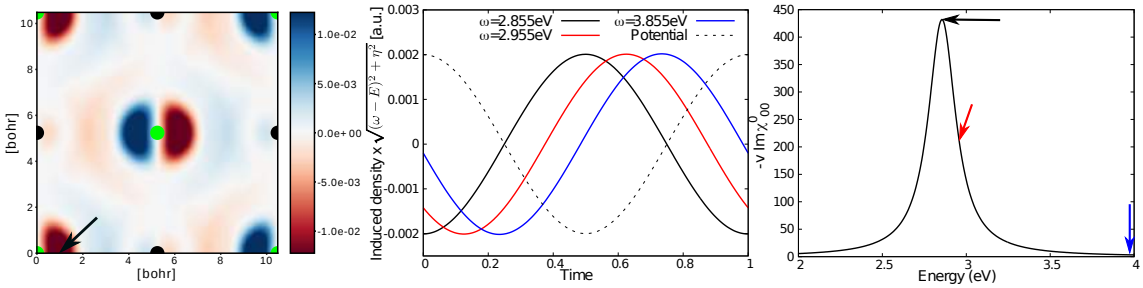

Figure 11.1: Response of silver chloride to a plane-wave perturbation in the independent particle approximation, and where only one threefold degenerate transition is taken into account. Left: Induced density represented in a 2D cut perpendicular to the direction [100] and in the plane of the atoms. Blue means an increase in the charge density while red means a decrease. The axis is taken such that a unit cell is shown. Atoms are represented by the colored disks: green for chlorine atoms and black for silver atoms. Center: Induced density at r=(0,1.055,0) [a.u.] (see arrow on the left plot) as a function of time. Time is normalized by the period of each perturbation. The perturbation (not at scale) is represented by the black dashed line. The different full curves show the density induced by perturbations with different energies. The induced density is multiplied by the factor $\sqrt{(\omega - E)^2 + \eta^2}$. Right: Minus the imaginary part of the inverse dielectric function as a function of the energy. This is proportional to the imaginary part of the first matrix element of the polarizability matrix, which is χ^0 in the IPA used here. The arrows indicate the energies at which the calculations presented in the middle plot were made.

by the spatial shape of the perturbation while ω_0 is the energy of the perturbation. R_λ will be described in a second part and we will first focus on the energy of the perturbation.

The energy of the perturbation is present in two terms: the phase of the cosinus and the denominator. A change of energy will thus have two effects: a change of the phase inside the cosinus through ϕ_E^λ and a change of the intensity though the denominator as discussed above. The first effect is equivalent to a shift in time, and changing the perturbation energy would just result in a shift in time of the induced density. In this simple case changing the energy of the perturbation will retard or advance the response of the system and modify the global intensity of the response. Here it should be noted that in this case the change of the transition energy or the broadening η have similar effects on the induced density.

The effect of the choice of the perturbation energy ω for a plane wave perturbation with wavevector $\mathbf{q}_0$ and frequency ω and adopting the IPA is illustrated in Figure 11.1. The system is silver chloride and the independent-particle polarizability matrix is computed with six transitions, three degenerate resonant transitions and the associated antiresonant transitions. The transitions are those coming from the $\mathbf{k} = \Gamma$ point between the three degenerate top valence bands and the bottom of the conduction band. Because of the degeneracy of the top valence bands we are forced to take three transitions (rather than one), but this does not alter the previous conclusion, for there is only one transition energy (and one broadening) involved. This can be understood by rewriting Eq 11.12,

$$\delta n(\mathbf{r}, t) = 2 \frac{\cos\left(\mathbf{q}_0.\mathbf{r} - \omega_0 t + \phi_E(\omega_0) + \phi(\mathbf{r})\right)}{|\omega_0 - E + i\eta|} \left| \sum_\lambda A_\lambda(\mathbf{r}, \mathbf{q}_0) B_\lambda^*(\mathbf{q}_0) \right|, \tag{11.14}$$

The terms $\phi_E^\lambda(\omega_0)$ and E_λ are the same for all transitions and can be factorized out. Where E is the energy of the transitions, ϕ_E the phase associated to the broadening, and where $\phi(\mathbf{r})$ is the phase associated to $\sum_\lambda A_\lambda(\mathbf{r}, \mathbf{q}_0) B_\lambda^\dagger(\mathbf{q}_0)$. As one can see, the sum of the degenerate transitions forms an effective transition.

But if this effective transition acts as one for its dependence with energy, this is not the case with regard to the perturbation shape, as for example a change of the shape of the perturbation

could lead to a modification of the shape of the induced density whereas this is not the case for a unique transition.

The momentum is taken as $\mathbf{q}_0$=(0,0.00012,0)[a.u.] in Cartesian coordinates. The polarizability matrix is computed at several energies between 2 eV and 4 eV. The broadening is set to 0.1 eV. To compute the induced density the number of **G**-vectors in the polarizability matrix is set to 893.

On the right panel we see the imaginary part of the inverse dielectric function as a function of the energy. In the IPA, it is proportional to Im χ. The peak generated by the transitions is visible at 2.85 eV. On the left panel we see the induced density perpendicular to the [100] direction and in the plane of the atoms. Since the result is time dependent, the picture is just a snapshot of a time-dependent density response evolution. The induced density is computed using Eq. (11.5). The external perturbation is a plane wave with energy $\omega_0 = 2.85$ eV .The color scale is given on the right side of the plot. Atoms are represented as full circle: chlorine atoms are green and silver atoms are black. We observe that the induced density is centered around atoms and has a recognizable shape. Indeed we can see the shape of a p state around chlorine atoms. We also note that there is little to no intensity around silver atoms.

As discussed in chapter 8.3, the top valence states at Γ have mostly a p state nature around chlorine while the bottom conduction state has mostly a s state nature around chlorine. This is in agreement with the density response picture, since the spatial shape is given by the product of the p and s wavefunctions (that gives essentially a p-like shape, seen that s is spherical), for the valence and conduction bands, respectively.

The center panel shows the evolution of the induced density as a function of the time. The induced density is taken at $\mathbf{r} = (0, 1.055, 0)$ [a.u.], shown by a red arrow on the left panel. The induced density is multiplied by the factor $\sqrt{(\omega - E)^2 + \eta^2}$ (where ω is the energy of the perturbation), in order to see all the induced densities at the same scale. The densities induced by different perturbations are plotted. They have different energies: 2.85 eV, 2.95 eV and 3.85 eV, respectively. These energies correspond to: i) the energy of the transition, ii) the energy of the perturbation plus 0.1 eV (same as the broadening) and iii) the energy of the perturbation plus 1 eV (ten times the broadening). These energies are indicated by arrows in the right panel. The dashed line represents the external potential (not to scale). Finally the time for each curve is divided by its period in order to be compared.

The induced density follows a sinusoide, mirroring the perturbation, with the predicted delay. At this point in space, the induced density is in phase opposition with the perturbative potential when the energy of the perturbation equals the transition energy. When increasing the energy of the perturbation the phase increases as well. These phases changes are in agreement with the theory: the phase of a transition due to the energy factor is given by

$$\phi_E(\omega) = -\arctan\left(\frac{\eta}{\omega - E}\right). \tag{11.15}$$

At $\omega - E$=0 the phase is $-\pi/2$, at $\omega - E = \eta$ the phase is $\pi/4$ and at $\omega - E = 1$ eV the phase is 0.1. The curves have the same amplitudes. This means that a change in the perturbation energy leads to a change in the induced density correctly described by the factor $\sqrt{(\omega - E)^2 + \eta^2}$.

In conclusion, in the case of a single transition (or multiple degenerate transitions) the change of the perturbation energy has the effect of changing the amplitude of the oscillations and the phase of these oscillations, as derived at the beginning of this subsection.

We will study later the effect of R^λ on the induced density.

Several transitions

In general, real materials give rise to more than one transition. One can wonder how these transitions will mix. The previous results are still valid at the level of each term, but they have to be summed as equation 11.11 shows. Each term has a different phase, global factor and spatial shape that will change the picture of the induced density when summed. Moreover each term will react differently to a change of the energy or shape of the perturbation.

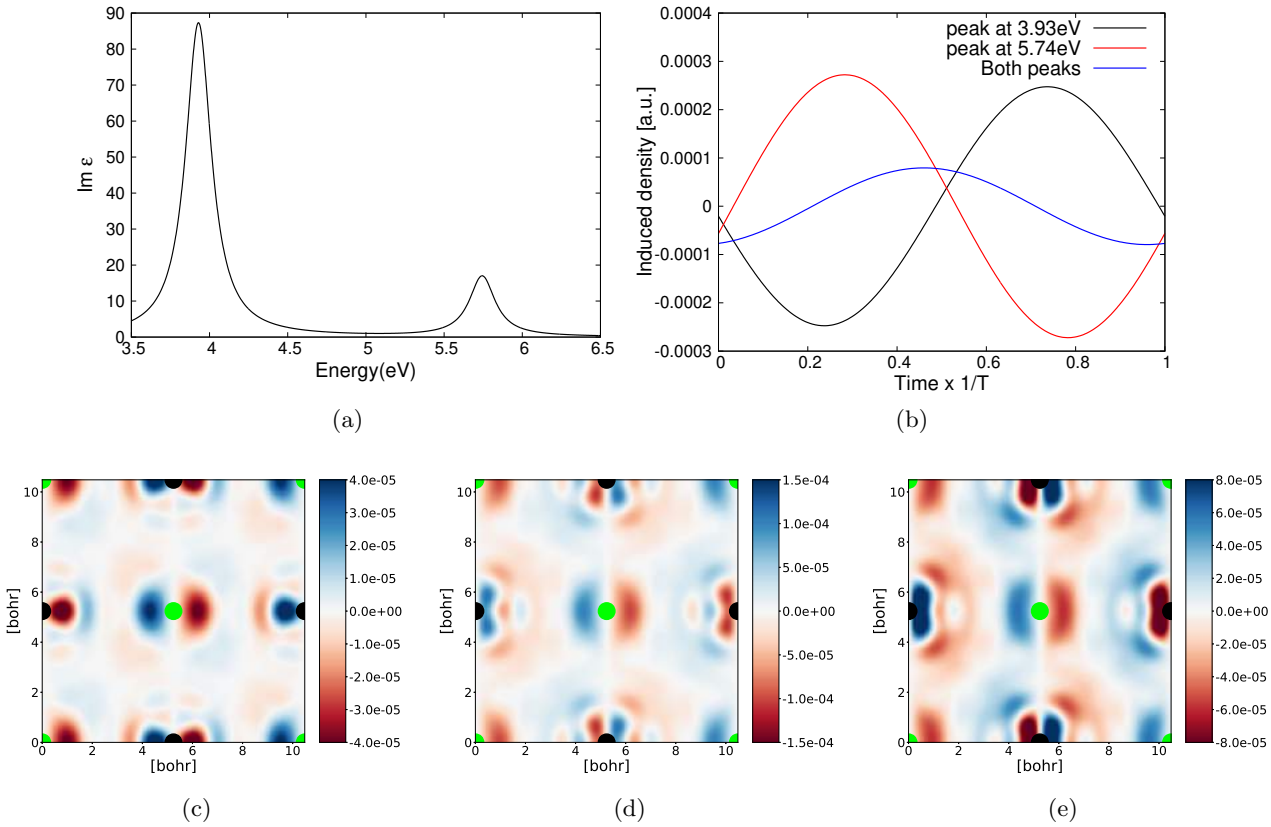

(a) (b)

(c) (d) (e)

Figure 11.2: Response of silver chloride to a plane wave perturbation in the independent particle approximation, taking into account two groups of degenerate transitions with energy 3.93 and 5.74 eV. (a) Imaginary part of the dielectric function as a function of the energy. (b) Induced density as a function of time. As in figure 11.1 the time is divided by the period T of the perturbation. The perturbation is a plane wave with energy 5.29 eV and momentum q=(0,0.00012,0)[a.u.]. The position at which the the density is shown is (5.7,0) bohr in the plane passing by the atoms and perpendicular to the direction [001]. The IPA polarizability used to get the induced density is computed with different parameters: only the transition at $\omega = 3.93$ eV, this is represented by the black curve, only the transition at $\omega = 5.74$ eV, this is represented by the red curve, and both transitions: this is represented by the blue curve. (c) 2D plot of the induced density for the calculation with only the low energy peak (black curve in (b)). (d) same as (c) but with the calculation with both transitions (blue curve). (e) same as (c) and (d) but taking into account only the high energy transition (red curve). For all snapshots, the time is taken at the maximum of the blue curve. The polarizability is calculated with the six $\mathbf{k} = L$ points in the Brillouin zone, with the three top valence bands (two of which are degenerate) and the bottom conduction band.

For a perturbation energy that lies between two transition energies (or, to be clear, in between two peaks in the spectrum), the response of the system will be the sum of each response. If ones changes the energy of the perturbation continuously, the induced density will move from the induced density associated to one peak to the density associated to the other. For a system with many transitions, the induced density will be a mix of lots of different transitions with close energies. However, transitions far from the energy of the perturbation can still have a visible impact if the density they induce is located at a point where no other transition induces density.

An example is shown on figure 11.2. Two different transition energies are included: 3.93 eV and 5.74 eV. The imaginary part of ϵ, shown on figure 11.2a, shows two peaks, but several degenerate transitions are included at these energies. They stem from transition between the three top valence band and the bottom conduction band at the six L points and they are all included for symmetry reasons. The independent-particle polarizability is computed at $\mathbf{q} = (0.00012, 0, 0)$ [a.u.] in Cartesian coordinates and $\omega = 5.29$ eV. The broadening was set to 0.1 eV and the 893×893 elements of the polarizability matrix were computed. As above, the independent-particle polarizability is used to compute the induced density. The induced density is thus the one generated by the total perturbation instead of the external perturbation. However, the result here is general and applies to any polarizability.

The perturbation is a plane wave with energy 5.29 eV and momentum q=(0,0.00012,0)[a.u.]. Three calculations of the polarizability are considered here: one with all transitions, one with only the transitions with an energy of 3.93 eV and one with only the transitions with an energy of 5.74 eV. The induced density generated by these calculations is represented by the blue, black and red curve on figure 11.2b. The 2D cuts of these cases are presented in the bottom row of figure 11.2.

We see on panel (c) and (e) that different transitions have different spatial shape, and different phase as can be seen in panels (b). From Eq. (11.12), one expects that the induced density will be the sum of the induced density due to each transition. This is indeed the case as the blue curve is the sum of the black and red curves. More generally, one can see that panel (d) is the sum of (c) and (e). The sum of the two transitions appears as one new transition with a different phase and different intensity. Nevertheless the comparison has to be stopped here as the behavior of the phase and intensity of this "new transition" is not the one seen in the previous section but rather a mixing between each individual behavior. For a different energy the mixing between the two will change in a non trivial way and the spatial shape will be changed.

Effect of the broadening

When considering more than one transition, the broadening used in the calculation of the polarizability will play an important role. In the dielectric function, it is well known how the broadening changes the shape of the spectrum. The effect of the broadening on the induced density, instead, remains to be elucidated. As described in section 11.2, the phase and the amplitude of each transition changes with the broadening through the prefactor. However, this does not lead to the same behavior as a change of the perturbation energy. This is even more important as the broadening is usually used as a tool to allow the calculation of the dielectric function on a coarse $\mathbf{k}$ points grid. The broadening is here the same for all transitions. This causes a difference with respect to the effect of the energy of the perturbation: while a change of the perturbation energy has a different impact on every term because it is subtracted from the transition energies, the broadening affects all terms the same way. To understand this better, as in the previous section, silver chloride with two groups of degenerate transitions is used to illustrate a simple case. Equation 11.12 reduces to:

$$\delta n(\mathbf{r},t) = 2\left|\frac{A_1(\mathbf{r},\mathbf{q})R_1^\dagger(\mathbf{q})}{\omega_0 - E^1 + i\eta}\right|\cos\left(\mathbf{q}.\mathbf{r} - \omega_0 t + \phi_1\right) + 2\left|\frac{A_2(\mathbf{r},\mathbf{q})R_2^\dagger(\mathbf{q})}{\omega_0 - E^2 + i\eta}\right|\cos\left(\mathbf{q}.\mathbf{r} - \omega_0 t + \phi_2\right), \quad (11.16)$$

where we have not explicitly shown the effect of summing over degenerate states, already discussed in Sec.11.2.

The induced density is the sum of the two transitions and when the broadening varies, the denominator will change as well as the phase in the cosinus (by virtue of Eq. (11.15)). There are different regimes for this sum: i) one term negligible with respect to the other, ii) both of the same order of magnitude (with either the same prefactor sign or with opposite sign) and iii) both terms vanishing.

Figure 11.3 shows the induced density with different broadening. The perturbation is the same as previously: a plane wave with energy of $\omega = 5.29$ eV and momentum $\mathbf{q} = (0, 0.00012, 0)$ [a.u.]. The left column shows a broadening in the vanishing limit ($\eta = 0.001$ eV). One can see on the top left panel that the black and red curve (corresponding respectively to the low and high energy transition) partially cancel out and share the same nodes. The two transitions are in opposition of phase. In this case (and it would have been possible also if they were in phase), it is possible to single out the cosinus. Of the three regimes described above, the vanishing broadening case explores two of them: the case in which the two contributions to the induced density both vanish (here at times t=0, t=0.5 and t=1, normalized with the period of the perturbation); and the case in which both contributions are not negligible (in this case in opposition of phase, so to partially cancel out the total induced density).

When the broadening increases ($\eta = 0.5$ eV), the two transitions are not in phase opposition anymore. This is due to the fact that the phase of the low energy transition becomes smaller while the phase of the high energy transition increases. We can notice also that intensities decreases, but only slightly because η^2 is still small compared to $(\omega - E)^2$. With this broadening, we can explore all the different regimes in the evolution of the induced density. If we look at a position of the induced density close to the silver atom: 1) the two contributions can have both negative sign (at the beginning and at the end of the cycle); 2) one of the two contributions can be zero while the other is finite; 3) the two contributions can have opposite sign and both non-zero; etc.

For large broadening (larger than the energy difference between the transitions and the energy of the perturbation), the two terms have the same phase. The intensity is also smaller, as dictated by the denominator. Around silver, the two transitions form a constructive sum which is visible on the bottom right plot.

In general, each transition can have its own phase, so a vanishing broadening doesn't necessary mean that all transitions are in phase or in opposition of pahse. In addition, more complex systems present of course many more transitions to sum. Nevertheless, some conclusions can be drawn: when the broadening increases, transitions with energy lower than the perturbation energy see their phase becoming smaller, while transitions with energy higher than the perturbation energy see there phase becoming bigger. Of course the intensity of all transitions decreases with increasing broadening since the intensity is smeared out. Finally, the principal effect of the broadening is a change in the dynamics of the induced density because transitions will mix in a different way. Therefore, the broadening has to be handled with care.

Response to different perturbations

In the previous subsections, the density induced by a plane-wave has been presented and the effects of the perturbation energy has been discussed, both in the case of one and more than one transitions. The broadening has also been studied. However, as stated at the beginning of subsection 11.2, one more ingredient has to be discussed: $R_\lambda(\mathbf{q})$. This quantity, defined as $R_\lambda(\mathbf{q}) = \sum_{\mathbf{G}} B^{\lambda *}_{\mathbf{G}}(\mathbf{q}) V^{\text{ext}}_{\mathbf{G}}(\mathbf{q}, \omega)$, depends on the spatial shape of the external perturbation. For example a plane wave perturbation with $\mathbf{q}_0 + \mathbf{G}_0$ momentum will have $R_\lambda = \delta(\mathbf{q} - \mathbf{q}_0) B^{\lambda *}_{\mathbf{G}_0}(\mathbf{q}_0)$, whereas for a localized perturbation $V^{\text{ext}}(\mathbf{r}, t) = \delta(\mathbf{r} - \mathbf{r}_0) V^{\text{ext}}(t)$, the factor becomes $R_\lambda(\mathbf{q}) = B^{\lambda *}(\mathbf{r}_0, \mathbf{q})$. From equation 11.11, R_λ controls the relative intensity of each transition. The form of this term changes completely between these two examples. This raises the question: how does this parameter affect the induced density ? A transition with a large R_λ will be well represented in the total induced density (if the energy term also allows it) while a zero R_λ would completely suppress this transition. Going from a delocalized potential to a localized one thus might have important effects as the R_λ of each transition changes. Indeed, $B^{\lambda *}(\mathbf{r}_0, \mathbf{q})$ might be zero while $B^{\lambda *}_{\mathbf{G}_0}$ might have a large value,

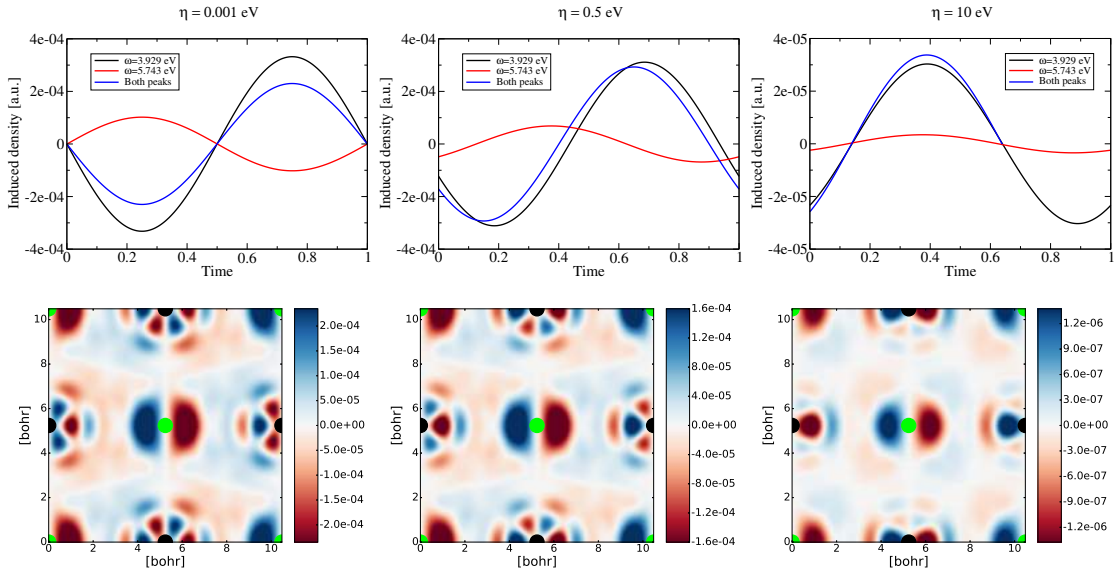

Figure 11.3: Response of silver chlorine to a plane wave perturbation in the independent particle approximation, with the same transitions as in the previous figure, and with polarizabilities computed with different broadening. Top row: Induced density as a function of time (normalized with the period of the perturbation) at $\mathbf{r} = (6.05, 0, 0)$ Bohr, close to a silver atom, in the plane passing by the atoms and perpendicular to the [001] direction. The black curve represents the polarizability computed with only the low energy peak, the red curve the calculation with only the high energy peak and the blue curve represents the calculation with both peaks. The bottom line presents the 2D plot of the induced density in the plane passing by the atoms and perpendicular to the [001] direction. The induced density generated by each peak individually is presented on figure 11.2. The different columns differ by the broadening used in the polarizability calculation. The left figure shows a calculation with $\eta = 0.001$ eV, the center figure shows a calculation with $\eta = 0.5$ eV and the right figure shows a calculation with $\eta = 10$ eV. All snapshots were taken at t=0.2 fs (that corresponds to t=0.26 T).

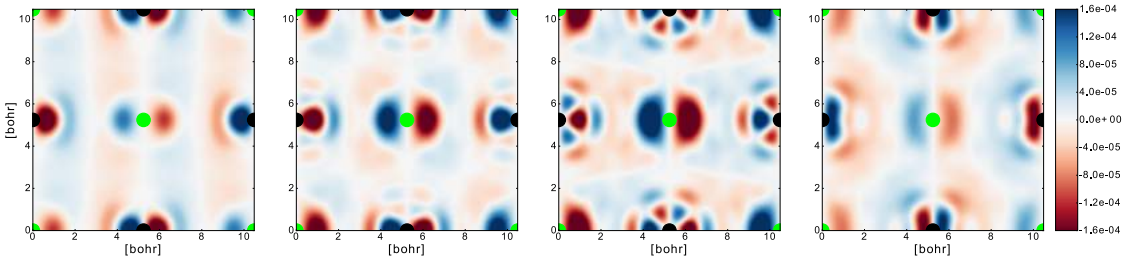

Figure 11.4: 2D plot of the induced density in the plane passing by the atoms and perpendicular to the [001] direction. The response is computed using the two groups of degenerate transitions. The broadening is $\eta = 0.5$ eV, corresponding to the center panel in Fig 11.3. The induced densities shown are taken at different time, expressed in unit of the period of the plane wave, leading to different ways of summing the two transitions. Left: the two degenerate transitions adds (t=0.05), center left: the low energy transition cancels (t=0.13), center right: the two transitions substract from each other (t=0.26), right: the high energy transition cancels (t=0.43).

causing the transition to either appear or disappear. In this subsection, an illustration of the effects of R_λ will be presented.

In the case of a one transition system R_λ only brings an overall factor:

$$\delta n(\mathbf{r},t) = 2\left|\frac{A_\lambda(\mathbf{r},\mathbf{q})R^\dagger_\lambda(\mathbf{q})}{\omega_0 - E^\lambda + i\eta}\right|\cos\left(\mathbf{q}.\mathbf{r} - \omega_0 t + \phi^\lambda_E(\omega_0) + \phi^\lambda_A(\mathbf{r}) + \phi^\lambda_R\right) \tag{11.17}$$

where $\mathbf{q}$ is the momentum transfer of the transition. In this situation it is not possible for R_λ to change the spatial distribution of the induced density, given by $A_\lambda(\mathbf{r},\mathbf{q})$, but only to change its global intensity and the phase in the cosinus. We will thus focus on systems with more than one transition. What do we expect? For a localized perturbation, knowing that $B^{\lambda *}(\mathbf{r},\mathbf{q})$ is linked to the overlaps between the valence and the conduction states of the transition at $\mathbf{r}$, only transitions with non vanishing overlap at the position of the perturbation will be visible and transitions with vanishing overlap at this position will have no intensity. For example in silver chloride, if the perturbation is localized around silver, only transitions from and to states localized around silver will be visible. This does not mean that it is not possible to observe induced density outside silver, as this is controlled by $A_\lambda(\mathbf{r})$, but it requires the same transition to have overlapping tail even far from silver.

This is different for the case of a delocalized perturbation, where the intensity is proportional to the Fourier component of the overlap which has the same momentum as the perturbation. For vanishing momentum, this overlap gives the dipole operator[2].

In the following, we will indeed investigate the effects of these two extreme cases, a delocalized plane-wave perturbation and a localized external potential. For a plane wave perturbation, with only one $\mathbf{q}+\mathbf{G}$ component, small and large momentum can be considered. A localized perturbation can be modeled by a Dirac delta function. However, since we consider the perturbation in reciprocal space, a cutoff has to be set in the Fourier transform

$$\delta(\mathbf{r}-\mathbf{r}_0) = 1/(2\pi)^3 \sum_{\mathbf{G}} \int d\mathbf{q} e^{i(\mathbf{q}+\mathbf{G})\cdot(\mathbf{r}-\mathbf{r}_0)}. \tag{11.18}$$

This Fourier transform contains a sum of reciprocal lattice vectors, which controls to the degree of localization: the more $\mathbf{G}$'s, the more localized, the more δ-like will be the perturbation. The integral over $\mathbf{q}$, instead, influences the periodicity of the perturbation (using only one $\mathbf{q}$ means a perfect periodicity of one unit cell; taking the integral over 4 $\mathbf{q}$'s corresponds to taking a periodicity of 4 unit cells, and so on). The convergence over both values has to be checked.

Let us compare the induced density generated by the different perturbations for silver chloride, evaluated with 256 symmetric k-points, 8 valence bands and 27 conduction bands. The polarizability is computed at $\omega_0 = 2.86$ eV, corresponding to the energy of the lowest transition[3]. Figure 11.5 shows the effect of three different perturbations (upper panels) on the induced density (lower panels) of AgCl . We have a plane wave perturbation in the left column, a perturbation localized close to an atom with a periodicity of one unit cell (only one $\mathbf{q}$ taken into account in Eq. (11.18)) in the center column, and a perturbation still localized but a periodicity of four unit cells (integral done over four $\mathbf{q}$ point in Eq. (11.18)) on the right. The position of the localized perturbation is set to be close to a chlorine atom ($\mathbf{r} = (0, 1.0, 0)$ a.u.), not at the exact position of the atom, because there the density vanishes and no response is expected in the material (see section 11.3). The plot associated to the plane-wave perturbation has only on color because the plane-wave momentum is vanishing, corresponding to infinite wavelength. The densities resulting from these perturbations are quite different.

The planewave perturbation, although homogeneous in space, creates a response with structure at the level of atoms. The perturbation localized with one unit cell periodicity (center) creates

[2] This restriction does not apply in the case of localized perturbation, which means that dipole forbidden transitions can contribute to the induced density for localized perturbation.

[3] The energy of the lowest transition does not have to be that of the direct gap, because transitions at $\mathbf{q} \neq 0$ can contribute to the induced density. This lowers the minimum transition energy in materials with indirect band-gap, for instance in AgCl with transitions between Γ and L.

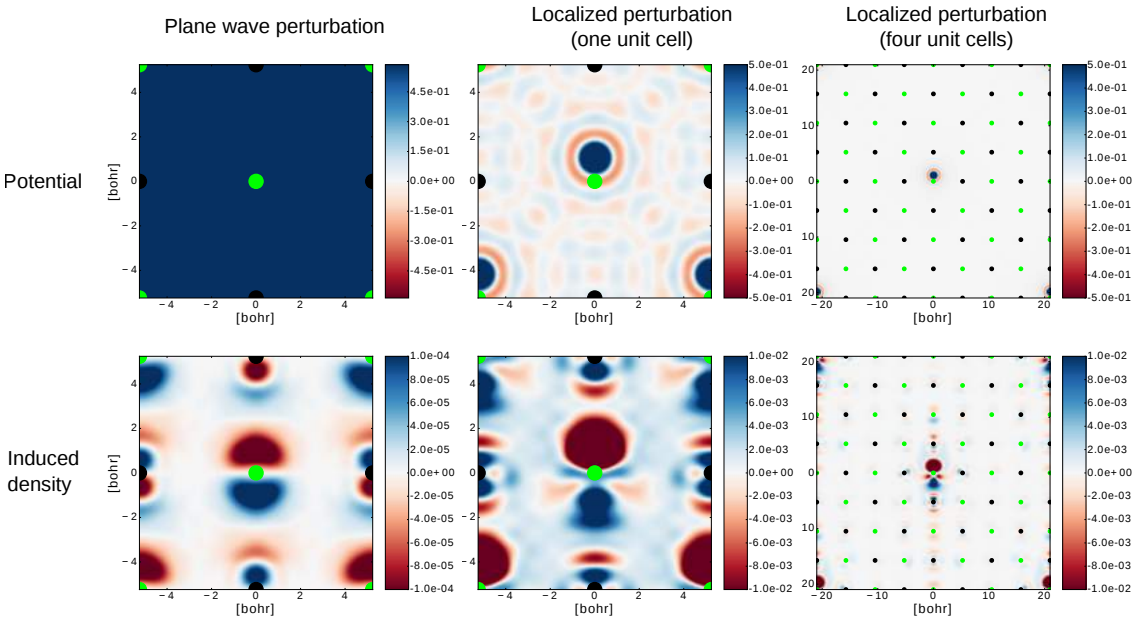

Figure 11.5: Response of silver chlorine to perturbations with different localization, in the independent particle approximation. Top: 2D cut of the perturbations used to compute the induced density, in the plane passing by the atoms and perpendicular to the [001] direction. Bottom: 2D cut in the same plane, of the induced densities generated with the corresponding perturbation on the top. Chlorine atoms are depicted in green, silver in black. Left column: Plane wave perturbation with transfered momentum of 0.00012 Bohr^{-1}. Center column: Localized perturbation with one unit cell periodicity. Right column: Localized perturbation with four unit cell periodicity. The calculation of the polarizability was realized with 256**k** points in the Brillouin zone, 8 valence bands and 27 conduction bands.

density where the intensity is now concentrated in a peak close to chlorine. The perturbation is defined as $V^{\text{ext}}(\mathbf{r},t) = \sum_R \delta(\mathbf{r}-\mathbf{r}_0+\mathbf{R})e^{i\omega t}$ or $V^{\text{ext}}_{\mathbf{G}}(\mathbf{q},\omega) = \delta(\omega-\omega_0)\delta(\mathbf{q})e^{i\mathbf{G}\cdot\mathbf{r}_0}$, which is equivalent to summing all the terms in $\mathbf{G},\mathbf{G}'$ in eq 11.5, but not doing the integral over $\mathbf{q}$ (we use only the $\chi^0(\mathbf{q}=[0,0001,0,0.0001])$. The induced density presents a larger intensity than in the delocalized case (note the changing scale) and a strong response peak occurs close to the chlorine atoms, at the position of the perturbation. The induced density around chlorine and silver changes. While for the planewave perturbation the induced density was symmetric around each atom and oriented in the direction of the momentum, the localization forces the polarization of the material toward the position of the perturbation. This cause the density around chlorine to become asymmetric. Another notable difference is the shape of the induced density around the silver atom (now more a *d*-like orbital shape). Because the induced density has the same periodicity as the perturbation, there are only two different atoms, and thus no other behavior can be expected. We see here the effect of the reorganization of the different transitions: while for the plane wave perturbation, transitions oriented in directions other than its momentum were suppressed, for the localized perturbation all transitions with intensity at the position of the perturbation were added.

If we now add a sum over $\mathbf{q}$ in the first Brillouin zone (see Eq. (11.18)), we increase the periodicity of the perturbation, and obtain the right column in the figure, with a 4-unit periodicity. The sum over reciprocal vectors is the same as previously and is realized for all BZ vectors. The induced density is localized around the center atom. Around the center chlorine and the silver atoms below and above it, the density is similar to the one-unit periodicity case, but further away it is vanishing rapidly. The induced density around the atoms is oriented towards the perturbation.

In this example, we saw that the form of the potential, through $R_\lambda(q)$ is a crucial parameter for the shape and intensity of the induced density. The change of R_λ causes a reorganization of

the relative intensity of the transitions. Still one of the parameters has been arbitrarily decided: this is $\mathbf{r}_0$, the position at which the perturbation is localized. One can wonder what is the effect of this parameter on the induced density. One can expect an important effect: for instance, the excitation of a region with few electrons will have a smaller response than that of a region with many electrons.

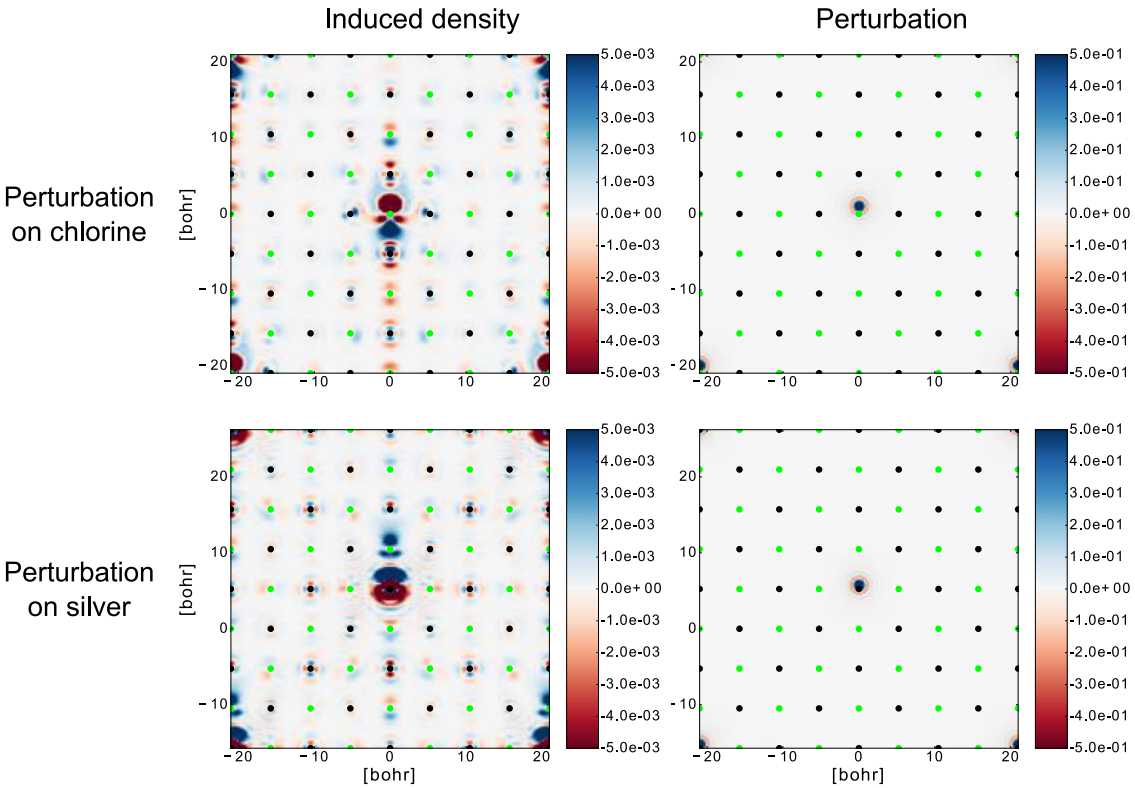

Figure 11.6: Response of silver chlorine to perturbations localizated close to silver and close to chlorine, in the independent particle approximation.The energy of the perturbation is ω=2.855 eV. Top: perturbation localized close to chlorine, bottom: perturbation localized close to silver. On the left hand side, the induced density is plotted on a 2D plot in the plane passing by the atoms and perpendicular to the [001] direction, the time of the snapshot is set to zero, that is to say at the maximum of the perturbation. On the middle column the induced density with respect to time at two different positions is plotted, one is close to the chlorine atom (black) and the other is close to the silver atom (red). On the right hand side the 2D plot of the perturbation is shown with the same cut in space and at the same time as the plots in the left panel.

We now consider two different localizations: one close to silver and one close to chlorine. The energy of the perturbation is set to 2.86 eV. Each of these perturbations will gives a different induced density. The results are shown in figure 11.6. The first row shows the results for a perturbation localized around chlorine ($\mathbf{r}_0 = (0, 1.05, 0)$ [a.u.]), this is the same result as the previous figure with a different color scale. The second line shows the results for a perturbation localized around silver ($\mathbf{r}_0 = (0, 6.29, 0)$ [a.u.]). The image is quite different, showing that indeed the induced density is sensitive to the position of the localization. There is an asymmetric localization around silver as in the previous case.

To conclude this section, we have seen the interplay of the various ingredients entering the induced density formula: the perturbation energy, the broadening, the shape of the perturbation and the localization. All these considerations will be used for the next step: the study of the induced density when we describe the system with different levels of approximation for the polarizability.

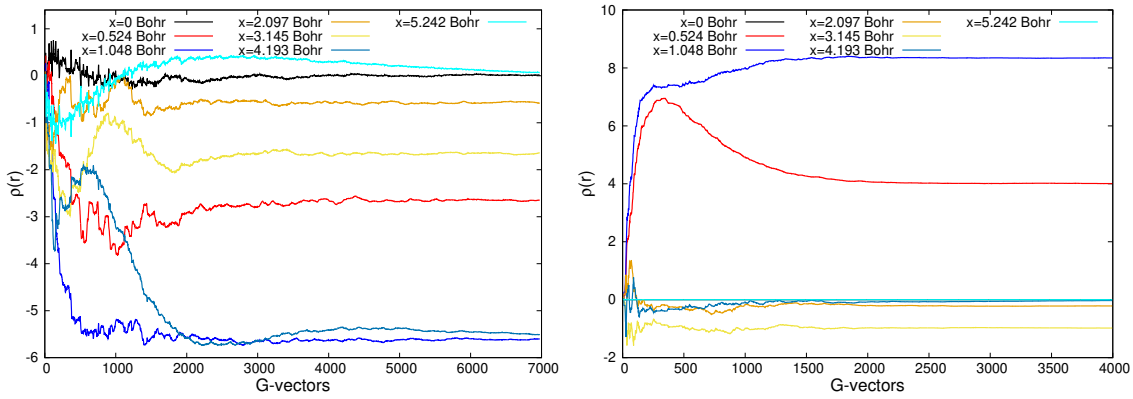

Figure 11.7: $\tilde{\rho}(\mathbf{r}) = \sum_{\mathbf{G}}^{\mathbf{G}_{max}} e^{i\mathbf{G}.\mathbf{r}}\tilde{\rho}(\mathbf{G})$ as a function of $\mathbf{G}_{max}$. Calculations are made for different positions $\mathbf{r}$. The left panel shows a transition between top valence and bottom conduction at k=(0.49,0.23,0.11). The right panel shows a transition between top valence and bottom conduction at $\mathbf{k} = \Gamma$.

11.3 Independent particle response

While in the previous section the major ingredients to the density response were discussed qualitatively, we will now elucidate the effect of calculating the polarizability on different levels of theory. Change of polarizability has strong effects on the dielectric function: the inclusion of the long range part of the coulomb potential in the polarizability creates plasmons, the short range contributions are responsible for crystal local field effects (see Appendix C), and the inclusion of the electron-hole interaction (through the Bethe-Salpeter equation) generates excitons. In this section we will focus on the simplest polarizability: the independent-particle polarizability. Results will be discussed for the real material AgCl. Therefore we start with a convergence study.

Convergence with respect to the size of the matrix

The density response calculation (through equation 11.5) presents a sum over $\mathbf{G}$ and $\mathbf{G}'$, the reciprocal lattice vectors. As mentioned before, in practice a cutoff is applied to these otherwise infinite sums. The two parameters (constrained by the size of the polarizability matrix as a maximum) control two elements in the induced density:

- The sum over $\mathbf{G}$ (the first index of $\chi_{\mathbf{G}\mathbf{G}'}$) controls the spatial resolution of the induced density as it is the inverse Fourier transform. It must have a cutoff large enough to give a correct description of the induced density at the scale we are interested in.
- The sum over $\mathbf{G}'$ (the second index of $\chi_{\mathbf{G}\mathbf{G}'}$) has to be large enough to include all of the perturbation Fourier components, or at least enough terms such that the induced density is converged to the precision we require. This is important in the cases of a plane wave with a very large momentum, as the corresponding $\mathbf{G}$ needs to be in the matrix, and for a localized perturbation, where its Fourier components are all non vanishing. This corresponds to the correct description of the term R_λ.

According to equation 11.6, for $\chi_{\mathbf{G}\mathbf{G}'}$ the dependence on $\mathbf{G}$ and $\mathbf{G}'$ appears through $A_{\mathbf{G}}$ and $B_{\mathbf{G}}$. In the case of the independent-particle polarizability, both terms equal the $\tilde{\rho}$. For other polarizabilities, they are related to the mixing of $\tilde{\rho}$. We can then expect to have similar convergence behaviour independently of the χ.

An example of the convergence of $\tilde{\rho}$ in real space with respect to the number of plane waves in the inverse Fourier transform is shown in figure 11.7. In the left panel we show the $\tilde{\rho}$ corresponding to the overlap between the top valence band and the bottom conduction at $\mathbf{k} = (0.49, 0.23, 0.11)$ as a function of the cutoff used in the inverse Fourier transform. The different curves show the

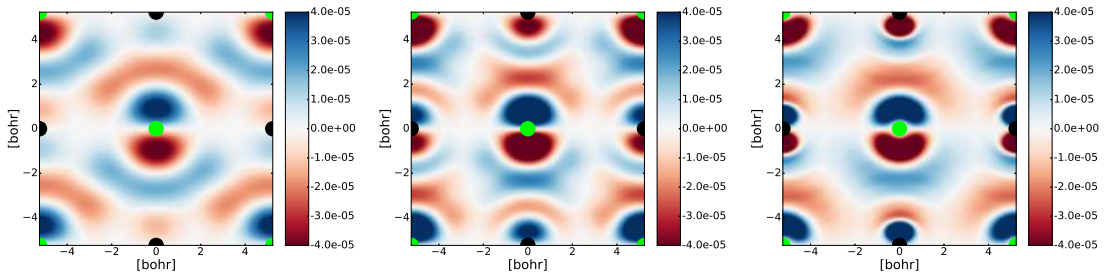

Figure 11.8: Induced density for a plane wave perturbation with vanishing momentum. The system is silver chloride with 8 valence bands and 30 conduction bands. The **k**-point grid is a 8×8×8 MP symmetric grid. Different sizes of matrix are used in the calculation of the induced density. Left: 89 **G**-vectors, center: 283 **G**-vectors, right: 2975 **G**-vectors. All induced densities are taken at the same time, t=0.6 fs. The plots are a 2D cut in the plane passing by the atoms and perpendicular to the [001] direction.

overlaps at different positions in space expressed in reduced coordinates. On the right panel, a similar plot is shown for $\mathbf{k} = \Gamma$. The chlorine atom is located at $r = 0$ while the silver atom is located at $r = 5.242$ Bohr. Different behaviors can be observed. First, not all points converge with the same number of **G**'s. The case $r = 5.24$, corresponding to the position of the Ag atom, is particularly bad. The overlaps are more difficult to converge close to atoms as the wavefunctions vary quickly around them. In general the convergence can be easy to achieve for some transitions and quite difficult for some other as we can see comparing the left and right panels of Fig.11.7, showing the convergence for two different k-points. Of course, in practice, it is impossible to carry out this detailed study for each transition in a real material. Nor it is pertinent, for, as we have seen in the previous section, not all transitions have the same importance. It is instead more convenient to look directly at the convergence of the induced density with respect to the **G**-vectors.

Figure 11.8 shows the convergence of the first **G** sum in the induced density. The perturbation is a plane wave with vanishing momentum and $\omega_0 = 2.86$eV. In this calculation we use a 8×8×8 **k**-point MP symmetric grid, 8 valence and 30 conduction bands. We see that structures around chlorine are already formed with 89 **G**-vectors, whereas structures around silver require at least 283 **G**-vectors. If we increase the number of **G**'s, we increase the intensity and change the fine details (without changing the overall picture). In the following, the sum will always run over the 2975 **G**-vectors.

For the second sum, convergence will be studied with a localized perturbation, around chlorine in this case (but localization around silver would have the same convergence behaviour). This is because the second parameter in the sum ($\mathbf{G}'$) has no effect if only a plane wave at $\mathbf{q} + \mathbf{G}$ is used as perturbation.

Fig. 11.9 shows, then, the induced density with a different degree of localization of the perturbation. The system is the same as considered previously, the perturbation is taken such that the periodicity is eight unit cells. With 89 **G**-vectors (left plot) the induced density is already well converged except for small structures which are not yet formed. With 2913 **G**-vectors, small structures appear, particularly around the perturbation. To show more quantitative results, a 1D cut is made in the 2D induced density plot, in the vertical direction and passing through the perturbation. Results are shown in figure 11.10. Around **r**=0, where we apply the perturbation, a strong peak goes to large negative values and, diverges with increasing number of **G**-vectors, for we are simulating a delta peak. Besides this quite unphysical point, the overall picture can be correctly interpreted as the density induced by a very localized perturbation: we can, for instance, see that the induced density goes to zero close to the atoms (indicated by colored arrows), as seen in Fig. 11.7.

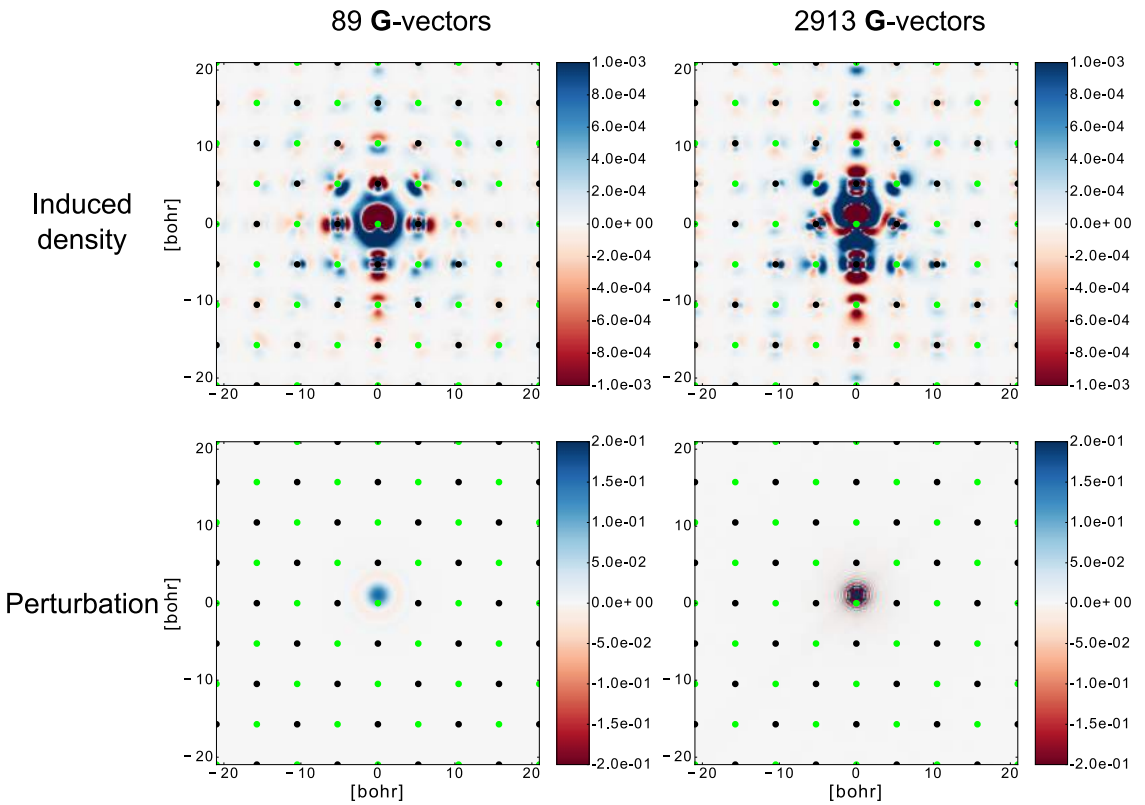

Figure 11.9: Response of silver chloride to a localized perturbation close to a chlorine atom, at $\mathbf{r}_0 = (0, 1.05)[a.u]$ in the coordinate of the 2D cut and with vanishing momentum and energy $\omega_0 = 2.855$ eV. Top row: induced density in the 2D plan passing by the atoms and perpendicular to the [001] direction. The parameters are the same as for the figure 11.8. Different matrix sizes are used in the calculation of the induced density. Left: 89 **G**-vectors, right: 2913 **G**-vectors. Bottom row: corresponding perturbation.

Convergence with respect to the periodicity of the potential

In the following we will deepen the discussion of the localization of the perturbation, already mentioned in section 11.2 and illustrated in figure 11.5. To be fully localized a perturbation must have an infinite period corresponding to an integral over the first Brillouin zone. This integral has to be discretized, which leads to periodicity of the perturbation (and of the induced density). This periodic perturbation can be thought of as the sum of a non periodic perturbation with replicas shifted by multiples of the period. As we use linear response, the density induced will be the sum of the density induced by each replica of the perturbation. This is sufficient to simulate a localized perturbation as long as the induced density replica do not significantly overlap, for it would falsify the results.

We test then perturbations with larger and larger periodicity, (including more and more **q**-vectors in the calculation), in order to check this effect. Fig. 11.11 shows localized perturbations with different periodicity and their associated induced density.

The left panel, with periodicity of two unit cells, presents the described problem: the perturbation replica are too close and the induced density overlaps. By comparing with the calculation with the largest periodicity, only the density around the center chlorine and around the first silver neighbor is correct. When increasing the periodicity, the induced density changes significantly. The comparison with the largest periodicity shows that the density is correct until the fourth closest neighbor of the central chlorine. With this periodicity, we already have a good image of the induced density. This shows that, in the case studied here, the induced density decays quickly

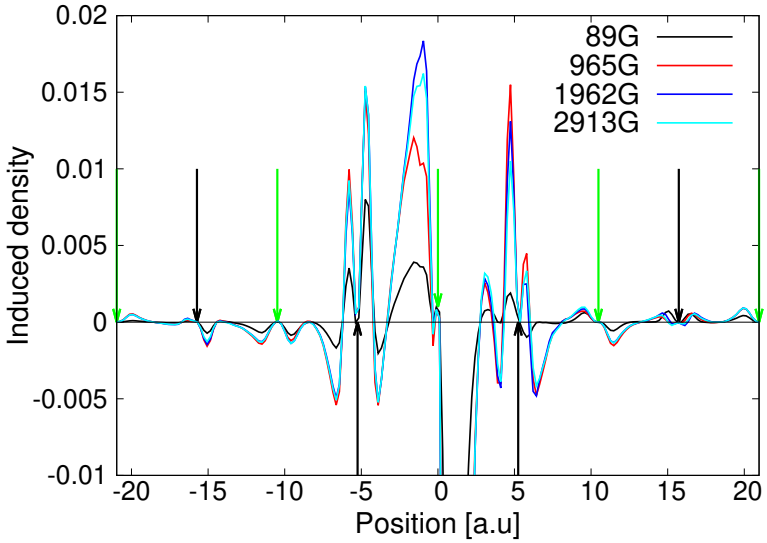

Figure 11.10: Induced density along a line. The line is taken in the vertical direction in the previous figure and at $x = 0$, it passes through chlorine and silver atoms at positions indicated by the green and black arrows, respectively. The induced density is computed with different number of **G**-vectors: 89 **G**-vectors in black (the left hand side of Fig. 11.9), 965 **G**-vectors in red, 1962 **G**-vectors in blue and 2913 **G**-vectors in cyan (the right hand side of Fig. 11.9).

with the distance to the perturbation. We will come back to this point in a comparison with the homogeneous electron gas in section 11.4.

Results for different perturbations

In this subsection, we use converged values for all parameters and present results for different perturbations.

Plane-wave perturbation

We start by considering the case of a plane-wave perturbation.

Figure 11.12 shows the induced density for two different momentum transfers ($\mathbf{q}_0 \to 0$ and $\mathbf{q}_0 = (1/2, 0, 1/2)$, in reduced lattice units) and two perturbation energies: in the left column we have vanishing energy $\omega_0 = 0$, while in the right column the energy is taken equal to the first excitation energy, i.e. $\omega_0 = 2.86$ eV for $\mathbf{q}_0 = 0$ and $\omega_0 = 1.98$ eV for $\mathbf{q}_0 = (1/2, 0, 1/2)$,

Several behaviors can be noticed: i) first of all, we see much bigger response at finite momentum, the maximum intensity around silver is 0.67 with a perturbation with finite energy, whereas it is 2.8 10^{-4} close to silver for a perturbation with vanishing momentum; ii) by looking at the right panels, we see that the induced density around the silver atom has an overall bigger intensity, at both momenta; iii) at vanishing momentum transfer, the induced density around silver has similar shape for both energies. By the way of contrast, close to chlorine, at vanishing energy, there is no intensity and only some induced density far from the atom is visible. At $\omega_0 = 2.86$ eV, the intensity around chlorine is quite different and has the shape of a p state. The transition corresponding to this energy is a transition at the Γ point.

Localized perturbation

Figure 11.13 shows the induced density for a localized perturbation at two positions: close to chlorine and close to silver. The calculation are made in the static limit and at ω_0=2.855 eV.

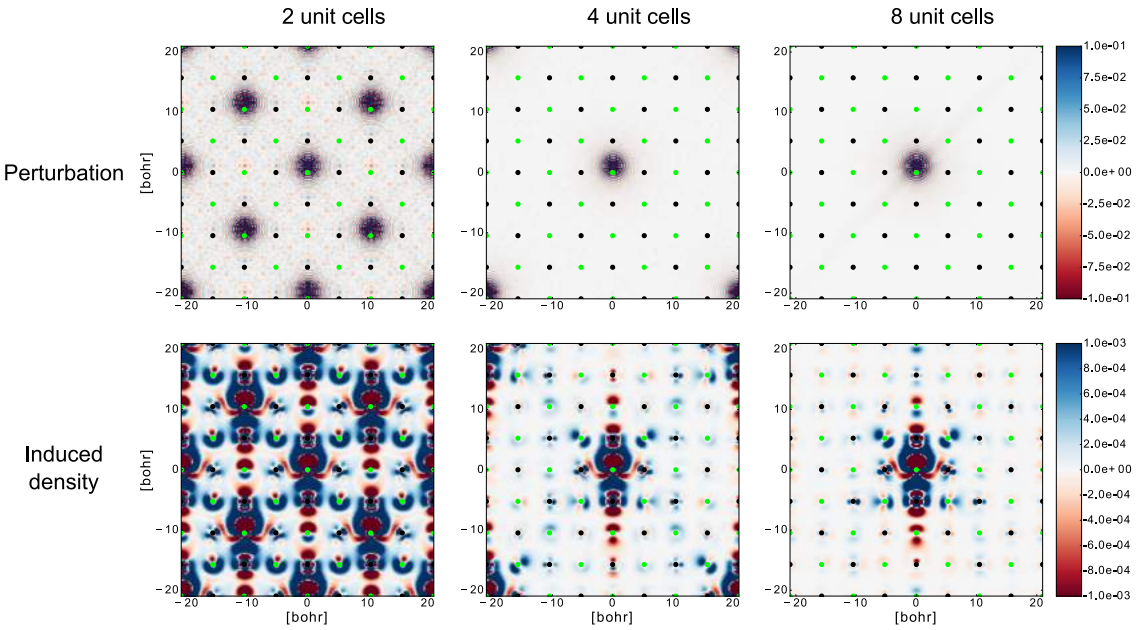

Figure 11.11: Induced density by a localized perturbation with periodicity over different number of unit cells. Left: periodicity over two unit cells, center: periodicity over four unit cells, right: periodicity over eight unit cells .

For silver and chlorine the reaction of the system at the position of the localization is in phase opposition to the potential. This is why the induced density is shown at t=0 fs, this is the point where it is maximal. We see that the induced density is mainly localized around the perturbation and decreases quickly when going away from it. This can be seen in Fig 11.14, which shows a cut of the induced density along the line passing through the perturbation, localized around chlorine (left panel) and silver (right panel). We see that the decrease is faster in the static limit than at ω_0=2.86 eV. We also see that the response of the system is stronger when the perturbation is localized around silver than around chlorine. Fig. 11.13 shows that the induced density has mostly a d shape around silver and a p shape around chlorine. These orbitals are oriented in the direction of the perturbation, testifying of a polarization of the material.

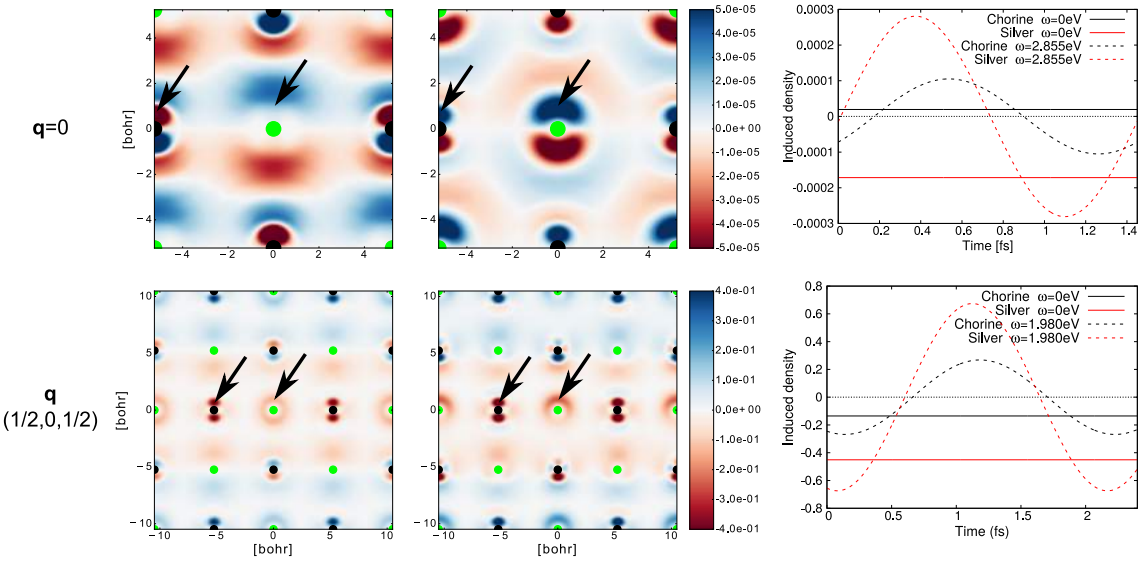

Figure 11.12: Response of silver chloride to plane-wave perturbations. The polarizability used is the independent-particle one. The left and center column show the induced density in a 2D plan passing by the atoms and perpendicular to the [001] direction. The left column shows the induced density for $\omega = 0$ eV and the center column shows it for $\omega = 1.98$ eV and $\omega = 2.86$ eV, for the $\mathbf{q} = 0$ and $\mathbf{q} = (1/2, 0, 1/2)$, respectively. The right column shows the induced density as a function of time, at two positions, one close to chlorine and the other close to silver, indicated by arrows on the 2D cuts. Top: vanishing momentum. Bottom: plane wave perturbation with momentum $\mathbf{q} = (1/2, 0, 1/2)$ in the reduced basis. For the top center panel, the snapshot is taken at t=0.66fs, corresponding to the time where the dahed red and dashed black curve cross in the top right panel. The others snapshots are taken at t=0fs.

11.4 Response in the Random phase approximation

The independent-particle polarizability alone does not give a good description of the response of a material. Indeed the changes in the Hartree potential have to be taken into account when the system reacts and the density changes. This has two main effects: the long range part of the coulomb interaction creates the plasmon excitation in the inverse dielectric function, while the other components of the coulomb interaction are responsible for the local field effects. As shown previously, the local field effects are negligible in the spectra. Strong changes due to the long-range component are expected to occur when a plasmon forms but also at other energies. This effect is present in the polarizability through the mixing of the independent-particle transitions.

Plane-wave perturbation

Figure 11.15 compares the induced density for independent particle and RPA polarizabilities using plane wave perturbations. Calculation at different energies and momenta have been realized. The principal change induced by the RPA is a strong reduction of the intensity of the response, while the shape remains similar. Also the phase slightly changes.

The reduction of the intensity can be easily understood: in the RPA, $\chi = \chi^0 + \chi^0 v \chi = \chi^0 \epsilon^{-1}$. This means that the external potential is screened, leading to an effective perturbation that is weaker than the external one.

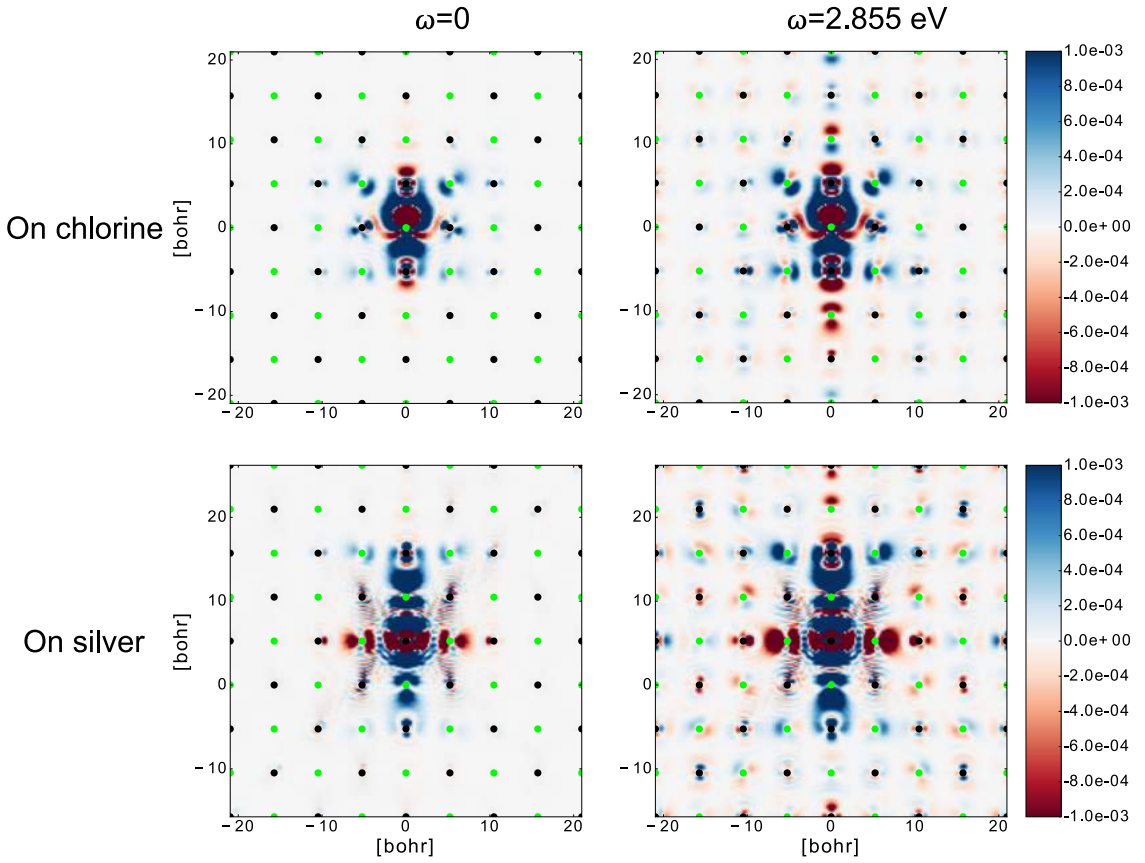

Figure 11.13: Response of silver chloride to localized perturbation. The induced densities are represented in a 2D plan passing by the atoms and perpendicular to the [001] direction. Top: the perturbation is localized around a chlorine atom. Bottom: the perturbation is localized around silver. The left panels show calculations with static perturbation and right panel show calculations for perturbation energy of $\omega = 2.855$eV. The snapshots are taken at t=0, when the external perturbation and the density response are at their maximum.

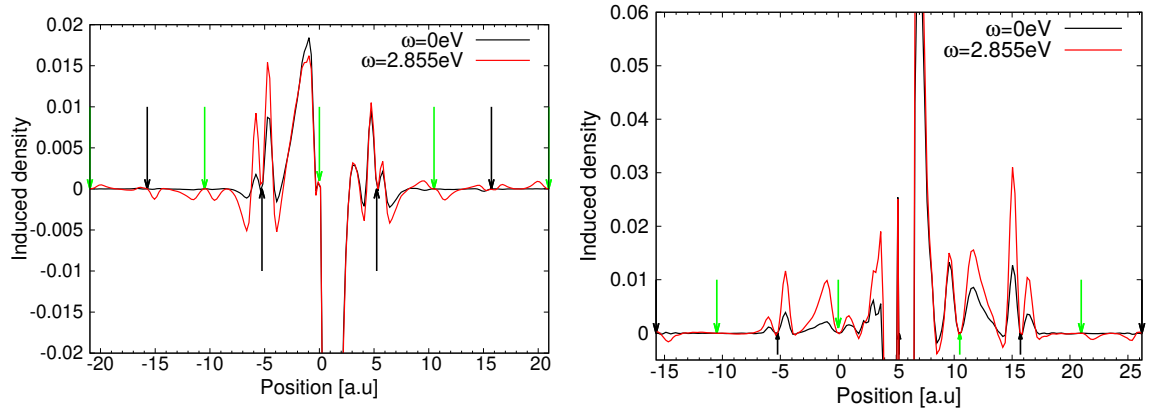

Figure 11.14: Induced density from Fig 11.13, along the line in the vertical direction and at $x = 0$, passing through chlorine and silver atoms at positions indicated by the green and black arrows, respectively. Left: perturbation localized at r=1.0 bohr, close to a chlorine atom. Right: Perturbation localized at r=5.8 bohr, around a silver atom. The density induced by a static perturbation is represented in black, while density induced by a perturbation with energy $\omega = 2.855$eV is represented in red.

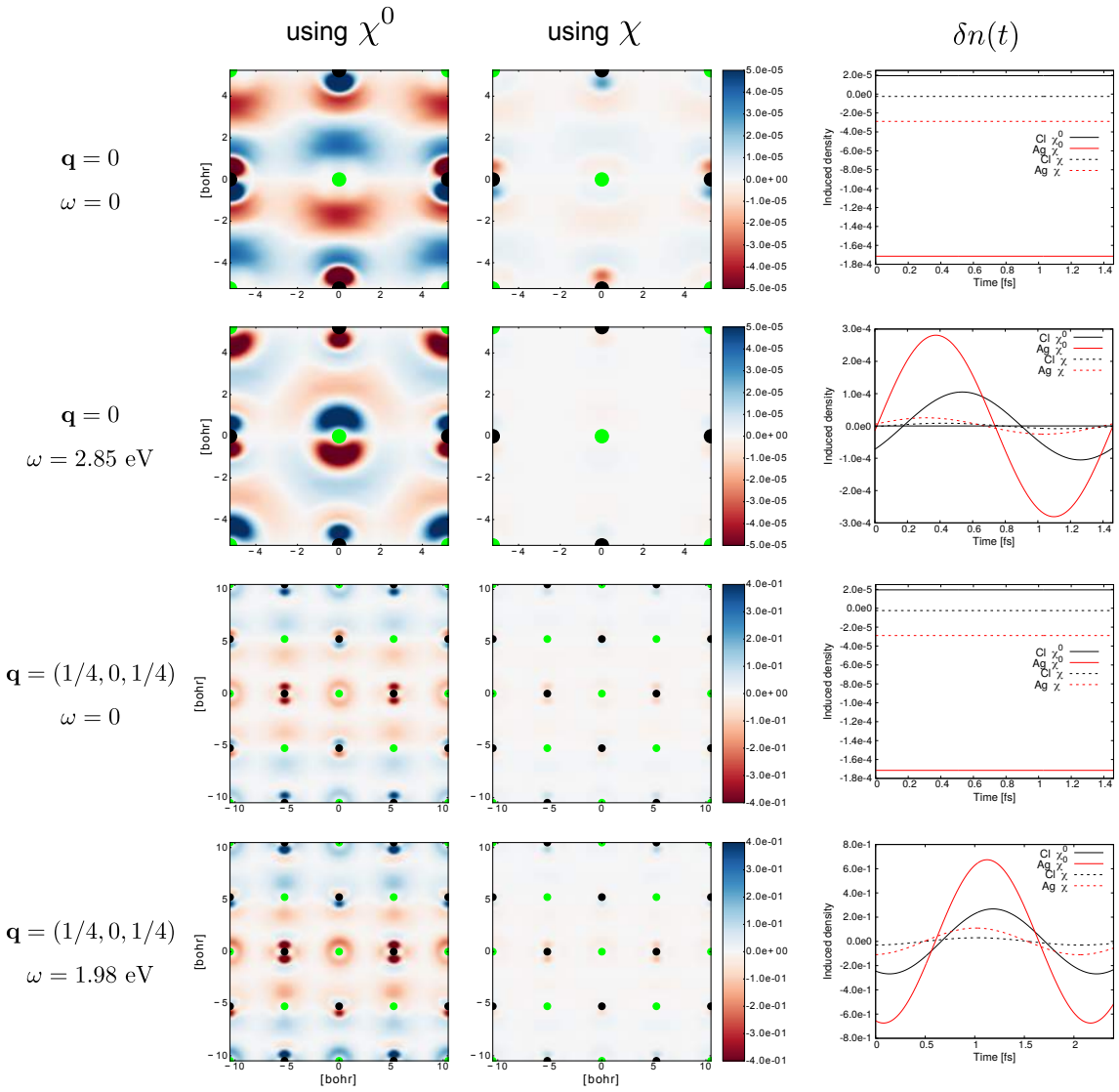

Figure 11.15: Response of silver chloride to plane-wave perturbations with different momenta and energies in the independent particle approximation and the random phase approximation. The left and center column show the induced density in a 2D plan passing by the atoms and perpendicular to the [001] direction. The left column presents the induced density computed with the independent particle polarizability wile the center column presents the induced density computed with the RPA polarizability. The right column compares the independent-particle and RPA induced density as a function of time at two positions, one close to silver and the other close to chlorine atoms. Theses positions are chosen because they are a local maximum close to each atom. The first row shows a perturbation with vanishing momentum and energy, the second row shows a perturbation with vanishing momentum and $\omega = 2.85$ eV. The third row shows a perturbation with momentum $\mathbf{q} = (1/4, 0, 1/4)$ and vanishing energy. The last row shows a perturbation with momentum $\mathbf{q} = (1/4, 0, 1/4)$ and energy $\omega = 1.98$ eV.

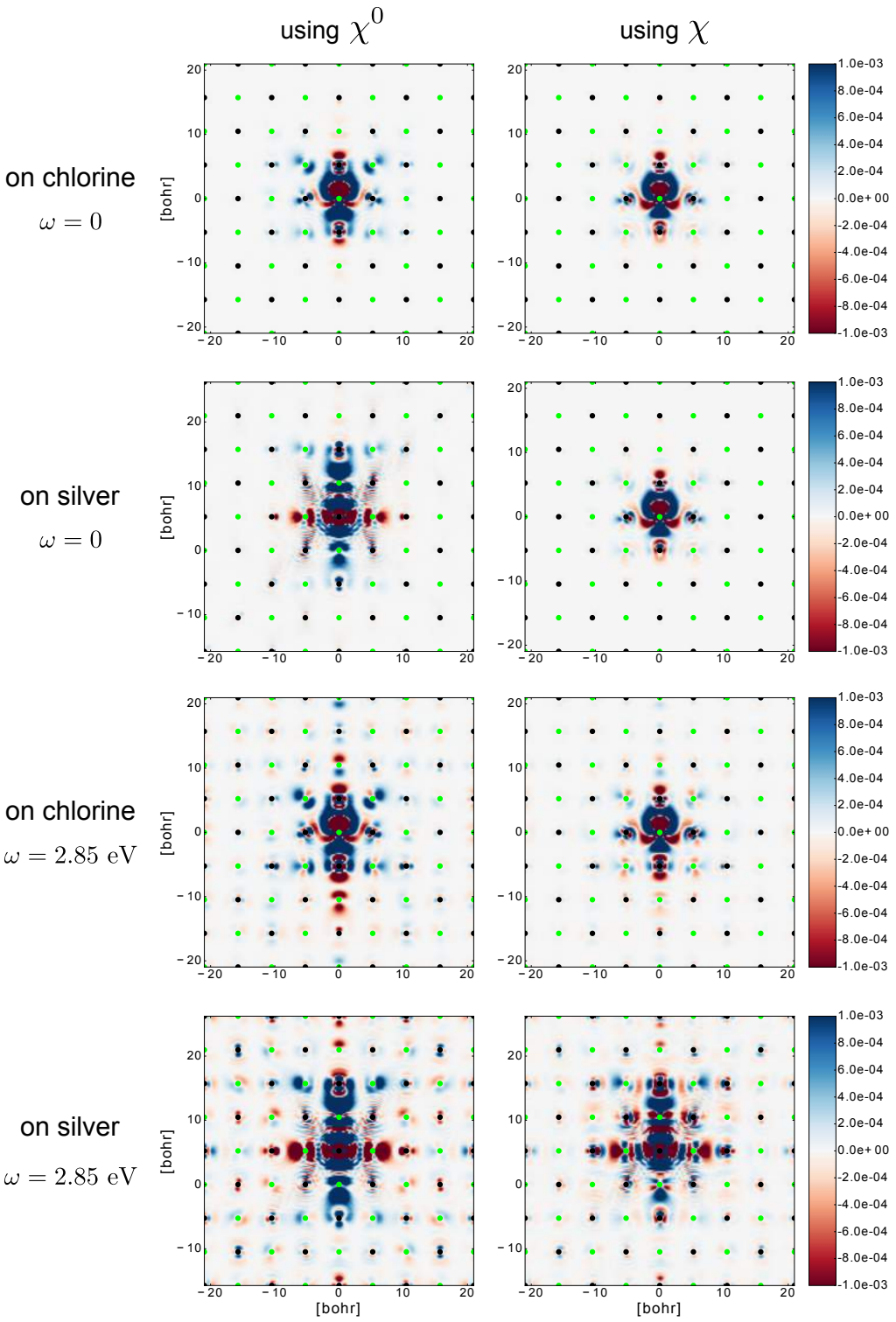

Figure 11.16: Response of silver chloride to localized perturbations with different energies and localized at different position in the independent particle approximation and the random phase approximation. Left column presents the induced density computed with IP polarizability. The center column presents induced density computed with the RPA polarizability. The first and second rows show a perturbation at zero frequency and localized close to the chlorine atom and to the silver atom, respectively. The third and fourth rows show a perturbation taken at $\omega = 2.85$ eV, localized close to the chlorine atom and to the silver atom, respectively.

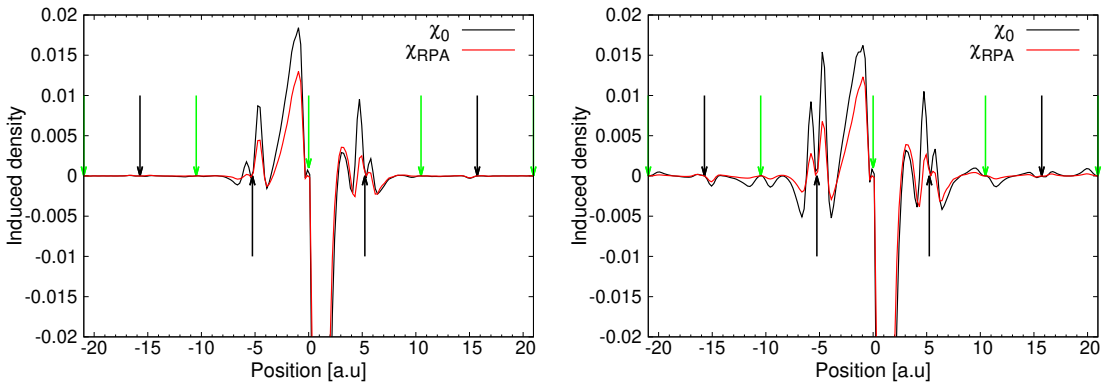

Figure 11.17: Induced density from Fig 11.16 for a perturbation localized around a chlorine atom along the line in the vertical direction and at $x = 0$, passing through chlorine and silver atoms at positions indicated by the green and black arrows, respectively. The black curve corresponds to the calculation with χ^0 and the red curve corresponds to the calculation with χ. Left $\omega = 0$, right: $\omega = 2.855$eV and $\omega = 2.858$eV.

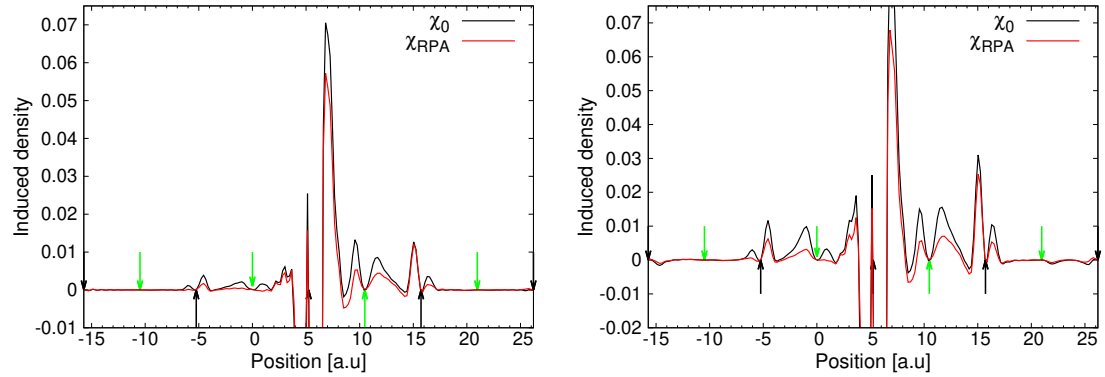

Figure 11.18: Induced density from Fig 11.16 for a perturbation localized around a silver atom along the line in the vertical direction and at $x = 0$, passing through chlorine and silver atoms at positions indicated by the green and black arrows, respectively. The black curve corresponds to the calculation with $\chi^0$and the red curve corresponds to the calculation with χ. Left $\omega = 0$, right: $\omega = 2.855$eV.

Localized perturbation

We now turn to localized perturbations. Figure 11.16 shows the difference between χ^0 and χ for a perturbation localized around chlorine or silver with both χ^0 and χ^{RPA}. The response of the system at the position of the localization is in phase opposition to the potential. The first difference to note is that the induced density is more localized in the case of the RPA than in the case of χ^0, as we can see comparing left and right columns. Figure 11.17 shows a cut along the [010] direction of the induced density for χ^0 and χ. The perturbation is localized around chlorine. The figure shows clearly that the intensity decreases when going from χ^0 to RPA, and that the RPA response decays faster than the independent particle one, especially for $\omega \neq 0$. Figure 11.18 shows the same thing, but for a perturbation localized on the silver atom. Globally, we have a more localized and weaker response of the system around the perturbation with RPA than with χ^0. However, the changes are smaller that one would naively expect by comparing the spectra of χ_0 and of the RPA (see for exemple Fig. 8.9). In order to understand whether these trends are specific features of AgCl or whether they can be understood on the basis of more general arguments, we will make a short excursion to the homogeneous electron gas (HEG).

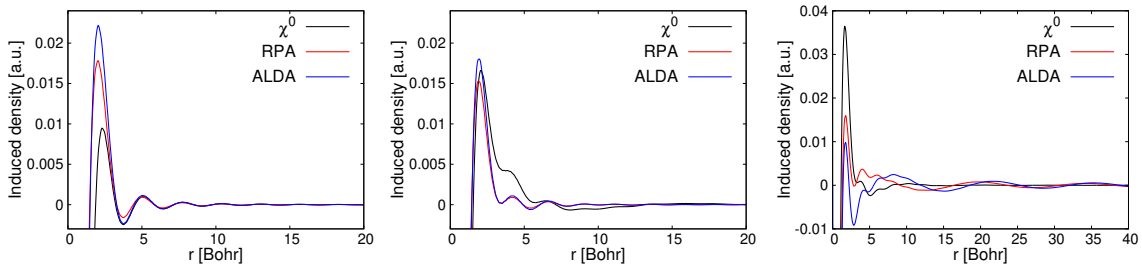

Figure 11.19: Response of the homogeneous electron gas with a density corresponding to $r_s = 1.6$: density induced by a localized perturbation situated at r=0 Bohr, as a function of the distance to the perturbation. The frequency of the perturbation is $\omega = 0$ (left), $\omega = 0.75\ E_F = 14.7$ eV (middle), and $\omega = 1.33\ E_F = 26$ eV (right panel).

Comparison with the homogeneous electron gas

In the HEG, the independent particle polarizability is given [190] as

$$\chi^0(q,\omega) = N\left(\frac{1}{2} - \frac{1-v_-^2}{4\bar{q}}\ln\left(\frac{v_-+1}{v_--1}\right) + \frac{1-v_+^2}{4\bar{q}}\ln\left(\frac{v_++1}{v_+-1}\right) + \frac{\pi i}{4\bar{q}}\left(\Theta\left(1-v_-^2\right)\left(1-v_-^2\right) - \theta\left(1-v_+^2\right)\left(1-v_+^2\right)\right)\right), \quad (11.19)$$

where $\bar{q}$= q/k_F, $v_\pm = \omega/qv_F \pm q/2k_F$ and N=$mk_F/2\pi^2\hbar^2$, with v_F the Fermi velocity and k_F the Fermi momentum. The Fermi energy E_F is defined as $k_F^2/2$ in atomic units. Note that because the system does not have a periodic potential, $\mathbf{q}$ runs over the full momentum space and χ^0 and χ are functions, not matrices. In particular, the RPA polarizability reads

$$\chi(q,\omega) = \frac{\chi^0(q,\omega)}{1 - v_q\chi^0(q,\omega)}. \quad (11.20)$$

Fig 11.19 shows the response of the HEG to a localized perturbation, comparing results obtained with χ^0 and χ, respectively. The parameter r_s is set such that it corresponds to the density in silver chloride, considering that only valence electrons, and not semi core electrons, contribute to the screening density. This correspond to $r_s \simeq 1.6$ Bohr. The different panels are results for different frequencies of the external perturbation. Since we have analytic expressions for the response functions, we can perform the full integration over momentum space and simulate the effect of a perfectly localized, δ-function perturbation, located at $r = 0$. As expected, the response is maximal at $r = 0$ where χ^0 diverges, followed by an oscillatory response at larger distances. The oscillations of the induced density are known as Friedel oscillations. They have a period π/k_F [191].

Because of the quite high density (small r_s), the system is strongly screening the perturbation. This screening is due to the density close to the perturbation, whereas after a distance of more than a few (less than 10) Bohr there is only little induced density, especially at $\omega = 0$. The RPA has globally a tendency to reduce the induced density with respect to the independent-particle response, which, as explained earlier for AgCl, can be understood by the fact that one can express the RPA response to an external potential as $\chi^{RPA}V^{\text{ext}} = \chi^0\epsilon^{-1}V^{\text{ext}}$, which means that the RPA sees an effective perturbation that is screened with respect to the external one. It should be noted that this also changes the shape of the effective perturbation; for example, for a localized external potential $\epsilon^{-1}V^{\text{ext}}$ may be more extended than V^{ext} alone. The extension of the induced density over a few Bohr and the reduction by the RPA observed in the HEG reproduce the tendencies observed in AgCl (see Sec.11.3), which means that these can be explained by an effect of the average density.

The response at the highest frequency, in the right panel, is much less localized and shows a new oscillation, of longer wavelength. To understand this phenomenon, it is useful to look at

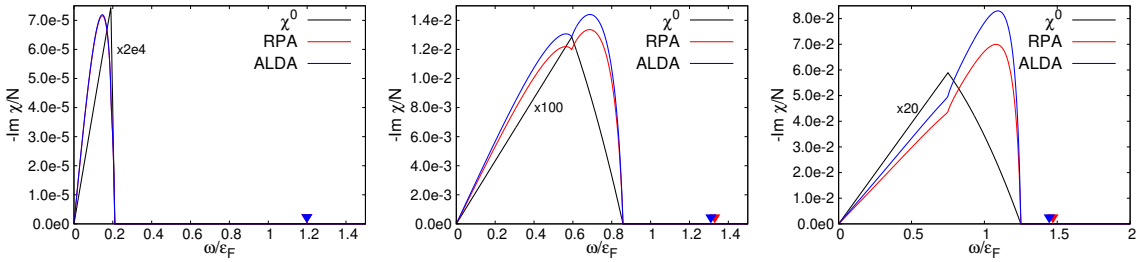

Figure 11.20: Response of the homogeneous electron gas with a density corresponding to $r_s = 1.6$: minus the imaginary part of the polarizability as a function of frequency. The independent particle polarizability is shown in black, the RPA polarizability in red, and the ALDA result in blue. The polarizability is computed at different momentums: 0.1 k_F in the left panel, 0.36 k_F in the middle panel and 0.56 k_F in the right panel. The position of the RPA (ALDA) plasmon peak is indicated by the red (blue) triangle.

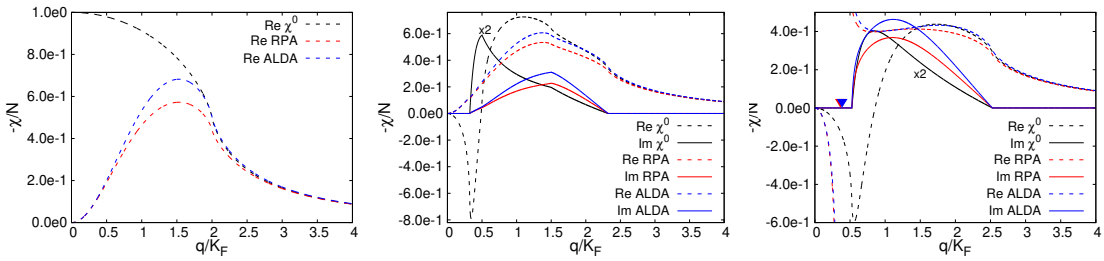

Figure 11.21: Response of the homogeneous electron gas with a density corresponding to $r_s = 1.6$: Minus the real and imaginary part of the polarizability as a function of momentum, at different frequencies. The independent particle polarizability is shown in black, the RPA polarizability in red, and the ALDA result in blue. The position of the RPA (ALDA) plasmon peak is indicated by the red (blue) triangle.

the spectra of the response functions. These are shown in Fig. 11.20 as function of frequency for different momentum transfers, and in Fig. 11.21 as function of momentum transfer for different frequencies. At first sight, Fig. 11.20 might suggest that the response functions are similar. However, note that the intensity of the imaginary part of χ^0 is scaled by a q-dependent factor in order for the spectrum to fit in the graph: the spectrum of χ^0 is more intense by orders of magnitude, especially at small q. Moreover, the red triangle on the frequency axis above $\omega = E_F$ indicates the position of a sharp plasmon that occurs in the RPA, but is absent in χ^0. It cannot be seen in the figure because the latter contains no extra broadening. It is, however, an important ingredient for the screening.

At $\omega = 0$, the real part of χ^0 is much larger than that of χ^{RPA} for small wavevector, whereas at larger wavevector the two curves join. Since our perturbation is localized, all wavevectors are integrated, and finally the screening change of the RPA with respect to χ^0 remains moderate. For a frequency ω where the dispersing plasmon frequency $\omega_p(q)$ yields a solution q_p to the equation $\omega = \omega_p(q_p)$, instead, the induced density will be dominated by the response function at q_p, which means that it oscillates with the period corresponding to q_p. As the figures show, there is, for example, a plasmon solution for $\omega = 1.33\ E_F$, which is $q_p = 0.36\ k_F$. This means that the period of the induced oscillation is $2\pi/(0.36k_F)$, about 6 times longer than the Friedel oscillation of period π/k_F, which is indeed what Fig. 11.19 shows. However, this result will be important for the exciton in AgCl, as we will see later. Since there is no plasmon in χ^0, no such oscillations are induced in the independent-particle response. We do not have a clear plasmon resonance in the frequency range studied in AgCl (see Fig. 8.8); for this reason, we could not observe this phenomenon for the plasmon in our material.

Finally, we can try to use use the HEG in a different way to imagine what might happen when the electron-hole interaction is included in the calculations. Although this will be done in the next section using the BSE for AgCl, we can get an idea by simply looking at some TDDFT results, approximated in the ALDA. In this case, the Coulomb interaction that appears in the RPA is reduced by a negative constant f_{xc}, since the new kernel of the Dyson equation is $v_c + f_{\text{xc}}$ instead of v_c (see Eq. (5.10)), and f_{xc} is just a negative number in the ALDA. We would therefore expect that the ALDA counter-balances the effect of the RPA. Moreover, since the Coulomb interaction decreases with increasing q, the relative effect of the ALDA should increase for larger wave vector, whereas it should not be visible for vanishing q, where the Coulomb interaction diverges. The blue curves in the spectra confirm this scenario. Moreover, the ALDA changes the position of the plasmon resonance, moving it, for a given q, to slightly lower energy. Vice versa, for a given frequency ω the ALDA q_p where $\omega = \omega_p(q_p)$ is larger than the RPA one, because the plasmon dispersion is $\omega_p(q) \approx \omega_p(q=0) + \alpha q^2$ with $\alpha > 0$. This leads to a more rapid oscillation of the induced charge in real space, which can indeed be observed in Fig. 11.20.

In AgCl, the electron-hole interaction creates a sharp bound exciton peak, which also has dispersion. The HEG has no gap, and therefore no bound exciton. However, we may expect a situation similar to the plasmon in the HEG: for a given energy in the range of the excitonic transitions, a certain wavevector should dominate the response, which will then lead to long-range induced density. The next section will explore to which extent this is true.

11.5 Effects of the electron-hole interaction on the induced density

In this section we study the effects of the electron-hole interaction on the induced density in AgCl and compare it to the induced density due to χ_0 and χ_{RPA}. In is known that the Bethe-Salpeter equation changes the transition energies, and also mixes the transitions. We thus expect a different picture of the induced density.

The BSE induced densities are calculated as explained in Ch. 5. The BSE calculations are G^0W^0+BSE calculation, meaning that the screening used is the RPA one and a scissor is of 1.9 eV is used in order to emulate the G^0W^0 correction to the Green function. As studied previously, getting a converged dielectric function with BSE requires a dense grid of **k**-points and a large number of valence and conduction bands. Moreover to calculate the full polarizability in a BSE calculation is a difficult task, because in our implementation the excitonic Hamiltonian has to be fully diagonalized. Finally no shifted grid can be used to help the convergence as the effect on the induced density is unknown. It is important to converge the polarizability matrix because, in addition to the need of many transitions at different energies to get a convergence with respect to the energy, the induced density of a single exciton needs an accurate description of the eigenvector (the A^{λ}_{cv} factor) to form this exciton. Thus a convergence of the induced density was realized with respect to the grid size and the number of bands included in the calculation, in order to confirm the validity of the results presented in the following. However, calculations of the induced density with BSE require the diagonalization of the excitonic Hamiltonian, a time consuming calculation, and even more so when this have to be done for many momenta. The convergence parameters are thus a trade off between convergence and limitation. The parameters used in the following are 8 valence bands, 8 conduction bands and a $4 \times 4 \times 4$ MP **k**-point grid.

Effect of the electron hole interaction

Inverse dielectric function

The imaginary part of the inverse and direct dielectric function at $\mathbf{q} \to 0$ are plotted in figure 11.22. RPA and BSE calculations are presented. For the inverse dielectric function, at low energy, the two spectra are similar, the main difference is a shift of roughly 0.3 eV at low energy. At higher energy, we observe a shift of the energy and a modification of the peak's intensity: the intensity increases when going from RPA to BSE. This is in contrast with what is happening for the real and imaginary part of the dielectric function, shown on the center and right panel where, especially

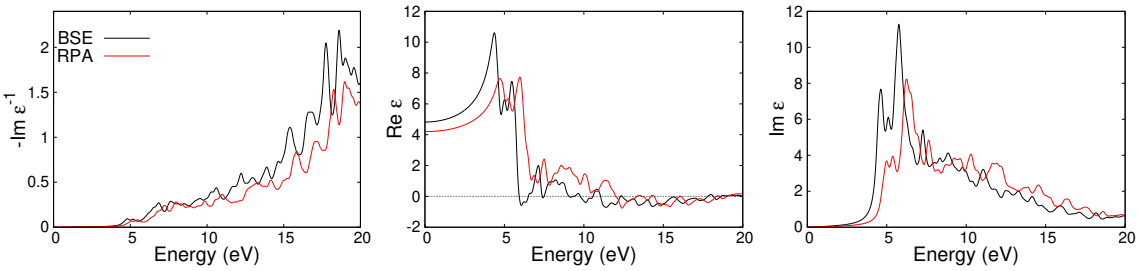

Figure 11.22: Left: Imaginary part of the inverse dielectric function. Center: real part of the dielectric function, right: imaginary part of the dielctric function. Two calculations are realized: a RPA calculation, shown in black, and a BSE calculation, shown in red.

in the imaginary part, one can see a crossover of the curves. Most importantly, one can see the formation of the exciton at low energy. Similar observations can be made for the real part of the dielectric function with a global shift and a change of intensity at all energies. Let us now see how this influences the induced density.

The energies used for the perturbation in the following are 0, and 4.776 eV for RPA and 4.541 eV for BSE. The low energy corresponds to the first transition visible in the respective spectrum with a small broadening of $\eta = 0.01$ eV.

Planewave perturbation

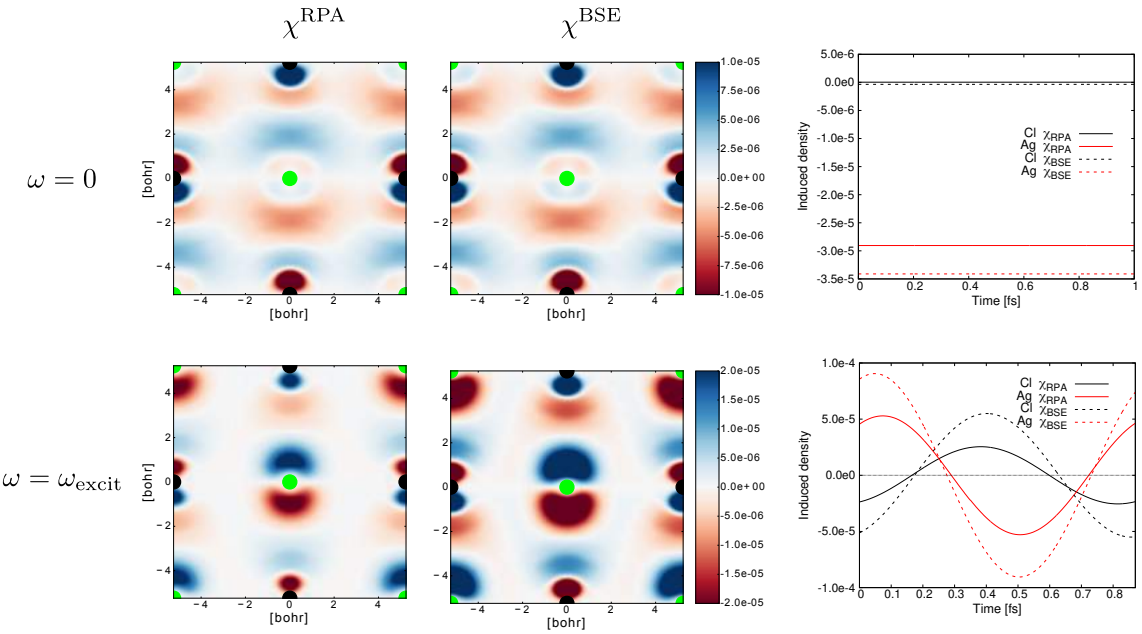

Figure 11.23: 2D cut of the induced density computed with different polarizabilities. The left column shows the induced density using the RPA polarizability and the center column show the induced density using the BSE polarizability. The right column shows the evolution in time of the induced density at two different positions. The perturbation is a plane wave with vanishing momentum oriented in the vertical direction. Two energies are used in this calculation: $\omega = 0$ on the top row, while the bottom row shows the case in which $\omega = \omega_{\mathrm{excit}}$, the lowest optically allowed excitation. In RPA $\omega_{\mathrm{excit}} = 4.77$ eV, while in BSE $\omega_{\mathrm{excit}} = 4.54$ eV. The momentum transfer is $\mathbf{q} \to 0$.

In figure 11.23 are shown 2D cuts of the induced density. The left hand-side shows the induced density computed with RPA and the right hand-side shows the induced density using the BSE. The shape of the induced density are similar for RPA and BSE. The intensity of the response of the system is larger for BSE than for RPA. This is valid both at vanishing and finite perturbation energy. This is in agreement with the expectation from the HEG, where the f_{xc} counteracts the effect of the RPA.

Localized perturbation

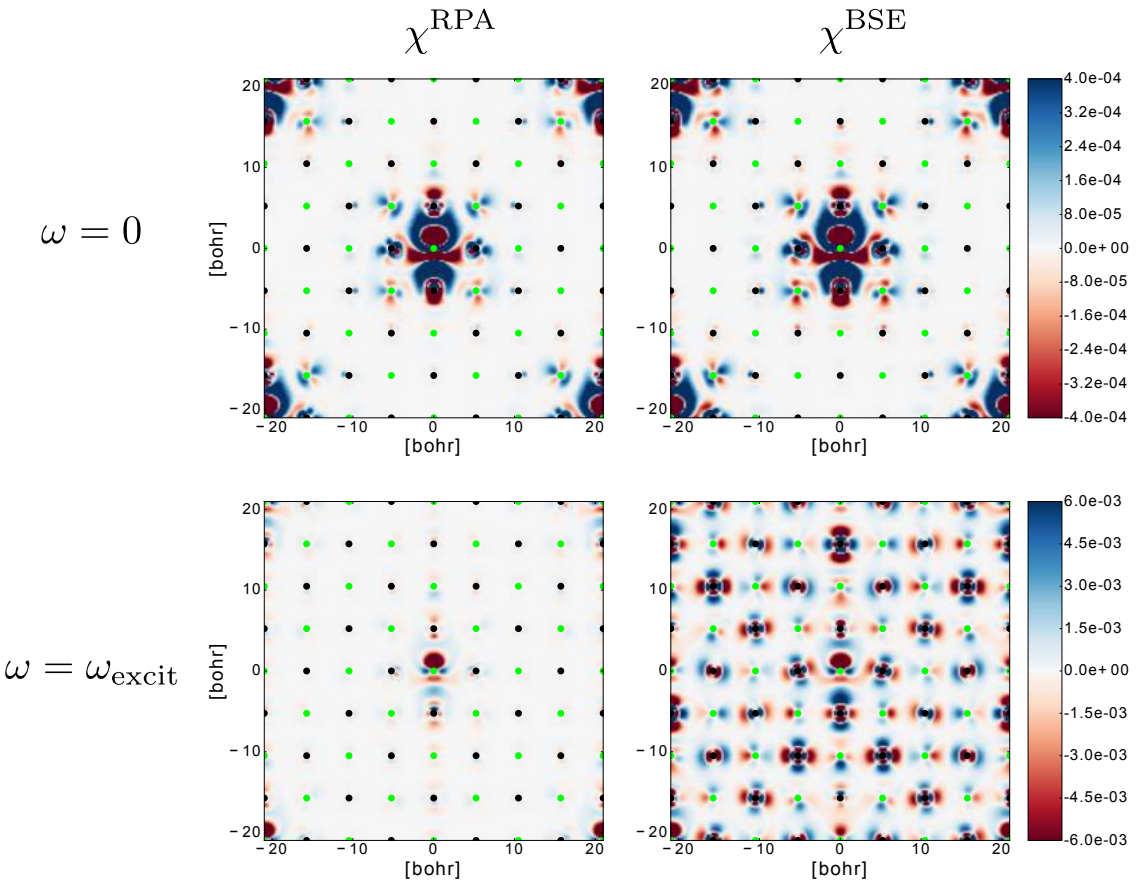

Figure 11.24: 2D cut of the induced density computed with different polarizabilities. The left column shows the induced density using the RPA polarizability and the right column shows the induced density using the BSE polarizability. The right column shows the evolution in time of the induced density at two different position. The perturbation is localized around chlorine. Two energies are used in this calculation. The first energy is $\omega = 0$ and is shown on the top row and the second is the energy of lowest optically allowed transition: 4.78 eV in RPA and 4.54 eV in BSE.

Figure 11.24 shows the induced density for a localized perturbation. Similarly to what has been done previously, figure 11.25 shows a 1D cut of the induced density in the vertical direction. At ω=0, the RPA and BSE induced densities look similar (also confirmed by the left panel of Fig. 11.25). The intensity for the BSE polarizability increases slightly with respect to the RPA polarizability.

One might find these results quite disappointing: whereas the exciton dominates the optical spectrum, it does not seem to have a significant impact on the induced charge. However, the analysis of the HEG tells us that major changes in the density response are found when one looks in the vicinity of a sharp resonance which, in the case of the HEG, was the plasmon. Here in AgCl,

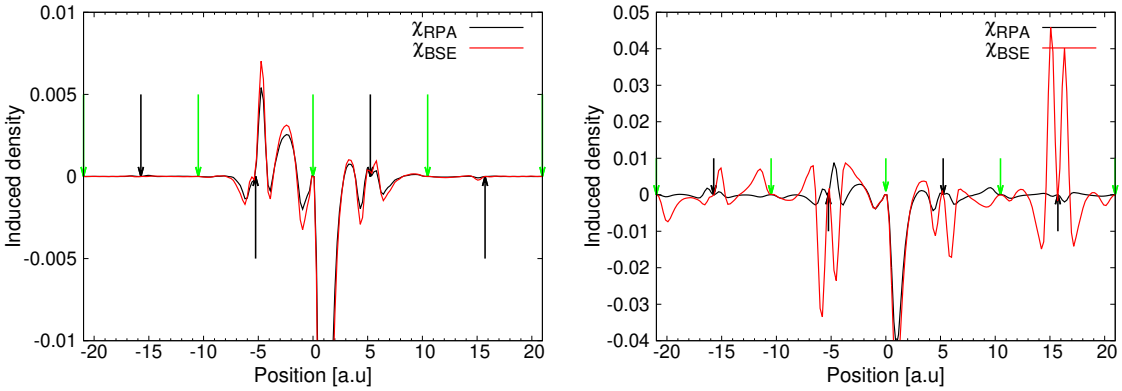

Figure 11.25: 1d cut of the induced density from fig.11.24. Left: $\omega = 0$, right: energy of the lowest optically allowed transition. The time is set to 0 fs.

the exciton may play a similar role, since it also constitutes a sharp, dispersing resonance in the response function. This can only be seen when the broadening is much smaller than the exciton binding energy, which explains our choice of $\eta = 0.02$ eV for this study. The second row of Fig. 13.24 shows the induced density when the frequency of the perturbation hits a resonance, here at q=0.

As in the case of the HEG plasmon, when hitting the exciton resonance the induced density exhibits a dramatic change, extending over the whole range of the picture. This is also highlighted by the line cut in Fig. 13.25. It only happens in the BSE calculation, since of course the RPA does not produce the bound exciton. A similar phenomenon is seen when the perturbation is localized around silver, as shown in Figure 13.26. Also note the detailed structure of the induced density, which always shows strong intensity on silver atoms with a characteristic *d*-shape, independently of the position of the perturbation.

In conclusion, this chapter contains a detailed analysis of methodological aspects, the rich phenomenology and its physical origin for the density induced by an external perturbation. Although silver chloride is far from the homogeneous electron gas, the HEG could be used to understand much of the observations. In particular, we could highlight the important changes induced by sharp resonances in the response function, which leads, in the case of a bound exciton, to an induced charge of very long range.

This is a pioneering study, since the effect of the electron-hole interaction on the induced density had not been analyzed in an ab initio framework. Therefore, much remains still to be done, in particular, exploring the dispersion of the exciton, and possible consequences on other properties of the material. This is left for future work.

Some videos of the real space time dependent induced densities can be found at https://etsf.polytechnique.fr/people/arnaud/density_movies.

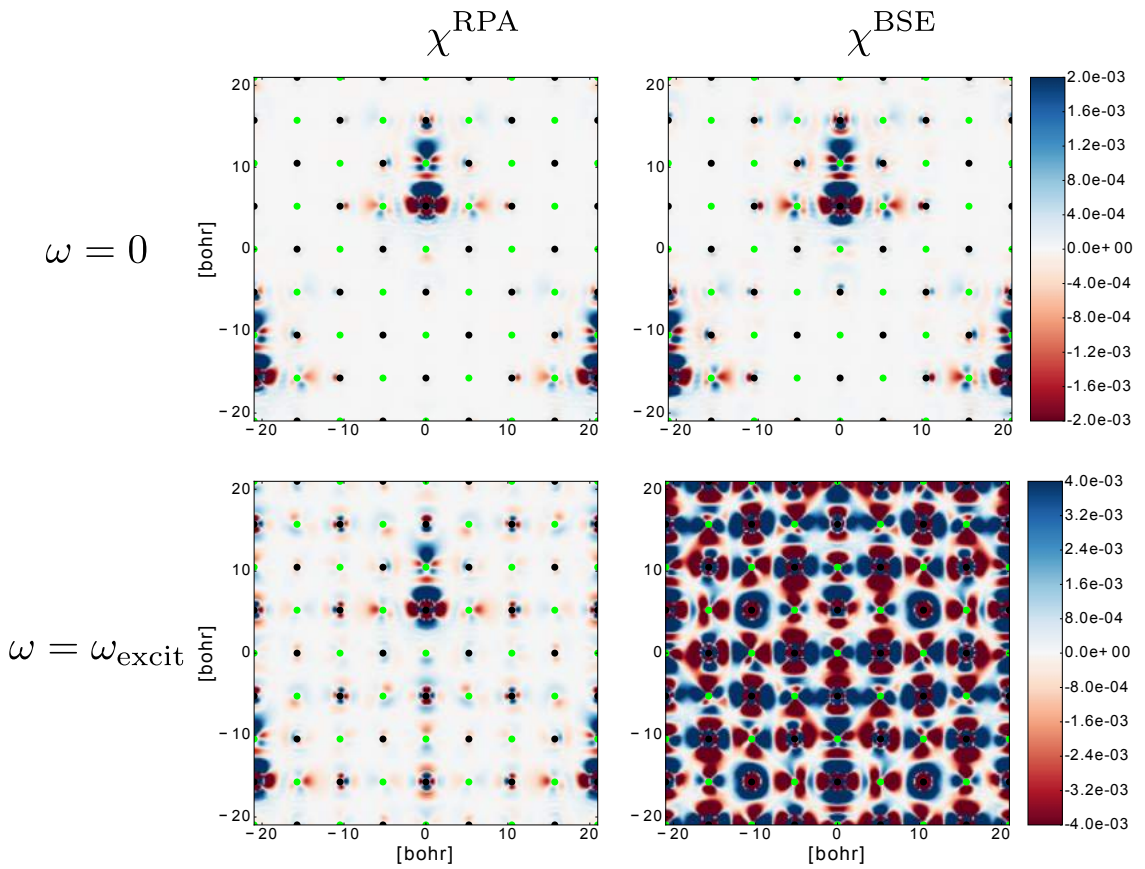

Figure 11.26: 2D cut of the induced density computed with different polarizabilities. The left column shows the induced density using the RPA polarizability and the right column shows the induced density using the BSE polarizability. The perturbation is localized around silver. Two energies are used in this calculation. The first energy is $\omega = 0$ and is shown on the top row and the second is the energy of the lowest optically allowed transition: 4.78 eV in RPA and 4.54 eV in BSE.

Chapter 12

Ag-AgCl heterostructures

As summarized in the Introduction (see Ch. 1), the colors of Becquerel's photography can be explained in terms of excitation and disexcitation processes involving Ag nanoparticles embedded in AgCl. In this context, a key question that should be addressed is what happens to the electronic charge at the interface between the Ag nanoparticles and AgCl when the electrons in the nanoparticles are excited by the light.

This question has a relevance that goes well beyond Becquerel's photography. Indeed, it is related to the general phenomenon of charge dynamics at the interfaces of different materials, which takes places in many other important situations, such as in photovoltaic devices. Therefore, the present study was driven also by the goal of developing a new theoretical tool of wider applicability. This methodological goal has required to build and study a simple model Ag-AgCl interface.

In this chapter, the electronic and dielectric properties of a model Ag-AgCl heterostructure will be presented on the basis of DFT and TDDFT calculations. How *ab initio* calculations can be simplified thanks to the effective medium theory will be further discussed. Finally, an outlook will be given on the calculation of induced charges at the interface.

12.1 Which Ag-AgCl interface?

The size of the nanoparticles observed in Becquerel's photochromatic images is of the order of 5 to 150 nm. It is hence clear that a fully *ab initio* description of those images is out of reach, and probably not even very useful. On the other side, the large size of the nanoparticles implies that one can safely model the interface between the Ag nanoparticles and AgCl as the interface between two planar surfaces of Ag and AgCl. Indeed, the electronic excitations at the interface between the real Ag nanoparticles and AgCl are expected not to depend strongly on the curvature of the nanoparticles in the real material, which can be neglected altogether. In the present computational scheme that makes use of periodic boundary conditions, this amounts to study a heterosystem made of two slabs, one of silver and the other of silver chloride, repeated infinitely. Each slab is also infinitely extended in the plane perpendicular to the stacking direction.

The following two issues need to be addressed in order to study this Ag-AgCl heterostructure. First, the lattice parameters of bulk Ag and AgCl do not match. Here the goal is to identify and model the simplest possible Ag-AgCl interface. Possible atomic relaxation or reconstruction effects are a whole subject of study on their own, beyond the scope of the present investigation. As a pragmatic solution to this issue, the lattice parameters and crystal structure of silver will be adapted in order to match those of silver chloride while still making sure that the main spectroscopic features of silver can be found in this model material. Second, the system under study is fully periodic: an infinite number of images of the two slabs are stacked on top of each other. This can produce spurious interactions between different slabs, which has to be avoided.

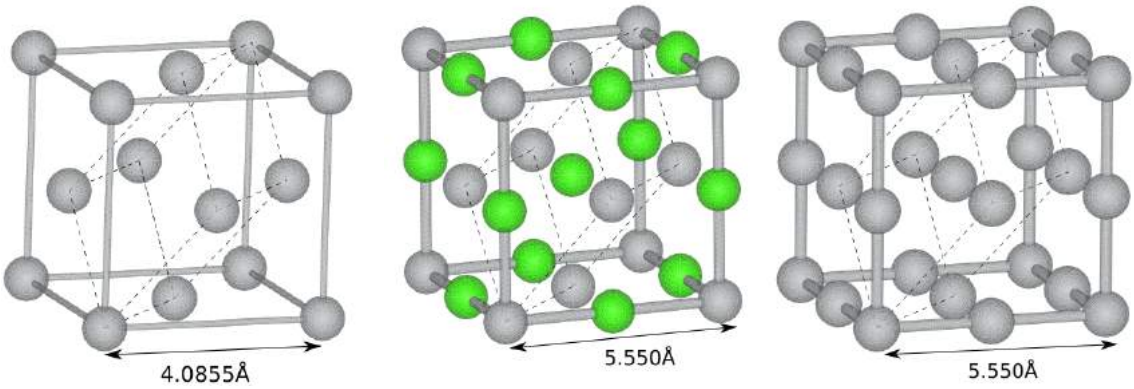

Figure 12.1: Different crystal structures studied here: (a) silver, (b) silver chloride and (c) silver in the silver chloride lattice: chlorine atoms are replaced by silver atoms everywhere. Silver (chlorine) atoms are grey (green).

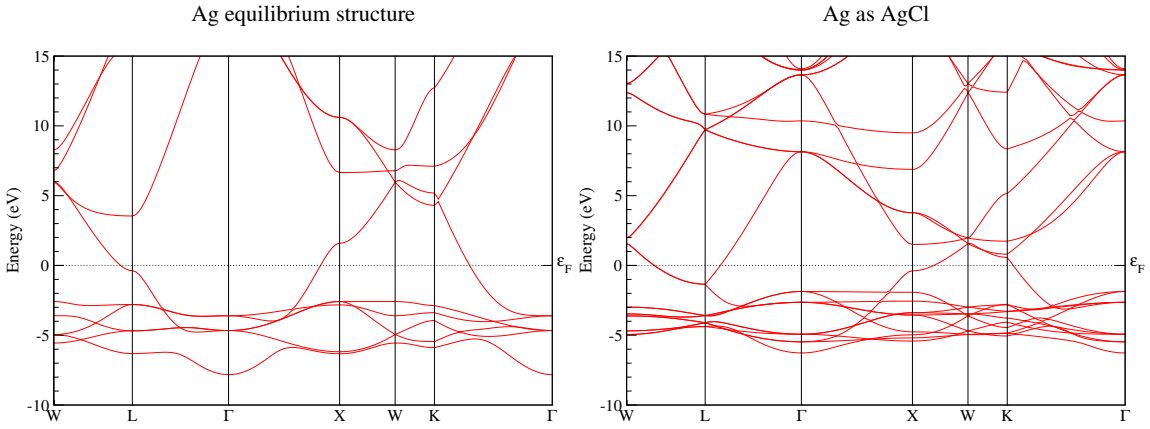

Figure 12.2: Left: LDA band structure of silver within its ground-state fcc crystal structure. Right: LDA band structure of silver within the crystal structure of silver chloride.

12.2 Silver with AgCl crystal structure

We will first compare the electronic properties of bulk Ag in its equilibrium crystal structure with a model silver in which silver atoms are located in the lattice of AgCl (see Fig. 12.1). In practice, this corresponds to replacing all Cl atoms of AgCl by Ag atoms. The aim of this study is to test if this model structure still provides a reasonable description of the electronic properties of real silver.

Silver has a fcc crystal structure with lattice constant $a = 4.0855$ Å. The nearest-neighbor distance is 2.8889 Å, while the mean electronic density is 0.0587 Å^{-3}. In the silver chloride structure, instead, the lattice constant is $a = 5.550$ Å and the nearest neighbor distance is 2.775 Å. The mean electronic density of this artificial silver thus becomes 0.0468 Å^{-3}, i.e. 20 % lower.

Band structure

The band structures of fcc silver and silver with the silver chloride crystal structure are shown in Fig. 12.2. The calculations are done within the LDA, using a $10 \times 10 \times 10$ **k**-point grid, a smearing of 0.01 Hartree and a cutoff energy of 150 Hartree.

Silver is metallic with both crystal structures (the Fermi energy is set to 0 in both cases). We further observe that going from the equilibrium fcc to the AgCl crystal structure, the lowest empty

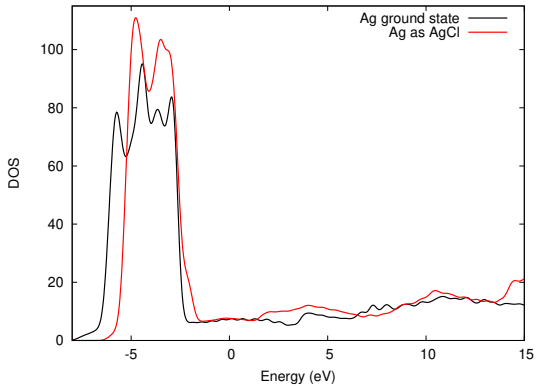

Figure 12.3: Density of states of silver in two different crystal structures. The black curve is fcc silver and the red curve is silver in the AgCl crystal structure. The Fermi energy is set to zero for both calculations.

bands are lowered and the fully occupied bands are slightly shifted upwards. The width of the occupied Ag 4*d* bands is reduced by 0.9 eV.

Density of states

The computed DOS for the two crystal configurations is plotted in Fig 12.3. Both calculations are done on a $18 \times 18 \times 18$ Monkhorst-Pack grid of **k**-points with 4 shifts, with a 0.01 Ha smearing and a cutoff energy of 150 Ha.

In the DOS we can identify a common feature for both structures, in the energy region between -7 eV and -2 eV, which corresponds to silver 4*d* states. The width of these Ag 4*d* states is smaller for the silver chloride structure than for the silver fcc crystal structure. Overall, the electronic structure remains qualitatively similar. We can therefore conclude that even though the atomic structure is strongly altered, the electronic properties of silver in the AgCl lattice are still a reasonable model to qualitatively describe real fcc silver, allowing for much simpler simulations of the Ag-AgCl interface.

12.3 The Ag-AgCl interface: electronic properties

The Ag-AgCl heterostructure is obtained alternating silver and silver chloride slabs. The Ag-AgCl layers are stacked along the [100] direction of AgCl (see Fig. 12.4). The primitive 2D unit cell of the AgCl layers is formed by 2 atoms: one Ag and one Cl. Each Ag layer has the same lattice as AgCl, with Ag at all sites. Also the distance between the two slabs of Ag and AgCl is set equal to the distance between the silver chloride layers.

One question that will be addressed is how many layers are needed in each slab in order to avoid spurious interactions between periodic replicas.

Evolution of the density of states with the number of layers

In this part we study the dependence of the density of states of the heterostructure on the number of layers in each slab. These DOS will be compared to the DOS of bulk silver chloride and bulk silver. In order to take into account the increasing number of states, the DOS of each heterostructure is normalized to the total number of layers per slab, while the DOS of silver and silver chloride is normalized such that the sum of their integrals is the same as integral of the DOS of the heterostructures.

Figures 12.5 and 12.6 show the density of states of the heterostructures for different numbers of layers, from 6 to 14. In each case, half of the number of layers is Ag and the other half is AgCl.

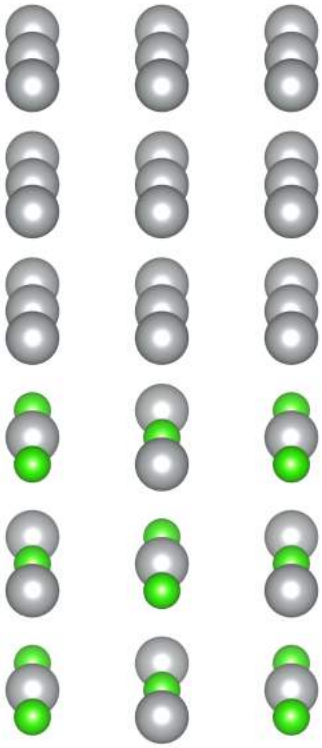

Figure 12.4: Heterostructure made of 6 layers, 3 of silver chloride and 3 of silver. The top layer is a repetition of the bottom layer.

In these comparisons, the first problem that arises is how to align the energy scales of the different DOS. Since Ag and the Ag-AgCl heterostructures are metallic, their Fermi energy can be simply set to zero. AgCl instead is insulating: the zero of the energy scale could be set anywhere inside the gap. We will align the Ag $4s$ semicore level of AgCl to the corresponding $4s$ level of Ag. With this aligment, the zero of the energy scale for AgCl turns out to be 1.0 eV above the top of the valence band.

The left panel of Fig. 12.5 shows an extended overview of the DOS, with the main features located at the following energies: the Ag $4s$ semicore levels at -90 eV, the Ag $4p$ at -55 eV, and the Cl $3s$ at -16 eV. The right panel of Fig. 12.5 shows a zoom on the valence band starting at -6 eV.

Fig. 12.6 compares the Ag $4s$ semicore levels at -90 eV (left panel) and Ag $4p$ at -55 eV (middle panel). In each case we observe three peaks. As the number of layers increases, the peak at lowest binding energy (i.e. on the right hand side of the plot) gains intensity, the middle peak loses intensity, and the highest binding energy peak (i.e. on the left hand side of the plot) has no significant change in intensity after the 8 layer structure. At the same time we observe a shift of the peak energies. These variations are due to the fact that silver is located in different environments. The first situation is silver surrounded only by silver atoms; the second case is silver surrounded by chlorine atoms; the third one is silver at the interface, a situation that corresponds to a combination of the first two environments.

For these semicore states, the DOS of bulk silver and silver chloride (dashed and solid grey lines) match well the DOS of the heterostructures. For both the $4s$ and $4p$ states, the peaks of bulk silver overlap with the peaks at highest absolute energy of the heterostructure, meaning that these states are due to Ag surrounded by Ag. The $4s$ and $4p$ peaks of AgCl match the corresponding low absolute energy peaks of the heterostructures (note that $4s$ states have been aligned), meaning that those peaks are due to Ag surrounded by Cl. The feature between the two peaks in the DOS of the heterostructure hence originates from the mixed environment of Ag. Its relative intensity

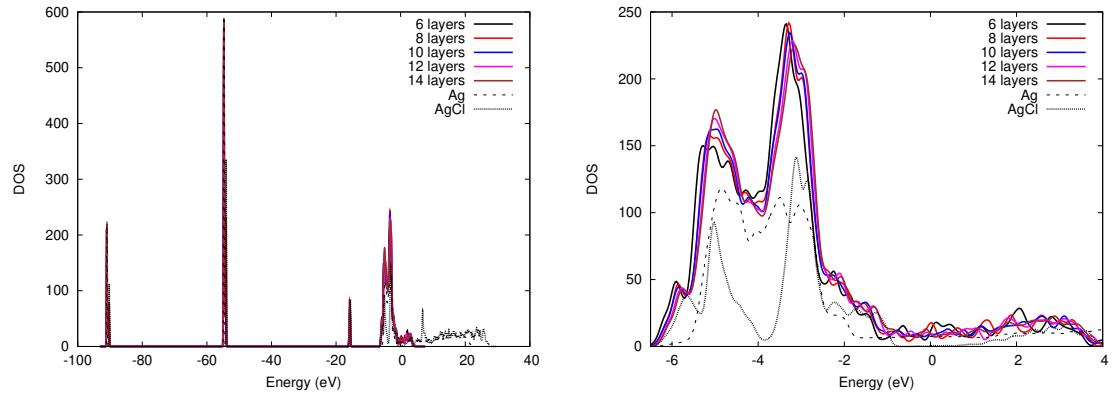

Figure 12.5: Density of states of the heterostructure for different number of layers normalized to the number of layers. Right: Zoom on the valence band.

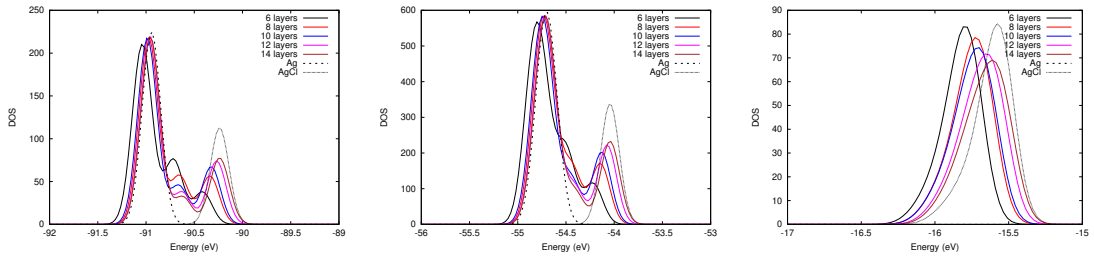

Figure 12.6: Density of states of the heterostructure for different number of layers. (Left) Ag $4s$ semicore states, (center) Ag $4p$, and (right) Cl $3s$ states.

is reduced as the number of layers increases, since the fraction of atoms at the interface decreases with respect to the total numbers of atoms.

On the contrary, comparing the DOS of bulk silver and silver chloride with the DOS of the heterostructures for the Cl $3s$ states (see right most panel in Fig. 12.6), we do not observe the appearance of new peaks. As a matter of fact, the close environment of chlorine is the same at the interface or in the bulk. Still we find a small shift to lower energies and a small increase of the width of this core level with increasing number of layers.

For the valence band (see right panel of Fig. 12.5) there is also a shift (0.2 eV between 6 layers and 14 layers) and a change in intensity of the different peaks: the peak at -5 eV increases while the peak at -3 eV loses intensity.

To make a detailed analysis of the valence band, in Fig. 12.7 we take the difference between the sum of the DOS of bulk Ag and AgCl and the DOS of the heterostructures with slabs of 6 layers (left panel), 10 layers (middle panel), and 14 layers (right panel). Overall we see that the sum of silver and silver chloride DOS (black lines) is able to reproduce correctly the shape of the DOS of the heterostructures. The agreement is better for the heterostructure with 14 layers than for the one with 6 layers: by increasing the number of layers the heterostructure tends to the sum of two bulk systems. The difference plots shown in the bottom part of each panel evidences the effect of the interface between Ag and AgCl. We find that the shape of the curves is qualitatively similar in the three cases.

Electronic density distribution at the Ag-AgCl interface

We now analyse the distribution of the electronic density in the heterostructure. To this end, we take the difference of the density of the Ag-AgCl heterostructure with the density of bulk silver on the Ag side of the slab and with the density of bulk silver chloride on the AgCl side of the slab.

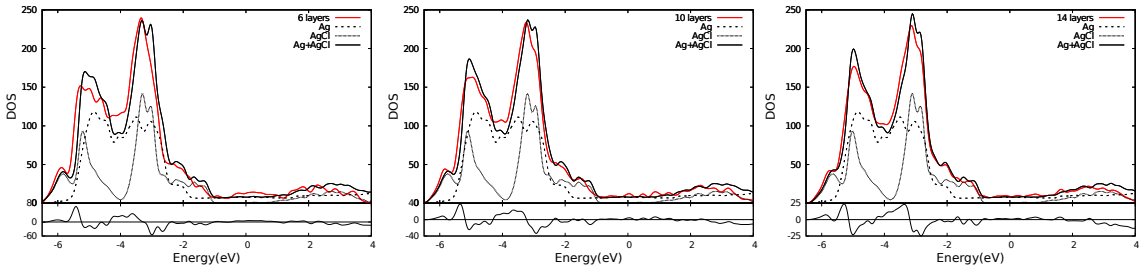

Figure 12.7: Density of states for the heterostructure (red lines), bulk Ag (dashed lines), bulk AgCl (grey thin lines) and the sum of Ag and AgCl (black lines). The heterostructure is made of 6 layers (left panel), 10 layers (middle panel), and 14 layers (right panel).

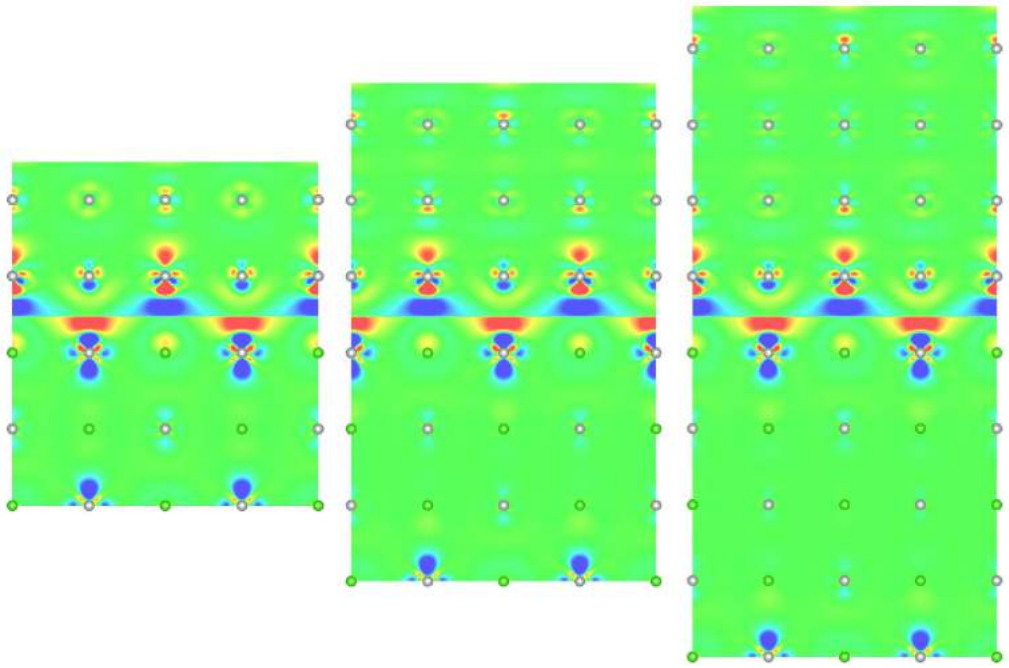

Figure 12.8: Difference between the electronic density of the heterostructure and the electronic density of bulk silver (in the top half of the slab) or bulk silver chloride (in the bottom half of the slab). The vertical direction is the stacking direction. The heterostructure has a total number of 6 layers (left panel), 8 layers (middle panel), and 10 layers (right panel). The color key goes from red (positive difference) to blue (negative difference), with a maximum at 0.04 and a minimum at -0.04 a.u.

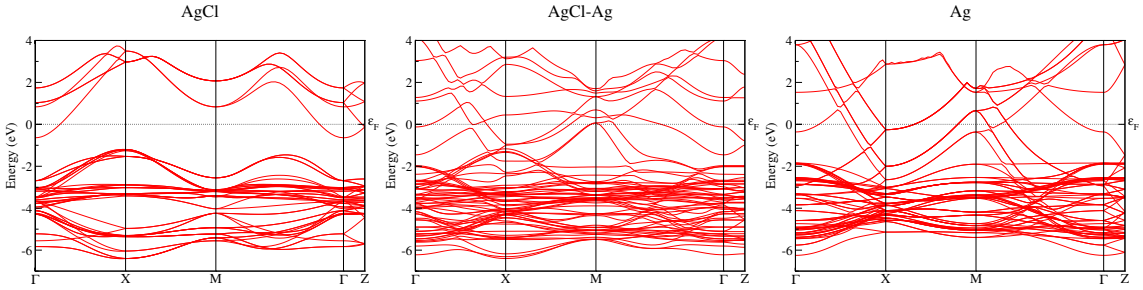

Figure 12.9: Valence and conduction band structure of the system with 6 layers. Left is pure silver chloride, right is pure silver and middle is the heterostructure

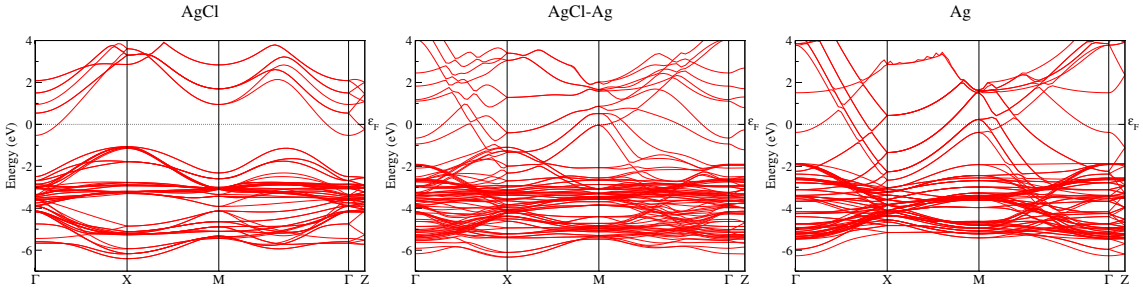

Figure 12.10: Valence and conduction band structure of the system with 8 layers. Left is pure silver chloride, right is pure silver and middle is the heterostructure.

The three panels of Fig 12.8 show the result for the heterostructures with 6, 8 and 10 layers, respectively. In each panel, the vertical direction is the stacking direction and the interface at the center separates the Ag slab (on the top) from the AgCl slab (at the bottom). Since the two slabs are periodically repeated, also the atoms at the top and at the bottom of each panel form other Ag-AgCl interfaces. Positive density differences are represented in red, while negative differences are represented in blue. The maximum of the color scale is +0.04 and the minimum is -0.04.

On the silver (top) side, atoms at the interface facing a chlorine atom get more electronic charge, while atoms facing silver atoms lose a fraction of electronic density. On the silver chloride (bottom) side, chlorine atoms at the interface get some charge in the direction towards the interface, while silver atoms at the interface lose electronic density. From the shape of the density differences we can identify a change of the occupation of the Ag 4*d* orbitals. The variations are more pronounced and extend deeper on the silver side. Those variations decay fast with the distance from the interface: two or three layers are enough to reach the bulk limit where the density difference is zero (green areas in the plots).

Band structure of the heterostructure

To conclude the analysis of the electronic properties of the heterostructure, in Figs. 12.9, 12.10, and 12.11 we compare the band structures of the heterostructures with 6 layers, 8 layers, and 10 layers, respectively, with the band structures of the slabs of Ag or AgCl with the same number of layers. For pure AgCl the zero of the energy axis has been set such that the 4*s* state of AgCl and of the heterostructures are aligned.

In all the cases the band structures of the heterosystems can be matched with those of the two components separately. It becomes evident that some empty bands of pure AgCl become occupied in the heterostructure.

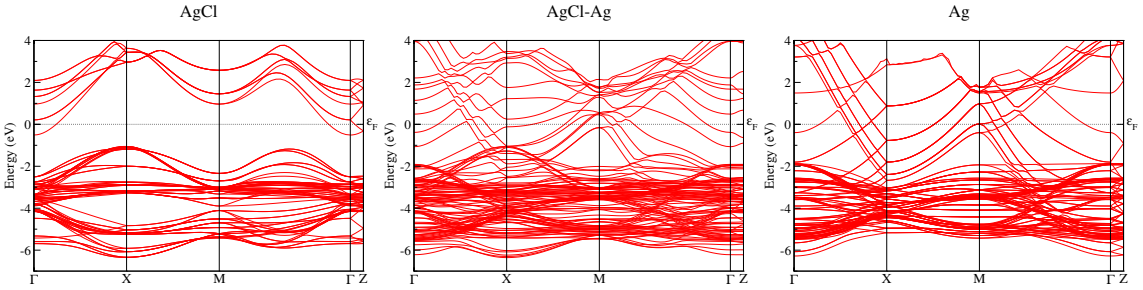

Figure 12.11: Valence and conduction band structure of the system with 10 layers. Left is pure silver chloride, right is pure silver and middle is the heterostructure.

12.4 Dielectric properties: *ab initio* calculations

In this section we will study the macroscopic dielectric function of the heterostructure. The calculations will be done within the RPA as a function of the number of Ag and AgCl layers in the slabs, and by varying the momentum transfer **q**. The RPA spectra will be also compared to calculations done within the ALDA.

The calculations are carried out with a $8\times8\times4$ grid of **k** points. The cutoff for the representation of the wavefunctions is set to 220 eV, while the cutoff of the dielectric matrix is 30 eV. All empty bands up to an energy of 24 eV above the Fermi level are included in the calculations.

Dependence on the number of layers

We first consider heterostructures where the number of silver layers is equal to the number of silver chloride layers. The total number of layers is 2, 4, 6, 14, and 20.

The real and imaginary parts of the macroscopic dielectric function, together with the loss functions are plotted in Fig 12.12. Two momentum transfers, $\mathbf{q} = (1/4, 0, 0)$ and $\mathbf{q} = (1/2, 0, 0)$, within the plane parallel to the interface are considered: their size is 0.21 $\text{Å}^{-1}$and 0.42 $\text{Å}^{-1}$for the left and right columns, respectively.

For the heterostructure with only one silver and one silver chloride layer, the imaginary part of the macroscopic dielectric function (top panels) has a structure on the low energy side around 2.5 eV that is is strongly damped by increasing the number of layers. At the same time, the energy of the main peak moves towards higher energy. Also by increasing the momentum transfer the spectral weight is shifted to larger energy. In the largest heterostructures with 10 Ag and 10 AgCl layers, the main peak for the larger **q** (top most right panel) is located at 7.5 eV. At the same momentum transfer, by increasing the number of layers a second structure also develops on the high energy side of the main peak. Its energy and intensity oscillate as a function of the number of layers. Its position finally converges to 9.7 eV for the largest heterostructure.

The oscillations of the real parts of the macroscopic dielectric function (middle panels), through the Kramers-Kronig relations, reflect the peaks in the imaginary parts. Their crossings with the zero axis are useful to identify plasmon resonances in the loss functions (bottom panels). Interband transitions characterise the loss function in the energy range between 0 and 10 eV, whereas a plasmon peak is located at around 10 eV for larger systems (e.g. for the 7-7 and 10-10 layers).

Figure 12.13 shows the spectra for a momentum transfer perpendicular to the interface. Its size is $q = 0.15$ Å^{-1}. In this direction the variations as a function of the number of layers are larger. The imaginary part of the dielectric function for small slabs has a main peak at low energy (1.2 eV for the 1 Ag - 1 AgCl structure), which disappears when the size of the system increases. A new peak emerges at 2.5 eV for the 2 Ag - 2 AgCl structure and moves to 3 eV for the largest structures.

In order to simulate an Ag nanoparticle embedded in AgCl, we should also consider the dependence of the spectra on the number of AgCl layers keeping fixed the number of silver layers. A thickness of 2.5 nm corresponds to 10 layers of Ag. The calculated imaginary parts of the macro-

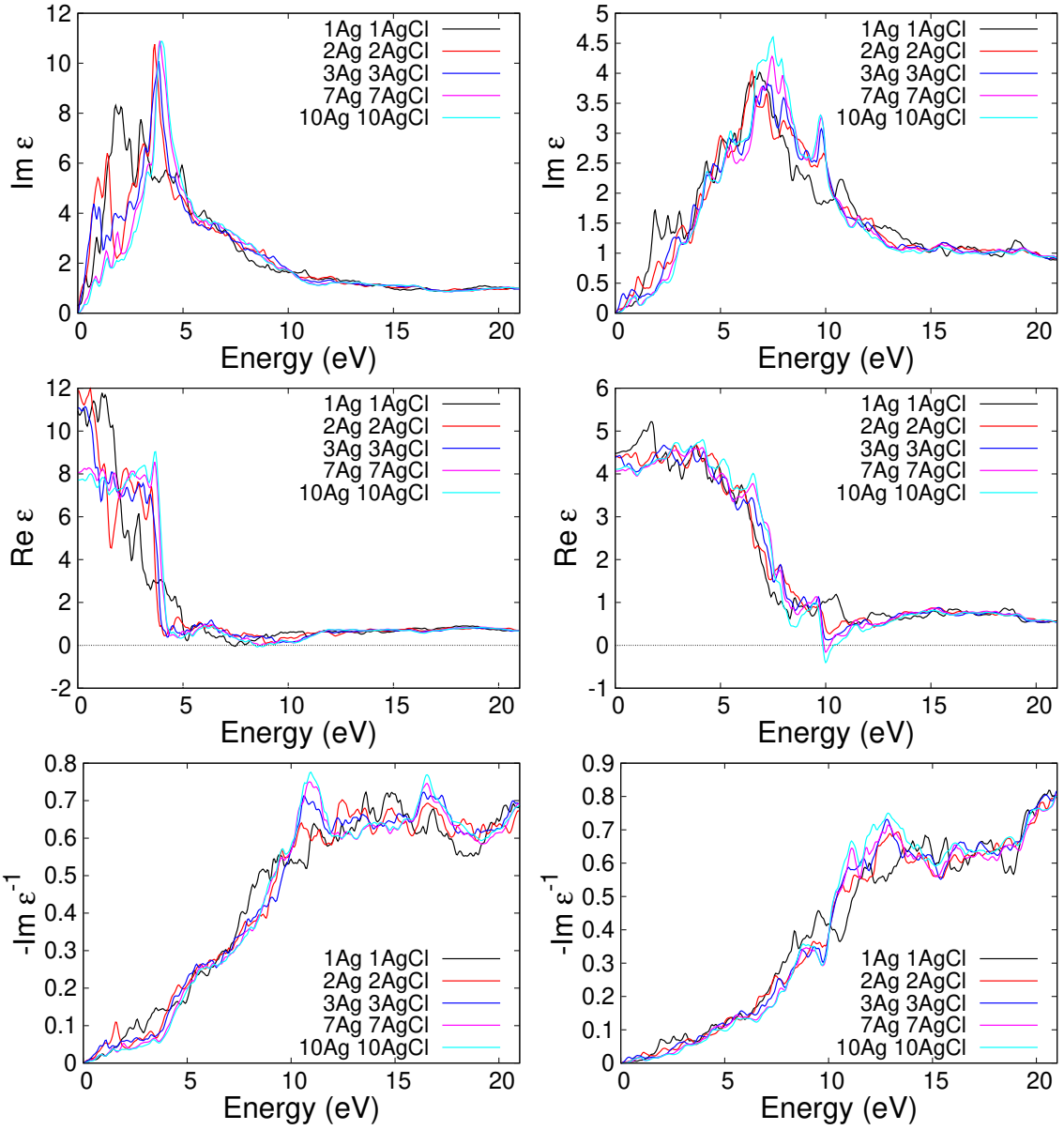

Figure 12.12: Imaginary (top panels) and real parts (middle panels) of the macroscopic dielectric function and loss functions (bottom panels) calculated as a function of the number of layers in each slab. The momentum transfer is in the plane of the layers: $\mathbf{q} = (1/4, 0, 0)$ for the left column and $\mathbf{q} = (1/2, 0, 0)$ for the right column.

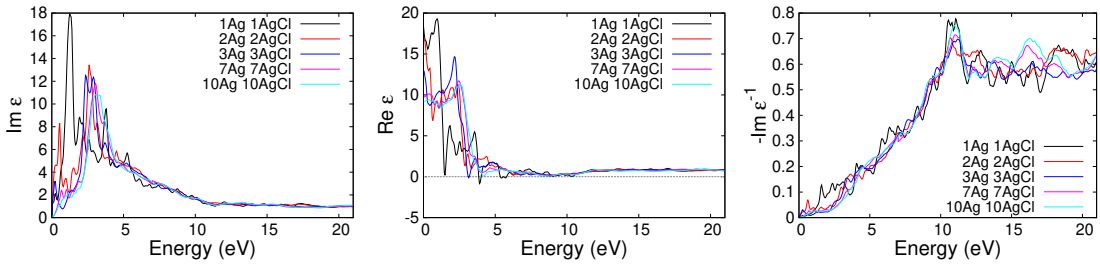

Figure 12.13: Imaginary part (left) and real part (middle) of the macroscopic dielectric function and loss function (right panel) as a function of the number of layers. The momentum transfer is perpendicular to the interface and has a size $q = 0.15\text{Å}^{-1}$.

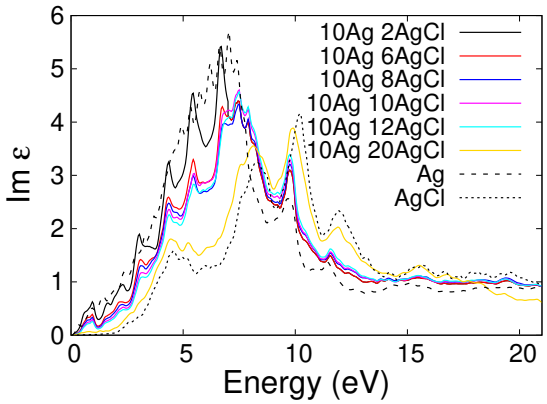

Figure 12.14: Imaginary part of the macroscopic dielectric function as a function of the number of AgCl layers for a number of Ag layers equal to 10. The in-plane momentum transfer is $\mathbf{q} = (1/2, 0, 0)$.

scopic dielectric function as a function of the number of AgCl layers are represented in Fig. 12.14 for a in-plane momentum transfer $\mathbf{q} = (1/2, 0, 0)$. For comparison, the spectra for the pure silver and silver chloride systems are also plotted (see dotted and dashed lines, respectively). As expected, the spectrum of the heterostructure tends to the one of pure silver when the number of silver chloride layers goes to zero and to the one of pure silver chloride when the it is very large. We see that 20 layers of silver chloride are enough to get a result that is close to bulk silver chloride.

Dependence on the momentum transfer

The dependence of the spectra on the momentum transfer has also been studied for the heterostructure with 10 layers of silver and 8 layers of silver chloride.

Fig. 12.15 shows the macroscopic dielectric function for different $\mathbf{q}$ oriented parallel to the interface. We observe a decrease of the intensity of the real and imaginary parts of the dielectric function with increasing q, together with a blueshift and a broadening of the peaks. Plasmon peaks in the loss function are visible within 5 and 10 eV for $\mathbf{q} = (1/4, 0, 0)$ and $\mathbf{q} = (1/2, 0, 0)$ but get damped for larger $\mathbf{q}$.

The macroscopic dielectric function for momentum oriented perpendicular to the interface is plotted figure 12.16. Similar conclusions can be drawn in this case.

ALDA

Finally, Fig. 12.17 compares spectra within the RPA and the ALDA for $\mathbf{q} = (1/2, 0, 0)$. In the ALDA the peaks in the imaginary part of the dielectric function are slightly shifted towards low energy and their intensity is increased. This is a typical effect of the ALDA kernel with respect

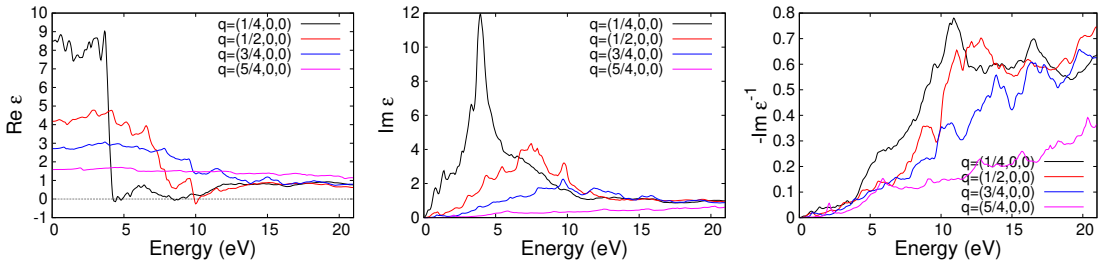

Figure 12.15: (Left) Real and (center) imaginary parts of the macroscopic dielectric function and (right) loss function for a heterostructure with 10 Ag layers and 8 AgCl layers as a function of momentum transfer parallel to the interface.

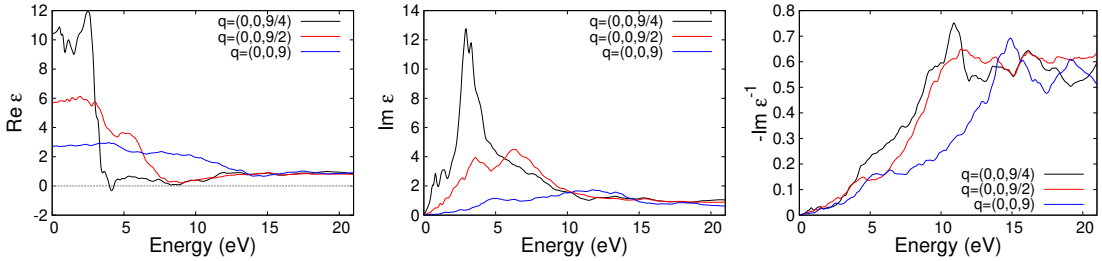

Figure 12.16: (Left) Real and (center) imaginary parts of the macroscopic dielectric function and (right) loss function at **q**=(1/2,0,0) for a heterostructure with 10 Ag layers and 8 AgCl layers as a function of momentum transfer perpendicular to the interface.

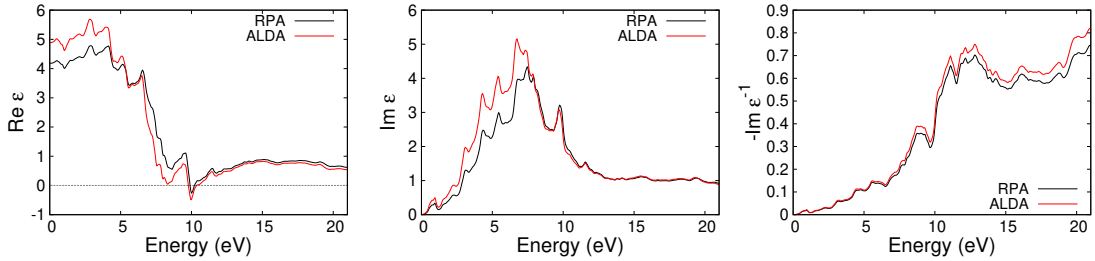

Figure 12.17: (Left) Real and (center) imaginary parts of the macroscopic dielectric function and (right) loss function for a heterostructure with 10 Ag layers and 8 AgCl layers: RPA results (black lines) are compared with ALDA (red lines).

to the RPA. In view of the difficulty of ALDA to describe AgCl (see Ch. 8), it would be desirable to use the BSE. However, calculations for the heterostructure were out of reach with the available computational resources. We therefore consider in the following a simplification of the calculations.

12.5 Effective Medium Theory

Large systems have a high computational cost, which even in TDDFT scales typically as N^4, where N is the number of atoms. It is then reasonable to wonder whether other computational approaches allow for similar results without the need for a full *ab initio* calculation. A convenient model for the dielectric properties of heterostructures is the Effective Medium Theory (EMT), which has been introduced in Chapter 7.

We test here the validity of the EMT by comparing it with fully *ab initio* calculations. Different directions and sizes of momentum transfers for various heterostructures will be examined.

The EMT spectra are obtained from the macroscopic dielectric function $\epsilon_M(\mathbf{q},\omega)$ of the artificial bulk of silver and silver chloride computed within TDDFT. Silver is simulated on a $12 \times 12 \times 12$ Monkhorst-Pack grid of $\mathbf{k}$ points with 4 shifts, with a cutoff energy of 743 eV and 67 empty bands corresponding to an energy of 65 eV above the Fermi level. The size of the dielectric matrix in reciprocal space has a cutoff of 156 eV. Silver chloride is calculated on a $8 \times 8 \times 8$ Monkhorst-Pack grid of $\mathbf{k}$ points with 4 shifts, with a cutoff energy of 743 eV and 67 empty bands corresponding to an energy of 70 eV above the Fermi level. The size of the dielectric matrix in reciprocal space has a cutoff of 195 eV. The *ab initio* results for the heterostructures are those dicussed in the previous section.

We will follow the same pattern as in the previous section: we will analyse RPA results as a function of the number of layers and of the momentum transfer. Moreover we will discuss the effect of local fields and we will compare the RPA with the ALDA.

Dependence on the number of layers

We first compare the EMT prediction with *ab initio* calculations on heterostructures of increasing size for equal number of silver and silver chloride layers. In this configuration, the EMT spectra do not depend on the thickness of the slabs. We expect the EMT to become more accurate when the number of layers is larger, since the microscopic details of the interface become less important. From this analyis we can assess the range of the validity of the EMT model.

Figure 12.18 shows the results for the real and imaginary parts of the dielectric function (left and middle panels, respectively) and the loss function (right panel) for an in-plane momentum transfer $\mathbf{q} = (1/2, 0, 0)$. The already discussed *ab initio* calculations are compared with the EMT prediction (yellow lines). Results for bulk silver (dotted lines) and silver chloride (dashed lines) are the input for the EMT calculation.

The spectra for the imaginary part of the dielectric function (middle panel) overlap quite well: peaks are at similar position and their intensities are close. The biggest discrepancy is found for the heterostructure with 1 Ag and 1 AgCl layer: its spectrum deviates from the others at both the low-energy and high-energy sides of the 7.5 eV main peak. Moreover, with increasing number of layers the *ab initio* calculations lead to an increase of the 7.5 eV peak, which is slightly underestimated in EMT. Comparing the spectra for the two bulk materials with the ones for the heterostructures, we can conclude that the main peak at 7.5 eV originates from electron-hole transitions inside silver, while the peak at 9.7 eV is due to transitions inside silver chloride.

Also for the real part of the dielectric function (left panel) the EMT is in good agreement for all systems larger than 1 Ag and 1 AgCl layer, though at large energies the EMT intensity is slightly larger than all *ab initio* spectra. This discrepancy can be explained as an underconvergence of the *ab initio* calculations with respect to the numbers of bands, which is much more demanding than for the imaginary part of the dielectric function. As a consequence, the same differences are also visible for the loss function (right panel) for energies above 10 eV, where the EMT intensity is lower than the *ab initio* spectra.

The same behavior is found also for momentum transfer $q = 0.15$ Å^{-1}perpendicular to the interface (see Fig. 12.19). Also in this case, large deviations from the EMT spectra are found only for the 1 Ag - 1 AgCl heterostructure. They are already largely reduced for the 2 Ag - 2 AgCl, showing a very fast convergence towards the EMT result.

From this analysis we can conclude that the EMT is reasonably accurate already starting from a heterostructure as small as the one made of 2 Ag and 2 AgCl layers. Thanks to the EMT, we can also assign the main peak in the imaginary part of the dielectric function to electronic transitions in silver, whereas the high energy peak is due to transitions in silver chloride.

Therefore, we can safely use the EMT to predict trends and analyze results where the *ab initio* computation becomes too expensive. As a representative example, Figure 12.20 shows the results for a heterostructure with 10 Ag layers and an increasing number of AgCl layers. The agreement between the EMT prediction (dashed lines) and *ab initio* results (solid lines) is good for the smallest systems, where the latter could be fully converged in the same energy range. For the largest systems, instead, the computational cost of the *ab initio* becomes too large and the

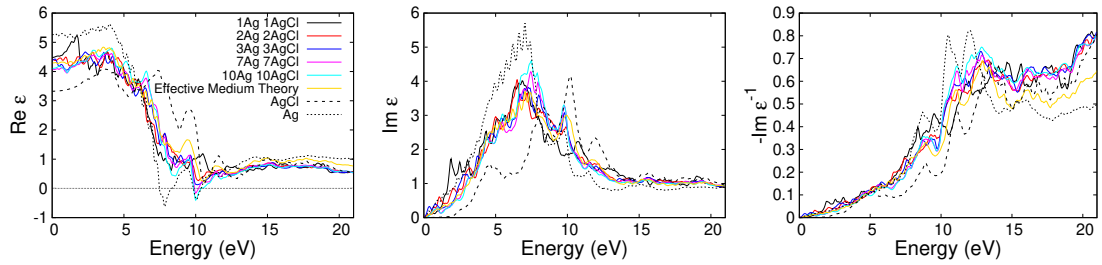

Figure 12.18: (Left) Real and (center) imaginary parts of the macroscopic dielectric function and (right) loss function for heterostructures of increasing number of Ag and AgCl layers and in-plane $\mathbf{q} = (1/2, 0, 0)$: *ab initio* spectra are compared to the EMT prediction. Results for bulk silver chloride (dashed lines) and silver (dotted lines) used as input in the EMT calculation are also shown.

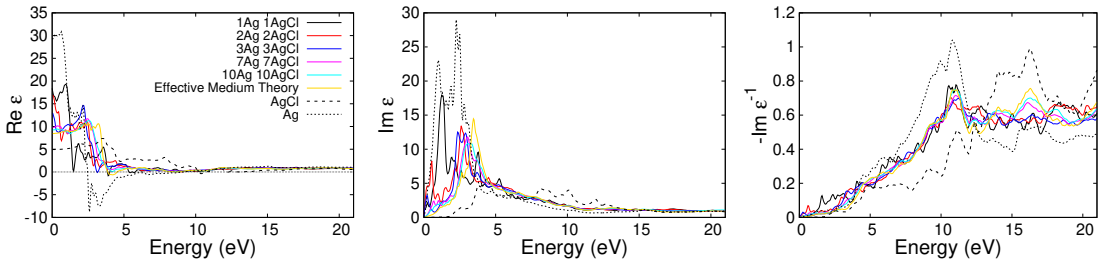

Figure 12.19: (Left) Real and (center) imaginary parts of the macroscopic dielectric function and (right) loss function for heterostructures of increasing number of Ag and AgCl layers and momentum transfer perpendicular to the interface $q = 0.15$ Å^{-1}. *Ab initio* spectra are compared to the EMT prediction. Results for bulk silver chloride (dashed lines) and silver (dotted lines) used in the EMT calculation are also shown.

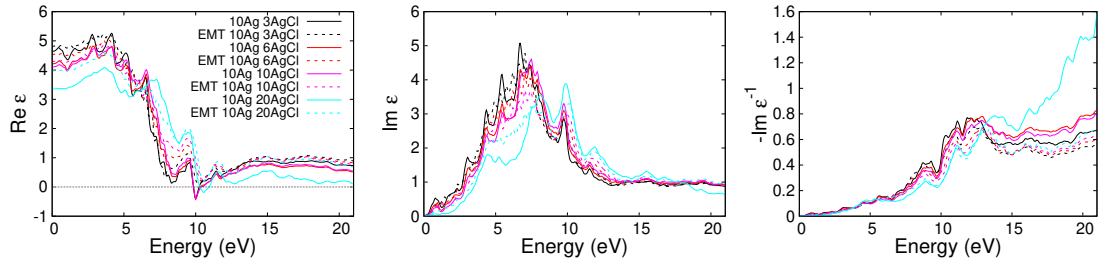

Figure 12.20: (Left) Real and (center) imaginary parts of the macroscopic dielectric function and (right) loss function for heterostructures made of 10 Ag layers and increasing number of AgCl layers for in-plane $\mathbf{q} = (1/2, 0, 0)$: *ab initio* spectra (solid lines) are compared to the EMT prediction (dashed lines).

differences with the EMT become noticeable. The EMT can be effectively used to bridge this computational gap.

Dependence on the momentum transfer: role of local fields

In this section we aim to assess the accuracy of EMT for different momentum transfers and at the same time discuss the impact of local fields on the spectra.

Ab initio calculations for a heterostructure made of 10 Ag and 8 AgCl layers were already discussed in Fig. 12.15 and 12.16 for in-plane and out-of-plane momentum transfers, respectively. The summary of the comparisons with the corresponding EMT results is now shown in Figs. 12.21

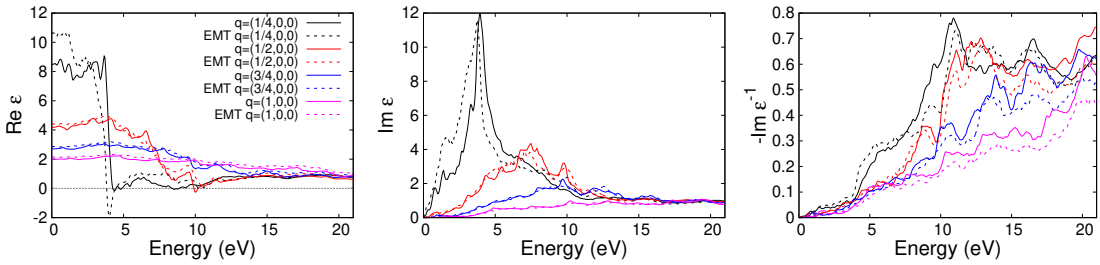

Figure 12.21: (Left) Real and (center) imaginary parts of the macroscopic dielectric function and (right) loss function for a heterostructure with 10 Ag and 8 AgCl layers as a function of in-plane momentum transfers: *ab initio* spectra (solid lines) are compared to the EMT prediction (dashed lines).

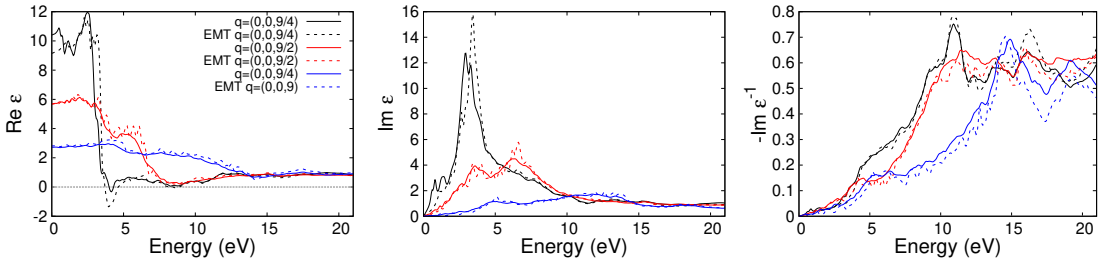

Figure 12.22: (Left) Real and (center) imaginary parts of the macroscopic dielectric function and (right) loss function for a heterostructure with 10 Ag and 8 AgCl layers as a function of momentum transfers perpendicular to the interface: *ab initio* spectra (solid lines) are compared to the EMT prediction (dashed lines).

and 12.22. The agreement is overall good, with differences that in an absolute scale are larger at small than at large momentum transfers, when the spectra also tend to become more flat.

In Figs. 12.23, 12.24, 12.25, and 12.26 for in-plane momentum transfers, and Figs. 12.27, 12.28 and 12.29 for out-of-plane momentum transfers, we make a more detailed comparison between EMT predictions (red lines) and *ab initio* results (black lines). In each case, also the spectra for bulk silver and silver chloride are shown, which are the inputs for EMT. In the top rows of all those figures local field effects are included in the calculations, while they are not included in the bottom rows. In the latter case the EMT spectra are obtained from calculations for bulk Ag and AgCl that also neglect local fields.

For all in-plane momentum transfers, the agreement between EMT and *ab initio* calculations is very good when local fields are neglected. When local field effects are included, the agreement is slightly worse. Especially at smaller momentum transfer, the spectral weight in $\mathrm{Im}\,\epsilon$ calculated *ab initio* is at higher energies than that of $\mathrm{Im}\,\epsilon$ in EMT. To see this better, Fig. 12.30 shows $\mathrm{Im}\,\epsilon$ at $\mathbf{q} = (1/4, 0, 0)$: results of EMT with and without local field effects are essentially on top of *ab initio* results obtained without local field effects, because the local field effects in the single constituents are small. However, local field effects shift spectral weight of the *ab initio* result of the heterostructure to higher energies, such creating some discrepancy between this and the EMT result. Visibly, the EMT is not able to correctly describe additional local field effects due to the presence of the interface when $\mathbf{q}$ is in plane. The effect is stronger at smaller wavevectors. For the momentum transfers perpendicular to the interface, instead, without local fields the agreement remains good only for large momentum transfers whereas it is bad for small q. In this case, only when local fields are explicitly taken into account, EMT and *ab initio* calculations agree.

How can we understand these findings? Local field effects are linked to inhomogeneities in the density response. In the direction perpendicular to the interface, there are two different sources of local fields: the microscopic inhomogeneity inside the Ag and AgCl slabs separately, and the inhomogeneity due to the presence of two different media with different electronic density.

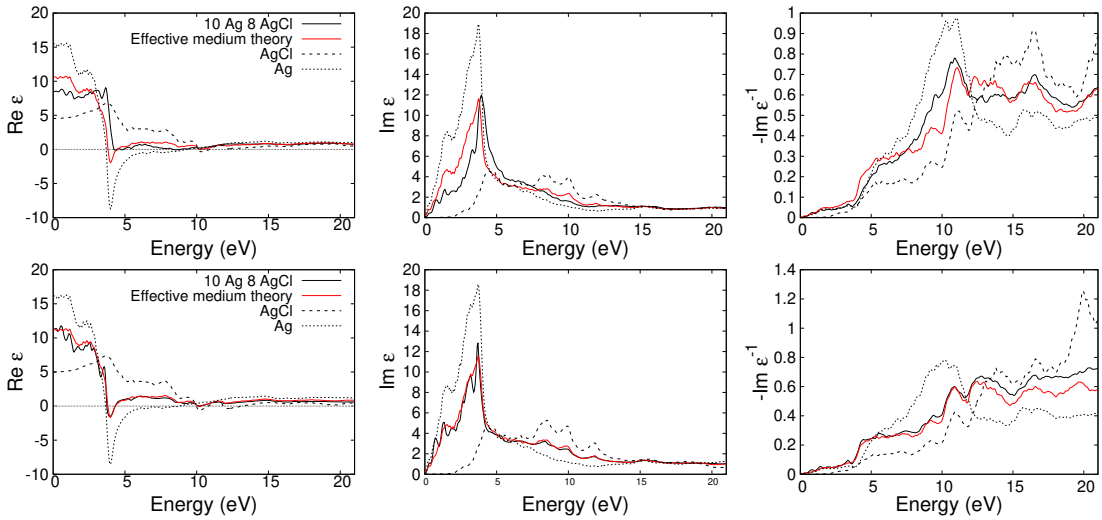

Figure 12.23: (Left) Real and (center) imaginary parts of the macroscopic dielectric function and (right) loss function for a heterostructure with 10 Ag and 8 AgCl layers for $\mathbf{q} = (1/4, 0, 0)$, with $q = 0.212$ Å^{-1}. *Ab initio* spectra (black lines) are compared with EMT results (red lines). Spectra for bulk silver (dotted lines) and silver chloride (dashed lines) are also reported. (Top row) Calculations with local fields included; (Bottom row) Calculations without local fields.

In *ab initio* calculations with inclusion of local fields both effects are accounted for, whereas a calculation without local fields does not take into account either effect. EMT results for $\mathbf{q}$ perpendicular to the interface, instead, always implicitly take into account the discontinuity between the two slabs, because the inverse dielectric functions are summed, while the local fields due to inhomogeneities inside the slabs are considered or neglected depending whether the input bulk results also consider or neglect them.

In the direction perpendicular to the interface, the local fields due to the presence of the discontinuity between the two material is the strongest effect. Therefore the EMT results, which in the perpendicular direction always account for this non-negligible effect, do not agree with *ab initio* spectra that neglect local fields, while the comparison is much better when they are included in the *ab initio* calculations. These findings are consistent with those of a study of the macroscopic dielectric constant og superlattices in [192]. Finally, in the in-plane direction, EMT sums ϵ, not $1/\epsilon$. Therefore EMT and *ab initio* calculations agree when local fields are neglected. When they are included, instead, EMT only includes the local fields of the constituents,but does not reflect those due to the presence of the interface. Since silver and silver chloride have a very different polarizability, the resulting discrepancy with *ab initio* calculations can be observed.

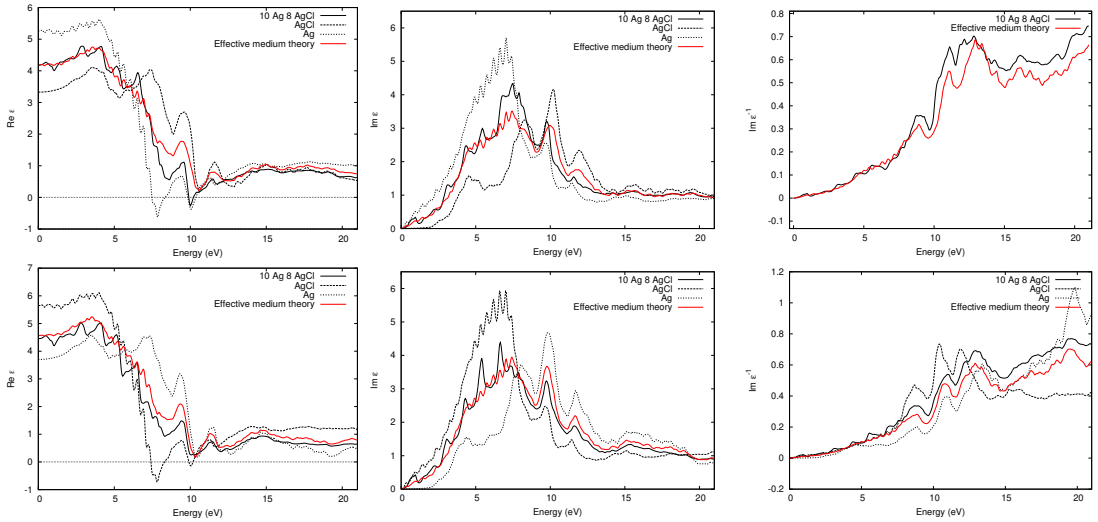

Figure 12.24: (Left) Real and (center) imaginary parts of the macroscopic dielectric function and (right) loss function for a heterostructure with 10 Ag and 8 AgCl layers for $\mathbf{q} = (1/2, 0, 0)$, with $q = 0.424$ Å^{-1}. *Ab initio* spectra (black lines) are compared with EMT results (red lines). Spectra for bulk silver (dotted lines) and silver chloride (dashed lines) are also reported. (Top row) Calculations with local fields included; (Bottom row) Calculations without local fields.

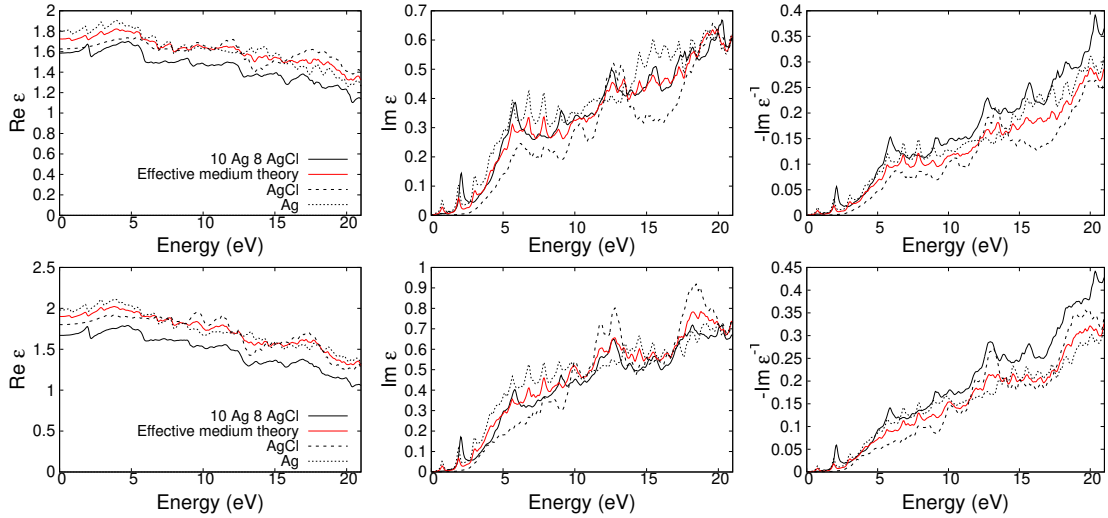

Figure 12.25: (Left) Real and (center) imaginary parts of the macroscopic dielectric function and (right) loss function for a heterostructure with 10 Ag and 8 AgCl layers for $\mathbf{q} = (5/4, 0, 0)$, $q = 1.060$ Å^{-1}. *Ab initio* spectra (black lines) are compared with EMT results (red lines). Spectra for bulk silver (dotted lines) and silver chloride (dashed lines) are also reported. (Top row) Calculations with local fields included; (Bottom row) Calculations without local fields.

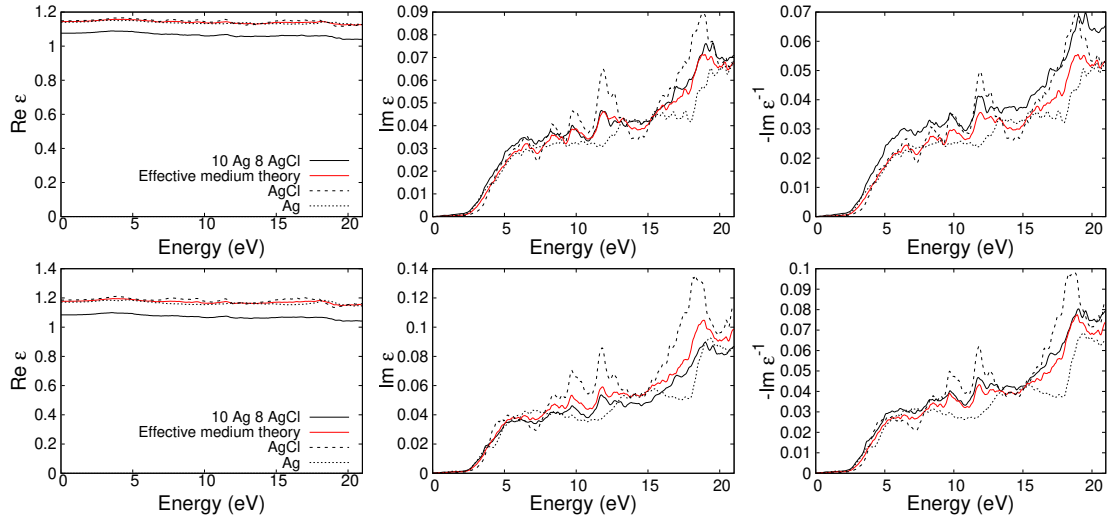

Figure 12.26: (Left) Real and (center) imaginary parts of the macroscopic dielectric function and (right) loss function for a heterostructure with 10 Ag and 8 AgCl layers for $\mathbf{q} = (9/4, 0, 0)$, with $q = 1.907$ Å^{-1}. *Ab initio* spectra (black lines) are compared with EMT results (red lines). Spectra for bulk silver (dotted lines) and silver chloride (dashed lines) are also reported. (Top row) Calculations with local fields included; (Bottom row) Calculations without local fields.

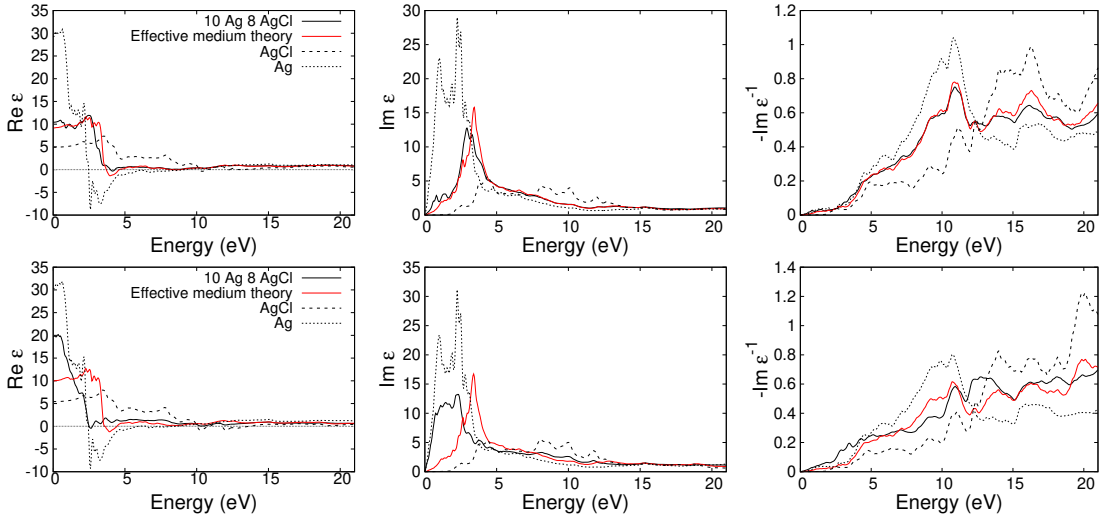

Figure 12.27: (Left) Real and (center) imaginary parts of the macroscopic dielectric function and (right) loss function for a heterostructure with 10 Ag and 8 AgCl layers for $\mathbf{q} = (0, 0, 9/4)$ with $q = 0.150$ Å^{-1}. *Ab initio* spectra (black lines) are compared with EMT results (red lines). Spectra for bulk silver (dotted lines) and silver chloride (dashed lines) are also reported. (Top row) Calculations with local fields included; (Bottom row) Calculations without local fields.

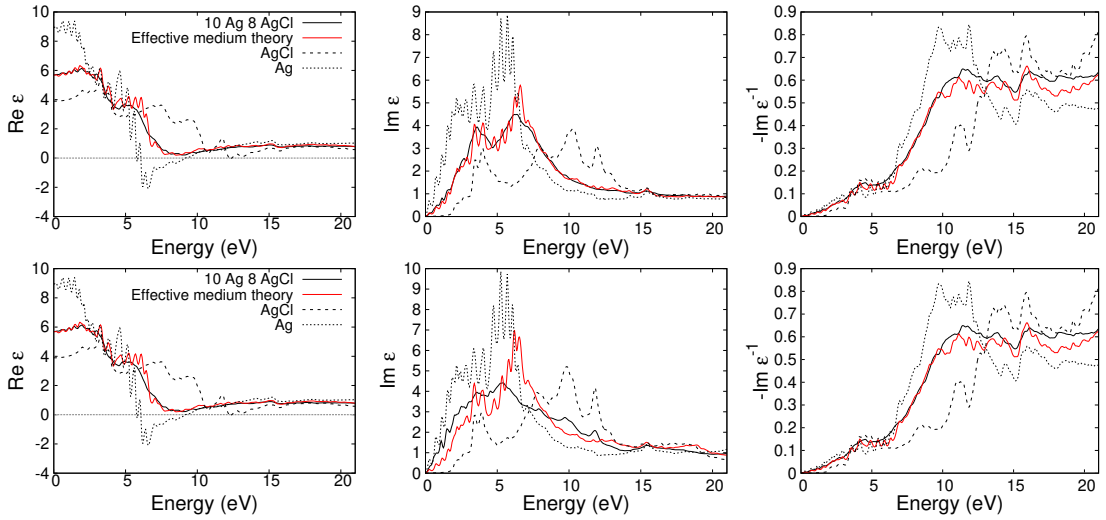

Figure 12.28: (Left) Real and (center) imaginary parts of the macroscopic dielectric function and (right) loss function for a heterostructure with 10 Ag and 8 AgCl layers for $\mathbf{q} = (0, 0, 9/2)$ with $q = 0.300$ Å^{-1}. *Ab initio* spectra (black lines) are compared with EMT results (red lines). Spectra for bulk silver (dotted lines) and silver chloride (dashed lines) are also reported. (Top row) Calculations with local fields included; (Bottom row) Calculations without local fields.

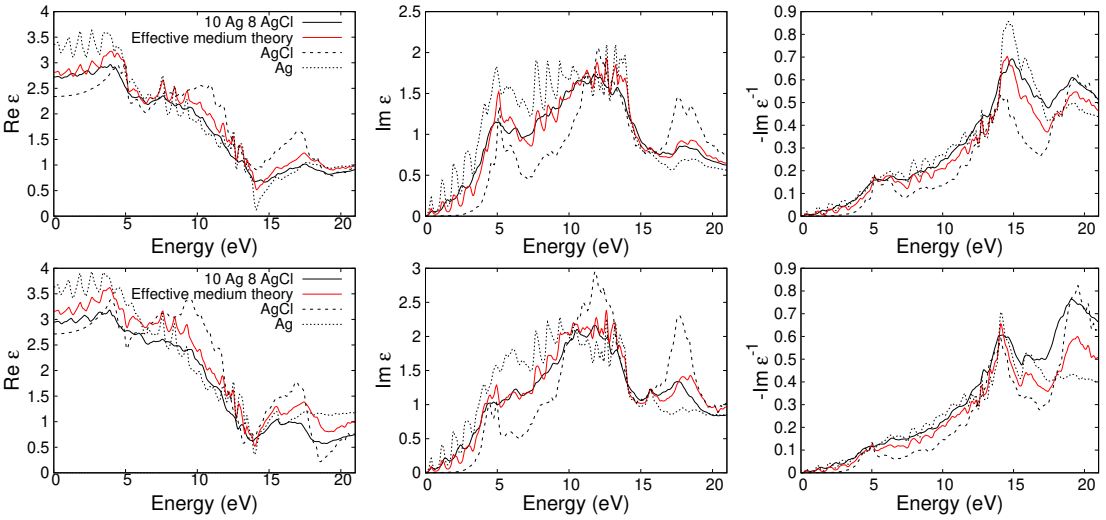

Figure 12.29: (Left) Real and (center) imaginary parts of the macroscopic dielectric function and (right) loss function for a heterostructure with 10 Ag and 8 AgCl layers for $\mathbf{q} = (0, 0, 9)$ with $q = 0.600$ Å^{-1}. *Ab initio* spectra (black lines) are compared with EMT results (red lines). Spectra for bulk silver (dotted lines) and silver chloride (dashed lines) are also reported. (Top row) Calculations with local fields included; (Bottom row) Calculations without local fields.

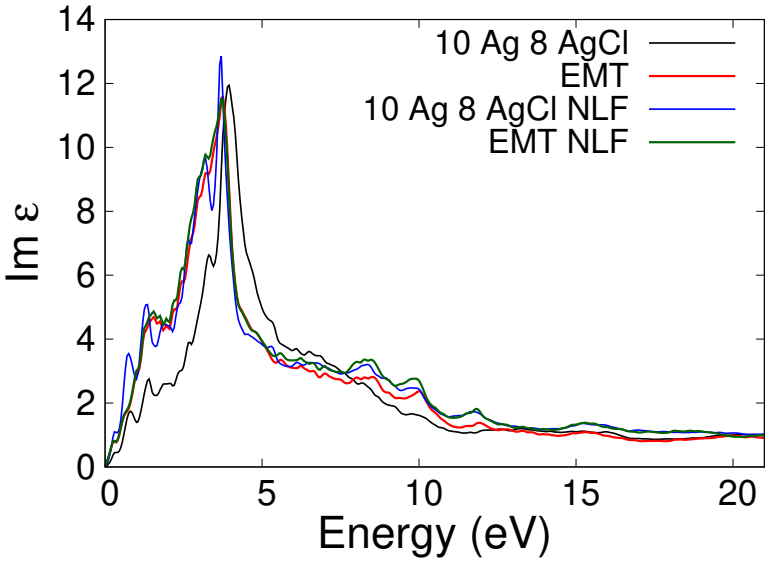

Figure 12.30: Imaginary parts of the macroscopic dielectric function for a heterostructure with 10 Ag and 8 AgCl layers for $\mathbf{q} = (1/4, 0, 0)$. *Ab initio* calculations with local fields (black line) and without local fields (blue line) compared with EMT results computed with local fields (red line) and without local fields (green line). The curves are the ones displayed in Fig. 12.23.

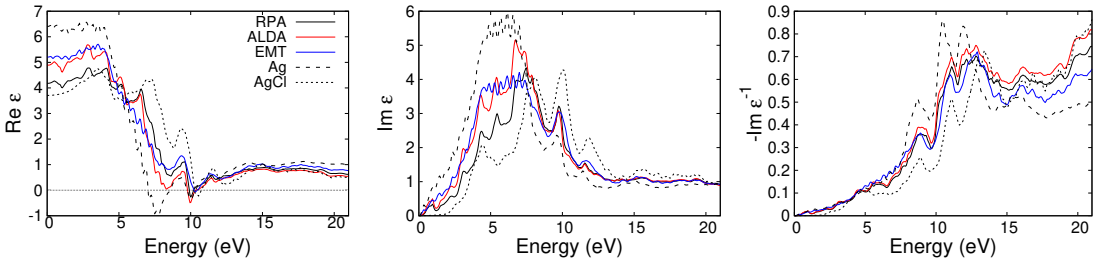

Figure 12.31: (Left) Real and (center) imaginary parts of the macroscopic dielectric function and (right) loss function for a heterostructure with 10 Ag and 8 AgCl layers for $\mathbf{q} = (1/2, 0, 0)$. *Ab initio* RPA (black lines) and ALDA (red lines) spectra are compared with EMT results (blue lines). ALDA spectra for bulk silver (dashed lines) and silver chloride (dotted lines) are also reported.

ALDA

The previous conclusions based on the RPA are confirmed also when both *ab initio* and EMT calculations are performed within the ALDA. In the EMT, this requires that input results for bulk silver and silver chloride are also obtained within the ALDA. Fig. 12.31 shows an example for an in-plane momentum transfer $\mathbf{q} = (1/2, 0, 0)$. The EMT spectra (blue lines) are in agreement with the ALDA results (red lines): as for the previous analysis small deviations in the high energy part of the spectra can be attributed to convergence problems in the *ab initio* calculations, whereas the discrepancy of the peak at 7.5eV is due to the deficiency of EMT for the description of the local field effects discussed above. In the ALDA, this discrepancy remains, but no additional problem appears. Therefore, we can conclude that EMT is capable to take into account the effect of the ALDA kernel with respect to the RPA spectra (black lines in Fig. 12.31).

12.6 Combining the Bethe-Salpeter equation with the effective medium theory

In the previous sections we have concluded that the EMT is able to describe reasonably well the dielectric function of the Ag-AgCl heterostructure. This result has been assessed at the level of both the RPA and the ALDA. We have validated the idea to use EMT to replace *ab initio* calculations that are out of reach from the computational point of view. In particular, a BSE calculation for the whole Ag-AgCl heterostructure, especially with a large number of layers, is computationally too heavy. Within the EMT approach, we can instead make predictions for the dielectric properties of the heteorstructures on the basis of accurate calculations for the bulk materials alone, which are computationally feasible.

For bulk silver it has been shown that the standard static BSE gives a similar absorption spectrum at $\mathbf{q} \to 0$ as the RPA [193]. Therefore, we will also assume that for silver the RPA is a sufficient level of approximation and that BSE calculations, to a first approximation, are not needed. For silver chloride, instead, excitonic effects have been extensively discussed in Ch. 10 on the basis of the BSE and will be taken into account also within the EMT.

Fig. 12.32 shows the result of EMT and *ab initio* calculations for $\mathbf{q} = (1/2, 0, 0)$ in the 10 Ag - 10 AgCl heterostructure. As already discussed in the previous section, also here we find that at the level of the RPA the EMT (red line) agrees reasonably well with the *ab initio* simulation of the whole heteostructure (black line) besides the shift of the oscillator strength in the *ab initio* calculations due to local field effects. We can therefore try to adopt the EMT approach also to obtain a valid prediction of the result of a BSE calculation.

Here we compare the EMT-BSE spectrum (blue line), obtained combining the RPA spectrum for Ag and the BSE spectrum for AgCl, with the EMT-RPA calculation (red line) obtained combining RPA inputs. The differences between these two spectra arise from excitonic effects, analogously to the difference between the *ab initio* RPA and BSE spectra (dashed and dotted lines, respectively) for bulk AgCl. We find that in the heterostructure excitonic effects at low energies are much smaller than for bulk AgCl and within the error bar of the EMT. The reason is that below 5 eV, where AgCl has a strong excitonic effect, its spectrum is buried under a strong absorption of silver. The main peak around 7.5 eV, instead, is clearly increased by the excitonic effects. A careful discussion is needed at this point, since this increase is similar to the discrepancy between the *ab initio* and EMT results on the RPA level, in other words, it lies within the error bar of the EMT in this frequency range. However, as we have analyzed earlier, that discrepancy is due to a problem on the level of local field effects. The difference between RPA and ALDA, instead, was well described by the EMT. We can therefore suppose that EMT also captures the *difference* between RPA and the solution of the Bethe-Salpeter equation, even though the RPA-EMT and BSE-EMT results themselves have some error. In the future, a combination of BSE-EMT with *ab initio* RPA might therefore be developed to simulate heterorstructures including excitonic effects. For now, in order to move on to the charge dynamics, and taking into account that no strong effect of a bound exciton is suggested by our results on the heterostructure, we will perform calculations on the RPA level.

12.7 Induced density in the heterostructure

Now that the optical properties of the heterostructure are understood, we can try to apply the methods developed in the previous chapter for the calculation of the induced density. The system used for this study is a heterostructure made of 3 layers of silver and 3 layers of silver chloride. This is a preliminary work and studies for larger structures still need to be done.

In the previous sections, it has been shown that the optical properties are quite different when the transfered momentum is oriented perpendicular of parallel to the interface. We expect similar behavior with the induced density. In order to verify that, calculations with in plane and perpendicular momenta have been realized.

Fig. 12.33 shows the effect of a plane wave with a momentum perpendicular to the interface. Two different perturbation energies are used: one energy in the gap at 0.44 eV where one expects

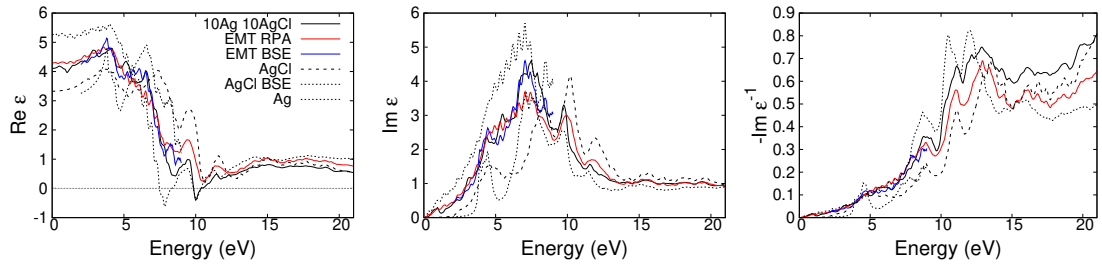

Figure 12.32: (Left) Real and (center) imaginary parts of the macroscopic dielectric function and (right) loss function for a heterostructure with 10 Ag and 10 AgCl layers for $\mathbf{q} = (1/2, 0, 0)$. *Ab initio* RPA calculations for the whole heterostructure (black lines) are compared with EMT-RPA (red lines) and EMT-BSE (blue lines) spectra. Calculations for the bulk materials are also shown: AgCl within the RPA (dashed lines) and the BSE (dotted lines) and bulk Ag (dotted lines).

the perturbation to only excite silver transitions, and a transition above the gap at 4.45 eV, where both systems can be excited. The wavelength of the perturbation is two unit cells, i.e. $\mathbf{q}$=(0,0,1/2). The induced density is oriented in the direction of $\mathbf{q}$ in both cases. In the snapshot at low energy, the response is dominant in silver chloride whereas it is weak in silver. This remains true at all times. It is at first sight surprising, since the frequency of the perturbation is inside the gap of AgCl. However, it can be explained by the effect of screening. When the calculation is done using χ^0 instead of χ^{RPA}, it appears that the induced density is situated at the surface. The Coulomb interaction in RPA has then the effect of screening this induced density. The screening is efficient on the silver side, which is a metal, but not efficient on the silver chloride side, a semi conductor. The response of the system is then concentrated on the silver chloride side. At the second energy, the density is induced on both sides of the interface. One can see that the response on the silver side of the interface is different when the atom is above a silver atom than when it is above a chlorine atom.

Fig. 12.35 shows the density response of the heterosystem to a plane wave which propagates in the plane of the interface. For the two energies, intensity is present on both sides. The intensity is oriented in the direction of the momentum. We observe that the interface has an effect on the induced density: the induced density close to the interface is oriented toward the interface.

In conclusion, in this chapter the question of the interplay between silver chloride and a silver nanoparticle in spectra and induced density was tackled. Approximations to the problem have been introduced, namely, a heterosystem with a model interface and the use of effective medium theory. Concerning optical and loss spectra the effective medium theory was used and compared with the full *ab initio* calculations. This approximation turned out to be quite good even for thin layers. It allows us to take into account excitonic effects without solving the BSE in the heterostructure. Finally, first *ab initio* calculations for the induced density have been presented on the RPA level. Interesting trends were found, in particular for a wavevectors perpendicular to the interface, where the difference of screening in silver and silver chloride leads to an unexpected distribution of the induced density. In the future, more calculations will have to be done to investigate this point. It will also interesting to combine EMT with the calculation of the induced density, in order to include excitonic effects in AgCl in an efficient way.

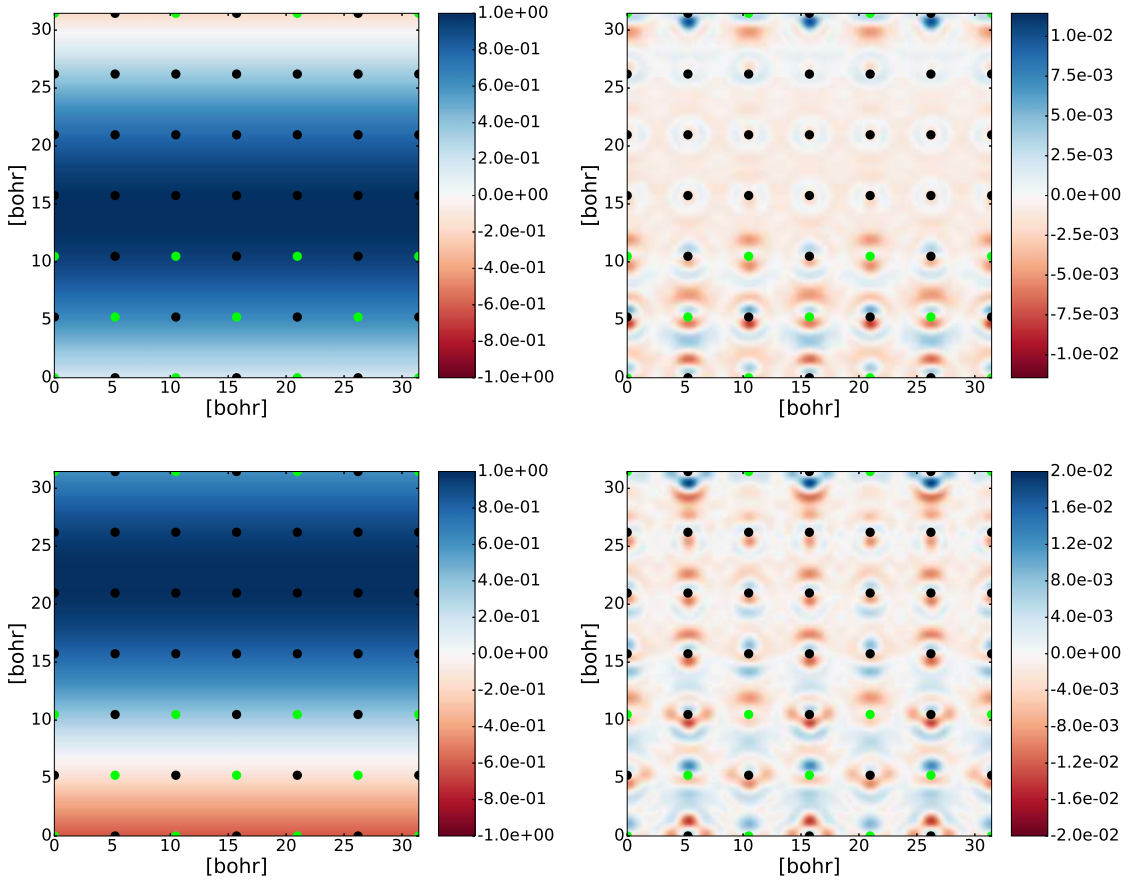

Figure 12.33: Density response to a plane wave perturbation with momentum perpendicular to the interface. The momentum is q=(0,0,1/2) in reduced reciprocal lattice coordinates. The top line shows the calculation with an energy of $\omega = 0.44$ eV and the bottom line shows the calculation with an energy of $\omega = 4.45$ eV . The potential is shown on the left panel and the induced density is shown on the right panel. In each line, potential and density snapshots are taken at the same time. Calculations are performed in the RPA.

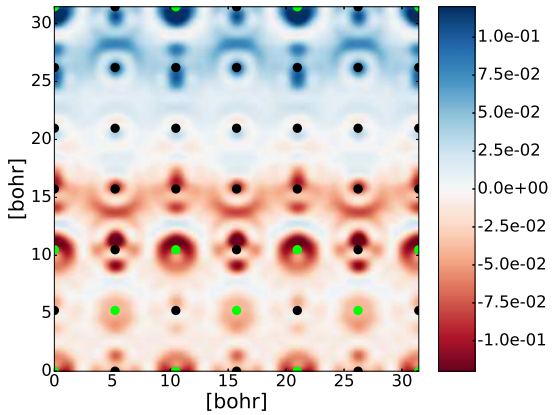

Figure 12.34: Same as Fig. 12.33, with ω=0.44 eV but using χ_0 instead of χ^{RPA}.

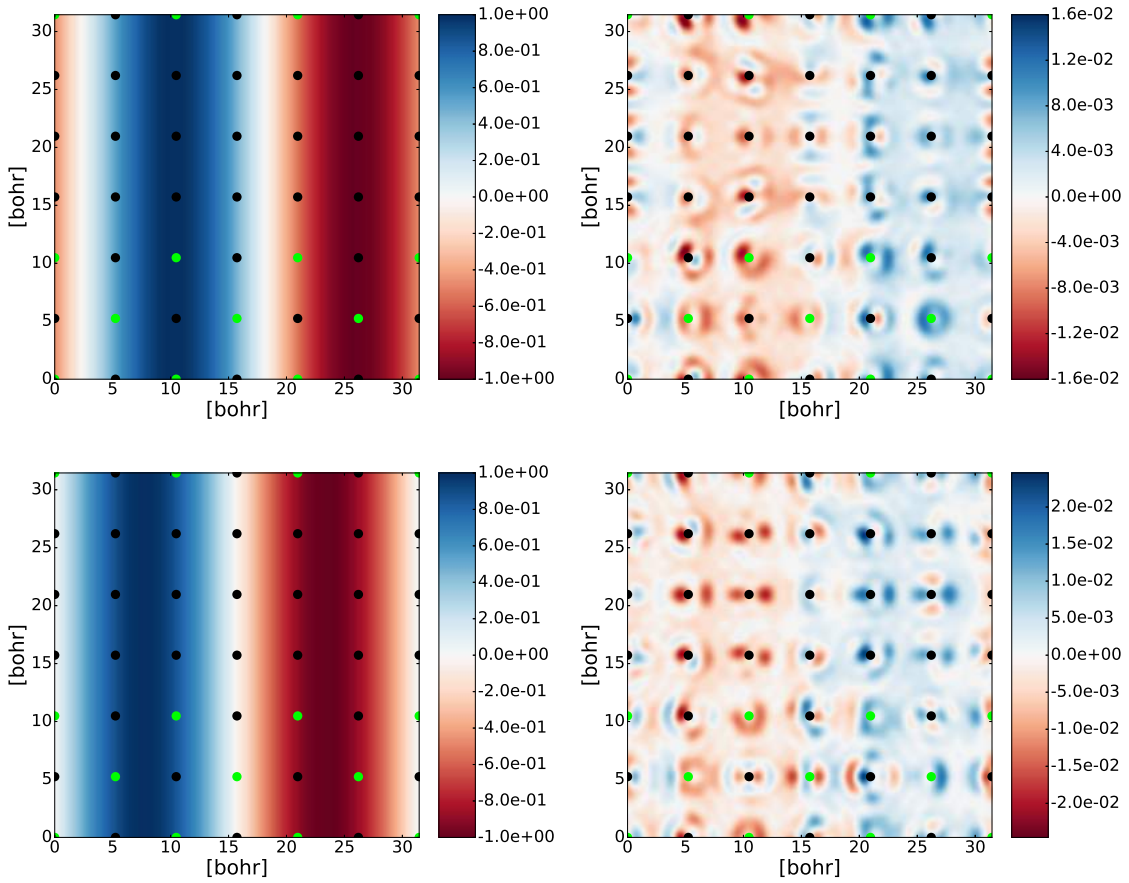

Figure 12.35: Density response to a plane wave perturbation with momentum in the plan of the interface. The momentum is q=(1/6,0,0) in reduced reciprocal lattice coordinates. The top line shows the calculation with an energy of $\omega = 0.99$ eV and the bottom line shows the calculation with an energy of $\omega = 4.05$ eV . The potential is shown on the left panel and the induced density is shown on the right panel. In each line, potential and density snapshots are taken at the the time. Calculations are performed in the RPA.

Part IV

Conclusions

Chapter 13

Conclusions and outlook

The project for this thesis was born out of the challenge to understand Becquerel's first color photography, posed by the Museum for Natural History in Paris. As it often happens in research, the work on the initial question gave rise to new challenges. Indeed, while researchers of the Museum came up with a reasonable explanation to solve the enigma shortly after the start of this thesis, the question of how a material responds to an external perturbation on a microscopic scale when interaction effects are important became more general and important. Therefore, this work has led to three main outcomes. On the materials side, silver chloride, the fundamental ingredient for Becquerel's photography as well as for many other applications such as other techniques of photography, or photocatalysis, has been studied using state-of-the-art *ab initio* methods. This required some methodological development to make calculations feasible. Second, no approach to describe the charge dynamics due to an external perturbation in presence of excitonic effects could be found in the literature, but our study showed that excitons in AgCl are important. Therefore, much effort has been invested into the development of a tool that would make the charge dynamics accessible. Finally, the explanation for Becquerel's photography highlighted the importance of charge dynamics at the interface between AgCl and silver nanoparticles, which led to an exploratory study of a model interface.

Results for the electronic structure and spectroscopic properties of silver chloride are presented in Ch. 8. Although AgCl is a bulk material with a simple crystal structure, getting reliable results turned out to be a challenge on its own, for several reasons. The presence of the silver $4d$ states in the valence region required the creation of a pseudopotential including the entire atomic shell $4spd$ in the valence, which also means that calculations had to be performed with a high cutoff. Moreover, the d states are localized, and they are not well described by standard functionals of DFT, such as the LDA. Therefore the Kohn-Sham band structure is not a very good starting point for the GW calculation of quasi-particle energies and the screening, and the GW had to be performed self-consistently. In the optical spectra of AgCl important excitonic effects due to the electron-hole interaction were found. In principle, optical spectra can also be computed using time-dependent DFT, but none of the available functionals that we have examined could describe these excitonic effects in AgCl. Therefore, the solution of the Bethe-Salpeter equation (BSE) turned out to be mandatory in order to obtain realistic optical spectra.

The BSE calculations are cumbersome, and the results of Ch. 8 showed that convergence with respect to the Brillouin zone sampling could not be achieved in a straightforward way. The bottleneck was the calculation of the screened Coulomb interaction as a function of wave vector $\mathbf{q}$ for many $\mathbf{q}$, as required by the $\mathbf{k}$-point grid. We therefore investigated in Ch. 9 the possibility to use a model screening. We showed that results were not satisfactory when the model is used in a standard way, and we found that the problem is related to the fact that the model takes as input the dielectric constant at vanishing wave vector, which is difficult to converge and which requires the cumbersome calculation of a commutator with the non-local pseudopotential, and the non-local self-energy in QSGW. We therefore proposed a modified version of the model that takes as input the dielectric constant at a non-vanishing wave vector. Our results show that this leads to efficient and reliable calculations of BSE spectra. Moreover, we showed that the model could

be used to predict the values of the macroscopic dielectric constant with reduced computational effort.

Using this approach, we obtained in Ch. 10 our final results for the absorption coefficients of AgCl with a band structure and screened electron-hole interaction obtained from QSGW. The spectra are in good agreement with experiment, much better than spectra based on the non self-consistent G_0W_0 approach used on top of the LDA. This highlights the need for a self-consistent GW calculation. Analysis of the spectra revealed a rich structure. The main exciton peak at the onset is formed by a three-fold degenerate bright exciton, while a two-fold degenerate dark exciton, which cannot be observed in the optical absorption spectrum, is present at lower energy. Our analysis showed that dark and bright excitons mostly stem from the same independent-particle transitions, which are mixed in different ways, with constructive or destructive interference for the bright or dark excitons, respectively.

Diagonalizing the electron-hole Hamiltonian gives access to the electron-hole correlation function. Its analysis shows that a hole close to a silver atom leads to a strong redistribution of the electron density, whereas the effect is much weaker when the hole is close to a chlorine atom. When the QSGW screening is used, the localization around the hole is enhanced with respect to a calculation with RPA screening. This is interesting, as it might have consequences for the coupling of electronic excitations in AgCl to the lattice, or for the migration of charge between AgCl as a substrate, and molecules adsorbed on its surface.

The density change induced by an external perturbation was explored in Ch. 11. Since this is a new topic for *ab initio* calculations in the many-body framework, the principles and technical details had to be settled before moving on to the results for silver chloride. Different levels of theory were used for the calculation of the polarizability. The effect of the inclusion of the Coulomb interaction in the RPA were shown to be minimal for energies close to the gap. Instead, the inclusion of the electron-hole interaction has much stronger effects for energies close to the absorption onset, where the strong excitionic peak is situated. However, this effect could be observed only for a localized perturbation. The main effect of the electron-hole interaction is to delocalize the induced density. We could explain this scenario as due to the sharp isolated excitonic transitions in the gap, which, at a given energy, favor a response with a well-defined wave vector, similar to the plasmon resonance in the homogeneous electron gas.

Finally, the question of the charge dynamics between silver nanoparticles and a silver chloride matrix was tackled in Ch. 12. The interface betwen a nanoparticle and silver chloride was modeled using a heterostructure made of slabs of silver and silver chloride. This supposes that the nanoparticles are large enough for the interface to be considered as planar. We first investigated the spectra of this structure. In particular, we showed how the presence of silver weakens the exciton in AgCl. Preliminary calculations of the induced density were performed in the RPA. To go beyond, we have investigated the reliability of effective medium theory, and shown that it is very efficient to describe spectra.

As we have seen throughout this thesis, the link between trends in spectra and in the microscopic density response of the system to an external perturbation is not always obvious, and more work is needed to translate our findings for the spectra of heterostructures into reliable approximations for the charge dynamics. In particular, it will be interesting to see to which extent effective medium theory can also be used to simplify calculations of the induced charge. The observation of dynamics phenomena with interaction between the bulk systems and the interface may require larger system. Therefore, investigation in this direction still remain to be done. It could be interesting to use other localized perturbations, in order to see if they have effects on the induced density and if charge transfer can be observed between silver and silver chloride.

Finally, the effects of the electron hole interaction on the induced density, explored in silver chloride, deserves a deeper examination in the case of metal/AgCl interface and other materials.

Part V

Appendix

Appendix A

Symmetry properties of χ_0

The independent-particle polarizability χ_0 has been introduced in Ch. 5. Here we will illustrate some of its symmetry properties[1]. In terms of single-particle orbitals, energies and occupation numbers χ^0 can be written as

$$\chi^0_{\mathbf{G},\mathbf{G}'}(\mathbf{q},\omega) = \sum_{l,j,\mathbf{k}} \frac{\langle l,\mathbf{k}|\, e^{-i(\mathbf{q}+\mathbf{G})\mathbf{r}}\, |j,\mathbf{k}+\mathbf{q}\rangle \,\langle j,\mathbf{k}+\mathbf{q}|\, e^{i(\mathbf{q}+\mathbf{G}')\mathbf{r}}\, |l,\mathbf{k}\rangle}{\omega - (\varepsilon_{j,\mathbf{k}+\mathbf{q}} - \varepsilon_{l,\mathbf{k}}) + i\eta}(f_{l\mathbf{k}} - f_{j\mathbf{k}+\mathbf{q}}). \tag{A.1}$$

In the general case $\chi^0_{\mathbf{G},\mathbf{G}'}(\mathbf{q},\omega)$ is a matrix in the reciprocal lattice vectors $\mathbf{G}$ and $\mathbf{G}'$, and a complex function of the first-Brillouin zone vector $\mathbf{q}$ and frequency ω. Its symmetry properties are connected to the properties of the electron system.

- A resonant transition is defined as a transition with a positive energy, i.e. a transition from a valence state $|v,\mathbf{k}\rangle$ to a conduction state $|c,\mathbf{k}+\mathbf{q}\rangle$; at the opposite, an antiresonant transition is a transition from a conduction band to a valence band. For a transition from the valence state $|v,\mathbf{k}\rangle$ to the conduction state $|c,\mathbf{k}+\mathbf{q}\rangle$, the associated antiresonant transition is the transition from $|c,\mathbf{k}+\mathbf{q}\rangle$ to $|v,\mathbf{k}\rangle$. Resonant transitions have a positive factor coming from the occupation numbers, whereas for antiresonant transitions this factor is negative. Equation (A.1) contains both these transitions. This guarantees that:

  $$\chi^0_{\mathbf{G},\mathbf{G}'}(\mathbf{q},\omega) = [\chi^0_{-\mathbf{G},-\mathbf{G}'}(-\mathbf{q},-\omega)]^*. \tag{A.2}$$

  This property is important as it enforces the fact that the Fourier transform of $\chi^0_{\mathbf{G},\mathbf{G}'}(\mathbf{q},\omega)$ is real.

- Time reversal is a symmetry of the electron system as long as the Hamiltonian is Hermitian (e.g. without a magnetic field). It links the wavefunction and its energy at one point $\mathbf{k}$ in the Brillouin zone to the one at the opposite point $-\mathbf{k}$. In this situation, the following property holds:

  $$\chi^0_{\mathbf{G},\mathbf{G}'}(\mathbf{q},\omega) = \chi^0_{-\mathbf{G},-\mathbf{G}'}(-\mathbf{q},\omega). \tag{A.3}$$

- The inversion symmetry is also a symmetry relating $\mathbf{k}$ and $-\mathbf{k}$. When the crystal has inversion symmetry, χ^0 is a symmetric matrix:

  $$\chi^0_{\mathbf{G},\mathbf{G}'}(\mathbf{q},\omega) = \chi^0_{\mathbf{G},\mathbf{G}'}(\mathbf{q},\omega). \tag{A.4}$$

  Moreover the matrix elements $\langle l,\mathbf{k}|\, e^{-i(\mathbf{q}+\mathbf{G})\mathbf{r}}\, |j,\mathbf{k}+\mathbf{q}\rangle$ are real.

- In a crystal a symmetry $\mathcal{R}_\mathbf{t}$ acts on a space-dependent function $f(\mathbf{x})$ as follows:

  $$\mathcal{R}_\mathbf{t} f(\mathbf{x}) = f(\mathcal{R}^{-1}(\mathbf{x}-\mathbf{t})) \tag{A.5}$$

[1] The same properties would hold also for the full polarizability χ. Here we study χ_0 for simplicity.

where $\mathbf{t}$ is the translation and $\mathcal{R}$ the rotation associated with the symmetry. If $\mathcal{R}_\mathbf{t}$ is a symmetry of the system, then χ^0 obeys the following relation:

$$\chi^0_{\mathbf{G},\mathbf{G}'}(\mathcal{R}\mathbf{q},\omega) = e^{i(\mathbf{G}'-\mathbf{G}).\mathbf{t}}\chi^0_{\mathcal{R}^{-1}\mathbf{G}\mathcal{R}^{-1}\mathbf{G}'}(\mathbf{q},\omega) \tag{A.6}$$

In the limit $\mathbf{q}\to 0$, further relations hold for the polarizability χ_0:

$$\chi^0_{0,\mathbf{G}}(-\mathbf{q},\omega) = -\chi^0_{0,\mathbf{G}}(\mathbf{q},\omega) \tag{A.7}$$
$$\chi^0_{\mathbf{G},0}(-\mathbf{q},\omega) = -\chi^0_{\mathbf{G},0}(\mathbf{q},\omega) \tag{A.8}$$
$$\chi^0_{\mathbf{G},\mathbf{G}'}(-\mathbf{q},\omega) = \chi^0_{\mathbf{G},\mathbf{G}'}(\mathbf{q},\omega) \tag{A.9}$$
$$\chi^0_{0,0}(-\mathbf{q},\omega) = \chi^0_{00}(\mathbf{q},\omega). \tag{A.10}$$

A.1 Analytical proofs

Let us write χ^0 in a more practical way[2]:

$$\chi^0_{G,G'}(q,\omega) = \sum_{cvk} \frac{\tilde\rho_{cvk,q}(G)\tilde\rho_{cvk,q}(G')^*}{\omega-(\varepsilon_{c,k+q}-\varepsilon_{v,k})+i\eta}(f_{vk}-f_{ck+q}) \tag{A.11}$$

with

$$\tilde\rho_{vkck+q}(G) = \langle vk|\, e^{i(q+G)r}\,|ck+q\rangle \tag{A.12}$$

and

$$\tilde\rho^*_{vkck+q}(G) = \langle ck+q|\, e^{-i(q+G)r}\,|vk\rangle = \rho_{ck+qvk}(-G). \tag{A.13}$$

Hermicity

Let us demonstrate the first property (A.2):

$$\begin{aligned}
[\chi^0_{GG'}(q,\omega)]^* &= \sum_{cvk}\frac{\tilde\rho_{vkck+q}(G)^*\tilde\rho_{vkck+q}(G')}{\omega-(\varepsilon_{c,k+q}-\varepsilon_{v,k})-i\eta}(f_{vk}-f_{ck+q})\\
&= -\sum_{cvk}\frac{\tilde\rho_{ck+qvk}(-G)\tilde\rho^*_{ck+qvk}(-G')}{-\omega-(\varepsilon_{v,k}-\varepsilon_{c,k+q})+i\eta}(f_{vk}-f_{ck+q})\\
&= \sum_{cvk}\frac{\tilde\rho_{vk+qck}(-G)\tilde\rho^*_{vk+qck}(-G')}{-\omega-(\varepsilon_{c,k}-\varepsilon_{v,k+q})+i\eta}(f_{vk+q}-f_{ck})\\
&= \sum_{cvk}\frac{\tilde\rho_{vkck-q}(-G)\tilde\rho^*_{vkck-q}(-G')}{-\omega-(\varepsilon_{c,k-q}-\varepsilon_{v,k})+i\eta}(f_{vk}-f_{ck-q})\\
&= \chi^0_{-G-G'}(-q,-\omega).
\end{aligned}$$

At the third line c and v have been swapped and at the last line the transformation $k\to k-q$ was applied. So for this relation to be valid, the sum has to include resonant and antiresonant terms. Here both v and c run over all bands. This proves the relation (A.2) and implies that χ_0 is real in real space and time:

$$\chi^0(r,r',t-t') = \iint d\omega dq \sum_{G,G'} e^{i(q+G)r}\chi^0_{GG'}(q,\omega)e^{-i(q+G')r+i\omega(t-t')}. \tag{A.14}$$

[2]For simplicity, the vector notation is omitted here.

$$
\begin{aligned}
[\chi^0(r,r',t-t')]^* &= \iint d\omega dq \sum_{G,G'} e^{-i(q+G)r}[\chi^0_{GG'}(q,\omega)]^* e^{i(q+G')r-i\omega(t-t')} \\
&= \iint d\omega dq \sum_{G,G'} e^{i(q+G)r}[\chi^0_{-G-G'}(-q,-\omega)]^* e^{-i(q+G')r+i\omega(t-t')} \\
&= \iint d\omega dq \sum_{G,G'} e^{i(q+G)r}\chi^0_{GG'}(q,\omega) e^{-i(q+G')r+i\omega(t-t')} \\
&= \chi^0(r,r',t-t').
\end{aligned}
$$

The property (A.2) has been used between the second to last and last lines. This demonstrates that $\chi^0(r,r',t-t')$ is real.

Time reversal

The time reversal operator is defined as

$$
\mathcal{T}\phi_{ck}(r,t) = \phi_{ck}(r,-t), \tag{A.15}
$$

where ϕ is a single particle wavefunctions. Let us assume the Hamiltonian to be Hermitian. Applying the time reversal operator $\mathcal{T}$ to the Schrödinger equation gives:

$$
\begin{aligned}
i\mathcal{T}\frac{\partial\phi}{\partial t}(r,t) &= \mathcal{T}\hat{H}(t)\phi(r,t) \\
-i\frac{\partial\phi}{\partial t}(r,-t) &= \hat{H}(t)\mathcal{T}\phi(r,t) \\
i\frac{\partial(\mathcal{T}\phi)^*}{\partial t}(r,t) &= \hat{H}(t)(\mathcal{T}\phi(r,t))^*.
\end{aligned}
$$

So $\mathcal{T}\phi = \phi^*$. The time reversal operator applied on a wave function yields its complex conjugate. In a crystal with time reversal symmetry, the conjugated wave function is also a solution of the Schrödinger equation with the same energy but opposite k vector:

$$
\begin{cases}
\phi^*_{ck}(r,t) = \phi_{c'-k}(r,t) \\
\varepsilon_{ck} = \varepsilon_{c'-k} \\
f_{ck} = f_{c'-k}.
\end{cases} \tag{A.16}
$$

In the case of non-degenerate states, the previous relations hold directly between ck and $c-k$ For degenerate states, one should consider a linear combination of the degenerate states. As a consequence of time-reserval symmetry one has:

$$
\begin{aligned}
\tilde{\rho}_{vkck+q}(G) &= \langle vk| e^{i(q+G)r} |ck+q\rangle \\
&= \int \phi^*_{vk}(r,t)\phi_{ck+q}(r,t)e^{i(q+G)r} \\
&= \int \phi_{v'-k}(r,t)\phi^*_{c'-(k+q)}(r,t)e^{i(q+G)r} \\
&= \tilde{\rho}_{c'-(k+q)v'-k}(G).
\end{aligned}
$$

Using this relation for χ^0 we indeed obtain the relation (A.3):

$$\begin{aligned}
\chi^0_{GG'}(q,\omega) &= \sum_{cvk} \frac{\tilde{\rho}_{vkck+q}(G)\tilde{\rho}^*_{vkck+q}(G')}{\omega - (\varepsilon_{c,k+q} - \varepsilon_{v,k}) + i\eta}(f_{vk} - f_{ck+q}) \\
&= \sum_{cvk} \frac{\tilde{\rho}_{c'-(k+q)v'-k}(G)\tilde{\rho}^*_{c'-(k+q)v'-k}(G')}{\omega - (\varepsilon_{c',-(k+q)} - \varepsilon_{v',-k}) + i\eta}(f_{v'-k} - f_{c'-(k+q)}) \\
&= \sum_{cvk} \frac{\tilde{\rho}_{ck-qvk}(G)\tilde{\rho}^*_{ck-qvk}(G')}{\omega - (\varepsilon_{c,k-q} - \varepsilon_{v,k}) + i\eta}(f_{vk} - f_{ck-q}) \\
&= \sum_{cvk} \frac{\tilde{\rho}_{vkck-q}(-G')\tilde{\rho}^*_{vkck-q}(-G)}{\omega - (\varepsilon_{c,k-q} - \varepsilon_{v,k}) + i\eta}(f_{vk} - f_{ck-q}) \\
&= \chi^0_{-G'-G}(-q,\omega).
\end{aligned}$$

The third line has been obtained by using the transformation $k \to -k$ and the bands have been reordered. Transitions from k to k+q and from -k to -k+q will be needed for this relation to hold.

Inversion

The inversion symmetry is defined by

$$I\phi(r) = \phi(-r). \tag{A.17}$$

If the inversion is a symmetry of the system one has

$$\begin{cases} I\phi_{ck}(r,t) = \phi_{ck}(-r,t) = \phi_{c'-k}(r,t) \\ \varepsilon_{ck} = \varepsilon_{c'-k} \\ f_{ck} = f_{c'-k} \end{cases}$$

and

$$\begin{aligned}
\tilde{\rho}_{vkck+q}(G) &= \int \phi^*_{vk}(r,t)\phi_{ck+q}(r,t)e^{i(q+G)r} \\
&= \int \phi^*_{v'-k}(r,t)\phi_{c'-(k+q)}(r,t)e^{-i(q+G)r} \\
&= \tilde{\rho}_{v'-kc'-(k+q)}(-G).
\end{aligned}$$

Combining this property with the time reversal symmetry we get:

$$\tilde{\rho}_{vkck+q}(G) = \tilde{\rho}_{c'k+qv'k}(-G) = \tilde{\rho}^*_{v'k'ck+q}(G). \tag{A.18}$$

If the states are not degenerate, then $\tilde{\rho}_{vkck+q}(G)$ is real. This for χ^0 implies that:

$$\begin{aligned}
\chi^0_{GG'}(q,\omega) &= \sum_{cvk} \frac{\tilde{\rho}^*_{vkck+q}(G)\tilde{\rho}_{vkck+q}(G')}{\omega - (\varepsilon_{c,k+q} - \varepsilon_{v,k}) + i\eta}(f_{vk} - f_{ck+q}) \\
&= \sum_{cvk} \frac{\tilde{\rho}^*_{c'k+qv'k}(-G)\tilde{\rho}_{c'k+qv'k}(-G')}{\omega - (\varepsilon_{c',k+q} - \varepsilon_{v',k}) + i\eta}(f_{v'k} - f_{c'k+q}) \\
&= \sum_{cvk} \frac{\tilde{\rho}^*_{v'kc'k+q}(G')\tilde{\rho}_{v'kc'k+q}(G)}{\omega - (\varepsilon_{c',k+q} - \varepsilon_{v',k}) + i\eta}(f_{v'k} - f_{c'k+q}) \\
&= \sum_{cvk} \frac{\tilde{\rho}^*_{vkck+q}(G')\tilde{\rho}_{vkck+q}(G)}{\omega - (\varepsilon_{c,k+q} - \varepsilon_{v,k}) + i\eta}(f_{vk} - f_{ck+q}) \\
&= \chi^0_{G'G}(q,\omega).
\end{aligned}$$

The $\chi^0_{GG'}(q,\omega)$ matrix is hence symmetric.

Numerical proofs

In this subsection, we numerically check the different symmetry properties of χ^0 found in the previous section.

To this end, I firstly created a fictitious electron system with no symmetry and I computed the irreducible polarizability χ_0 for 1 conduction band and 1 valence band at two **k**-points $k_1 \neq -k_2$. Then χ^0 could be numerically evaluated at $q = \pm(k_1 - k_2)$, i.e. at $q = (-0.5, 0, -0.5)$ or $(0.5, 0, 0.5)$

In Figs. A.1,A.2,A.3, A.4 the real and imaginary parts of the $G = (1, 1, 0)$ and $G' = (1, 0, 0)$ elements of χ^0 are plotted as a function of ω in the following 4 combinations: $\chi^0_{GG'}(q)$, $\chi^0_{G'G}$, $\chi^0_{-G-G'}(-q)$ and $\chi^0_{-G'-G}(-q)$.

- Fig. A.1: χ^0 with no antiresonant terms and no time conjugate terms. χ_0 does not have any symmetry.
- Fig. A.2: χ^0 with antiresonant terms and no time conjugate terms. χ_0 is hermitian.
- Fig. A.3: χ^0 with no antiresonant terms and time conjugate terms. χ_0 has the time-reversal property (A.3)
- Fig. A.4: χ^0 with antiresonant terms and time conjugate terms. χ_0 has the time-reversal property (A.3)

In all cases, the numerator of χ^0 is not real. This implies that the real and imaginary parts of χ_0 do not behave as $\frac{\omega - \Delta E}{(\omega - \Delta E)^2 + \eta^2}$ and $\frac{\eta}{(\omega - \Delta E)^2 + \eta^2}$, respectively.

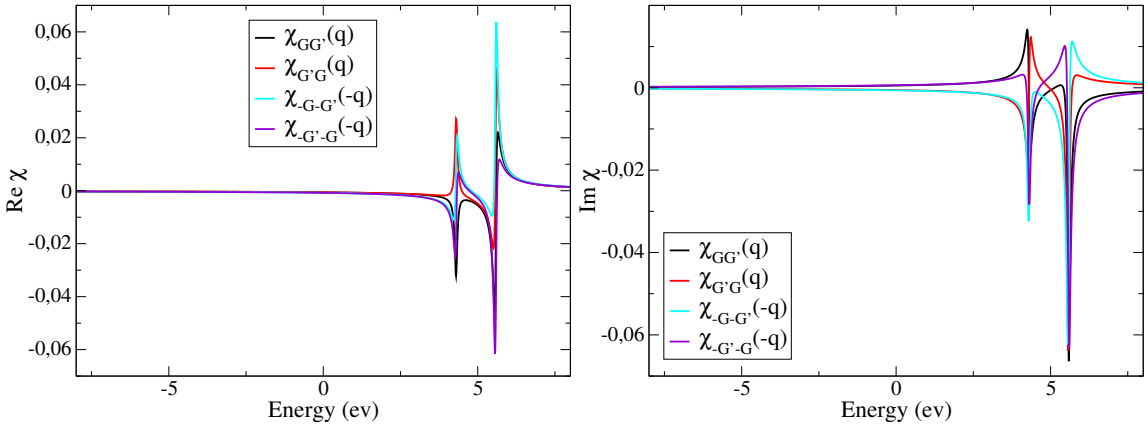

Figure A.1: Real (left) and imaginary (right) parts of χ^0 without antiresonant terms and without time conjugate terms. $G = (1, 1, 0), G' = (1, 0, 0), q = (-0.5, 0, -0.5)$.

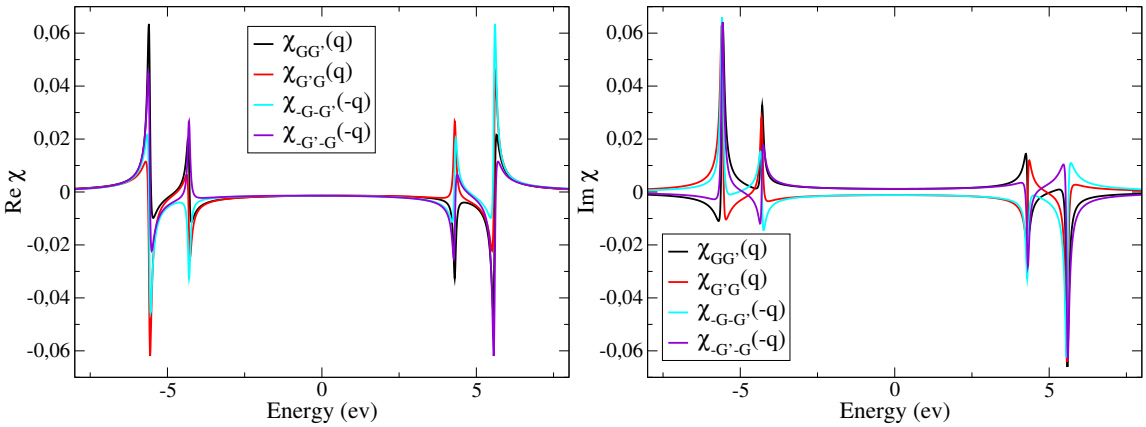

Figure A.2: Real (left) and imaginary (right) parts of χ^0 with antiresonant terms and without time conjugate terms. $G = (1,1,0), G' = (1,0,0), q = (-0.5,0,-0.5)$.

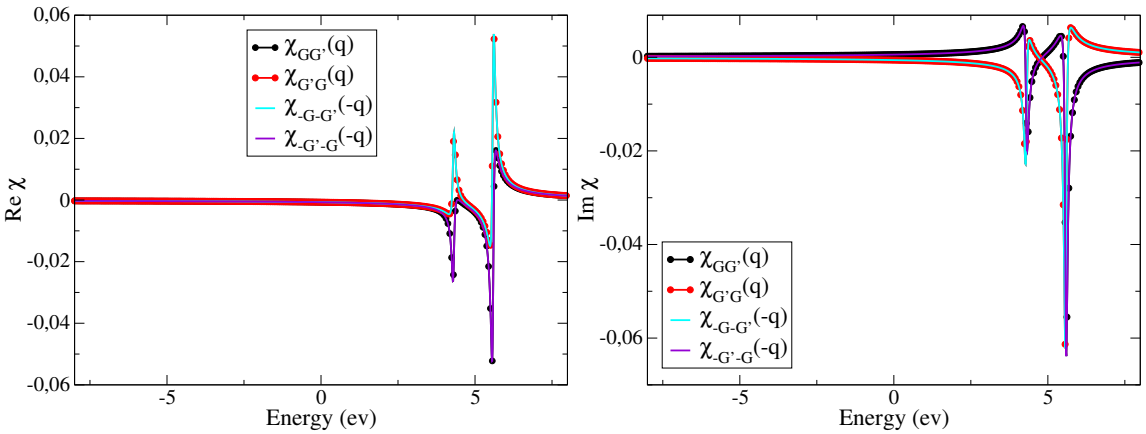

Figure A.3: Real (left) and imaginary (right) parts of χ^0 without antiresonant terms and with time conjugate terms. $G = (1,1,0), G' = (1,0,0), q = (-0.5,0,-0.5)$.

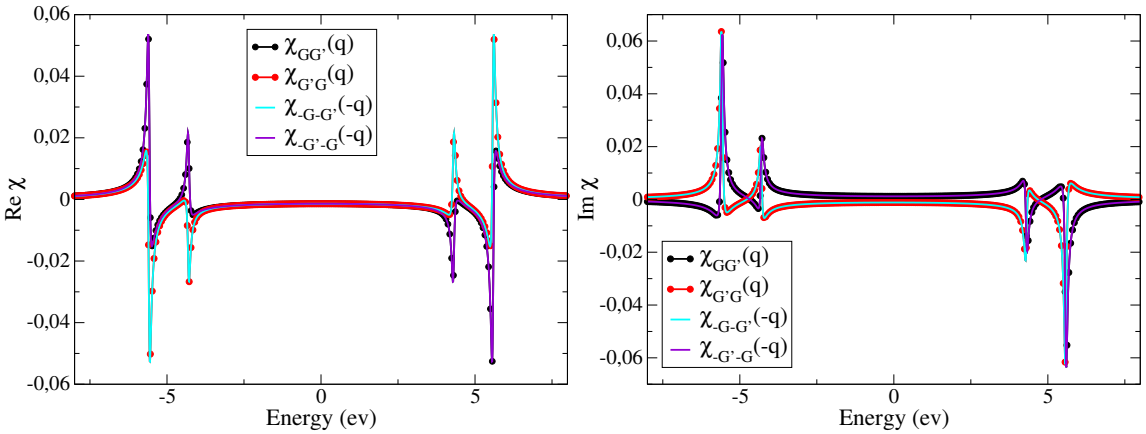

Figure A.4: Real (left) and imaginary (right) parts of χ^0 with antiresonant terms and time conjugate terms. $G = (1,1,0), G' = (1,0,0), q = (-0.5,0,-0.5)$.

Appendix B

Code details

In order to create the (real space, real time) induced densities that we see in Chapters 11 and 12, we use a post-processing tool, called `SRden.py` [194], written in Python, that reads the polarizability files issued by Dp [163] or Exc [166]. The development of this code, starting from previous results obtained by Igor Reshetnyak, Ralf Hambach and Giulia Pegolotti, was part of this thesis.

The execution of this tool is very simple

```
user@host:~$ python SRden.py -i <inputfile>
```

A typical input file for the script follows:

```
real_time=           True  # Fourier transform in real time
save_real_time=      True  # Save the real time results

savemem = True  # Save memory by reading chi on the fly and not once at the begining

qlistfile=[
"_0.0001_0.0_0.0",
"_0.0001_0.0001_0.0",
"_0.0_0.0_-0.5",
"_0.0_-0.25_-0.5",
"_0.0_-0.5_-0.125",
"_-0.125_-0.125_0.0",
"_-0.125_-0.125_-0.125",
"_-0.125_-0.125_-0.5",
"_-0.125_0.25_0.375",
]

filelist=[]
for i in qlistfile:
filelist.append("../"+i+"/chi0"+i+".dat")

outfile_name='85k'

#REAL SPACE PARAMETERS
NUM      = (200,200,1);         # Number of point in the real space
nx= 01.0;ny=01;nz=0.5
ax=10.4830;             # [bohr]
ay=10.4830;             # [bohr]
az=10.4830;             # [bohr]

DIM=np.array(
```

```
[[  -0.5*ax   ,  (-0.5+nx)*ax  ], # in experimental coordinates [bohr]
[  -0.5*ay   ,  (-0.5+ny)*ay  ],
[ 0   ,  nz*az  ]]);# only relevant for atoms drawn

cut = 'xy'

#TIME PARAMETERS
nt=          0
t_resol =    0.005 # nt has priority
Tbeg=        0.000
Tend=        1.600


diag='full' # diag or full, take the diagonal part of the matrix or not,
            # default=full

#Number of G to include (cutoff of the matrix)
npwmat   = 2975

#real_part='energy' # Choose 'energy' for simplifying the calculation
                       #with energy or 'momentum' for simplifycation with q

# Use the symmetry V(q,omega) = V(-q,-omega)*, only need chi for (q,omega)

#pot_form='from_file' # 'time_loc' will localise in time > exp(i*2Pi*E*t0)
#pot_form='space_loc' # 'time_loc' will localise in time > exp(i*2Pi*E*t0)
pot_form='use_vpert'
x0= [0.1,-0.1,0.1]
#x0= [0.,0.,0.]

g_pert=65   # Add the first gmax G vector (no need to be closed shell),
            # negative values will add all the G available


#List directly in energy
Elist=[2.855]

# Enter directly (q,G,E,V)
Vpert=[]
Vpert.append([[0.0001,0.0000,0.0001],[0,0,0],2.855,1.0+0j])


t_plot=[56]
r_ind=[[0,8,0],[0,82,0],[74,9,0]]


verboselevel = 2
```

The first parameter is a flag for choosing among different types of calculations and output. The `filelist` parameter contains the path to the polarizability files. `outfile_name` gives the root for the names of the output files. The grid of real points at which the calculation is realized is set up by the parameters `DIM`, which gives the minimum and maximum value of the grid in each direction

(in Bohr) and `NUM`, which gives the number of points for each direction. The grid can be either a 3D cube or a 2D plan by setting up one of the values of `NUM` to one. The time grid is defined by `Tbeg`, `Tend`, both in femtosecond, and either `nt`, the number of points between the two values or by `t_resol`, the interval between two points. `nt` has priority and `t_resol` is only used if `nt` is not defined. A cutoff to the size of the matrix can be applied with the parameter `npwmat`; this helps to reduce calculation time when the matrix is too large. If set to `None`, its value is the size of the matrix in the file.

The perturbation $V_{\mathbf{G}}(\mathbf{q},\omega)$ is given in reciprocal space and frequency domain. The perturbation is controlled by `pot_form`. Different options are possible for this parameter: i) `'from_file'` will try to open the file pot.dat to read the potential; ii) `'use_vpert'` generates a potential from scratch by reading the parameter `Vpert`, which is a table of elements in the form ($\mathbf{q}$,$\mathbf{G}$,ω,$V_{\mathbf{G}}(\mathbf{q},\omega)$); iii) `'space_loc'` is used to generate a potential localized at `x0`, it takes all frequencies given in `E_list`, all wavevectors given in `q_list` and the first `G_pert` reciprocal vectors[1] found in the polarizability file (negative value automaticaly include all reciprocal vectors); the amplitude given to each triplet ($\mathbf{G}$,$\mathbf{q}$,ω) of parameters is then used as $e^{i(\mathbf{q}+\mathbf{G})\cdot x_0}$; iv) it also exists the possibility, given by parameter `time_loc`, for a potential localized in time at `t0`, but it is not exploited in this thesis.

Once the perturbation is generated (or read from file), the induced density is calculated via Eq. (11.5) (path chosen via the flag `real_part`). The code takes advantage of the spatial symmetres of the crystal.

`diag` gives the possibilty to do the calculation with or without the diagonal elements of the polarizability matrix.

Also some output parameters are defined: `t_plot` gives the time at which we want to take a snapshot of the time-dependent induced density (it produces a 2D-cut in a file .eps); `r_ind` selects a position in space, for which the evolution of the induced density is plotted as a function of time (for instance, Fig. 11.1 middle panel is obtained with this option).

Finally, it is possible to save the calculated data (and read them /modify them again), thanks to the flag `save_real_time`.

[1] The reciprocal vectors are sorted by increasing length

Appendix C

Spectroscopic quantities

A plane wave propagating in vacuum can be described in terms of the oscillating electric field $\mathbf{E}(\mathbf{r},t) = \mathbf{E}_0 e^{i(\mathbf{q}\cdot\mathbf{r}-\omega t)}$. In the case of prapagation in matter, the formula would slightly change, to describe the damping of the wave, as in

$$\mathbf{E}(\mathbf{r},t) = \mathbf{E}_0 e^{i\left(\omega\sqrt{\epsilon}\hat{\mathbf{q}}\cdot\mathbf{r}-\omega t\right)}. \tag{C.1}$$

where we suppose that the dielectric function of the medium is ϵ, and that the medium is non-magnetic. In general ϵ is a complex function of the energy, and it enters in the macroscopic constitutive equation $\mathbf{D} = \epsilon\mathbf{E}$, with $\mathbf{D}$ and $\mathbf{E}$ representing the macroscopic electric displacement and the total electric field, respectively.[1] The following definitions apply

$$\sqrt{\epsilon} \quad \text{complex refractive index} \tag{C.2}$$

$$n = \mathrm{Re}\{\sqrt{\epsilon}\} \quad \text{refraction index} \tag{C.3}$$

$$\kappa = \mathrm{Im}\{\sqrt{\epsilon}\} \quad \text{extinction coefficient} \tag{C.4}$$

$$\mathrm{Im}\{\epsilon\} \quad \text{absorption coefficient} \tag{C.5}$$

$$-\mathrm{Im}\left\{\frac{1}{\epsilon}\right\} \quad \text{loss function} \tag{C.6}$$

and are used throughout the thesis. An important point here is the connection between all these *macroscopic* quantities with their *microscopic* equivalent calculated in Chapters 5 and 6. Following Refs.[195–197] we define the macroscopic dielectric function as the average operation of the (reciprocal space) microscopic quantity

$$\epsilon_M(\mathbf{q},\omega) = \frac{1}{\epsilon^{-1}_{\mathbf{G}=\mathbf{G}'=0}(\mathbf{q},\omega)}, \tag{C.7}$$

where the macroscopic dielectric function (here the *macroscopic* is highlighted by the pedix M) is the ϵ that appears in Definitions (C.2) – (C.6). In general, $\epsilon^{-1}_{00} \neq \frac{1}{\epsilon_{00}}$. The equality only holds in homogeneous media. The difference reflects the so-called crystal local field effects.

In the specific case in which the plane wave has a vanishing momentum (this the typical case for visible light, with a wavelength of the order of hundreds of nanometers, i.e. much bigger than the unit cell of a crystal), Eq. (C.7) becomes

$$\epsilon_M(\omega) = \lim_{\mathbf{q}\to 0} \frac{1}{\epsilon^{-1}_{00}(\mathbf{q},\omega)}, \tag{C.8}$$

which is normally used for optical absorption and related quantities.

[1] Mathematically, ϵ is a rank-2 tensor for it depends both on the direction of $\mathbf{D}$ and $\mathbf{E}$.

Part VI

Bibliography

Bibliography

[1] E. Becquerel. "De l'image photographique colorée du spectre solaire". In: *Annales de Chimie et de Physique* 22 (1848), pp. 451–459 (cit. on pp. 3–5).

[2] J. M. Eder. *History of photography*. Dover Publications, New York, 1978 (cit. on p. 3).

[3] T. Ang. *Photography: The Definitive Visual History*. DK, 2014 (cit. on p. 3).

[4] *History of Photography*. https://www.tandfonline.com/toc/thph20/current. 1977-present (cit. on p. 3).

[5] R. Hunt. "XLVIII. Experiments and observations on light which has permeated coloured media, and on the chemical action of the solar spectrum". In: *The London, Edinburgh, and Dublin Philosophical Magazine and Journal of Science* 16.103 (1840), pp. 267–275. eprint: https://doi.org/10.1080/14786444008650041 (cit. on p. 4).

[6] J. F. W. Herschel. "I. On the chemical action of the rays of the solar spectrum on preparations of silver and other substances, both metallic and non-metallic, and on some photographic processes". In: *Philosophical Transactions of the Royal Society of London* 130 (1840), pp. 1–59. eprint: https://royalsocietypublishing.org/doi/pdf/10.1098/rstl.1840.0002 (cit. on p. 4).

[7] S. A. des Plaques et Papier A. Lumière et ses fils. "Sensitised plates for a process of colour photography". In: *J. Soc. of Chem. Industry* 24 (1905), p. 118 (cit. on p. 4).

[8] M. Cotte et al. "Inside Cover: Rediscovering Ducos du Hauron's Color Photography through a Review of His Three-Color Printing Processes and Synchrotron Microanalysis of His Prints". In: *Angewandte Chemie International Edition* 57 (2018), pp. 7258–7258 (cit. on p. 4).

[9] G. Lippmann. "La photographie des couleurs". In: *Comptes Rendus des Seances de l'Academie des Sciences* 112 (1891), p. 274 (cit. on p. 4).

[10] G. Lippmann. "Sur la théorie de la photographie des couleurs simples et composées par la méthode interférentielle". In: *J. Phys. Theor. Appl.* 3.1 (1894), pp. 97–107 (cit. on p. 4).

[11] H. I. Bjelkhagen. "Lippmann photography". In: *History of Photography* 23.3 (1999), pp. 274–280 (cit. on p. 4).

[12] H. I. Bjelkhagen. "Improved Optical Document Security Techniques Based on Volume Holography and Lippmann Photography". In: *Optical Imaging Sensors and Systems for Homeland Security Applications*. Ed. by B. Javidi. New York, NY: Springer New York, 2006, pp. 385–400 (cit. on p. 4).

[13] M. Carey Lea. "Red and purple chloride, bromide and iodide of silver; Part I". In: *Am. J. Sci.* 33 (1887), pp. 349–364 (cit. on p. 5).

[14] W. D. W. Abney. "I. The acceleration of oxidation caused by the least refrangible end of the spectrum". In: *Proceedings of the Royal Society of London* 27.185-189 (1878), pp. 291–292. eprint: https://royalsocietypublishing.org/doi/pdf/10.1098/rspl.1878.0050 (cit. on p. 5).

[15] O. Wiener. "Farbenphotographie durch Körperfarben und mechanische Farbenanpassung in der Natur". In: *Annalen der Physik* 291.6 (1895), pp. 225–281. eprint: https://onlinelibrary.wiley.com/doi/pdf/10.1002/andp.18952910602 (cit. on p. 5).

[16] W. Zenker. *Lehrbuch der Photochromie (Photographie in natürlichen Farben) nach den wichtigsten Entdeckungen von E. Becquerel ...* Humboldt-Universität zu Berlin, 1868 (cit. on p. 5).

[17] V. de Seauve. "On the origin of colours of Edmond Becquerel's photochromatic images: a spectroscopy and electron microscopy study". PhD thesis. Paris Sciences et Lettres, 2018 (cit. on p. 5).

[18] V. d. Seauve. "On the origin of colours of Edmond Becquerel's photochromatic images : a spectroscopy and electron microscopy study". Theses. PSL Research University, Dec. 2018 (cit. on p. 6).

[19] Y. A. Krutyakov et al. "New frontiers in water purification: highly stable amphopolycarboxyglycinate-stabilized Ag–AgCl nanocomposite and its newly discovered potential". In: *Journal of Physics D: Applied Physics* 49.37 (2016), p. 375501 (cit. on p. 6).

[20] P. Wang et al. "Ag@AgCl: A Highly Efficient and Stable Photocatalyst Active under Visible Light". In: *Angewandte Chemie International Edition* 47.41 (2008), pp. 7931–7933. eprint: https://www.onlinelibrary.wiley.com/doi/pdf/10.1002/anie.200802483 (cit. on pp. 6, 9).

[21] J. Song et al. "Low temperature aqueous phase synthesis of silver/silver chloride plasmonic nanoparticles as visible light photocatalysts". In: *Dalton Trans.* 42 (38 2013), pp. 13897–13904 (cit. on p. 6).

[22] Y. Ohko et al. "Multicolour photochromism of TiO2 films loaded with silver nanoparticles". In: *Nature Materials* 2 (2003), pp. 29–31 (cit. on p. 6).

[23] K. Naoi, Y. Ohko, and T. Tatsuma. "TiO2 Films Loaded with Silver Nanoparticles: Control of Multicolor Photochromic Behavior". In: *Journal of the American Chemical Society* 126.11 (2004). PMID: 15025496, pp. 3664–3668 (cit. on p. 6).

[24] K. Matsubara and T. Tatsuma. "Morphological Changes and Multicolor Photochromism of Ag Nanoparticles Deposited on Single-crystalline TiO2 Surfaces". In: *Advanced Materials* 19.19 (2007), pp. 2802–2806. eprint: https://onlinelibrary.wiley.com/doi/pdf/10.1002/adma.200602823 (cit. on p. 6).

[25] C. Marquardt, R. Williams, and M. Kabler. "Hole self trapping and recombination luminescence in AgCl at low temperatures". In: *Solid State Communications* 9 (1971), pp. 2285–2288 (cit. on p. 6).

[26] I. Pelant and J. Hála. "Note on coexistence of free and self-trapped excitons in AgCl". In: *Solid State Communications* 78.2 (1991), pp. 141 –144 (cit. on p. 6).

[27] E. Becquerel. "De l'image photographique colorée du spectre solaire". In: *Ann. Chim. Phys* 22 (1848), pp. 451–459 (cit. on p. 9).

[28] R. G. Bates and J. MacAskill. In: *Pure & Appl. Chem.* 50 (1978), pp. 1701–1706 (cit. on p. 9).

[29] Y. Kang et al. "Antimicrobial Silver Chloride Nanoparticles Stabilized with Chitosan Oligomer for the Healing of Burns". In: *Materials (Basel)* 9 (2016), p. 215 (cit. on p. 9).

[30] N. D. Trinh, T. T. B. Nguyen, and T. H. Nguyen. "Preparation and characterization of silver chloride nanoparticles as an antibacterial agent". In: *Adv. Nat. Sci.: Nanosci. Nanotechnol.* 6 (2015), p. 045011 (cit. on p. 9).

[31] A. Adams, E. Santschi, and M. Mellencamp. "Antibacterial Properties of a Silver Chloride-Coated Nylon Wound Dressing". In: *Veterinary Surgery* 28.4 (1999), pp. 219–225 (cit. on p. 9).

[32] D. Schuerch et al. "The Silver Chloride Photoanode in Photoelectrochemical Water Splitting". In: *J. Phys. Chem. B* 106 (2002), p. 12764 (cit. on p. 9).

[33] Z. Lou et al. "The synthesis of the near-spherical AgCl crystal for visible light photocatalytic applications". In: *Dalton Trans.* 40 (16 2011), pp. 4104–4110 (cit. on p. 9).

[34] X. Zhang et al. "Plasmonic photocatalysis". In: *Reports on Progress in Physics* 76.4 (2013), p. 046401 (cit. on p. 9).

[35] B. Cai et al. "A distinctive red Ag/AgCl photocatalyst with efficient photocatalytic oxidative and reductive activities". In: *J. Mater. Chem. A* 2 (15 2014), pp. 5280–5286 (cit. on p. 9).

[36] D. Jembrih-Simberger et al. "The colour of silver stained glass: analytical investigations carried out with XRF, SEM/EDX, TEM, and IBA". In: *J. Anal. At. Spectrom.* 17 (2002), p. 321 (cit. on p. 9).

[37] W. H. Armistead and S. D. Stookey. "Photochromic silicate glasses sensitized by silver halides". In: *Science* 144 (1964), p. 150 (cit. on p. 9).

[38] J. Hamilton. "The silver halide photographic process". In: *Advances in Physics* 37.4 (1988), pp. 359–441. eprint: https://doi.org/10.1080/00018738800101399 (cit. on p. 9).

[39] R. S. Eachus, A. P. Marchetti, and A. A. Muenter. "THE PHOTOPHYSICS OF SILVER HALIDE IMAGING MATERIALS". In: *Annual Review of Physical Chemistry* 50.1 (1999). PMID: 15012408, pp. 117–144 (cit. on p. 9).

[40] C. K. Mees. *The Theory of the Photographic Process*. The MacMillan Company, New York, 1942 (cit. on p. 9).

[41] W. von der Osten. "Excitons and Exciton Relaxation in Silver Halides". In: *Polarons and Excitons in Polar Semiconductors and Ionic Crystals*. Ed. by J. Devreese and F. Peeters. Nato ASI Subseries B. New York: Springer, 1984, pp. 293–342 (cit. on pp. 9, 40).

[42] M. Ueta et al. *Excitonic processes in solids*. Springer Series in Solid-State Sciences. Springer-Verlag, 1986 (cit. on pp. 9, 40).

[43] R. Hilsch and R. W. Pohl. "Zur Photochemie der Alkali- und Silberhalogenidkristalle". In: *Zeitschrift für Physik* 64 (1930), pp. 606 –622 (cit. on p. 9).

[44] F. C. Brown and N. Wainfan. "Photolytic Darkening and Electronic Range in AgCl". In: *Phys. Rev.* 105 (1 1957), pp. 93–99 (cit. on p. 9).

[45] F. Moser, N. Nail, and F. Urbach. "Optical absorption studies of the volume photolysis of large silver chloride crystals". In: *Journal of Physics and Chemistry of Solids* 9.3 (1959), pp. 217 –234 (cit. on p. 9).

[46] L. A. Ageev, V. K. Miloslavskii, and K. I. El-Ashkhab. "Spectral photoadaptation in light-sensitive AgCl:Ag thin films". In: *Optics and Spectroscopy* 73.2 (Aug. 1992), pp. 213–216 (cit. on p. 9).

[47] W. Sesselmann and T. Chuang. "Reaction of chlorine with Ag surfaces and radiation effects by X-ray photons and Ar+ ions". In: *Surface Science* 184.3 (1987), pp. 374 –388 (cit. on p. 9).

[48] R. Egerton, P. Li, and M. Malac. "Radiation damage in the TEM and SEM". In: *Micron* 35.6 (2004). International Wuhan Symposium on Advanced Electron Microscopy, pp. 399 –409 (cit. on p. 9).

[49] G. Shi et al. "Electron Beam Induced Growth of Silver Nanoparticles". In: *Scanning* 35.2 (2013), pp. 69–74. eprint: https://onlinelibrary.wiley.com/doi/pdf/10.1002/sca.21035 (cit. on p. 9).

[50] F. Brown, T. Masumi, and H. Tippins. "Fine structure in the absorption edge of the silver halides". In: *Journal of Physics and Chemistry of Solids* 22.Supplement C (1961), pp. 101 –107 (cit. on pp. 9, 40, 44).

[51] N. J. Carrera and F. C. Brown. "Optical Response of AgCl and AgBr in the Near and Extreme Ultraviolet". In: *Phys. Rev. B* 4 (10 1971), pp. 3651–3660 (cit. on pp. 9, 10, 40, 44, 46, 48, 59).

[52] J. J. White and J. W. Straley. "Optical Properties of Silver Chloride*". In: *J. Opt. Soc. Am.* 58.6 (1968), pp. 759–763 (cit. on pp. 9, 11).

[53] P. G. Aline. "Optical and Electrical Properties of Silver Chloride". In: *Phys. Rev.* 105 (2 1957), pp. 406–412 (cit. on p. 9).

[54] P. L. Hartman and R. C. Merrill. "Reflectivity of Silver Chloride in the Ultraviolet*". In: *J. Opt. Soc. Am.* 51.2 (1961), pp. 168–170 (cit. on pp. 9, 10).

[55] S. Tutihasi. "Optical Absorption by Silver Halides". In: *Phys. Rev.* 105 (3 1957), pp. 882–884 (cit. on p. 9).

[56] F. Moser and F. Urbach. "Optical Absorption of Pure Silver Halides". In: *Phys. Rev.* 102 (6 1956), pp. 1519–1523 (cit. on p. 9).

[57] F. Bassani, R. S. Knox, and W. B. Fowler. "Band Structure and Electronic Properties of AgCl and AgBr". In: *Phys. Rev.* 137 (4A 1965), A1217–A1225 (cit. on pp. 11, 40).

[58] J. S.-Y. Wang, M. Schlüter, and M. L. Cohen. "The electronic structure of AgCl. Energy bands, densities of states, and charge densities". In: *physica status solidi (b)* 77.1 (1976), pp. 295–300 (cit. on p. 11).

[59] X. Ma et al. "The Role of Effective Mass of Carrier in the Photocatalytic Behavior of Silver Halide-Based Ag@AgX (X=Cl, Br, I): A Theoretical Study". In: *ChemPhysChem* 13.9 (2012), pp. 2304–2309 (cit. on pp. 11, 39).

[60] T. Benmessabih et al. "Computational study of AgCl and AgBr semiconductors". In: *Physica B: Condensed Matter* 392.1 (2007), pp. 309 –317 (cit. on pp. 11, 39).

[61] B. Amrani, F. E. H. Hassan], and M. Zoaeter. "First-principles study of rock-salt AgClxBr1-x alloy". In: *Physica B: Condensed Matter* 396.1 (2007), pp. 192 –198 (cit. on p. 11).

[62] A. Zaoui, M. Ferhat, and J. Hugel. "Ab initio investigation of the electronic structure of AgCl". In: *Superlattices and Microstructures* 38.1 (2005), pp. 57 –68 (cit. on p. 11).

[63] C. Okoye. "Full-Potential Study of the Electronic Structure of Silver Halides". In: *physica status solidi (b)* 234.2 (2002), pp. 580–589 (cit. on pp. 11, 39).

[64] P. K. de Boer and R. A. de Groot. "Conduction Band of the Photographic Compound AgCl". In: *The Journal of Physical Chemistry A* 103.26 (1999), pp. 5113–5115 (cit. on pp. 11, 41).

[65] D. Vogel, P. Krüger, and J. Pollmann. "Ab initio electronic structure of silver halides calculated with self-interaction and relaxation-corrected pseudopotentials". In: *Phys. Rev. B* 58 (7 1998), pp. 3865–3869 (cit. on pp. 11, 39).

[66] P. Hohenberg and W. Kohn. "Inhomogeneous Electron Gas". In: *Phys. Rev.* 136 (3B 1964), B864–B871 (cit. on pp. 11, 17).

[67] W. Kohn and L. J. Sham. "Self-Consistent Equations Including Exchange and Correlation Effects". In: *Phys. Rev.* 140 (4A 1965), A1133–A1138 (cit. on pp. 11, 18, 19).

[68] L. Hedin. "New Method for Calculating the One-Particle Green's Function with Application to the Electron-Gas Problem". In: *Phys. Rev.* 139 (3A 1965), A796–A823 (cit. on pp. 11, 25–27).

[69] A. L. Fetter and J. D. Walecka. *Quantum theory of many-particle systems*. McGraw-Hill, New York, 1971 (cit. on p. 11).

[70] M. J. van Setten et al. "Automation methodologies and large-scale validation for GW: Towards high-throughput GW calculations". In: *Phys. Rev. B* 96 (15 2017), p. 155207 (cit. on pp. 11, 42).

[71] W. Gao et al. "Quasiparticle band structures of CuCl, CuBr, AgCl, and AgBr: The extreme case". In: *Phys. Rev. B* 98 (4 2018), p. 045108 (cit. on pp. 11, 43, 54).

[72] M.-Y. Zhang and H. Jiang. "Electronic band structure of cuprous and silver halides: An all-electron GW study". In: *Phys. Rev. B* 100 (20 2019), p. 205123 (cit. on pp. 11, 42, 43).

[73] K. Burke. "Perspective on density functional theory". In: *The Journal of Chemical Physics* 136.15 (2012), p. 150901 (cit. on p. 17).

[74] R. G. Parr and W. Yang. *Density-Functional Theory of Atoms and Molecules*. Oxford University Press, 1989 (cit. on pp. 17, 18).

[75] R. M. Dreizler and E. K. U. Gross. *Density Functional Theory: An Approach to the Quantum Many-Body Problem*. Springer, 1990 (cit. on pp. 17, 18).

[76] R. M. Martin. *Electronic Structure. Basic Theory and Practical Methods*. Cambridge University Press, 2008 (cit. on pp. 17, 18).

[77] R. van Leeuwen. "Density functional approach to the many-body problem: key concepts and exact functionals". In: *Adv. Quantum Chem.* 43 (2003), p. 25 (cit. on p. 17).

[78] K. Capelle. "A bird's-eye view of density-functional theory". In: *Brazilian Journal of Physics* 36 (2006), pp. 1318 –1343 (cit. on p. 17).

[79] K. Burke and L. O. Wagner. "DFT in a nutshell". In: *International Journal of Quantum Chemistry* 113 (2013), p. 96 (cit. on p. 17).

[80] R. Van Noorden, B. Maher, and R. Nuzzo. "The top 100 papers". In: *Nature* 514 (2014), p. 550 (cit. on p. 19).

[81] D. M. Ceperley and B. J. Alder. "Ground State of the Electron Gas by a Stochastic Method". In: *Phys. Rev. Lett.* 45 (7 1980), pp. 566–569 (cit. on p. 19).

[82] M. Bühl et al. "Geometries of Third-Row Transition-Metal Complexes from Density-Functional Theory". In: *Journal of Chemical Theory and Computation* 4.9 (2008), pp. 1449–1459 (cit. on p. 19).

[83] J. P. Perdew et al. "Restoring the Density-Gradient Expansion for Exchange in Solids and Surfaces". In: *Phys. Rev. Lett.* 100 (2008), p. 136406 (cit. on p. 19).

[84] J. P. Perdew, K. Burke, and M. Ernzerhof. "Generalized Gradient Approximation Made Simple". In: *Phys. Rev. Lett.* 77 (1996), pp. 3865–3868 (cit. on pp. 20, 39).

[85] V. N. Staroverov et al. "Tests of a ladder of density functionals for bulk solids and surfaces". In: *Phys. Rev. B* 69 (2004), p. 075102 (cit. on p. 20).

[86] Y. Zhao and D. G. Truhlar. "Construction of a generalized gradient approximation by restoring the density-gradient expansion and enforcing a tight Lieb–Oxford bound". In: *The Journal of Chemical Physics* 128.18 (2008), p. 184109 (cit. on p. 20).

[87] A. D. Becke. "A new mixing of Hartree-Fock and local density-functional theories". In: *J. Chem. Phys.* 98 (1993), pp. 1372–1377 (cit. on p. 20).

[88] F. Furche and J. P. Perdew. "The performance of semilocal and hybrid density functionals in 3d transition-metal chemistry". In: *The Journal of Chemical Physics* 124.4 (2006), p. 044103 (cit. on p. 20).

[89] D. Hait and M. Head-Gordon. "How Accurate Is Density Functional Theory at Predicting Dipole Moments? An Assessment Using a New Database of 200 Benchmark Values". In: *Journal of Chemical Theory and Computation* 14 (2018), pp. 1969–1981 (cit. on p. 20).

[90] J. P. Perdew et al. "Density-Functional Theory for Fractional Particle Number: Derivative Discontinuities of the Energy". In: *Phys. Rev. Lett.* 49 (23 1982), pp. 1691–1694 (cit. on p. 20).

[91] P. Mori-Sánchez and A. Cohen. "The derivative discontinuity of the exchange-correlation functional". In: *Physical chemistry chemical physics : PCCP* 16 (Mar. 2014) (cit. on p. 20).

[92] M. Kuisma et al. "Kohn-Sham potential with discontinuity for band gap materials". In: *Phys. Rev. B* 82 (11 2010), p. 115106 (cit. on p. 20).

[93] E. Baerends. "From the Kohn-Sham band gap to the fundamental gap in solids. An integer electron approach". In: *Phys. Chem. Chem. Phys.* 19 (June 2017) (cit. on p. 20).

[94] S. Cavo, J. A. Berger, and P. Romaniello. "Accurate optical spectra of solids from pure time-dependent density functional theory". In: *Phys. Rev. B* 101 (11 2020), p. 115109 (cit. on p. 20).

[95] E. Runge and E. K. U. Gross. "Density-Functional Theory for Time-Dependent Systems". In: *Phys. Rev. Lett.* 52 (12 1984), pp. 997–1000 (cit. on p. 21).

[96] V. Peuckert. In: *J. Phys. C* 11 (1978), p. 4945 (cit. on p. 21).

[97] A. Zangwill and P. Soven. In: *Phys. Rev. A* 21 (1980), p. 1561 (cit. on p. 21).

[98] M. A. Marques et al., eds. *Time-Dependent Density Functional Theory*. Springer, Berlin, Heidelberg, 2006 (cit. on p. 21).

[99] C. A. Ullrich. *Time-Dependent Density-Functional Theory: Concepts and Applications*. Oxford Scholarship Online, 2011 (cit. on p. 21).

[100] M. A. Marques et al., eds. *Fundamentals of Time-Dependent Density Functional Theory*. Springer, Berlin, Heidelberg, 2012 (cit. on p. 21).

[101] P. Ghosez, X. Gonze, and R. W. Godby. In: *Phys. Rev. B* 56 (1997), p. 12811 (cit. on pp. 24, 47).

[102] L. Reining et al. "Excitonic Effects in Solids Described by Time-Dependent Density-Functional Theory". In: *Phys. Rev. Lett.* 88 (6 2002), p. 066404 (cit. on pp. 24, 47).

[103] S. Botti et al. "Long-range contribution to the exchange-correlation kernel of time-dependent density functional theory". In: *Phys. Rev. B* 69 (15 2004), p. 155112 (cit. on pp. 24, 47).

[104] P. E. Trevisanutto et al. "Optical spectra of solids obtained by time-dependent density functional theory with the jellium-with-gap-model exchange-correlation kernel". In: *Phys. Rev. B* 87 (20 2013), p. 205143 (cit. on pp. 24, 47).

[105] M. Hellgren and E. K. U. Gross. "Discontinuous functional for linear-response time-dependent density-functional theory: The exact-exchange kernel and approximate forms". In: *Phys. Rev. A* 88 (5 2013), p. 052507 (cit. on pp. 24, 47).

[106] S. Sharma et al. "Bootstrap Approximation for the Exchange-Correlation Kernel of Time-Dependent Density-Functional Theory". In: *Phys. Rev. Lett.* 107 (18 2011), p. 186401 (cit. on pp. 24, 47).

[107] S. Rigamonti et al. "Estimating Excitonic Effects in the Absorption Spectra of Solids: Problems and Insight from a Guided Iteration Scheme". In: *Phys. Rev. Lett.* 114 (14 2015), p. 146402 (cit. on pp. 24, 47).

[108] E. Economou. *Green's Functions in Quantum Physics*. Springer Series in Solid-State Sciences. Springer, 2006 (cit. on p. 25).

[109] F. Sottile. "Response functions of semiconductors and insulators : from the Bethe-Salpeter equation to time-dependent density functional theory". Theses. Ecole Polytechnique X, Sept. 2003 (cit. on pp. 25, 31).

[110] M. Gatti. "Ab-Initio Calculations of Many body effects in electronic spectre." Theses. Ecole Polytechnique X, Dec. 2007 (cit. on p. 25).

[111] R. Martin, L. Reining, and D. Ceperley. *Interacting Electrons: Theory and computational Approaches*. Cambridge: Cambridge University Press, 2016 (cit. on pp. 27, 28, 44).

[112] M. S. Hybertsen and S. G. Louie. "Electron correlation in semiconductors and insulators: Band gaps and quasiparticle energies". In: *Phys. Rev. B* 34.8 (1986), pp. 5390–5413 (cit. on pp. 27, 43).

[113] R. W. Godby, M. Schlüter, and L. J. Sham. "Self-energy operators and exchange-correlation potentials in semiconductors". In: *Phys. Rev. B* 37.17 (1988), pp. 10159–10175 (cit. on p. 27).

[114] F. Aryasetiawan and O. Gunnarsson. In: *Rep. Prog. Phys.* 61 (1998), p. 237 (cit. on pp. 27, 28).

[115] W. G. Aulbur, L. Jönsson, and J. W. Wilkins. In: *Solid State Phys.* 54 (1999), p. 1 (cit. on pp. 27, 28).

[116] F. Bechstedt. *Many-Body Approach to Electronic Excitations: Concepts and Applications*. Springer Series in Solid-State Sciences. Springer Berlin Heidelberg, 2014 (cit. on p. 28).

[117] S. V. Faleev, M. van Schilfgaarde, and T. Kotani. "All-Electron Self-Consistent GW Approximation: Application to Si, MnO, and NiO". In: *Phys. Rev. Lett.* 93 (12 2004), p. 126406 (cit. on p. 28).

[118] M. van Schilfgaarde, T. Kotani, and S. Faleev. "Quasiparticle Self-Consistent GW Theory". In: *Phys. Rev. Lett.* 96 (20 2006), pp. 226402–226402 (cit. on pp. 28, 43, 44).

[119] F. Bruneval, N. Vast, and L. Reining. "Effect of self-consistency on quasiparticles in solids". In: *Phys. Rev. B* 74.4, 045102 (2006), p. 045102 (cit. on p. 28).

[120] F. Bruneval and M. Gatti. "Quasiparticle Self-Consistent GW Method for the Spectral Properties of Complex Materials". In: *Top. Curr. Chem.* 347 (2014), pp. 99–135 (cit. on pp. 28, 44).

[121] R. W. Godby and R. J. Needs. "Metal-insulator transition in Kohn-Sham theory and quasiparticle theory". In: *Phys. Rev. Lett.* 62 (10 1989), pp. 1169–1172 (cit. on p. 28).

[122] S. Lebègue et al. "Implementation of an all-electron GW approximation based on the projector augmented wave method without plasmon pole approximation: Application to Si, SiC, AlAs, InAs, NaH, and KH". In: *Phys. Rev. B* 67 (15 2003), p. 155208 (cit. on p. 28).

[123] H. A. Bethe and E. E. Salpeter. "A RELATIVISTIC EQUATION FOR BOUND STATE PROBLEMS". English. In: *Phys. Rev.* 82 (2 1951), pp. 309–310 (cit. on p. 29).

[124] G. Strinati. In: *Rivista del Nuovo Cimento* 11 (1988). and references therein, p. 1 (cit. on p. 29).

[125] W. Hanke and L. J. Sham. "Many-Particle Effects in the Optical Excitations of a Semiconductor". In: *Phys. Rev. Lett.* 144.5 (1979), pp. 387–390 (cit. on p. 29).

[126] S. Albrecht et al. "Ab Initio Calculation of Excitonic Effects in the Optical Spectra of Semiconductors". In: *Phys. Rev. Lett.* 80.20 (1998), pp. 4510–4513 (cit. on pp. 29, 49).

[127] M. Rohlfing and S. G. Louie. In: *Phys. Rev. B* 62 (2000), p. 4927 (cit. on pp. 29, 61).

[128] G. Onida, L. Reining, and A. Rubio. "Electronic excitations: density-functional versus many-body Green's-function approaches". In: *Rev. Mod. Phys.* 74 (2 2002), pp. 601–659 (cit. on pp. 29, 46, 49).

[129] I. Tamm. "Relativistic Interaction of Elementary Particles". In: *J. Phys. (USSR)* 9 (1945), p. 449 (cit. on p. 30).

[130] S. M. Dancoff. "Non-Adiabatic Meson Theory of Nuclear Forces". In: *Phys. Rev.* 78 (4 1950), pp. 382–385 (cit. on p. 30).

[131] I. Reshetnyak. "Computing optical properties and photo-emission spectra : a new starting point ". Theses. Ecole Polytechnique, Sept. 2015 (cit. on p. 31).

[132] In: () (cit. on p. 33).

[133] J. C. M. Garnett and J. Larmor. "XII. Colours in metal glasses and in metallic films". In: *Philosophical Transactions of the Royal Society of London. Series A, Containing Papers of a Mathematical or Physical Character* 203.359-371 (1904), pp. 385–420. eprint: https://royalsocietypublishing.org/doi/pdf/10.1098/rsta.1904.0024 (cit. on p. 33).

[134] D. J. Bergman. "The dielectric constant of a composite material: A problem in classical physics". In: *Physics Reports* 43.9 (1978), pp. 377 –407 (cit. on p. 33).

[135] V. Agranovich and V. Kravtsov. "Notes on crystal optics of superlattices". In: *Solid State Communications* 55.1 (1985), pp. 85 –90 (cit. on p. 33).

[136] V. de Seauve et al. "Replication and study of the colouration of Edmond Becquerel's photochromatic images". In: *Journal of Cultural Heritage* (2020) (cit. on p. 37).

[137] A. Lorin et al. "First-principles study of excitons in the optical spectra of silver chloride". In: (2020). arXiv: 2009.08699 [cond-mat.mtrl-sci] (cit. on p. 37).

[138] N. Troullier and J. L. Martins. "Efficient pseudopotentials for plane-wave calculations". In: *Phys. Rev. B* 43 (3 1991), pp. 1993–2006 (cit. on p. 37).

[139] M. Fuchs and M. Scheffler. "Ab initio pseudopotentials for electronic structure calculations of poly-atomic systems using density-functional theory". In: *Computer Physics Communications* 119.1 (1999), pp. 67 –98 (cit. on pp. 37, 38).

[140] J. P. Perdew and Y. Wang. "Accurate and simple analytic representation of the electron-gas correlation energy". In: *Phys. Rev. B* 45 (23 1992), pp. 13244–13249 (cit. on p. 37).

[141] G. B. Bachelet, D. R. Hamann, and M. Schlüter. "Pseudopotentials that work: From H to Pu". In: *Phys. Rev. B* 26 (8 1982), pp. 4199–4228 (cit. on p. 37).

[142] M. Rohlfing, P. Krüger, and J. Pollmann. "Quasiparticle Band Structure of CdS". In: *Phys. Rev. Lett.* 75 (19 1995), pp. 3489–3492 (cit. on p. 37).

[143] A. Marini, G. Onida, and R. Del Sole. "Quasiparticle Electronic Structure of Copper in the GW Approximation". In: *Phys. Rev. Lett.* 88.1 (2001), p. 016403 (cit. on p. 37).

[144] F. Bruneval et al. "Exchange and Correlation Effects in Electronic Excitations of Cu[sub 2]O". In: *Phys. Rev. Lett.* 97.26, 267601 (2006), p. 267601 (cit. on p. 37).

[145] X. Gonze et al. "A brief introduction to the ABINIT software package". In: *Z. Kristallogr* 220 (2005), pp. 558–562 (cit. on p. 38).

[146] R. W. Wyckoff. *The Structure Of Crystals*. The Chemical Catalog Company Inc., 1963 (cit. on p. 39).

[147] C. R. Berry. "Physical Defects in Silver Halides". In: *Phys. Rev.* 97 (3 Berry), pp. 676–679 (cit. on p. 39).

[148] H. J. Monkhorst and J. D. Pack. "Special points for Brillouin-zone integrations". In: *Phys. Rev. B* 13.12 (June 1976), pp. 5188–5192 (cit. on p. 39).

[149] B. R. Lawn. "Thermal expansion of silver halides". In: *Acta Crystallographica* 16.11 (1963), pp. 1163–1169 (cit. on p. 39).

[150] K Nakamura and W von der Osten. "Exciton relaxation in AgCl studied by resonant Raman scattering". In: *Journal of Physics C: Solid State Physics* 16.34 (1983), pp. 6669–6680 (cit. on p. 40).

[151] J. Tejeda et al. "Valence bands of AgCl and AgBr: uv photoemission and theory". In: *Phys. Rev. B* 12 (4 1975), pp. 1557–1566 (cit. on pp. 40–43).

[152] A. B. Kunz. "Electronic structure of AgF, AgCl, and AgBr". In: *Phys. Rev. B* 26 (4 1982), pp. 2070–2075 (cit. on p. 40).

[153] M. G. Mason. "Photoelectron spectroscopy studies of the band structures of silver halides". In: *Phys. Rev. B* 11 (12 1975), pp. 5094–5102 (cit. on pp. 41–43).

[154] J. Yeh and I. Lindau. "Atomic subshell photoionization cross sections and asymmetry parameters: 1 ¡ Z ¡ 103". In: *Atomic Data and Nuclear Data Tables* 32.1 (1985), pp. 1 –155 (cit. on p. 41).

[155] X. Gonze et al. "Recent developments in the ABINIT software package". In: *Comput. Phys. Commun.* 205 (2016), pp. 106–131 (cit. on p. 41).

[156] B.-C. Shih et al. "Quasiparticle Band Gap of ZnO: High Accuracy from the Conventional G0W0 Approach". In: *Phys. Rev. Lett.* 105 (14 2010), p. 146401 (cit. on p. 43).

[157] C. Friedrich, M. C. Müller, and S. Blügel. "Band convergence and linearization error correction of all-electron GW calculations: The extreme case of zinc oxide". In: *Phys. Rev. B* 83 (8 2011), p. 081101 (cit. on p. 43).

[158] M. Stankovski et al. "G0W0 band gap of ZnO: Effects of plasmon-pole models". In: *Phys. Rev. B* 84 (24 2011), p. 241201 (cit. on p. 43).

[159] W. Kang and M. S. Hybertsen. "Quasiparticle and optical properties of rutile and anatase TiO2". In: *Phys. Rev. B* 82 (8 2010), p. 085203 (cit. on p. 43).

[160] J. A. Berger, L. Reining, and F. Sottile. "Ab initio calculations of electronic excitations: Collapsing spectral sums". In: *Phys. Rev. B* 82 (4 2010), p. 041103 (cit. on p. 43).

[161] A. Svane et al. "Quasiparticle band structures of β-HgS, HgSe, and HgTe". In: *Phys. Rev. B* 84 (20 2011), p. 205205 (cit. on p. 44).

[162] V. de Seauve et al. "Spectroscopies and Electron Microscopies Unravel the Origin of the First Colour Photographs". In: *Angewandte Chemie International Edition* 59.23 (2020), pp. 9113–9119 (cit. on p. 45).

[163] F. Sottile, L. Reining, and V. Olevano. *The DP code*. `https://etsf.polytechnique.fr/software/Ab_Initio/` (cit. on pp. 45, 129).

[164] L. X. Benedict, E. L. Shirley, and R. B. Bohn. "Optical Absorption of Insulators and the Electron-Hole Interaction: An Ab Initio Calculation". In: *Phys. Rev. Lett.* 80 (1998), pp. 4514–4517 (cit. on pp. 45, 48).

[165] L. W. Tilton, E. K. Plyler, and R. E. Stephens. "Refractive Index of Silver Chloride for Visible and Infra-Red Radiant Energy*". In: *J. Opt. Soc. Am.* 40.8 (1950), pp. 540–543 (cit. on p. 47).

[166] L. Reining et al. *The EXC Code*. `https://etsf.polytechnique.fr/software/Ab_Initio/`. unpublished (cit. on pp. 48, 129).

[167] R. Haydock. "The recursive solution of the Schrodinger equation". In: *Computer Physics Communications* 20 (1980), pp. 11 –16 (cit. on p. 48).

[168] L. X. Benedict, E. L. Shirley, and R. B. Bohn. "Theory of optical absorption in diamond, Si, Ge, and GaAs". In: *Phys. Rev. B* 57 (16 1998), R9385–R9387 (cit. on p. 48).

[169] B. I. Lundqvist. "Single-particle spectrum of the degenerate electron gas". In: *Physik der kondensierten Materie* 6.3 (Sept. 1967), pp. 206–217 (cit. on p. 51).

[170] D. L. Johnson. "Local field effects and the dielectric response matrix of insulators: A model". In: *Phys. Rev. B* 9 (10 1974), pp. 4475–4484 (cit. on p. 51).

[171] Z. H. Levine and S. G. Louie. "New model dielectric function and exchange-correlation potential for semiconductors and insulators". In: *Phys. Rev. B* 25 (10 1982), pp. 6310–6316 (cit. on p. 51).

[172] F BECHSTEDT et al. "MODEL FOR INVERSE DIELECTRIC MATRICES OF SEMICONDUCTORS". In: *SOLID STATE COMMUNICATIONS* 89.8 (1994), pp. 669–672 (cit. on p. 51).

[173] E. L. Shirley. "Local screening of a core hole: A real-space approach applied to hafnium oxide". In: *Ultramicroscopy* 106.11 (2006). Proceedings of the International Workshop on Enhanced Data Generated by Electrons, pp. 986 –993 (cit. on p. 51).

[174] M. Rohlfing. "Electronic excitations from a perturbative LDA+GdW approach". In: *Phys. Rev. B* 82 (20 2010), p. 205127 (cit. on p. 51).

[175] A. Tal et al. *Accurate optical spectra through time-dependent density functional theory based on screening-dependent hybrid functionals*. 2020. arXiv: `2002.02222 [cond-mat.mtrl-sci]` (cit. on p. 51).

[176] J. Vinson and E. L. Shirley. *Revisiting a local, real-space approach to dielectric screening calculations*. 2020. arXiv: `2005.07834 [cond-mat.mtrl-sci]` (cit. on p. 51).

[177] L. V. Keldysh. In: *JETP Lett.* 29 (1979), p. 658 (cit. on p. 51).

[178] P. Cudazzo, I. V. Tokatly, and A. Rubio. "Dielectric screening in two-dimensional insulators: Implications for excitonic and impurity states in graphane". In: *Phys. Rev. B* 84 (8 2011), p. 085406 (cit. on p. 51).

[179] S. Latini, T. Olsen, and K. S. Thygesen. "Excitons in van der Waals heterostructures: The important role of dielectric screening". In: *Phys. Rev. B* 92 (24 2015), p. 245123 (cit. on p. 51).

[180] M. L. Trolle, T. G. Pedersen, and V. Veniard. "Model dielectric function for 2D semiconductors including substrate screening". In: *SCIENTIFIC REPORTS* 7 (2017) (cit. on p. 51).

[181] G. Cappellini et al. "Model dielectric function for semiconductors". In: *Phys. Rev. B* 47 (15 1993), pp. 9892–9895 (cit. on p. 51).

[182] S. Baroni and R. Resta. "Ab initio calculation of the macroscopic dielectric constant in silicon". In: *Phys. Rev. B* 33 (10 1986), pp. 7017–7021 (cit. on p. 51).

[183] K. Wakamura et al. "Photo induced narrowing of TO-LO splitting and mobile defect in AgCl". In: *Physica B: Condensed Matter* 219-220 (1996), pp. 457 –459 (cit. on p. 54).

[184] R. P. Lowndes. "Anharmonicity in the Silver and Thallium Halides: Low-Frequency Dielectric Response". In: *Phys. Rev. B* 6 (12 1972), pp. 4667–4674 (cit. on p. 54).

[185] M. Gatti, F. Sottile, and L. Reining. "Electron-hole interactions in correlated electron materials: Optical properties of vanadium dioxide from first principles". In: *Phys. Rev. B* 91 (19 2015), p. 195137 (cit. on p. 57).

[186] H. Ehrenreich, H. R. Philipp, and B. Segall. "Optical Properties of Aluminum". In: *Phys. Rev.* 132 (5 1963), pp. 1918–1928 (cit. on p. 59).

[187] W. A. Harrison. "Parallel-Band Effects in Interband Optical Absorption". In: *Phys. Rev.* 147 (2 1966), pp. 467–469 (cit. on p. 59).

[188] M. Rohlfing and S. G. Louie. "Electron-Hole Excitations in Semiconductors and Insulators". In: *Phys. Rev. Lett.* 81 (11 1998), pp. 2312–2315 (cit. on p. 61).

[189] M. Gatti and F. Sottile. "Exciton dispersion from first principles". In: *Phys. Rev. B* 88 (15 2013), p. 155113 (cit. on p. 61).

[190] G. E. Simion and G. F. Giuliani. "Friedel oscillations in a Fermi liquid". In: *Phys. Rev. B* 72 (4 2005), p. 045127 (cit. on p. 85).

[191] G. F. Giuliani and G. Vignale. *Quantum theory of the electron liquid*. Cambridge: Cambridge Univ. Press, 2005 (cit. on p. 85).

[192] S. Botti et al. "Ab Initio Calculations of the Anisotropic Dielectric Tensor of GaAs/AlAs Superlattices". In: *Phys. Rev. Lett.* 89 (21 2002), p. 216803 (cit. on p. 107).

[193] A. Marini, R. Del Sole, and A. Rubio. "Bound Excitons in Time-Dependent Density-Functional Theory: Optical and Energy-Loss Spectra". In: *Phys. Rev. Lett.* 91.25 (2003), p. 256402 (cit. on p. 112).

[194] *SRden: a tool to plot the induced density*. to be published, under a BSD-like license (cit. on p. 129).

[195] S. L. Adler. "Quantum Theory of the Dielectric Constant in Real Solids". In: *Phys. Rev.* 126 (2 1962), pp. 413–420 (cit. on p. 133).

[196] N. Wiser. "Dielectric Constant with Local Field Effects Included". In: *Phys. Rev.* 129 (1 1963), pp. 62–69 (cit. on p. 133).

[197] O. Dolgov and E. Maksimov. "The Dielectric Function of Crystalline Systems". In: ed. by L. Keldysh, D. Kirzhnitz, and A. Maradudin. Elsevier Science Publishing, 1989 (cit. on p. 133).

ECOLE DOCTORALE

Titre: Propriétés électroniques du chlorure d'argent: l'influence des excitons sur la dynamique des charges

Mots clés: Excitations électronique, Ab initio, Propriétés optiques

Résumé: En 1848, Edmond Becquerel proposa une des toutes premières techniques de photographie en couleur. Ce procédé suscita parmi la communauté scientifique de nombreux débats sur l'origine des couleurs observées. En 2019, Victor de Seauve, dans une thèse au Muséum National d'Histoire Naturelle à Paris, a apporté de nombreuses clarifications, proposant une nouvelle explication. Le facteur clé de cette explication est la dynamique des charges, en réaction à la lumière, dans un composé de chlorure d'argent (AgCl) qui contient des nanoparticules d'argent. L'objectif de la présente thèse est de participer à cet effort de compréhension en apportant un éclairage théorique. La première question concerne le niveau de théorie nécessaire pour décrire correctement les propriétés électroniques et optiques d'AgCl. Nos calculs ont montré que seule la solution de l'équation Bethe-Salpeter peut décrire le spectre optique d'AgCl, car ce spectre est dominé par un fort pic d'absorption dû à un exciton lié. De plus, le calcul doit s'appuyer sur une structure de bandes qui est déterminée de manière auto-cohérente dans un calcul GW, très lourd numériquement. Afin de pouvoir réaliser le calcul dans le cadre de l'équation de Bethe-Salpeter, une fonction diélectrique modèle a été utilisée et améliorée. Les résultats de nos calculs décrivent bien les spectres mesurés, et nous ont permis d'analyser et d'interpréter les observations. Dans l'hypothèse avancée par l'équipe du Muséum, la lumière excite une nanoparticule d'argent, ce qui provoque un transfert de charges à l'interface entre la nanoparticule et AgCl. Avec l'objectif de pouvoir étudier ce phénomène, une approche numérique pour accéder à la dynamique des charges induites par une perturbation externe a été développée. Cette approche a en particulier permis de montrer qu'un état excitonique lié influence la dynamique des charges de façon très importante. Enfin, nous avons effectué une première modélisation du transfert de charge aux interfaces entre une nanoparticule d'argent et AgCl, en étudiant une hétéro-structure simplifiée. Nous avons montré le changement du spectre de AgCl dû au voisinage de l'argent métallique et validé l'utilisation de la théorie des milieux effectifs pour décrire ces changements. Des calculs de la densité induite par des perturbations périodiques ont été réalisés. Ces calculs restent lourds, et l'étude se poursuivra avec l'idée de combiner les calculs *ab initio* avec la théorie des milieux effectifs.

Title: Electronic properties of silver chloride: influence of excitons on the charge dynamics

Keywords: Electronic excitations, Ab initio, Optical properties

Abstract: In 1848, Edmond Becquerel proposed one of the first techniques of color photography. This technique raised a long-standing debate in the scientific community concerning the origin of the observed colors. In 2019, Victor de Seauve, during his thesis at the Muséum National d'Histoire Naturelle in Paris, could clarify some important issues, proposing a new explanation. The aim of the present thesis was to participate in this effort of comprehension, by adding theoretical insight. The first question is which level of theory one may adopt in order to correctly describe the electronic and optical properties of AgCl. Our calculations show that only the solution of the Bethe-Salpeter equation is able to describe the optical spectrum of AgCl, since the spectrum is dominated by a strong peak at the absorption onset, due to a bound exciton. Moreover, the calculation has to be based on a band structure that results from a self-consistent GW calculation. In order to make the Bethe-Salpeter calculations possible, a previously proposed model dielectric function was used in an improved way. Our results well describe the measured absorption spectra, and enable us to analyse and interpret the observations. In the hypothesis brought forward by the team at the Museum, the light excites a silver nanoparticle, followed by a transfer of charge at the interface between the nanoparticle and AgCl. In order to be able to study this phenomenon, we have developed a numerical approach describing the charge dynamics due to an external perturbation. In particular, this approach has allowed us to show that a bound exciton influences the charge dynamics significantly. Finally, we have set up a first model meant to simulate the charge transfer between a silver nanoparticle and AgCl, based on a simplified heterostructure. We have shown how the absorption spectrum of AgCl changes due to its neighbourhood to the silver metal, and how these changes can be described by the effective medium theory. Calculations of the density induced by a periodic perturbation have been carried out.These calculations remain cumbersome, and the study will continue with the idea to combine *ab initio* calculations with effective medium theory.

Institut Polytechnique de Paris
91120 Palaiseau, France